11th INTERNATIONAL CONFERENCE ON MATERIALS SCIENCE AND CONDENSED MATTER PHYSICS

dedicated to the
100th anniversary of the birth of Academician Sergiu Rădăuțan,
90th anniversary of the birth of Academician Pavel Vlad,
80th anniversary of the foundation of Moldova State University

ABSTRACTS

MSCMP 2026



mscmp CHIȘINAU 2026

Chișinău, Moldova, September 1-4, 2026


VITAE DISCIMUS


FA


FACULTATEA FIZICĂ ȘI INGINERIE


INSTITUTUL DE CHIMIE


NATO
OTAN
The Science for Peace and Security (SPS) Programme


INFLPR
NATIONAL INSTITUTE FOR LASER,
PLASMA AND RADIATION PHYSICS


PHANOS


RONEXPRIM
35
1991
2026
YEARS
WE DELIVER PERFORMANCE


CHROMAVANSA


LABROMED LABORATOR


schaefer scientific
SINCE 1963

11th INTERNATIONAL CONFERENCE ON MATERIALS SCIENCE AND CONDENSED MATTER PHYSICS



dedicated to the
100th anniversary of the birth of Academician Sergiu Rădăuțan,
90th anniversary of the birth of Academician Pavel Vlad,
80th anniversary of the foundation of Moldova State University

Chisinau 2026

Descrierea CIP a Camerei Naţionale a Cărţii din Republica Moldova

"Materials Science and Condensed Matter Physics", international conference (11 ; 2026 ; Chisinau). 11th International Conference on Materials Science and Condensed Matter Physics : MSCMP : Chisinau 2026, September 1-4, 2026 / conference organizers: Leonid Culiuc (Kulyuk) (chair) [et al.]. – Chisinau : [S. n.], 2026 (CEP USM). – 219 p. : fig. color, tab.

Antetit.: Institute of Applied Physics, Faculty of Physics and Engineering, Institute of Chemistry of Moldova State University [et al.]. – Ref. bibliogr. la sfârşitul abstractelor. – Ind. de nume: p. 199-219. – 210 ex.

ISBN 978-9975-77-570-0.
Text : nemediat.
538.9/539(082)
M 47

ISBN 978-9975-77-570-0.
© Editura USM, 2026

To the reader,

This book comprises the abstracts of the communications presented at the ***11th International Conference on Materials Science and Condensed Matter Physics (MSCMP 2026)****, held on 1–4 September 2026 in Chișinău, Republic of Moldova.*

MSCMP is a traditional biennial forum, founded and developed over the decades by the Institute of Applied Physics, which brings together the materials science and condensed matter physics communities of the Republic of Moldova and their partners from abroad. The present edition is organised by the Institute of Applied Physics together with Faculty of Physcis and Engineering and the Institute of Chemistry of Moldova State University. The joint effort reflects the character of contemporary materials research, in which the design and synthesis of new compounds, their structural characterisation and the study of their physical properties can no longer be treated separately.

The 11th edition of the conference is dedicated to three anniversaries that are inseparable from the history of science and higher education in our country:

- *the* ***100th anniversary of the birth of Academician Sergiu Rădăuțan (1926–1998)****, founder of the Moldovan school of physics and chemistry of semiconductor materials, founder of the Laboratory of Semiconductor Compounds of the Institute of Applied Physics and first rector of the Polytechnic Institute of Chișinău;*
- *the* ***90th anniversary of the birth of Academician Pavel Vlad (1936–2017)****, founder of the school of organic and bioorganic chemistry and of the chemistry of natural and physiologically active compounds, and long-standing director of the Institute of Chemistry;*
- *the* ***80th anniversary of the foundation of Moldova State University****, the alma mater of both scholars and the institution that today brings together the research institutes hosting this conference.*

The aim of the event is two-fold. First, it offers a valuable opportunity for discussion and for the dissemination of the latest results on selected topics in materials science, condensed matter physics and chemistry of functional materials. On the other hand, through plenary lectures, contributed oral communications and poster presentations, it allows the participants – and in particular the younger among them – to get a broad perspective of current scientific research and technological development.

The Programme of the Conference consists of plenary lectures and of contributed oral and poster presentations, distributed into 6 sections:

- ***Condensed Matter Theory (CMT)***
- ***Growth and Properties of Advanced Materials (GPAM)***
- ***Design and Structural Engineering of Functional Materials (DSEFM)***
- ***Solid State Nanophysics and Nanotechnology (SSNN)***
- ***Electromagnetic Radiation Detection and Conversion (EMDC)***
- ***Materials Engineering for Innovative and Sustainable Technologies (MEST)***

Within the current edition of the MSCMP conference, the following workshop took place:

- ***„Nanostructured High-Entropy Materials" within the NATO SPS Project G6153 "Stealth Coatings Based on 3D Architectures of High Entropy Materials"***

The Organising Committee expresses its gratitude to all the participants, to the members of the International Advisory Committee and to the sponsors of the conference for their contribution to this event.

L. Kulyuk — Conference Chair

S. Vatavu — Co-chair of the Conference

CONFERENCE ORGANIZERS

Leonid Culiuc (Kulyuk)	Conference Chair	Institute of Applied Physics, Moldova State University, Moldova
Sergiu Vatavu	Conference Co-chair	Faculty of Physics and Engineering, Moldova State University, Moldova
Ernest Arushanov	Programme Committee Chair	Institute of Applied Physics, Moldova State University, Moldova
Nikita Siminel	Secretary of the Conference	Institute of Applied Physics, Moldova State University, Moldova

PROGRAMME COMMITTEE

Ernest Arushanov	Programme Committee Chair	Institute of Applied Physics, Moldova State University, Moldova

Section*: **Condensed matter theory (CMT)***

Mihai Macovei - Section Chair	Institute of Applied Physics, Moldova State University, Moldova
Denis Nika	E. Pokatilov Laboratory of Physics and Engineering of Nanostructures, Moldova State University, Moldova

Section: ***Growth and Properties of Advanced Materials (GPAM)***

Vladimir Tsurkan - Section Chair	Institute of Applied Physics, Moldova State University, Moldova; Center for Electronic Correlations and Magnetism, University of Augsburg, Germany
Vadim Sirkeli	E. Pokatilov Laboratory of Physics and Engineering of Nanostructures, Moldova State University, Moldova

Section: ***Design and Structural Engineering of Functional Materials (DSEFM)***

Aculina Aricu - Section Chair	Institute of Chemistry, Moldova State University, Moldova
Elena Gorincioi	Institute of Chemistry, Moldova State University, Moldova

Section: ***Solid State Nanophysics and Nanotehnology (SSNN)***

Veacheslav Ursachi - Section Chair	Academy of Sciences of Moldova, Moldova
Alexandr Cocemasov	E. Pokatilov Laboratory of Physics and Engineering of Nanostructures, Moldova State University, Moldova

Section: ***Electromagnetic Radiation Detection and Conversion (EMDC)***

Marin Rusu - Section Chair	Helmholtz-Zentrum Berlin für Materialien und Energie; Department of Applied Physics and Computer Science, Moldova State University, Moldova
Elena Achimova	Institute of Applied Physics, Moldova State University, Moldova

Section: ***Materials engineering for Innovative and Sustainable Technologies (MEST)***

Tsyntsaru Natalia - Section Chair	Institute of Applied Physics, Moldova State University, Moldova
Oleg Șapoval	Physics of Semiconductors and Devices Laboratory, Moldova State University, Moldova

INTERNATIONAL ADVISORY COMMITTEE

Vladimir Fomin - Chair of the International Advisory Committee	Leibniz Institute for Solid State and Materials Research, Germany
Susan Schorr	Department Structure and Dynamics of Energy Materials, Helmholtz-Zentrum Berlin für Materialien und Energie, Germany
Veaceslav Coropceanu	Department of Chemistry and Biochemistry, University of Arisona, USA
Valentin Crăciun	National Institute for Laser, Plasma & Radiation Physics, Romania
Chris S. Ferekides	University of South Florida, USA
Henrikas Cesiulis	Vilnius University, Lithuania
Silvio Decurtins	Department of Chemistry and Biochemistry, University of Bern, Switzerland
Ion Tiginyanu	Academy of Sciences of Moldova, Moldova
Dimitris Pavlidis	Florida International University, USA
Mădălin Bunoiu	Universitatea de Vest din Timișoara, Romania
Tomas Tamulevičius	Kaunas University of Technology (KTU), Lithuania
Muhammed Fatih Toy	Istanbul Medipol University, Türkiye
Boris Tsukerblat	Ben-Gurion University of the Negev, Israel
Felicia Iacomi	Alexandru Ioan Cuza University of Iasi, Romania
Wojciech Knap	CENTERA Laboratories, Institute of High Pressure Physics, Polish Academy of Sciences, Poland

CONFERENCE ORGANIZING COMMITTEE

Sergiu Vatavu – Chair of the Organizing Committee
Faculty of Physics and Engineering, MSU, Moldova

Institute of Applied Physics, Moldova State University, Moldova
Olga Shikimaka
Alexei Meshalkin
Dorina Croitori
Marianna Roman
Nicolai Curmei
Oleg Reu
Serghei Ostrovsky
Natalia Kazak
Anatolii Siminel
Alexandru Micu
Valentin Batîr
Anatolii Cuharuc

Scientific association "Materials Science and Engineering"
Irina Filippova
Nina Iuzva

Faculty of Physics and Engineering, Moldova State University, Moldova
Natalia Nedeoglo
Vadim Sirkeli
Dorin Spoială
Elmira Vatavu
Elena Bercu
Igor Narolschi
Alisa Moșneaga,
Irina Maistruc
Gheorghe Ghilețchii
Varzari Alexandru
Eugeniu Spinei
Rostovțev Oxana
Adrian Scafaru
Vasile Gramovich

ORGANIZED BY

Institute of Applied Physics of Moldova State University

Faculty of Physcis and Engineering of Moldova State University

Institute of Chemistry of Moldova State University

Scientific Association “Materials Science and Engineering”

NATO SPS Project G6153

“Stealth Coatings Based on 3D Architectures of High Entropy Materials"

SUPPORTED BY

Moldova State University

NATO SPS Project G6153

“Stealth Coatings Based on 3D Architectures of High Entropy Materials"

National Institute for Laser, Plasma and Radiation Physics, Romania

PHANOS Technologies SRL

RONEXPRIM S.R.L.

CHROMAVANSA S.R.L

Labromed Laborator S.R.L

Schaefer Scientific GmbH

CULTURAL PARTNER

Public Institution “PALACE OF THE REPUBLIC”

CONTENTS

PLENARY LECTURES

PROGRESS IN RESEARCH ON TERNARY MAGNETIC SPINELS: IN MEMORY OF THE ACADEMICIAN S. RADAUTSAN 20
V. Tsurkan

EXPANDING THE CHALCOGENIDE SEMICONDUCTOR LANDSCAPE TOWARDS NARRO AND WIDE GAP MATERIALS 22
S. Schorr

ALTERMAGNETS AND THEIR OPTICAL PROPERTIES 23
J. Deisenhofer

MICROWAVE ABSORBERS BASED ON HIGH-ENTROPY ALLOYS DEVELOPED BY PHYSICAL VAPOR DEPOSITION TECHNIQUES 24
S. Irimiciuc, P. Hruška, E. Marešová, L. Volfova, S. Cichoň, S. Chertopalov, V. Grumezescu, V. Craciun, S. Vatavu, J. Lancok

MAGNETOPLASMONIC CRYSTALS 25
P. Sai, V. Korotyeyev, M. Dub, M. Orlita, W. Knap

LUMINESCENCE OF RARE-EARTH IONS DOPED IN FLUORITE CRYSTALS 26
M. Stef, C. Schörnig, P. Veber, G. Buse, M. Poienar, D. Vizman

ELECTRON BEAM LITHOGRAPHY FOR 2D MATERIAL-BASED DEVICES 27
A. Dinescu, M. Dragoman, D. Dragoman, A. Avram, O. Simionescu, C. Parvulescu

QUANTUM INTERFERENCE IN QUANTUM RINGS 28
V. M. Fomin

FRACTIONALIZED EXCITATIONS PROBED BY ULTRASOUND 29
S. Zherlitsyn

EXTENDED FEYNMAN VARIATIONAL PRINCIPLE AND RELATED ANALYTICAL METHODS FOR LATTICE POLARONS 30
S. N. Klimin, J. Tempere, M. Houtput, I. Zappacosta, S. Ragni, T. Hahn, L. Celiberti, C. Franchini, A. S. Mishchenko

QUANTUM GENERATING FUNCTIONS AND UNIVERSAL FAMILY-VICSEK SCALING IN NONEQUILIBRIUM QUANTUM MANY-BODY SYSTEMS 31
C. P. Moca

FROM BINARY TUNGSTEN ALLOYS TO HIGH-ENTROPY ELECTROCATALYSTS: BALANCING ACTIVITY AND STABILITY IN HIGHLY ALKALINE MEDIA 32
N. Tsyntsaru, T. K. Ratajczyk, H. Cesiulis, M. Donten

DEVELOPING AI-DRIVEN TOOLS FOR ACCELERATED RESEARCH AND INDUSTRIAL PROCESSES MONITORING 33
G. Y. Soracá-Pérez, J. Garí-Galíndez, R.-F. Rubio, E. Niemi, M. Israr-Qadir, A. Pérez-Rodríguez, P. Vidal-Fuentes, V. Izquierdo-Roca, M. Guc

BAND-GAP SPECTRA AND HARMONIC WAVE MODES IN AN INFINITE STRING WITH PERIODIC ELASTIC CONSTRAINTS 34
A. A. Barsuk, F. Paladi

INTRINSIC STABILIZATION OF THIN-PLATE ACOUSTIC RESONATORS AGAINST BOTH TEMPERATURE AND PRESSURE VARIATIONS 35
S. Cojocaru, L. Dohotaru

ENHANCING THE PERFORMANCE OF InGaN-BASED GREEN LEDs THROUGH SUBSTRATE POLARITY ENGINEERING: FROM POLAR c-PLANE TO SEMIPOLAR STRUCTURES 36
V. P. Sirkeli

CHANGE IN MAGNETIC AND POLARIZATION CHARACTERISTICS FACILITATED BY REDISTRIBUTION OF ELECTRON DENSITY IN THE [FeCo] COMPLEX 37
S. Ostrovsky, S. Klokishner

ELECTROCHEMICAL AND SPECTROSCOPIC SIGNATURES OF THE JAHN–TELLER EFFECT IN PLATINUM-MONODOPED $Au_{24}Pt(SR)_{18}$ CLUSTERS 38
K. Zdunek, T. Korona, A. Więckowska

MODELING OF THE VALENCE TAUTOMERIC TRANSFORMATION IN COBALT COMPLEXES: INTERACTION OF MOLECULAR MODES WITH PHONONS 39
S. Klokishner, O. Reu, S. Ostrovsky

SPIN TRANSFORMATION INDUCED BY THE PROTON TRANSFER IN THE IRON (II) HYDRAZONE CRYSTALLINE COMPOUND $[Fe(HL\text{-}F)_2](AsF_6)_2$ 40
O. Reu, S. I. Klokishner

ON THE DOUBLE DEGENERACY OF QUASI-ENERGY LEVELS 41
I. I. Geru

REACTIVE FILLERS AS A TOOL FOR MICROSTRUCTURE ENGINEERING IN Bi_2Te_3-BASED THERMOELECTRIC COMPOSITES 42
M. Zhezhu, V. Mehrabyan, V. Torosyan, D. Vanyan, M. Yaprintsev, O. Ivanov, A. Vasil'ev

QUANTUM WELL ENGINEERING FOR HIGH-EFFICIENCY InGaN-BASED RED LEDs 43
V. P. Sirkeli, S. I. Caragacian, Iu. B. Boris, D. L. Nika

SINGLE - AND TWO - QUANTA PROCESSES IN COUPLED HYBRID SYSTEMS 44
M. A. Macovei, T. Mihaescu, A. Isar

COHERENT SPIN DYNAMICS OF ELECTRONS AND HOLES PHOTOGENERATED WITH LARGE KINETIC ENERGY IN LEAD HALIDE PEROVSKITE CRYSTALS 45
E. A. Zhukov, D. R. Yakovlev, N. E. Kopteva, M. Bayer

COMPLEX DYNAMICS OF INTERACTION BETWEEN CANCER AND IMMUNE SYSTEMS 46
N. Gubceac, N. Ciobanu, V. Tronciu

COOPERATIVE EMISSION AND NONCLASSICAL PHOTON STATISTICS OF THREE ATOMS IN AN EQUILATERAL-TRIANGLE GEOMETRY 47
A. Rotari, M. A. Macovei

***Ab initio* RESONANT RAMAN SCATTERING STUDY OF MONOLAYER AND BULK MoS_2** 48
P. Milev, F. Paleari, D. Sangalli

SUPPRESSION OF THERMAL TRANSPORT IN CUBIC In_2O_3 WITH Pb-Tl DEFECTS 49
A. Cocemasov, V. Brinzari, D. L. Nika

GENERATION OF QUANTUM CORRELATIONS IN CONTINUOUS-VARIABLE OPEN QUANTUM SYSTEMS 50
A. Stoica, A. Isar

NEGATIVE PARTIAL TRANSPOSE ENTANGLEMENT WITNESSES BASED ON SECOND MOMENTS 51
T. Mihaescu

PASSIVE QUANTUM COOLING IN OPTOMECHANICAL DEVICES 52
V. Ceban, A. Cudreașov, A. Rotari, I. Cebotari

CMT P1 **THEORETICAL STUDY OF SHORT PULSE IN DFB LASERS BY RATE EQUATION MODEL** 53
V. Tronciu, S. Rusu, V. Dobrovolschi

CMT P2 **MACHINE LEARNING-BASED OPTIMIZATION OF DFB LASER PARAMETERS FOR SHORT PULSE GENERATION** 54
V. Tronciu, S. Zaporojan, N. Gubceac, R. R. Slavescu

CMT P3 **MODELING OF DYNAMIC EQUILIBRIUM IN THE OXIDANT-ANTIOXIDANT SYSTEM ACCOUNTING FOR THE SYNERGETIC EFFECT OF VITAMINS E, C, AND BIOFLAVONOIDS** 55
O. V. Yaltychenko, E. Yu. Kanarovskii

CMT P4 **PHONON-ASSISTED GENERATION OF ENTANGLED TWO-QUBIT STATES** 56
E. Cecoi, V. Ciornea, A. Isar, M. A. Macovei

CMT P5 **MODELING OF MULTICENTER CORE-SHELL NANOCLUSTERS** 57
E. Yu. Kanarovskii, O. V. Yaltychenko

CMT P6 **A DFT-TB2J INSIGHT INTO THE MAGNETIC BEHAVIOR AND INTRACHAIN INTERACTIONS OF THE 1D Co(II) PIVALATE COORDINATION POLYMER WITH HEXAMETHYLENETETRAMINE** 58
Yu. Chumakov, E. Beleaev, S. G. Baca

CMT P7 **MONO- AND TETRASULFO-DERIVATIVES OF ZINC PHTHALOCYANINE AND THEIR CHITOSAN-BASED COMPOSITIONS** 59
Ş. Robu, V. Stegariov, I. Lungu, M. Diru, T. Potlog

CMT P8 **TWO DIPOLE-DIPOLE INTERACTING EMITTERS IN A MODERATELY STRONG LASER FIELD** 60
A. S. Cudreasov, M. A. Macovei

CMT P9 **MODELING BLOOD FLOW IN STENOSED ARTERIES: PRESSURE LOSSE** 61
I. M. Cernica

CMT P10 **MODELING BLOOD FLOW IN STENOSED ARTERIES: BLOOD FLOW RATE** 62
I. M. Cernica

CMT P11 **THE PEIERLS STRUCTURAL TRANSITION IN QUASI-ONE-DIMENSIONAL TTT2I3 ORGANIC CRYSTALS WITH CONSIDERIND INTERCHAIN INTERACTION** 63
S. C. Andronic, I. I. Sanduleac

CMT P12 **INDIRECT POPULATION OF AN EMPTY OPTICAL CAVITY VIA COLLECTIVE ATOMIC EFFECTS** 64
S. Cârlig, V. Ciornea, C. Gherman, M. A. Macovei

ATOMIC STRUCTURE AND STRUCTURAL DISORDER VS. DEVICE EFFICIENCY IN KESTERITE MONOGRAIN SOLAR CELLS 65

G. Gurieva, K. Ernits, A. Manjon Sanz, D. Sheptyakov, M. Avdeev, N. Siminel, M. Kirkham, D. Meissner, S. Schorr

FROM $Cu_2ZnSiSe_4$ TO $Cu_2ZnGeSe_4$: EVOLUTION OF VIBRATIONAL PROPERTIES WITH Ge INCORPORATION 66

V. Rotaru, G. Gurieva, P. Vidal Fuentes, A. Pérez-Rodríguez, V. Izquierdo Roca, S. Schorr, M. Guc

INTRINSIC POINT DEFECTS IN ALKALI-DOPED KESTERITE-TYPE SEMICONDUCTORS AND THEIR INFLUENCE ON SOLAR CELL PERFORMANCE 67

H. Prell, G. Gurieva, M. Rusu, M Grossberg-Kuusk, M. Kauk-Kuusik, S. Schorr

DISORDER-CONTROLLED MAGNETISM IN POLAR ANTIFERROMAGNETS $M_2Mo_3O_8$ 68

L. Prodan, I. Filippova, D. Croitori, S. Moldovanu, O. G. Grendal, S. Shova, A. Tsirlin, I. Kézsmárki, V. Tsurkan

INSIGHTS INTO THE PHOTOLUMINESCENT AND STRUCTURAL PROPERTIES OF THE BINUCLEAR COMPLEX $[Eu_2(o\text{-MBA})_6(phen)_2]$ 69

V. Ghenea, I. Culeac, E. Melnic, I. Cojocaru, V. Verlan, A. Siminel, I. Bulhac, A. Buzdugan, A.-G. Pantazi, M. Enachescu

STRUCTURAL CHIRALITY AND FUNCTIONALITY IN INCOMMENSURATE MODULATED TETRAGONAL TUNGSTEN BRONZES 70

O. Grendal, C. R. Zeiger, R. S. Dragland, R. Sjøkvist, R. Beanland, D. Meier, M. Senn

GPAM P1 **$[Eu(DBM)_3Phen]$ SUBLIMATED THIN FILMS FOR OPTOELECTRONIC DEVICES** 71

I. Culeac, V. Verlan, V. Ghenea, I. Bulhac, I. Cojocaru, A.-G. Pantazi, M. Enachescu

GPAM P2 **SYNTHESIS AND SPECTROSCOPIC PROPERTIES OF ZN(II)/CD(II) SCHIFF BASE COMPLEXES** 72

V. Ghenea, I. Culeac, I. Bulhac, L. Cuba

GPAM P3 **FEATURES OF ZEEMAN SPLITTING IN UNIAXIALLY DEFORMED BISMUTH WIRES** 73

E. Condrea

GPAM P4 **OBSERVATION OF RESONANT PHOTOLUMINESCENCE FROM DEEP ENERGY CONTINUUM OF LAYER SEMICONDUCTOR InSe** 74

D. P. Dvornikov, A. V. Siminel

GPAM P5 **STRUCTURAL, VIBRATIONAL AND OPTICAL PROPERTIES OF $Ag_2(Zn,Cd)(Sn,Ge)S_4$ THIN FILMS SUBJECTED TO THERMAL ANNEALING** 75

V. Batîr, I. Anefnaf, S. Aazou, N. Curmei, L. Dermenji, Z. Sekkat, E. Arushanov, M. Guc

GPAM P6 **RADIATIVE PROPERTIES OF NANOSIZED ZnO:Ag POWDERS** 76

N. Nedeoglo, T. Goglidze, E. Goncearenco, V. Sirkeli, D. Nedeoglo

GPAM P7 **EFFECT OF SYNTHESIS ATMOSPHERE ON STRUCTURAL AND TRANSPORT PROPERTIES OF $(Ag_xCu_{1-x})_2ZnSnS_4$ SOLID SOLUTIONS** 77

V. Batîr, D. Usenco, N. Curmei, L. Dermenji, K. G. Lisunov, E. Arushanov

GPAM P8 **SYNTHESIS AND CRYSTAL GROWTH OF ALTERMAGNET CANDIDAT $Fe_{2-x}Zn_xMo_3O_8$: COMPOZITION AND STRUCTURAL ANALYSIS** 78

L. Prodan, I. Filippova, D. Croitori, S. Moldovanu, S. Shova, O. Grendal, V. Tsurkan

GPAM P9 **PROSPECTS OF CHEMICAL VAPOR TRANSPORT FOR SINTERING OF $ZnO_{1-x}Se_x$ ALLOYS** 79
I. Inculet, M. A. Koltsov, S. Moldovanu, N. Spalatu, G. V. Colibaba

GPAM P10 **COMPARATIVE ANALYSIS OF ENERGY TRANSFER AND RADIATIVE RECOMBINATION PROCESSES IN $ZnIn_2S_4$ AND $CdIn_2S_4$ SINGLE CRYSTALS STUDIED BY LUMINESCENCE SPECTROSCOPY** 80
V. Pintea, E. Arama, T. Shemyakova

GPAM P11 **STRUCTURAL, OPTICAL AND ELECTRICAL PROPERTIES OF $(ZnO)_k \cdot Ga_2O_3$ CERAMICS AND THIN FILMS** 81
D. Rusnac, N. Spalatu, G. V. Colibaba

GPAM P12 **LOW-TEMPERATURE SINTERING OF $Zn_kIn_2O_{k+3}$ COMPOUND OXIDES BY CHEMICAL VAPOR TRANSPORT** 82
G. V. Colibaba, S. Moldovanu, D. Rusnac, N. Spalatu

GPAM P13 **QUANTUM NEMATIC TRANSITION IN THE $EuMe_2Pn_2$ COMPOUNDS** 83
A. Nateprov, Yu. Goryunov

GPAM P14 **FEATURES OF BI_2S_3 CRYSTAL GROWTH** 84
G. V. Colibaba, M. A. Koltsov, N. Spalatu

GPAM P15 **SYNTHESIS OF ACZTS THIN FILMS IN DIFFERENT GAS ATMOSPHERES** 85
L. Dermenji, V. Batîr, N. Curmei, V. Zalamai, G. Gurieva, D. Podgornîi, D. Usenco, E. Arushanov

SECTION DESIGN AND STRUCTURAL ENGINEERING OF FUNCTIONAL MATERIALS (DSEFM)

DESIGN AND SYNTHESIS OF A COPPER (II) COMPOUND WITH N-(4-METHOXYPHENYL)-2-[1-(PYRIDIN-2-YL)ETHYLIDENE]HYDRAZINE-1-CARBOTHIOAMIDE 86
A. Pîntea, R. Rusnac, V. Tsapkov, S. Shova, A. Gulea

SYNTHESIS AND MAGNETIC PROPERTIES OF HEXANUCLEAR $\{Fe_4Ln_2\}$ CLUSTERS BASED ON CARBOXYLATE AND AMINO-POLYALCOHOL LIGANDS 87
D. Podgornii, J. van Leusen, V. Ch. Kravtsov, Y. Skourski, P. Kögerler, S. G. Baca

SYNTHESIS AND XRD STUDY OF SOME α-HEXYLCINNAMALDEHYDE THIOSEMICARBAZONES 88
A. Ciursin, R. Rusnac, G. Ghileţchii, S. Vatavu, A. Gulea

SYNTHESIS OF NOVEL MOLECULAR HYBRIDS: 2-(1-ETHYL-2-OXOINDOLIN-3-YLIDENE)HYDRAZONO)-THIAZOLIDIN-4-ONE AND ITS DERIVATIVE BY KNOEVENAGEL CONDENSATION 89
A. S. Batanov, N. S. Sucman, S. Shova, G. Balan, E. C. Gorincioi, F. Z. Macaev

MULTICOMPONENT MATRICES FOR CORNEAL REGENERATION WITH INSULIN/ GLUCOSE SENSITIVE FLUORESCENCE 90
A. Chiaburu, A. Besliu, I. Coretchi, I. Casian, A. Casian, E. Pavlovschi, I.-R. Tigoianu, B.-I. Ciubotaru, M.-F. Zaltariov

SYNTHESIS AND CHARACTERIZATION OF A MULTIFUNCTIONAL THERMOSTABLE CONDUCTIVE NANO-SIZED OLIGOMER BASED ON ORTHO-PHENYLENEDIAMINE AND CATECHOL 91
R. Rzayev, N. Sucman, B. A. Mammadov, R. Akhmedova, F. Macaev

CRYSTAL ENGINEERING OF Co(II/III) CLUSTER-BASED COORDINATION POLYMERS 92
E. Beleaev, S. G. Baca

NOVEL BIOACTIVE AMINONAPHTHOQUINONES: DESIGN, SYNTHESIS AND SPECTROSCOPIC STUDIES 93
D. Feldman, A. Simion, E. Gorincioi, N. E. Dina, F. Z. Macaev

NMR SPECTROSCOPY AS A TOOL FOR STRUCTURAL ELUCIDATION OF OLIGOMERS OBTAINED BY OXIDATIVE POLYCONDENSATION OF AROMATIC AMINES WITH DIHYDROXYBENZENES 94
N. Sucman, R. Rzayev, I. Geru, F.Macaev

MECHANISTIC INSIGHTS INTO THE SYNERGISTIC AND ANTAGONISTIC RADICAL-SCAVENGING DYNAMICS OF RESVERATROL-ASCORBIC ACID COMBINATIONS 95
N. Bolocan, E. Gorincioi, C. Vicol, A. Barba, G. Duca

OPTIMIZED THERMOACCUMULATION AS A CONDITION *SINE QUA NON* FOR ENSURING SUSTAINABLE DEVELOPMENT 96
Iu. Bosneaga

DSEFM P1 **SPECTROSCOPIC STUDY OF ALUMINUM AND SILICON CHLOROPHTHALOCYANINES** 97
T. Potlog, I. Lungu, R. Tigoianu, A. Airinei

DSEFM P2 **FROM BUTTERFLIES TO WHEELS: EVOLUTION OF NUCLEARITY AND TOPOLOGY IN HETEROMETALLIC Co-La CLUSTERS DIRECTED BY AMINO-ALCOHOL AND CARBOXYLATE LIGANDS** 98
D. Stati, V. Ch. Kravtsov, P. Kögerler, S. G. Baca

DSEFM P3 **A NEW COBALT(II) COORDINATION POLYMER BASED ON DINUCLEAR PIVALATE BUILDING UNITS AND PYRAZINE LINKERS** 99
E. Beleaev, V. Ch. Kravtsov, S. G. Baca

DSEFM P4 **A HEPTANUCLEAR HETEROMETALLIC $\{Co^{III}_4Co^{II}_2Gd^{III}\}$ PIVALATE CLUSTER SUPPORTED BY *N*-BUTYLDIETHANOLAMINE LIGANDS** 100
E. Beleaev, D. Brüx, J. van Leusen, P. Kögerler, S. G. Baca

DSEFM P5 **NEW HEXANUCLEAR $\{Co_3Tb_3\}$ NANOCLUSTER CONSTRUCTED BY METHYLDIETHANOLAMINE AND PIVALATE LIGANDS** 101
E. Beleaev, D. Brüx, J. van Leusen, P. Kögerler, S. G. Baca

DSEFM P6 **SYNTHESIS AND CHARACTERISATION OF A NOVEL Cu(II) SEBACATE WITH 2,2′-BIPYRIDINE** 102
P. Cebotaru, O. Cuzan, S. Shova, V. Lozan

DSEFM P7 **CRYSTAL STRUCTURE OF 1D COORDINATION POLYMER CATENA-(BIS(μ_2-4,4′-OXYDIANILINE)-(μ_2-PHENANTHROLINE)-CADMIUM (II) PERCHLORATE)** 103
N. Craciun, V. Ch. Kravtsov, M. S. Fonari

DSEFM P8 **CRYSTAL AND ELECTRONIC STRUCTURE OF MACROCYCLIC TRINUCLEAR COMPLEX OF Co(II)** 104
O. Danilescu, I. Bulhac, M. Cocu, P. Bourosh, Yu. Chumakov

DSEFM P9 **TUNING THE PHOTOLUMINESCENCE PERFORMANCE OF Cd(II) POLYMERS THROUGH POLYMORPHISM** 105
O. Danilescu, I. Bulhac, P. Bourosh, O. Kulikova, Yu. Chumakov

DSEFM P10 **PHOTOLUMINESCENCE PROPERTIES AND DFT CALCULATIONS OF ISOMORPHIC ONE-DIMENSIONAL COORDINATION POLYMERS OF Zn(II) AND Cd(II) BASED ON A DIHYDRAZONE LIGAND WITH TERMINAL N-DONOR PYRIDINE FRAGMENTS** 106
Yu. Chumakov, M. Cocu, I. Bulhac, V. Kravtsov, P. Bourosh, O. Kulikova, O. Danilescu

DSEFM P11 **MONONUCLEAR Eu(III) COMPLEX OF 2,6-DIACETYLPYRIDINE BIS(NICOTINOYLHYDRAZONE): SYNTHESIS AND CRYSTAL STRUCTURE** 107
I. Bulhac, E. Melnic, V. Ghenea, O. Danilescu, I. Culeac

DSEFM P12 **A NOVEL ONE-DIMENSIONAL CADMIUM(II) COORDINATION POLYMER: SYNTHESIS AND STRUCTURAL CHARACTERIZATION** 108
A. A. Vitiu, P. N. Bourosh

DSEFM P13 **DESIGN AND CHARACTERIZATION OF A NEW CADMIUM(II) METAL–ORGANIC FRAMEWORK** 109
S. Melnic, D. Bejan, S. Shova, V. Lozan

DSEFM P14 **CRYSTAL PACKING-DIRECTED LUMINESCENCE IN POTASSIUM COORDINATION POLYMERS BASED ON POSITIONAL ISOMERS OF CHLORONITROBENZOIC ACID** 110
A. Gorobet, M. E. Crisan, P. N. Bourosh, O. V. Kulikova, L. Croitor

DSEFM P15 **THE COORDINATION COMPOUND OF Mn(II) DERIVED FROM 5-(4-CARBOXY-5-METHYL-1*H*-1,2,3-TRIAZOL-1-YL)ISOPHTHALIC ACID** 111
V. Gorinchoy, G. Roman, S. Shova, V. Lozan

DSEFM P16 **DINUCLEAR COPPER(II) COMPLEX WITH 5-CHLOROSALICYLIC ACID** 112
V. Gorinchoy, S. Melnic, O. Cuzan, S. Shova

DSEFM P17 **CRYSTAL STRUCTURE OF ZINC(II) PENTANUCLEAR CLUSTER BASED ON BENZOTRIAZOLE** 113
V. Avdeev, M. S. Fonari, P. Bourosh

DSEFM P18 **3D COORDINATION POLYMERS OF LANTHANIDES WITH 5-(4-CARBOXYPHENYL)-1-PHENYL-1H-PYRAZOLE-3-CARBOXYLIC ACID** 114
E. Neguta, S. Shova, G. Roman, A. Siminel, Y. Chumakov, V. Lozan

DSEFM P19 **SYNTHESIS AND STRUCTURAL CHARACTERIZATION OF A SERIES OF Cu(II) COMPLEXES WITH 2-SALICYLIDENHYDRAZON-THIAZOLIDIN-4-ONE AND MONO- OR BIDENTATE AMINES** 115
M. Mînăscurtă, T. Jovmir, S. Shova, V. Lozan

DSEFM P20 **EFFICIENT SYNTHESIS OF TRANS-DIOXIMES THROUGH THE CONDENSATION OF PYRIDINE AND *γ*-PICOLINE WITH DICHLOROGLYOXIME** 116
D. Ureche, P. Bourosh, I. Bulhac

DSEFM P21 **SYNTHESIS AND CHARACTERIZATION OF A TRINUCLEAR HETEROMETALLIC {$CeCu_2$} CLUSTER WITH PIVALATE AND TRIETHANOLAMINE LIGANDS** 117
O. Capbătut, D. Brüx, J. van Leusen, P. Kögerler, S. G. Baca

DSEFM P22 **A DODECANUCLEAR Mn(II, III) CLUSTER BASED ON ISOBUTYRIC AND 1,1,1-TRIS(HYDROXYMETHYL)PROPANE LIGANDS** 118
R. Derivolcova, O. Capbătut, V. Ch. Kravtsov, S. G. Baca

DSEFM P23 **PREPARATION OF TETRACHLOROFERRATES(III) IONIC LIQUIDS CONTAINING IMIDAZOLIUM AND PYRIDINIUM CATIONS** 119
M. Ceabanova, E. Stîngaci, N. Sucman, V. Pogrebnoi, M. Neamtu, F. Z. Macaev

DSEFM P24 **A 1D COORDINATION POLYMER BASED ON HETEROMETALLIC OXO-CENTERED {Na_2Fe_6} CLUSTERS: SYNTHESIS AND STRUCTURAL CHARACTERIZATION** 120
A. Trofaila, V. Ch. Kravtsov, S. G. Baca

DSEFM P25 **MOLECULAR STRUCTURE OF A NEW 1D COBALT(II) COORDINATION POLYMER BASED ON SEBACIC ACID AND 4,4′-BIS(1H-IMIDAZOL-1-YLMETHYL)BENZENE** 121
I. Voda, V. Druta, S. Shova, V. Lozan

DSEFM P26 **SYNTHESIS AND LUMINESCENT PROPERTIES OF Zn(II) COORDINATION COMPOUNDS BASED ON 1,5-*BIS*(3,5-DI-TERT-BUTYL-SALICYLALDEHYDE)CARBOHYDRAZONE** 122
N. Talmaci, D. Dragancea, S. Shova

DSEFM P27 **SYNTHESIS AND CHARACTERIZATION OF COORDINATION COMPOUNDS OF Cu(II) AND Bi(III) WITH SOME BENZOYLHYDRAZONES AND AMINOPOLYCARBOXYLATE LIGANDS** 123
B. Mindrescu, N. Popa, S. Shova, I. Bulimestru

DSEFM P28 **SYNTHESIS AND X-RAY ANALYSIS OF *N*-(13,14,15,16-TETRANORLABD-7-OXO-8-EN-11-OYL)PHENOTHIAZINE** 124
L. Lungu, A. Ciocârlan, S. Shova, A. Arîcu

DSEFM P29 **COMPUTATIONAL MODELING OF MB ADSORPTION ON THE PAH-AC SURFACE** 125
I. Balan, R. Nastas

DSEFM P30 **DESIGN AND ANTIRADICAL ACTIVITY OF A NOVEL MOLECULAR HYBRID BASED ON A HOMODRIMANE SCAFFOLD INCORPORATING THIOSEMICARBAZIDE AND OXADIAZOLE UNITS** 126
L. Lungu, C. Vicol, V. Pogrebnoi, A. Ciocârlan, A. Arîcu

DSEFM P31 **CRYSTAL STRUCTURES OF TWO MIXED-LIGAND COPPER(II) COORDINATION COMPOUND WITH METHYL *N′*-[(2-HYDROXYPHENYL)METHYLIDENE]-*N*-(PROP-2-EN-1-YL)CARBAMOHYDRAZONOTHIOATE** 127
P. N. Bourosh, V. Ch. Kravtsov, I. S. Kravchuk, V. O. Graur, A. S. Cotovaia, O. S. Garbuz, A. P. Gulea

DSEFM P32 **ANTIOXIDANT ACTIVITY OF IONIC LIQUIDS FORMED BY CARNITINE AND FOOD ACIDS: A COMPUTATIONAL STUDY** 128
I. Balan, M. Gorbaciov, N. Gorinchoy, O. Moroz

DSEFM P33 **CRYSTAL STRUCTURES OF TWO SUBSTITUTED PYRUVAMIDE THIOSEMICARBAZONES** 129
E. I. Melnic, P. N. Bourosh, I. I. Graur, V. O. Graur, O. S. Garbuz, V. I. Tsapkov, A. P. Gulea

DSEFM P34 **CRYSTAL STRUCTURES OF A PYRUVAMIDE THIOSEMICARBAZONE AND ITS NICKEL(II) COORDINATION COMPOUND** 130
E. I. Melnic, P. N. Bourosh, I. I. Graur, V. O. Graur, O. S. Garbuz, V. I. Tsapkov, A. P. Gulea

DSEFM P35 **KAEMPFEROL-BASED BIOCOMPOSITES: PREPARATION, CHARACTERIZATION AND APPLICATION IN CORNEAL HEALING** 131
A. Besliu, A. Chiaburu, I. Casian, A. Casian, I. Coretchi, A. Sulaiman, D. Peptanariu, M.-F. Zaltariov, B.-I. Ciubotaru

DSEFM P36 **GOLD NANOPARTICLE-CONJUGATED PHTHALOCYANINES (AuNPs)** 132
V. Suman

DSEFM P37 **ADVANCES IN KAEMPFEROL FORMULATIONS: EXTRACTION, STRUCTURAL CHARACTERIZATION AND BIOLOGICAL ACTIVITY** 133
I. Coretchi, A. Casian, I. Casian, A. Besliu, A. Chiaburu, C. Ceban, D. Peptanariu, M. Balan-Porcarasu, S. L. Nica, M.-F. Zaltariov

DSEFM P38 **MICROWAVE ASSISTED REACTION OF FLUORESCENT PYRROLOQUINOLINE BUILDING BLOCKS** 134
G. Zbancioc, A. M. Birgoanu, C. Moldoveanu, I. I. Mangalagiu, G. Tataringa, A. M. Zbancioc

DSEFM P39 **NOVEL QUATERNARY AMMONIUM SALT OF 2-*TERT*-BUTYL-3-(1*H*-1,2,4-TRIAZOL-1-YL)-2*H*-CHROMEN-2-OL WITH POTENT ANTIFUNGAL ACTIVITY** 135
M. P. Ceabanova, E. P. Stingaci, E. C. Gorincioi, G. Balan, N. E. Dina, F. Z. Macaev

DSEFM P40 **NEW BIS-IMIDAZOLIUM IONIC LIQUIDS WITH DIFFERENT ANIONS** 136
V. S. Pogrebnoi, N. Sucman, M. Ceabanova, M. Neamtu, S. Shova, F. Z. Macaev

DSEFM P41 **MECHANICAL PROPERTIES MODIFICATION OF 316L STAINLESS STEEL AFTER SHOT PEENING TREATMENT** 137
M. Hitsiuc, O. Shikimaka, N. Serban, C. Pyrtsac, N. Kazak, A. Cuharuc

DSEFM P42 **THIOSEMICARBAZIDE BASED MATERIALS AS DUAL MR2 RNR AND COLCHICINE-SITE TUBULIN INHIBITORS** 138
O. Palamarciuc, B. I. Ciubotaru, A. C. Stoica, M. Balan-Porcarasu, S. Shova, D. Peptanariu, M. Dascalu, M. Cazacu, V. B. Arion

DSEFM P43 **SYNTHESIS AND FUNCTIONAL EVALUATION OF TiO_2-MODIFIED ACTIVATED CARBON COMPOSITES OBTAINED FROM PEACH STONES** 139
R. Nastas, M. Stefan, I. Ceban, A. Varadi, I. Nesterovschi, D. Toloman, A. Popa, I. Balan, S. Macavei, T. Lupascu

DSEFM P44 **NEW 3,4-DIHYDROPYRIMIDIN-2(1*H*)-THIONE DERIVATIVE THAT ACTIVATES THE Nrf2-DRIVEN ANTIOXIDANT RESPONSE** 140
N. Ciobanu, B. Buttari, E. Profumo, N. Sucman, N. Bolocan, M. Rusu, E. Gorincioi, F. Z. Macaev

DSEFM P45 **NEW ANTICANCER QUATERNARY AMMONIUM SALT OF 2-*TERT*-BUTYL-3-(1*H* -1,2,4-TRIAZOL-1-YL)-2*H*-CHROMEN-2-OL WITH IMPROVED BIOAVAILABILITY** 141
E. P. Stingaci, M. P. Ceabanova, E. C. Gorincioi, N. E. Dina, K. Vuković Đerfi, T. Matijević Glavan, F. Z. Macaev

SECTION SOLID STATE NANOPHYSICS AND NANOTEHNOLOGY (SSNN)

Ga_2O_3 BASED COMPOSITE FIMS AND AEROMATERIALS FOR MICROFLUIDIC, OPTOELECTRONIC AND PHOTO-ELECTROCHEMICAL APPLICATIONS 142
V. V. Ursaki, V. Morari, I. M. Tiginyanu

FUNCTIONAL NANOSTRUCTURES AND NANOMATERIALS FOR NEUROMORPHIC COMPUTING 143
A. S. Sidorenko

LAYERED SEMICONDUCTORS AND THEIR NANOSTRUCTURES: EXCITONS, POLARITONS, AND OPTICAL PHENOMENA 144
V. V. Zalamai, A. V. Tiron, I. G. Stamov, E. V. Rusu

MORPHOLOGY DESIGN IN POROUS GALLIUM ARSENIDE THROUGH CRYSTALLOGRAPHIC CONTROL AND ELECTROCHEMICAL NANOSTRUCTURING 145
E. V. Monaico, E. I. Monaico, V. V. Ursaki, I. M. Tiginyanu

THICKNESS-INDUCED TUNING OF ELECTRICAL AND PHOTOELECTRIC PROPERTIES IN ULTRALIGHT AERO-GaN/ZnO TETRAPOD NETWORKS 146
T. Braniste, I. Tiginyanu

NANOINDENTATION OF MgO: POP-IN EVENTS DEVELOPMENT UNDER DIFFERENT LOADING CONDITIONS 147
O. Shikimaka, D. Grabco, C. Pyrtsac, A. Prisacaru, D. Spoiala

NONLINEAR DYNAMICS OF QUANTUM DOT LASERS UNDER CONVENTIONAL AND FILTERED OPTICAL FEEDBACK 148
V. Tronciu, S. Rusu, T. Oloinic

LUMINESCENCE AND RADIATIVE DECAY KINETICS OF BOUND EXCITONS IN HALOGEN-INTERCALATED TRANSITION METAL DICHALCOGENIDES 149
N. Siminel, A. Micu, K. Slobodeniuc, A. Siminel, L. Kulyuk

SSNN P1 **MAGNETIC METAMATERIALS FOR SPIN – VALVE STRUCTURES AND FOR ARTIFICIAL NEURAL NETWORK BASE ELEMENTS** 150
V. I. Boian, R. Morari, V. M. Fomin, N. P. Rodriguez, J. Scheiter, A. Sidorenko

SSNN P2 **OBSERVATION OF YAMAJI MAGIC ANGLES IN BISMUTH SURFACES** 151
L. A. Konopko, A. A. Nikolaeva, T. E. Huber

SSNN P3 **ELECTRICAL TRANSPORT PROPERTIES OF $Bi_{0.98}Sb_{0.02}$ NANOWIRES IN SEMIMETAL AND SEMICONDUCTOR STATES** 152
A. A. Nikolaeva, L. A. Konopko, T. E. Huber, Gh. I. Para, I. Gh. Ghergishan

SSNN P4 **ELECTRICAL AND PHOTOELECTRICAL PROPERTIES OF Ga-DOPED Zn2:1Sn THIN FILMS OBTAINED BY SPRAY PYROLYSIS** 153
V. Morari, D. Bragari, V. Suman, E. V. Rusu

SSNN P5 **INTRINSIC PEROXIDASE-LIKE ACTIVITY OF ZnO/$MgFe_2O_4$ PEG NANOCOMPOSITES AND THEIR APPLICATION IN THE COLORIMETRIC DETECTION OF H_2O_2** 154
T. D. Gutsul, I. O. Rastimesina, A. J. Sibaev, E. P. Condrea, I. I. Belotercovschii

SSNN P6 **MICRO AND NANOWIRE AND ITS APPLICATION** 155
S. A. Baranov

SSNN P7 **SOLVENT-DEPENDENT EFFICIENCY OF ULTRASONIC LIQUID-PHASE EXFOLIATION OF TMD CRYSTALS** 156
S. Barladean, N. Siminel

SSNN P8 **OPTIMIZATION OF THE GROWTH TECHNOLOGY OF TiS_2, WS_2, AND MoS_2 SINGLE CRYSTALS FOR SUPERCAPACITOR APPLICATIONS** 157
V. Goremichin, N. Siminel, C. Slobodeniuc, L. Kulyuk

SECTION ELECTROMAGNETIC RADIATION DETECTION AND CONVERSION (EMDC)

HIGH-ENTROPY $(FeCoNiCrMn)_3O_4$ FILMS FOR CAMOUFLAGE COATINGS IN MICROWAVE REGION 158
S. Vatavu, Ig. Narolschi, O. Shapoval, M. Rusu, A. Belenchuk, Gh. Ghileţchii, A. Varzari, V. Crăciun, J. Lančok, Ş.-A. Irimiciuc

PHASE-TRANSITION-DRIVEN THERMOCHROMIC RESPONSE MODELLING IN VO_2-LIKE SYSTEMS 159
A. Varzari, A. Cliucanov, Gh. Ghileţchii, S. Vatavu

MASKLESS ONE-STEP MICROPATTERNING OF AZOPOLYMER THIN FILMS BY DIRECT ELECTRON BEAM RECORDING 160
C. Losmanschii, E. Achimova, V. Abaskin, S. Moldovanu, V. Botnari, A. Meshalkin, V. Cazac, D. Muntean, D. Spoială

TECHNOLOGY AND ELECTRONIC PROPERTIES OF NiO DOPED BY Cu AND Ga FOR CHROMOGENIC AND PHOTOVOLTAIC APPLICATIONS 161
Gh. Ghileţchii, O. Shapoval, M. Rusu, A. Varzari, A. Belenchuk, Ig. Narolschi, V. Nicorici, V. Crăciun, P. Garoi, V. Grumezescu, Ş.-A. Irimiciuc, S. Vatavu

DIFFRACTION EFFICIENCY AS A MEASURE OF OPTICAL PARAMETER MODULATION IN RECORDING MEDIA 162
A. Meshalkin, E. Achimova, V. Abaskin, C. Losmanschii, V. Botnari, D. Muntean

EMDC P1 **MULTI-BEAM LIGHT DIFFRACTION FROM CROSSED GRATINGS** 163
S. Sergeev, A. Meshalkin, I. Cojocaru

EMDC P2 **POLYMER/CHALCOGENIDE SEMICONDUCTOR STRUCTURE FOR X-RAY AND HOLOGRAPHIC IMAGING** 164
A. Chirita, N. Nasedchina, S. Vatavu

EMDC P3 **TOPOLOGICAL AND PHOTOELECTRICAL PROPERTIES OF In- AND Al-DOPED ZnSnO THIN FILMS PREPARED BY SPRAY PYROLYSIS** 165
V. Morari, V. Suman, E. Monaico, E. V. Rusu

EMDC P4 **DFB LASER-BASED PROTOTYPE METHANE SENSOR** 166
D. P. Dvornikov, A. V. Siminel

EMDC P5 **INVESTIGATION OF CLOSE-SPACED SUBLIMATION DEPOSITION OF SOLAR CELL ABSORBER LAYERS USING $AgSbS_2$ AS SOURCE MATERIAL** 167
D. Untila, D. Rusnac, G. Colibaba, C. Radu, A. E. Bocirnea, C. Besleaga, A. C. Galca, M. Koltsov, A. Katerski, I. O. Acik, N. Spalatu

EMDC P6 **HETEROGUNCTION DEVICES FABRICATED USING n-TYPE ZnO SPUTTERING COMBINED WITH p-TYPE Cu_2O RF SPUTTERING** 168
V. Suman, L. Ghimpu, V. Morari, I. Lungu, V. Ursu, V. Zalamai, E. Monaico, E. Rusu, Ed. Monaico

EMDC P7 **ASSESSMENT OF RADIOFREQUENCY LEVELS FOR PUBLIC ELECTROMAGNETIC FIELD EXPOSURE CHARACTERIZATION IN URBAN 2G–5G AND WI-FI NETWORKS: A CASE STUDY** 169
A. Prisacaru, C. M. Popescu, V. Mirovski

EMDC P8 **JONES MATRIX CHARACTERIZATION OF POLARIZATION GRATINGS RECORDED IN As_2S_3–Se NANOMULTILAYERS** 170
V. Botnari, V. Cazac, V. Abashkin, E. Achimova, C. Losmanschii, D. Muntean

EMDC P9 **STUDY OF ELECTROHYDRODYNAMIC INSTABILITIES IN AN ELECTRICALLY CHARGED DIELECTRIC LIQUID UNDER MICROGRAVITY FOR ELECTROMAGNETIC RADIATION DETECTION AND CONVERSION** 171
B. Constantinov

EMDC P10 **TECHNOLOGICAL AND MORPHOLOGICAL ASPECTS OF GaSe THIN FILMS PREPARED ON SAPPHIRE SUBSTRATES** 172
D. Spoială, E. Vatavu, Ig. Narolschi, V. Nicorici, M. Rusu, S. Vatavu

EMDC P11 **EXTERNAL FACTORS' INFLUENCE ON THE PARAMETERS OF InP PHOTOVOLTAIC CELLS** 173
E. Bercu, L. Gorceac, A. Scafaru, P. I. Chetruș, I. Maistruc, S. Vatavu

SYNTHESIS AND CRYSTAL STRUCTURE OF A NOVEL Cu(II) COORDINATION POLYMER BASED ON N-(2-(MORPHOLIN-4-YL)ETHYL)THIOSEMICARBAZONE OF 3-ETHOXYSALICYLALDEHYDE 174
A. Ciursin, R. Rusnac, S. Shova, A. Gulea

2-SUBSTITUTED 1H-PERIMIDINES AS A BUILDING BLOCKS FOR ELECTROACTIVE FUNCTIONAL MATERIALS 175
B. Gajewska, R. Malik, R. Motyka, A. Blacha-Grzechnik, M. Łapkowski, M. Czichy

INVESTIGATION OF ACRIDAN DERIVATIVES ELECTROCHEMISTRY BEHAVIOUR WITH IN-SITU AND EX-SITU METHODS 176
N. Kareva, M. Czichy

MEST P1 **FUNCTIONAL TiO_2 NANOMATERIALS AND IRON-BASED CATALYTIC SYSTEMS FOR ADVANCED OXIDATION OF EMERGING PHARMACEUTICAL POLLUTANTS** 177
L. Mocanu, M. Gonta

MEST P2 **ASPECTS OF DIFFERENTIATED FRACTIONATION OF SERUM PROTEINS DURING WHEY ELECTROACTIVATION** 178
I. V. Paladii, E. Gh. Vrabie, V. Gh. Vrabie, T. G. Stepurina, A. A. Policarpov, C. Gh. Sprincean

MEST P3 **METHODS FOR OBTAINING MoS_2 NANOMATERIALS VIA ULTRASOUND-ASSISTED ELECTROCHEMICAL INTERCALATION AND EXFOLIATION** 179
R. I. Lascova-Baciu, S. S. Belevskiy

MEST P4 **INVESTIGATION OF THE EFFICIENCY OF THE EXTRACTION TECHNOLOGY FROM KIWI USING ELECTROPLASMOLYSIS AND MICROWAVE TREATMENT** 180
A. Ya. Papchenko, G. D. Grecu

MEST P5 **INDUSTRIAL-SCALE TESTING OF THE MODIFIED BIOGAS TREATMENT TECHNOLOGY OF LIQUID WINERY WASTES** 181
Gh. Duca, O. Covaliova, L. Romanciuc, C. Tasca

MEST P6 **TRIBOLOGICAL BEHAVIOR OF ELECTRICAL CONTACTS PRODUCED BY THE ELECTROSPARK ALLOYING METHOD** 182
V. Mihailov, S. Ivaşcu, M. V. Lungu, D. Croitoru, Sp. Iaţco, A. Ianachevici, I. Ion, D. Pătroi, V. E. Marinescu, D. Tălpeanu

MEST P7 **INTENSIFICATION OF PHASE-STRUCTURAL TRANSFORMATIONS IN THE SURFACE LAYERS OF METALS UNDER THE COMBINED ACTION OF ELECTRIC-SPARK ALLOYING, PLASTIC DEFORMATION AND PLASMA-CHEMICAL TREATMENT** 183
V. Mihailov, S. Ivascu, N. Kazak, A. Ianachevici

MEST P8 **MODIFICATION OF METAL SURFACES THROUGH THE DEVELOPMENT OF ELECTRIC SPARK ALLOYING TECHNOLOGIES USING POWDERS** 184
S. Ivaşcu, V. Mihailov, D. Croitoru, Sp. Iaţco, A. Ianachevici

MEST P9 **MICROSTRUCTURE AND TRIBOMECHANICAL PROPERTIES OF ELECTROSPARK-DEPOSITED SILVER-BASED COATINGS ON COPPER SUBSTRATES** 185
M. V. Lungu, V. Mihailov, S. Ivaşcu, D. Pătroi, V. E. Marinescu, D. Tălpeanu, I. Ion, E. M. Lungulescu, A. R. Caramitu, E. Manta

MEST P10 **PHYSICO-CHEMICAL PROPERTIES OF INDUSTRIAL GLASSWARE FROM THE POSITION OF SYSTEM ANALYSIS** 186
V. A. Sharagov, G. I. Curicheru

MEST P11 **IMPROVING PHYSICO-CHEMICAL PROPERTIES OF ANNEALED HOLLOW INDUSTRIAL GLASSWARE** 187
V. A. Sharagov, G. I. Curicheru, I. N. Olaru

MEST P12 **ULTRASONICALLY ASSISTED EXTRACTION (UAE) OF BIOLOGICALLY ACTIVE SUBSTANCES FROM SPIRULINA** 188
T. D. Kubritskaya, G. K. Balan, T. D. Shemyakova

MEST P13 **IMPACT OF ANION ASYMMETRY MIXED SODIUM SALTS ELECTROLYTES ON ELECTRICAL CONDUCTIVITY** 189
K. D. Pershina, M. I. Gorobets, T. V. Trifonova

MEST P14 **KINETICS OF TETRACYCLINE HYDROCHLORIDE DEGRADATION IN UV/$S_2O_8^{2-}$ AQUEOUS SYSTEM** 190
T. Isac-Gutsul, D. L. Nika

MEST P15 **VISIBLE-LIGHT ACTIVE PHOTOCATALYST. EFFECT OF ELECTROCHEMICAL SYNTHESIS CONDITIONS ON THE PROPERTIES** 191
T. Ya. Datsko, V. I. Zelentsov, D. P. Dvornikov

MEST P16 **CALCULATION OF THERMODYNAMIC FUNCTIONS OF METHYLENE BLUE SORPTION ON DIATOMITE** 192
V. Zelentsov, T. Datsko, O. Bolotin

MEST P17 **SYNTHESIS AND PHYSICO-CHEMICAL CHARACTERIZATION OF TiO_2 – MODIFIED ACTIVATED CARBONS FOR PHOTOCATALYTIC AND ADSORPTION APPLICATIONS** 193
I. Ceban, R. Nastas, N. Timbaliuc, I. Nesterovschi, M. Stefan, A. Varadi, D. Toloman, A. Popa

MEST P18 **DEVELOPMENT OF CITRIC ACID-MODIFIED ACTIVATED CARBONS FROM WALNUT SHELL BIOMASS: STRUCTURAL, CHEMICAL AND SURFACE CHARACTERIZATION** 194
I. Ceban, C. Vicol, E. Moraru, M. Buga, M. Rusu, V. Ceban, S. Moldovanu, M. Mihet

MEST P19 **REMOVAL OF Fe(II) IONS ON CARBONACEOUS CATALYSTS AT DIFFERENT pH CONDITIONS** 195
I. Ceban, R. Nastas, T. Lupascu

MEST P20 **IN-SITU REAL TIME MEASUREMENT OF LASER INDUCED DAMAGE THRESHOLD OF METALLIC THIN FILMS USED FOR NS AND FS LASER MIRRORS** 196
C. Milos, D. Craciun, R. Udrea, P. Garoi, S. A. Irimiciuc, G. Dorcioman, G. Bleotu, F. Al-abedj, P. Pandele, R. Radoi, E. Matache, S. Das, D. Sandu, D. Cracana, T. Jitsuno, A. Tanaseanu, D. Ursescu, V. Craciun

MEST P21 **INCORPORATION OF SnS_2 IN NANOFIBERS FOR PHOTOCATALYTIC APPLICATIONS** 197
C. Creciunel, A. Tiron, V. Ciobanu, A. Mamoico, T. Galatonova, E. Rusu, I. Tiginyanu

MEST P22 **COMPARISION OF UV, UV/H_2O_2 AND UV/$S_2O_8^{2-}$ PROCESSES FOR THE DEGRADATION OF ROSUVASTATIN IN AQUEOUS SOLUTION** 198
E. I. Tutovan, T. V. Isac-Gutul

MEST P23 **ELECTRODEPOSITION OF IRON ALLOYS FROM CITRATE AND GLUCONATE ELECTROLYTES** 199
S. Kh. Ivashku, Zh. I. Bobanova, S. P. Yuschenko, S. M. Iatco

AUTHOR INDEX **200**

PROGRESS IN RESEARCH ON TERNARY MAGNETIC SPINELS: IN MEMORY OF THE ACADEMICIAN S. RADAUTSAN

V. Tsurkan

[1] *Laboratory of Physics of Semiconductor Compounds "Sergiu Rădăuțan", Institute of Applied Physics, Moldova State University, MD-2028 Chisinau, Republic of Moldova,*

[2]*Experimental Physics V, Center for Electronic Correlations and Magnetism,University of Augsburg, Augsburg 86135, Germany*

*E-mail: vladimir.turcan@ifa.usm.md

This communication presents an overview of progress in research of complex magnetic materials with spinel structure. This direction of research at the Institute of Applied Physics of the Academy of Sciences of Moldova and Technical University was founded in 1972 by academician S. Radautsan, Chief of Laboratory of Semiconductor Compounds. This year, the scientific community of the Republic of Moldova and its colleagues from Romania, Ukraine, Lithuania and other countries of Eastern and Western Europe celebrated his 100th anniversary.

Being a very energetic and ambitious person, academician S. Radautsan embraced with great enthusiasm the new scientific directions that were emerging in the field of complex semiconductor materials in the early 1970s. One of these new areas of research has become the physics of magnetic semiconductors (MS), a recently discovered group of compounds that possess both semiconductor properties and long-range magnetic order: ferromagnetic (FM), ferrimagnetic (FiM), or antiferromagnetic (AFM). The interaction between the charge carriers and localized magnetic moments in MS allows mutual control of their electronic and magnetic states. The representative examples of the novel physical effects revealed at that time in MS are the giant magnetoresistance (GMR) and photo-ferromagnetic effect (PFE) [1-2]. In the direct effect, GMR, one can reduce the resistance of a sample by two- three orders of value applying a moderate magnetic field (< 1 T). In the inverse effect, PFE, one can modify the magnetic parameters by illuminating a sample in the IR. These intriguing effects were thought to be of significant importance and to offer great promise for the development of new magnetoelectronic devices that exploit the strong coupling between magnetic and electronic properties.

The "renaissance" of magnetic semiconductors, and in particular magnetic spinels, occurred simultaneously with the discovery of the colossal magnetoresistance (CMR) effect in double-exchange manganites at the end of the 20th and beginning of the 21st centuries. In FiM ternary magnetic spinel $FeCr_2S_4$, it was shown that the CMR effect does not necessarily needs a double exchange [3]. Soon, a colossal magnetocapacitace effect and multiferroic behavior in another ternary FM spinel, $CdCr_2S_4$, was revealed [4]. These two landmark results appear to have stimulated a resurgence of research interest in magnetic spinels, which has been reflected in the avalanche of papers subsequently published by numerous research groups from Germany, Japan, Switzerland, the USA, China, France, Italy, Poland and other EU countries.

Below a review of several fundamental results obtained in last 20 years by researches from the Institute of Applied Physics (Moldova) in collaboration with their foreign partners is given. This review covers ternary and multinary magnetic materials with a spinel structure of the general formula AB_2X_4 (*A*=Fe, Co, Mn, Cu, Cd, Zn, Mg, Hg, Ga, Ge; *B*=Cr, Co, V, Sc, Al, Er, Yb, Nb, Ta; *X*=O, S, Se).

The spinel structure contains two different types of cationic sites. It can incorporate practically all metals from the periodic table. The driving force of the novel phenomena and unconventional ground states revealed in the magnetic spinels are the strong entanglements of charge, spin and orbital degrees of freedom, which are coupled to the lattice. Additional complexity stems from the topology of the

lattice leading to magnetic frustration, which can be either geometrical, like for magnetic *B*-site ions on the *pyrochlore* sublattice of corner-shearing tetrahedra, or of the bond type related to competing nearest-neighbor and further-neighbor exchange interactions between the magnetic *A*-site ions on the *diamond* sublattice. As a result of these correlations, a variety of emerging novel phenomena, like spin-liquids, spin-spiral liquids, spin-orbital liquids, orbital glass, spin-driven Jahn-Teller effect, appears in magnetic spinels.

Among the outstanding results obtained by collaborating research teams one can notice:

- discovery of colossal magnetocapacitance and multiferroic behavior in ternary FM spinel $CdCr_2S_4$ [4] followed by finding of similar effects in related FM $CdCr_2Se_4$ and $HgCr_2S_4$ with helical spin ordering;
- evidence of orbital-glass state in FiM spinel $FeCr_2S_4$ [5];
- evidence of spin-orbital-liquid ground state in bond-frustrated *A*-site spinel $FeSc_2S_4$ [6];
- finding of spiral-spin-liquid state and emergence of a vortex state in the *A*-site spinel $MnSc_2S_4$ with complex AFM order [7];
- evidence of spin-driven structural transformations (spin Jahn-Teller effect) by observation of splitting of the phonon modes in spinels $ZnCr_2S_4$, $ZnCr_2O_4$, $CdCr_2O_4$, and $MgCr_2O_4$;
- evidence of strong spin-lattice coupling in spinel $ZnCr_2S_4$ and magneto-structural transition revealed by sound-velocity measurements in magnetic fields up to 60 T [8];
- discovery of the metastable high-field phase in the spinel $CoCr_2O_4$ with complex spin structure revealed by ultrasound measurements in pulsed magnetic fields up to 60 T [9];
- evidence of low-temperature structural transformations and field-induced spin reorientation in $FeCr_2S_4$ [10];
- establishing a complete (*H*-*T*) phase diagram and exotic spin configurations in FiM spinel $MnCr_2S_4$ with Yafet-Kittel ground state in magnetic fields up to 100 T [11];
- observation of fractional antiferromagnetic skyrmion lattice induced by anisotropic couplings in spinel $MnSc_2S_4$ with complex AFM ordering [12];
- discovery of Néel-type skyrmion lattice in lacunar spinel GaV_4S_8 and GaV_4Se_8 [13].

The research results have been published in more than 150 articles in leading scientific journals, including Nature, Nature Physics, Nature Materials, Science Advances, Nature Communications, Phys. Rev. Letters, Phys. Rev. B, J. Appl. Physics, *etc*. These papers were cited more than 3700 times. The results on magnetic spinels are reviewed in Ref. [14].

[1] R. P. van Stapele, *Ferromagnetic Materials* (ed. E. P.Wohlfarth) **3**, 603 (1982).
[2] V. G.Veselago *et al*, *Letters to JETP* **15**, 316-318 (1972); W. Lems *et al*, *Phys. Rev. Lett.* **21**, 1643 (1968).
[3] A. P. Ramirez, R. J. Cava, and J. Krajewski, *Nature* (London) **386**, 156 (1997).
[4] J. Hemberger, P. Lunkenheimer, R. Fichtl, H.-A. Krug von Nidda, V. Tsurkan, and A. Loidl, *Nature* (London) **434**, 364 (2005).
[5] V. Tsurkan *et al*, *J. Phys. Chem Solids*, **66**, 2036 (2005), R. Fichtl *et al*, *Phys. Rev. Lett.* **94**, 027601 (2005).
[6] V. Fritsch *et al*, *Phys. Rev. Lett.* **92**, 116401(2004).
[7] S. Gao, O. Zaharko, V. Tsurkan, *et al*, *Nature Physics* **13**, 158-162 (2017).
[8] V. Tsurkan, S. Zherlitsyn, V. Felea, *et al*, *Phys. Rev. Lett.* **106,** 247202 (2011).
[9] V. Tsurkan, S. Zherlitsyn, S. Yasin, *et al*, *Phys.Rev. Lett.* **110**, 115502 (2013).
[10] J. Deisenhofer *et al*, *Phys. Rev.* B **100,** 144428 (2019); D. M. Evans *et al*, *Phys. Rev.* B **105**, 174107 (2022); L. Prodan *et al*, *Phys. Rev.* B **104**, L020410 (2021).
[11] A. Miyata *et al*, *Phys. Rev.* B **101**, 054432 (2020).
[12] S. Gao *et al*, *Nature* **586**, 37- 41 (2020).
[13] I. Kézsmárki *et al*, *Nature Materials* **14**, 1116-+ (2015).
[14] V. Tsurkan, H.-A. Krug von Nidda, J. Deisenhofer, P. Lunkenheimer, A. Loidl, "On the complexity of spinels: Magnetic, electronic, and polar ground states". *Physics Reports* **926**, 1–86 (2021).

EXPANDING THE CHALCOGENIDE SEMICONDUCTOR LANDSCAPE TOWARDS NARRO AND WIDE GAP MATERIALS

S. Schorr[1,2*]
[1]*Helmholtz-Zentrum Berlin for Materials and Energy, Berlin, Germany;*
[2]*Freie Universität Berlin, Institute of Geological Sciences, Berlin, Germany*
*E-mail: susan.schorr@helmholtz-berlin.de

Quaternary semiconductors belonging to the Cu_2BCX_4 compounds (B=Zn, Mn, Cd; C=Sn, Ge, Si; X=S,Se) present a remarkable compositional sandbox for the development of highly efficient integrated photovoltaics (multijunction devices or BIPV), low-light Internet of Things (IoT) sensors (indoor PV), and photoelectrochemical (PEC) water-splitting devices. By strategically replacing ions across the cation and anion substructures, these compounds can cover an expansive bandgap window spanning from the near-infrared (0.9 eV) to the ultraviolet (3.1 eV) spectrum. Fully exploiting this expansive material landscape requires looking beyond simple nominal stoichiometry, as the macroscopic optoelectronic performance of these materials is strongly dictated by fine crystallographic details like structural disorder and local structure distortions. Our systematic structural and optical investigation allowed to derive structure-function-relations of both the quaternary end-members and their corresponding substitution series.

A major hurdle in characterizing these quaternary phases using standard X-ray diffraction (XRD) is the differentiation problem, where elements with highly similar atomic numbers exhibit nearly identical X-ray scattering factors. This effect masks native anti-site disorder between electronically similar elements. To bypass this limitation, powder neutron diffraction was applied as the primary structural tool, exploiting the fact that neutrons interact directly with atomic nuclei to provide vastly different, non-monotonic coherent scattering lengths for electronically similar neighbors. [1]

Through comprehensive Rietveld refinement of these neutron diffraction profiles, this work successfully identifies and quantifies intrinsic point defect complexes and structural disorder, with a major focus placed on tracking Cu/B cation disorder or swapping mechanisms within the host networks. [2] Furthermore, the local structural distortions of the Cu_2BCX_4 endmembers were quantified by tracking the tetrahedral angle variance of the coordinate cation polyhedra. The mis-match in ionic radii on the B and C cation sites introduces systematic strain into the chalcogen sub-structure, forcing the anions away from ideal tetrahedral coordinates. Our findings show a clear link between this tetrahedral angle variance and changes in the optical bandgap, as the distortion alters the orbital overlap between the copper d-orbitals and the chalcogen p-orbitals, shifting the valence band maximum.

By mapping out cation and anion substitution series, we demonstrate that the optical bandgap can be predictably modified. On the narrow-gap end of the spectrum (0.9–1.4 eV), selenium- and tin-rich series compress the bandgap, lowering the conduction band minimum to optimize these materials for infrared harvesting and IoT deployment. Conversely, introducing sulfur and silicon widens the bandgap up to 3.1 eV. Because of the naturally high energy level of the copper d-orbitals these wide-gap phases retain exceptionally high conduction band minimum positions, allowing them to easily straddle the thermodynamic water reduction and oxidation potentials without requiring a large external bias. Ultimately, expanding the chalcogenide landscape to these narrow- and wide-gap extremes via precise control over structural disorder, composition, and tetrahedral distortions enables these copper-based semiconductors to move beyond standard single-junction configurations and into advanced, multi-functional roles.

[1] S. Schorr, C. Stephan, D. Toebbens, R. Gunder, T. Toerndal, in: *Advanced Characterization techniques for thin-film solar cells*, ed. By D. Abou-Ras, T. Kirchartz, U. Rau, Wiley, 2016.
[2] S. Schorr, G.Gurieva, M. Guc, M. Dimitrievska, A. Perez-Rodriguez, V. Izquierdo-Roca, C. Schnohr, J. Kim, W, Jo, M. Merino, *J. Phys: Energy* **2** (2020) 012002.

ALTERMAGNETS AND THEIR OPTICAL PROPERTIES

J. Deisenhofer[1]
[1]*Experimental Physics V, Center for Electronic Correlations and Magnetism, Institute for Physics, University of Augsburg, D-86159 Augsburg, Germany*
*E-mail: joachim.deisenhofer@physik.uni-augsburg.de

Altermagnets are collinear antiferromagnets, where a broken PT-symmetry lifts the Kramers degeneracy, and electronic and magnon bands can split-split at general points in the Brillouin zone, which make these materials interesting for spintronic applications. Ideal altermagnets and their secondary multipolar order parameters are described by non-relativistic spin groups instead of the relativistic magnetic space and point groups, which are commonly used to obtain selection rules and the form of symmetry-allowed tensors.

I will discuss, how one can try to find features of altermagnetism by optical spectroscopy experiments, although many of the candidate materials have been investigated optically over the past decades. In particular I will focus on phonon selection rules [1] and magneto-optical effects such as the Faraday effect and linear magnetic birefringence. The material platform consists mainly of the polar $A_2Mo_3O_8$ magnets with *A*=Fe, Co, Mn, which fulfill the criteria for altermagnetism, but show clear signs of spin-orbit coupling phenomena and the necessity to use the magnetic point group description to understand its properties [2,3,4].

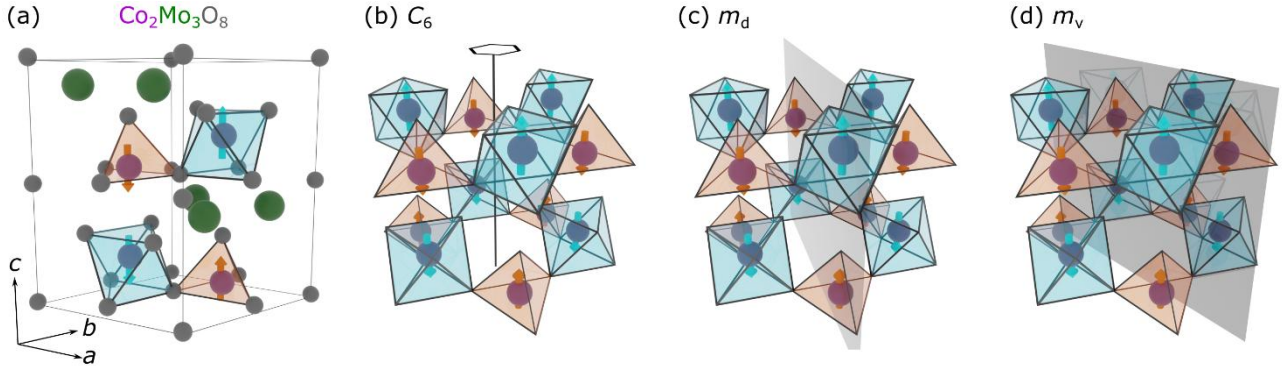


Figure 1. Crystal structure and magnetic ordering of $Co_2Mo_3O_8$: (a) Crystallographic and magnetic unit cell. (b)-(d) Symmetry elements generating the crystallographic point group 6mm.

[1] F. Schilberth, M. Konda´kor, D. Ukolov, A. Pawbake, K. Vasin, O. Ercem, L. Prodan, V. Tsurkan, A. A. Tsirlin, C. Faugeras, P. Lemmens, K. Penc, I. Ke´zsma´rki, S. Borda´cs, and J. Deisenhofer, Optical phonons as a testing ground for spin group symmetries, *npj Quantum Materials* **11** (2026) 26. Doi: https://doi.org/10.1038/s41535-026-00857-9.
[2] S. Reschke, D. G. Farkas, A. Strinic, S. Ghara, K. Guratinder, O. Zaharko, L. Prodan, V. Tsurkan, D. Szaller, S. Bordacs, J. Deisenhofer, and I. Kezsmarki, Confirming the trilinear form of the optical magnetoelectric effect in the polar honeycomb antiferromagnet $Co_2Mo_3O_8$, *npj Quantum Materials* **7** (2022) 1.
[3] K.V. Vasin, A. Strinic, F. Schilberth, S. Reschke, L. Prodan, V. Tsurkan, A. R. Nurmukhametov, M. V. Eremin, I. Kezsmarki, and J. Deisenhofer, Optical magnetoelectric effect in the polar honeycomb antiferromagnet $Fe_2Mo_3O_8$, *Phys. Rev. B* **110** (2024) 054401.
[4] D. Szaller, K. Szasz, S. Bordacs, J. Viirok, T. Room, U. Nagel, A. Shuvaev, L. Weymann, A. Pimenov, A. A. Tsirlin, A. Jesche, L. Prodan, V. Tsurkan, and I. Kezsmarki, Magnetic anisotropy and exchange paths for octahedrally and tetrahedrally coordi- nated Mn^{2+} ions in the honeycomb multiferroic Mn_2Mo_3O, *Phys. Rev. B* **102** (2020) 144410.

MICROWAVE ABSORBERS BASED ON HIGH-ENTROPY ALLOYS DEVELOPED BY PHYSICAL VAPOR DEPOSITION TECHNIQUES

S. Irimiciuc[1,2,*], P. Hruška[1], E. Marešová[1], L. Volfova[1], S.Cichoň[1], S. Chertopalov[1], V.Grumezescu[2], V. Craciun, S. Vatavu[3], J. Lancok[1]

[1]*Institute of Physics of the Czech Academy of Sciences, Na Slovance 1999/2, Prague, Czechia;*

[2]*National Institute for Laser, Plasma and Radiation Physics, 409 Atomistilor Street, Bucharest, Romania;*

[3]*Moldova State University, Alexei Mateevici St 60, Chișinău, Republic of Moldova*

*E-mail: irimiciuc@fzu.cz; stefan.irimiciuc@inflpr.ro

Complex high-entropy materials (HEMs), particularly high-entropy alloys (HEAs), high-entropy oxides (HEOs), and high-entropy nitrides (HENs), have been at the center of consistent groundbreaking results in various applications due to their multi-principal element composition that enable the exploration of diverse and variable properties within a single multielement system. While multiple routes for development of high-quality HEA coatings are often gravitating around magnetron sputtering, pulsed laser deposition, due to the fundamental non-equilibrium and non-thermal qualities, it can allow the generation of various high entropy stoichiometry and thus unlocking new generation of materials based around certain established core 5-6 elements.

In this work, we report on the fabrication of HfNbTaTiZr high entropy thin films with variable stoichiometries using pulsed laser deposition under a broad range of processing conditions, including inert (Ar) and reactive (O_2, N_2) atmospheres, pressures up to 100 Pa, substrate temperatures up to 800 °C, and variable laser fluences. These parameters were systematically adjusted to modulate the energy distribution and gas phase chemistry of the expanding metallic ions. Complementary in situ plasma diagnostics, specifically space resolved optical emission spectroscopy and angle resolved electrical probing, were employed to characterize plasma behavior during deposition. The monitoring of the plasma allowed us to define a clear deposition geometry where gas phase oxidation is limited. Comprehensive morphological and structural characterization was performed using Atomic Force Microscopy (AFM), Scanning Electron Microscopy (SEM), X ray Diffraction (XRD), X ray Photoelectron Spectroscopy (XPS), and MW absorption. An optimization framework was subsequently developed to correlate deposition parameters with the resulting film properties. The findings demonstrate that precise control over ion dynamics during growth enables systematic tuning of thin film characteristics, yielding a wide spectrum of microstructures—from amorphous and nanocrystalline phases to mixed phase architectures – as well as diverse compositional profiles and surface morphologies, ranging from smooth, compact layers to rough, granular nanostructures. The coatings showed absorption above 80% for thicknesses bellow 400 nm indicating surface dominating effects induced by the high entropy quality of the samples.

ACKNOWLEDGEMENTS. This work was supported by the NATO grant SPS MYP G6153.

MAGNETOPLASMONIC CRYSTALS

Pavlo Sai[1,2,3,*], Vadym Korotyeyev[1,4], Maksym Dub[1,3], Milan Orlita[5], Wojciech Knap[1,3]
[1]CENTERA Labs Institute of High Pressure Physics PAS, Warsaw, Poland; [2]Department of Physics, University of Duisburg-Essen, Duisburg, Germany; [3]CENTERA, CEZAMAT, Warsaw University of Technology, Warsaw, Poland; [4]V. Ye. Lashkaryov Institute of Semiconductor Physics (ISP), NASU, Kyiv, Ukraine; [5]LNCMI, CNRS-UGA-UPS-INSA-EMFL, France
*E-mail: psai@unipress.waw.pl

Plasmonic crystals, consisting of periodic plasmonic cavities with subwavelength periodicity, enable engineering of plasmonic band structures and strong confinement of terahertz (THz) radiation. While electrical and structural tuning of plasmonic crystals has been extensively investigated [1,2], the impact of magnetic fields on their band structure remains largely unexplored. Here, we report studies on high magnetic field influence on plasmonic crystals formed by periodic arrangements of carrier cavities in grating-gate AlGaN/GaN with high-mobility two-dimensional electron gas (2DEG). We show strong modification of the crystal structures related to interaction of plasmonic collective excitation with harmonics of single particle cyclotron resonance (CR) electron excitations. The investigated structures were fabricated from AlGaN/GaN heterostructures grown on semi-insulating SiC substrates, with sub-micron grating gates patterned by electron-beam lithography. A schematic cross-section of the device is shown in Fig. 1(a). Magnetotransmission measurements were performed using Fourier-transform infrared spectroscopy in magnetic fields up to 16 T at 4.2 K.

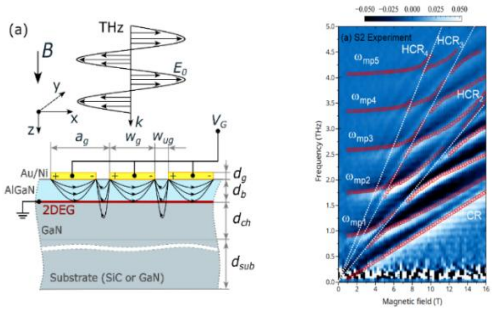


Figure 1. (a) Schematic view of AlGaN/GaN-based plasmonic crystal integrated with metal grating. (b) Magneto transmission of sample with 87% grating filling factor.

The key parameter that decides about the plasmonic crystal band structure is the filling factor (ratio of metalized and uncovered crystal surface). AlGaN/GaN grating-gate plasmonic crystals with different filling factors were investigated. We show that for plasmonic crystals with low grating filling factor, the fundamental plasmon mode exhibits anticrossing with higher harmonics of CR – HCR, leading to the formation of Bernstein modes and magnetic-field-induced band splitting. Increasing the grating filling factor results in excitation of multiple magnetoplasmon modes with energies up to 5 THz. As shown in Fig.1(b), these modes (ω_{mp}) strongly hybridize with HCR up to the fourth order modifying plasmonic crystal energy band structure by appearance of a complex spectrum of Bernstein modes.

The experimental observations are accurately reproduced by our electrodynamic model incorporating the magnetic-field-dependent conductivity tensor of the 2DEG without fitting parameters. The results demonstrate that plasmonic crystals provide a versatile platform for engineering tunable THz excitations in strong magnetic fields and open prospects for magnetoplasmonic THz devices.

[1] P. Sai, et al., Phys. Rev. X 13, 041003 (2023).
[2] P. Sai, et al., Advanced Optical Materials 13(21), 2500716 (2025).

LUMINESCENCE OF RARE-EARTH IONS DOPED IN FLUORITE CRYSTALS

M. Stef[1,*], C. Schörnig[1], P. Veber[1], G. Buse[2], M. Poienar[2], D. Vizman[1]
[1]*Faculty of Physics and Mathematics, West University of Timişoara, Timişoara, Romania;*
[2]*Institute for Advanced Environmental Research (ICAM), West University of Timişoara, Timişoara, Romania*
*E-mail: marius.stef@e-uvt.ro

Fluorite-type crystals (CaF_2 and BaF_2) doped with trivalent rare-earth ions combine high chemical and thermal stability, low phonon energy and easy polishing, making them attractive hosts for solid-state laser, dosimetry and photobiomodulation applications. In this work, TmF_3, CeF_3 and TbF_3-doped CaF_2 and BaF_2 single crystals, as well as (Er,Yb) co-doped BaF_2 crystals, were grown by the vertical Bridgman technique and characterized structurally and spectroscopically.

Structural defects were evaluated by chemical etching of freshly cleaved (111) planes; dislocation densities of the TmF_3-doped crystals were found to be on the order of 10^3–10^5 cm^{-2}, increasing with dopant concentration and confirming good crystal quality for optical measurements [1,2]. Dielectric relaxation studies on CaF_2:TmF_3 and BaF_2:TmF_3 evidenced dipolar defects associated with C_{3v} and C_{4v} charge-compensation sites, and the segregation coefficients of Tm^{2+} and Tm^{3+} ions along the crystals were determined from the Scheil equation and the Beer–Lambert law.

Optical absorption and emission spectra revealed the characteristic transitions of Tm^{3+} and Tm^{2+} ions in CaF_2, with strong UV–VIS emission and concentration quenching above 1 mol% dopant, and a new UV emission band at 353 nm (Tm^{2+}) and 343 nm (Tm^{3+}) was identified. In BaF_2:TmF_3 the Tm^{2+} absorption bands were not observed, suggesting a host-dependent charge-conversion mechanism. X-ray irradiation of CaF_2:TmF_3 produced a reversible enhancement of the Tm^{2+} band at 590 nm, following an exponential saturation model. Gamma-irradiated CeF_3-doped BaF_2 crystals showed an unstable colour centre absorbing at 520 nm, decaying with a multi-exponential lifetime, together with a previously unreported red emission of Ce^{3+} at 605 and 648 nm.

Judd–Ofelt analysis of Tm^{3+} in CaF_2 and BaF_2 [1] and of the (Er,Yb) co-doped BaF_2 crystal [3] yielded the intensity parameters Ω_t (t = 2, 4, 6), radiative transition probabilities, branching ratios and radiative lifetimes, and confirmed strong radiative transitions (e.g. $\Omega_2 = 0.59$, $\Omega_4 = 0.38$, $\Omega_6 = 0.27$, in units of 10^{-20} cm^2, for BaF_2:Er^{3+}/Yb^{3+} [3]). The UV-A and green emissions of these crystals are relevant for photofunctionalization and photobiomodulation of dental implant surfaces.

These results demonstrate that rare-earth-doped fluorite single crystals grown by the Bridgman method combine good structural quality with favourable spectroscopic properties, supporting their further development for laser and biomedical applications.

Acknowledgements: This work was supported by a grant of the Ministry of Education and Research, CCCDI – UEFISCDI, project number PN-IV-P6-6.1-CoEx-2024-0154, within PNCDI IV.

[1] C. Schörnig, M. Ştef, G. Buse, M. Poienar, P. Veber, D. Vizman. *Materials* **17** (2024) 4965.
[2] G. Buse, C. Schörnig, M. Ştef, M. Poienar, D. Tatomirescu, A. Popescu, J. Debray, V. Motto-Ros, F. Pelascini, D. Vizman, P. Veber. *J. Alloys Compd.* **1010** (2025) 177784.
[3] M. Ştef, C. Schörnig, G. Buse. *Materials* **18** (2025) 1915.

ELECTRON BEAM LITHOGRAPHY FOR 2D MATERIAL-BASED DEVICES

A. Dinescu*, M. Dragoman, D. Dragoman, A. Avram, O. Simionescu, C. Parvulescu
IMT Bucharest, Voluntari, Romania
*E-mail: adrian.dinescu@imt.ro

2D materials-based devices represent a possible solution for the nanoelectronics of the future. Their functionality strongly depends on the shape of the layer itself. For example, some unpatterned 2D materials have no bandgap, being not suitable for the fabrication of many devices like the digital field effect transistors, because the "off state" could not be achieved (1). While 2D materials enable absolute electrostatic gate control for extreme device scaling, three fabrication bottlenecks proved to be extremely important: high contact resistance, interface contamination and thermal budgets. The fabrication of such devices involves synthesizing atomically thin sheets, transferring them to target substrates, and patterning them into functional microelectronic circuits. In order to obtain their desired functionalities, the active layer is patterned at the nanoscale by various nano lithographic techniques, one of the most important being the electron beam lithography. It features ultra-high resolution and great flexibility, proving to be a very useful tool for shaping 2D materials with details in the sub 100nm range (2). The main objective of this talk is to present precise fabrication using e-beam lithography for a series of devices like: graphene ballistic transistors producing negative differential resistance with large peak to valley ratio (3), graphene field-effect-transistors with nano perforated graphene channels (4), ultrathin SnS_2 and $SnSe_2$-based FETs (4) and MoS_2 self-switching diode (fig.1) and memristor and photodetector (5). The basics of e-beam lithography will be introduced, also pattern transfer, e-beam resists, material interaction, resolution limits, throughput, proximity effect correction and characteristics of different e-beam lithography tools, all these connected with the special requirements of deposition and etching processes.

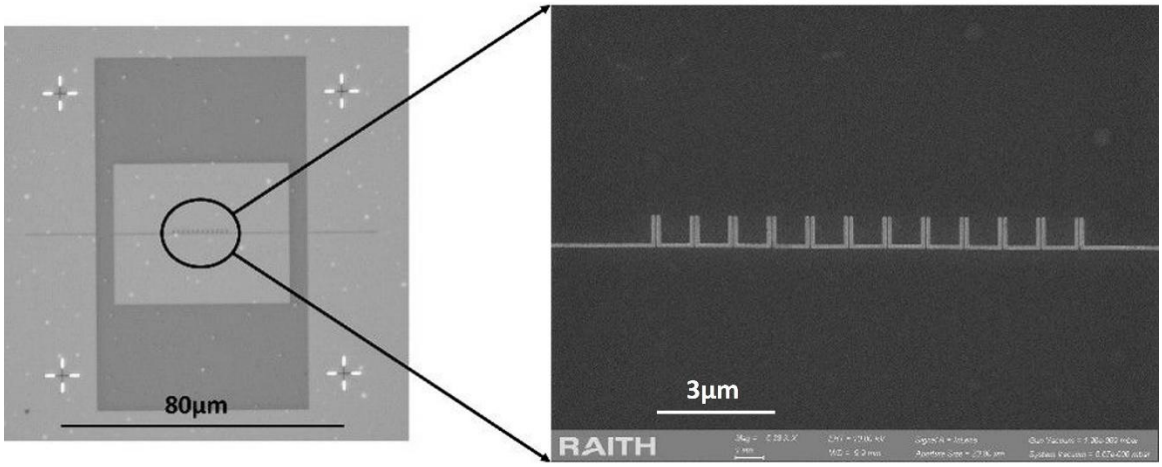


Figure 1. Self-switching diodes (SSD) fabricated at the wafer level on a 2D few-layer MoS_2 thin film

[1] A.K. Geim, K.S. Novoselov, *Nat. Mater*., **6** (2007) 183
[2] A. Dinescu et al, *International Conference on Nanotechnologies and Biomedical Engineering*, *Springer Nature Switzerland* (2023) 278-283.
[3] M. Dragoman et al., *Nanotechnology*, **25(41)** 2014, 415201
[4] Andrea Sessa et al., *Advanced Electronic Materials*, 2025, e00327
[5] M. Dragoman et al., Physica E: *Low-dimensional Systems and Nanostructures*, **126**, February 2021, 114451

QUANTUM INTERFERENCE IN QUANTUM RINGS

V. M. Fomin[1,2*]
[1]*Institute for Emerging Electronic Technologies, Leibniz Institute for Solid State and Materials Research (IFW) Dresden, D-01069 Dresden, Germany;*
[2]*Department of Physics and Engineering, Moldova State University, MD-2009 Chişinău, Republic of Moldova*
*E-mail: v.fomin@ifw-dresden.de

Quantum rings are a special class of modern high-tech nanostructures, which provide a unique playground for the quantum-mechanical paradigm and topological physics [1]. The frontline methods of fabrication and characterization of quantum rings together with the sophisticated cutting-edge theoretical research and numerical simulations have allowed for accumulation of a significant thesaurus of fundamental information on their behavior. Among the fabrication methods, I will represent their formation by molecular beam epitaxy and droplet epitaxy of semiconductors, as well as their topology-driven electronic, optical, and magnetic properties. Highly complex theoretical models have been developed to adequately explain the specific features of quantum rings, related to spin dynamics and the spin-orbit interaction, in particular, tunable exciton topology in type II InAs/GaAsSb quantum nanostructures [1, 2] and spin interference in quantum rings subject to the Rashba spin-orbit interaction [1, 3] (see Figure 1).

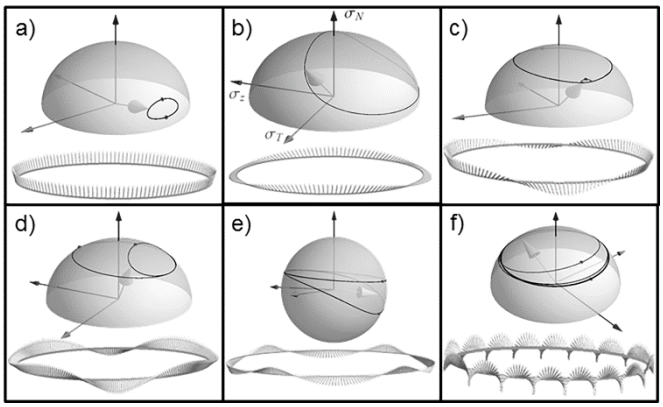


Figure 1. Electronic trajectories shown on the Bloch-Frenet-Serret sphere and spin textures in the lab frame for an elliptical quantum ring with ratio between the minor and major axes a/b=0.4 and six values of the spin-orbit coupling strength α. Panels (a)-(f) correspond to $m^*\alpha L/\hbar$ = 1,4,8,10,12,50, where m^* is the effective mass of the spin carriers and L is the total length of the ring. (After Ref. [3].)

I will provide an overview of the recent advancements in the physics of quantum rings related to the electron-phonon interaction in ring-like structures, quantum-interference manifestations in novel materials, e.g., graphene cylinders, cyclocarbons, MoS_2, effects of the electric field and the THz radiation on optical properties of quantum rings and quantum-ring molecules. Special emphasis will be made on fascinating novel effects emerging due to double-connectedness in various physical systems, embracing the occurrence of the continuous geometric phase provoking formation of non-integer mode numbers in Möbius microring light cavities [1, 4], the inverse Faraday effect on the generation of current states in an array of superconductor nanorings, and the emergence of lightning-like magnetic flux bursts into a macroscopic superconductor ring. This highly diversified knowledge underpins numerous suggestions for prospective applications of quantum rings and other nanostructures with nontrivial topology as a highly tunable elemental base for future device design and optimization in optoelectronics, spintronics, information storage and processing, as magnetic memory elements as well as photonic sources and detectors.

[1] V. M. Fomin (Ed.), Physics of Quantum Rings, 3rd edition, Springer International Switzerland, Cham, 2025.
[2] J. M. Llorens, E. R. Cardozo de Oliveira, L. Wevior, V. Lopes-Oliveira, V. López-Richard, J. M. Ulloa, M. D. Teodoro, G. E. Marques, A. García-Cristóbal, G. Quiang-Hai, B. Alén. *Phys. Rev. Applied* **11** (2019) 044011.
[3] Z.-J. Ying, P. Gentile, C. Ortix, and M. Cuoco. *Phys. Rev. B* **94** (2016) 081406.
[4] J. Wang, S. Valligatla, Y. Yin, L. Schwarz, M. Medina-Sánchez, S. Baunack, C. H. Lee, R.Thomale, S. Li, V. M. Fomin, L. Ma, O. G. Schmidt. *Nature Photonics* **17** (2023) 120-125.

FRACTIONALIZED EXCITATIONS PROBED BY ULTRASOUND

S. Zherlitsyn*
Hochfeld-Magnetlabor Dresden (HLD-EMFL), Helmholtz-Zentrum Dresden-Rossendorf (HZDR), 01328 Dresden, Germany
*E-mail: s.zherlitsyn@hzdr.de

In my talk, I will present a study of magnetoelastic interactions in α−$RuCl_3$ - a prototypical material for the Kitaev spin model on the honeycomb lattice, with a possible spin-liquid state featuring Majorana fermions and $\mathbb{Z}_2$-flux excitations [1]. I will show results of the temperature and in-plane magnetic-field dependence of the sound velocity and sound attenuation for several longitudinal and transverse phonon modes propagating along high-symmetry crystallographic directions. A comprehensive data analysis above the magnetically ordered state provides strong evidence of phonon scattering by Majorana fermions. This scattering depends sensitively on the value of the phonon velocities relative to the characteristic velocity of the low-energy fermionic excitations describing the spin dynamics of the underlying Kitaev magnet. Moreover, the data displays a distinct reduction of anisotropy of the sound attenuation, consistent with the presence of thermally excited $\mathbb{Z}_2$ visons. Using ultrasound measurements at pressures up to 1.16 GPa, we reveal significant modifications of the acoustic properties and the H−T phase diagram of this material [2]. Hydrostatic pressure suppresses the three-dimensional magnetic order and induces a dimerization transition at higher pressures. At low pressures, the sound attenuation exhibits a linear temperature dependence, while above 0.28 GPa, it becomes nearly temperature independent, suggesting a shift in the phonon scattering regime dominated by Majorana fermions. We demonstrate the potential of phonon dynamics as a promising probe for uncovering fractionalized excitations in α−$RuCl_3$ and provide new insights into the H−T−P phase diagram of this material.

ACKNOWLEDGEMENTS. Author acknowledge the support of the HLD at HZDR, member of the European Magnetic Field Laboratory (EMFL).

[1] A. Hauspurg, S. Zherlitsyn, T. Helm, V. Felea, J. Wosnitza, V. Tsurkan, K.-Y. Choi, S.-H. Do, Mengxing Ye, W. Brenig, and Natalia B. Perkins, Fractionalized excitations probed by ultrasound, *Phys. Rev. B* **109** (2024) 144415.
[2] A. Hauspurg, Susmita Singh, T. Yanagisawa, V. Tsurkan, J. Wosnitza, W. Brenig, Natalia B. Perkins, and S. Zherlitsyn, Spin-strain interactions under hydrostatic pressure in α-$RuCl_3$, *Phys. Rev. B* **112** (2025) 134405.

EXTENDED FEYNMAN VARIATIONAL PRINCIPLE AND RELATED ANALYTICAL METHODS FOR LATTICE POLARONS

S. N. Klimin[1,*], J. Tempere[1], M. Houtput[1], I. Zappacosta[1], S. Ragni[2], T. Hahn[3], L. Celiberti[4], C. Franchini[4] and A. S. Mishchenko[2]
[1]*TQC, Universiteit Antwerpen, Antwerpen, Belgium;*
[2]*Institute of Physics, Zagreb, Croatia;*
[3]*Flatiron Institute, New York, USA;*
[4]*Computational Materials Physics, University of Vienna, Austria*
*E-mail: sergei.klimin@uantwerpen.be

We develop and compare analytical approaches for the polaron problem in finite-width, non-parabolic conduction bands [1, 2]. Our main result is an extension of the Feynman variational method to tight-binding lattices [1], where the effective-mass approximation breaks down. We also revisit analytical methods originally formulated for continuum polarons, including canonical transformations and improved self-consistent Wigner–Brillouin approximations, and generalize them to lattice systems. In a finite-bandwidth lattice, these approaches exhibit qualitative features absent in the continuum case, such as a nontrivial connection between weak- and strong-coupling limits. An improved Wigner–Brillouin scheme yields a momentum-dependent polaron self-energy free of resonances and consistent with perturbation theory at zero momentum.

The methods are applied to the Holstein model and benchmarked against numerically exact calculations, including Diagrammatic Monte Carlo, exact diagonalization, and density-matrix renormalization-group results, and are further extended to polarons with Rashba spin–orbit coupling.

The self-energy of a Holstein polaron exhibits close agreement between the modified Feynman variational method and numerically exact results. The developed approaches are promising for theoretical study of polarons with different types of particle-phonon interaction.

[1] S. N. Klimin, J. Tempere, M. Houtput, I. Zappacosta, S. Ragni, T. Hahn, L. Celiberti, C. Franchini and A. S. Mishchenko, *Phys. Rev. B* **113** (2026) 245128.
[2] S. N. Klimin, J. Tempere, M. Houtput, S. Ragni, T. Hahn, C. Franchini and A. S. Mishchenko, *Phys. Rev. B* **110** (2024) 075107.
[3] G. L. Goodvin, M. Berciu, and G. A. Sawatzky, *Phys. Rev. B* **74** (2006) 245104.

QUANTUM GENERATING FUNCTIONS AND UNIVERSAL FAMILY-VICSEK SCALING IN NONEQUILIBRIUM QUANTUM MANY-BODY SYSTEMS

Cătălin Paşcu Moca[1,2,*]
[1]*Department of Physics, University of Oradea, Oradea, Romania;*
[2]*Department of Theoretical Physics, Budapest University of Technology and Economics, Budapest, Hungary*
*Email: mocap@uoradea.ro

We present a numerical framework for computing quantum generating functions (QGFs) of local observables in one-dimensional quantum many-body systems at high temperature, enabling accurate determination of cumulants and full counting statistics at time scales beyond the reach of existing classical and quantum simulation techniques. Using this approach, we investigate the dynamics of spin fluctuations in integrable and non-integrable quantum spin chains and establish a direct connection between full counting statistics and universal dynamical scaling. In particular, we demonstrate that the second cumulant of transferred magnetization obeys the quantum analogue of Family-Vicsek scaling, providing a unified description of fluctuation growth and finite-size saturation. For SU(N)-symmetric spin chains, including the XXZ and Izergin-Korepin models, we identify distinct transport universality classes characterized by ballistic (z=1), Kardar-Parisi-Zhang superdiffusive (z=3/2), and diffusive Edwards-Wilkinson (z=2) scaling, while integrability breaking universally drives the system into the diffusive regime. Extending the analysis to dissipative XXZ chains with homogeneous gain and loss, we derive an exact solution in the non-interacting limit and show that dissipation continuously interpolates between coherent ballistic transport and dissipation-dominated dynamics. Our results establish quantum generating functions as a powerful tool for accessing universal nonequilibrium dynamics and reveal that Family-Vicsek scaling provides a unifying framework for fluctuation growth in both closed and open quantum many-body systems.

[1] Angelo Valli, Cătălin Paşcu Moca, Miklós Antal Werner, Márton Kormos, Žiga Krajnik, Tomaž Prosen, Gergely Zaránd, Efficient computation of cumulant evolution and full counting statistics: application to infinite temperature quantum spin chains, *Phys. Rev. Lett.* **135** (2025) 100401
[2] Cătălin Paşcu Moca, Balázs Dóra, Doru Sticlet, Angelo Valli, Tomaž Prosen, Gergely Zaránd, Dynamic scaling and Family-Vicsek universality in SU(N) quantum spin chains, *Phys. Rev. B* **113** (2026) L020405
[3] Cătălin Paşcu Moca, Doru Sticlet, Tamás Vicsek, Balázs Dóra, Two-parameter Family-Vicsek scaling in a dissipative XXZ spin chain, arXiv:2603.23388

FROM BINARY TUNGSTEN ALLOYS TO HIGH-ENTROPY ELECTROCATALYSTS: BALANCING ACTIVITY AND STABILITY IN HIGHLY ALKALINE MEDIA

N. Tsyntsaru[1,2,*], T. K. Ratajczyk[3], H. Cesiulis[2], M. Donten[3]
[1]*Institute of Applied Physics, Moldova State University, Chisinau, Republic of Moldova*
[2]*Institute of Chemistry, Faculty of Chemistry and Geosciences, Vilnius University, Vilnius, Lithuania;*
[3]*Faculty of Chemistry, University of Warsaw, Warsaw, Poland*
*E-mail: ashra_nt@yahoo.com

Compositionally complex alloys offer a promising route to noble-metal-free electrocatalysts because several functional contributions can be integrated within a single material. However, increasing the number of elements does not automatically improve performance: the role of each component and the resulting activity-stability trade-off must be established systematically. This study presents the transition from conventional binary tungsten alloys to medium- and high-entropy electrodeposited materials for the hydrogen evolution reaction in highly alkaline media.

FeW, CoW, NiW, CoFeW, CoFeNiW and CoCuFeNiW coatings were prepared by induced electrodeposition and evaluated in 10 M KOH using polarization measurements, electrochemical impedance spectroscopy, scanning electron microscopy and cross-sectional compositional analysis. Corrosion parameters were additionally obtained by fitting polarization data near the corrosion potential using the Butler-Volmer equation, thereby enabling analysis of systems whose complex anodic branches do not permit conventional Tafel extrapolation.

The results reveal distinct and complementary functions of the alloying elements. Cobalt shifts hydrogen evolution towards less negative potentials, whereas iron provides favourable Tafel slopes of approximately 67 mV dec^{-1}. Nickel markedly improves corrosion resistance, limits tungsten dissolution and promotes thinner, more stable surface layers, although binary NiW displays comparatively sluggish hydrogen-evolution kinetics. Copper reduces internal stress and severe cracking. Consequently, CoFeW gives the highest catalytic activity, reaching 100 mA cm^{-2} at an overpotential of approximately 220 mV, but remains vulnerable to corrosion. CoFeNiW and CoCuFeNiW retain favourable kinetics while providing substantially improved structural and electrochemical stability.

These findings demonstrate that the main benefit of compositionally complex tungsten alloys is not a generic high-entropy effect, but the deliberate integration of element-specific functions. Knowledge-guided compositional design therefore provides a pathway towards scalable, noble-metal-free cathodes that combine rapid hydrogen evolution with resistance to aggressive alkaline environments and operational standby conditions.

ACKNOWLEDGMENTS. The authors gratefully acknowledge the institutional support of their respective institutions, including funding from the Research Council of Lithuania, grant no. S-MIP-24-11 and by the Excellence Initiative Research University, microgrant no. BOB-IDUB-622-10/2025 (IV.4.1.) from the Ministry of Science and Higher Education, Warsaw, Poland.

DEVELOPING AI-DRIVEN TOOLS FOR ACCELERATED RESEARCH AND INDUSTRIAL PROCESSES MONITORING

Gina Y. Soracá-Pérez[1,3], Jon Garí-Galíndez[1,4], Robert-Fonoll Rubio[1], Esko Niemi[2], M. Israr-Qadir[2], Alejandro Pérez-Rodríguez[1,3], Pedro Vidal-Fuentes[1], Victor Izquierdo-Roca[1], Maxim Guc[1]*
[1]Catalonia Institute for Energy Research (IREC), Barcelona, Spain; [2]Midsummer AB, Järfälla, Sweden; [3]IN[2]UB, Departament d'Enginyeria Electrònica i Biomèdica, Universitat de Barcelona, Barcelona, Spain; [4]Departament de Física, Universitat Politècnica de Catalunya, Barcelona, Spain
*E-mail: mguc@irec.cat

Research on thin-film photovoltaic (PV) devices has attracted increasing attention due to their advantages for decentralized applications such as the Internet of Things, building- and vehicle-integrated photovoltaics, and agrivoltaics. However, the complex multilayer architecture of thin-film technologies, based on multicomponent compounds, poses significant challenges for both laboratory-scale research and industrial scale-up. The large number of optimization parameters in these complex systems leads to long development cycles, often spanning decades, and requires substantial human and material resources to achieve performance levels attractive for industrial implementation. During technology scale-up, process inhomogeneities frequently arise, resulting in significant variability in device performance within and between production batches, further complicating the transfer of laboratory developments to industrial manufacturing. Consequently, there is a strong demand for universal methodologies applicable throughout both technology development and industrial production.

In this work, an artificial intelligence (AI)-driven methodology is presented for the rapid analysis of heterogeneous laboratory characterization data and real-time industrial process monitoring. The proposed approach combines automated multimodal characterization of thin-film PV devices with the analysis of synthesis parameters, physical properties, and device performance using explainable AI models. This enables the exploration of large multimodal datasets that are inaccessible to conventional analysis methods and allows the identification of synergies and causal relationships between critical material and device properties, revealing the fundamental physical and chemical factors limiting the technology at its current stage of development. Furthermore, the methodology naturally provides strategies for seamless integration into industrial process-monitoring systems.

Flexible Cu(In,Ga)Se_2 (CIGS) solar modules fabricated on stainless-steel substrates using Midsummer's industrial production line are used as a case study. A set of samples with controlled deviations in the manufacturing process, specifically variations in the deposition energy of the Mo:Na back-contact layer (from 70 to 120 kJ), was investigated. The resulting dataset combines production parameters, high-throughput multimodal characterization data, and optoelectronic properties from more than 1,500 individual solar cells. The multilevel analysis and classification of this dataset enabled the identification of the key physicochemical properties governing efficiency variations under both controlled and uncontrolled process fluctuations. In addition, methodologies for deposition-process monitoring and device-efficiency prediction were developed, demonstrating the strong potential of AI-driven approaches to accelerate research and enable advanced control of complex thin-film PV manufacturing processes.

BAND-GAP SPECTRA AND HARMONIC WAVE MODES IN AN INFINITE STRING WITH PERIODIC ELASTIC CONSTRAINTS

Alexandr A. Barsuk*, Florentin Paladi
Department of Theoretical Physics and ePhysMCS Research Laboratory,
Moldova State University, A. Mateevici str. 60, MD-2009 Chisinau, Republic of Moldova
*E-mail: a.a.barsuk@mail.ru

This study provides a comprehensive analytical investigation of free harmonic vibrations of an infinite string with periodically distributed identical elastic supports. The problem is formulated as a periodic multipoint spectral problem for the classical string vibration equation posed on the entire real axis. By exploiting the periodic structure of the system, the original differential formulation is reduced to an equivalent linear homogeneous finite-difference equation with constant coefficients governing the nodal displacements at the support locations. This transformation enables a complete characterization of the admissible vibration frequencies and associated wave modes.

It is shown that the spectrum possesses a characteristic band-gap structure typical of periodic media, where admissible frequencies form continuous propagation bands separated by forbidden intervals. Explicit analytical equations defining the boundaries of the frequency bands are derived, and the dependence of these boundaries on the stiffness of the elastic supports is established. A variational formulation based on the Rayleigh quotient is developed and used to analyze the monotonic behavior of the eigenfrequencies with respect to the support stiffness. Frequencies corresponding to modes with nonzero support displacements increase monotonically as the support stiffness grows, whereas modes vanishing at the support points remain unaffected by this parameter.

An equivalent formulation of the spectral problem is also obtained, reducing the infinite-domain problem to a boundary-value problem with non-standard parameter-dependent boundary conditions induced by periodicity. The vibration modes associated with the edges of the spectral bands are constructed explicitly and classified according to their symmetry properties. Furthermore, asymptotic analysis demonstrates the continuous transition of the spectrum to limiting configurations corresponding to a string on a continuous elastic foundation and to a string with perfectly rigid periodic supports.

The obtained results provide a complete analytical description of the spectral properties and wave propagation characteristics of periodically supported strings. As a result of the universal nature of periodic spectral phenomena, the developed framework may also serve as a representative analytical model for more complex periodic systems arising in structural dynamics, wave mechanics, phononic materials, and vibration control applications. For example, the results are relevant to phononic and acoustic metamaterials, in which periodic constraints or inclusions are introduced intentionally to control wave propagation. Also, band-gap phenomena analogous to those derived in the present work form the physical basis of vibration filters, waveguides, and locally resonant metamaterials used in noise and vibration mitigation [1].

ACKNOWLEDGEMENTS. Authors gratefully acknowledge support provided by the National Agency for Research and Development through the grant number 25.80013.5007.07RE, and the Ministry of Education and Research of the Republic of Moldova through the grant number 011210.

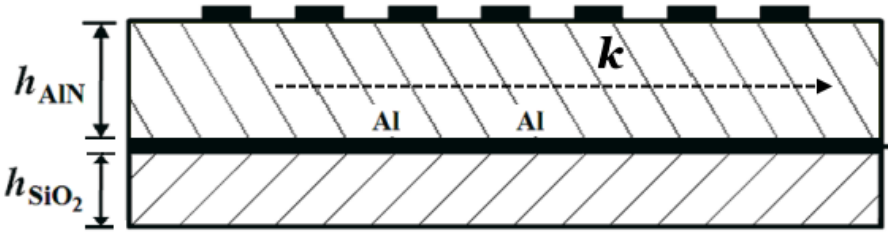
[1] A.A. Barsuk, F. Paladi, Free harmonic vibrations of an infinite string with periodic elastic supports. *AIP Advances* (2026) in press.

INTRINSIC STABILIZATION OF THIN-PLATE ACOUSTIC RESONATORS AGAINST BOTH TEMPERATURE AND PRESSURE VARIATIONS

S. Cojocaru[1,*], L. Dohotaru[2]
[1]*Horia Hulubei National Institute for Physics and Nuclear Engineering, Magurele, Romania;*
[2]*Technical University of Moldova, Chisinau, Republic of Moldova*
*E-mail: scojocaru@theory.nipne.ro

Stabilization of the resonance frequency in thin-plate acoustic devices (MEMS in acoustic generation and filtering, various sensing applications, etc.) against variations in environmental conditions is commonly reduced to the passive or active compensation of a single factor (usually temperature), while all other factors (e.g., pressure or mass loading) are addressed through isolation techniques or separate correction circuits. We discuss a possibility of dual – factor compensation, in which the response of a multilayer thin structure to both temperature and ambient pressure variations vanishes through an appropriate choice of intrinsic parameters, namely the constituent materials and layer-thickness ratios.

Response functions are derived analytically for the S_0 Lamb mode in the long-wavelength limit and expressed explicitly in terms of bulk material properties. We demonstrate that dual-factor intrinsic stabilization requires at least a three-layer structure and can be achieved using materials commonly employed in temperature – compensated devices, such as aluminum nitride, fused silica, and aluminum. Due to the anomalous elastic properties of silicate glasses, it is possible to implement a fully (T, P) – compensated thin – layer acoustic resonator [1]. The figure shows the cross-section of the considered structure, where h are the respective thicknesses and k is the wave-vector of the S_0 mode.



We also discuss the possibility of frequency stabilization against other factors. Identification of the key material properties governing the existence of a stability solution may enable the targeted design of such composites and facilitate the development of new multiple – factor – compensated thin – plate devices.

[1] S. Cojocaru, *Appl. Sci.* ***15(17)*** (2025), 9349, Doi: https://doi.org/10.3390/app15179349.

ENHANCING THE PERFORMANCE OF InGaN-BASED GREEN LEDs THROUGH SUBSTRATE POLARITY ENGINEERING: FROM POLAR c-PLANE TO SEMIPOLAR STRUCTURES

V. P. Sirkeli[1,2,*]

[1]*E. Pokatilov Laboratory of Physics and Engineering of Nanomaterials, Institute of Applied Physics, Moldova State University, 60 A. Mateevici str., Chisinau, MD-2009, Moldova;*

[2]*Department of Applied Physics and Computer Science, Faculty of Physics and Engineering, Moldova State University, A. Mateevici str. 60, MD-2009 Chisinau, Moldova;*

*E-mail: vadim.sirkeli@gmail.com

The development of highly efficient green light-emitting diodes (LEDs) remains a critical challenge for next-generation solid-state lighting and full-color micro-LED display technologies. Compared with blue-emitting InGaN devices, green LEDs require a higher indium content in the active region, which leads to stronger strain-induced polarization fields, enhanced quantum-confined Stark effect (QCSE), reduced electron–hole wave function overlap, and ultimately lower quantum efficiency. This phenomenon, commonly referred to as the "green gap," continues to limit the performance of InGaN-based green emitters [1-3].

In this work, a comprehensive numerical study of InGaN-based green LEDs grown on polar c-plane (0001) and semipolar (11–22), (11–21), and (10–12) substrates is presented. The device performance was analyzed using a self-consistent Schrödinger–Poisson and drift–diffusion simulation framework that accounts for carrier transport, polarization effects, radiative recombination, Shockley–Read–Hall recombination, Auger processes, and carrier leakage mechanisms. The investigated structures consisted of five-period InGaN/InGaN multiple quantum wells designed for green emission.

The simulation results reveal a significant influence of substrate polarity on carrier confinement and recombination dynamics. Semipolar substrates substantially reduce polarization-induced electric fields, transforming the quantum-well potential profile from a strongly tilted triangular shape into a nearly rectangular configuration. As a consequence, electron leakage is suppressed, hole injection is enhanced, and carrier balance within the active region is improved. The semipolar LEDs exhibit considerably lower turn-on voltages of approximately 3.6–3.9 V compared with about 5.0 V for the conventional c-plane device.

Among the investigated structures, the LED grown on the semipolar (10–12) substrate demonstrated the best overall performance, achieving a wall-plug efficiency of 14.7% at 100 A/cm², compared with 11.5% for the c-plane LED. The highest internal quantum efficiency of 66.6% was obtained for the LED on the semipolar (11–21) substrate. In addition, semipolar devices showed superior spectral stability, with electroluminescence peak wavelengths near 500 nm and significantly smaller current-induced wavelength shifts than the conventional c-plane structure.

These results demonstrate that substrate polarity engineering is an effective approach for mitigating polarization-related limitations in InGaN green LEDs and provides a promising pathway toward high-efficiency green emitters for future RGB micro-LED displays and advanced solid-state lighting systems.

ACKNOWLEDGEMENTS. The author acknowledge the financial support from the Ministry of Education and Research of the Republic of Moldova (research program no. 011208).

[1] V. P. Sirkeli, O. Yilmazoglu, Sh. Al-Daffaie et al., *J. Phys. D: Appl. Phys.*, vol. **50** (2017), 035108.
[2] V. P. Sirkeli, *Semiconductors*, vol. **58** (2024), 928-935.
[3] V. P. Sirkeli, S. I. Caragacian, Iu. B. Boris, D. L. Nika, *Phys. Solid State*, vol. **67** (2025), 655–663.

CHANGE IN MAGNETIC AND POLARIZATION CHARACTERISTICS FACILITATED BY REDISTRIBUTION OF ELECTRON DENSITY IN THE [FeCo] COMPLEX

Serghei Ostrovsky*, Sophia Klokishner
Moldova State University, Institute of Applied Physics, Chișinău, Republic of Moldova
*E-mail: sm_ostrovsky@yahoo.com

A theoretical model for the description of the spin transformation in FeCo dimeric complexes accompanied by the change of macroscopic polarization due to reversible intramolecular electron transfer between ligand and Fe center has been developed. Taking into account the molecular structure of the crystals demonstrating this transformation, the cooperative interaction between the molecular modes forming the spectrum of a single complex and crystalline modes assuring the cooperativity in the system is assumed to be responsible for the spin transformation. The dipole-dipole interaction between complexes in the whole crystal is included in the model as well. For the explanation of the experimental change of the macroscopic polarization with the temperature increase, along with the ground configuration of the FeCo dimeric complex two excited configurations were included in the model (see Fig.1). The approach, suggested by Hizhnyakov and co-authors for the impurity centers in crystals [1] and modified for the description of spin crossover in complexes of different nuclearity and charge transfer induced spin transitions [2], was generalized to the case when more than two electronic states are involved in the spin transition. The developed model was applied for the explanation of the magnetic and polarization characteristics of the [(Fe(*RR*-cth))(Co(*SS*-cth))(μ-dhbq)]$(AsF_6)_3$ compound [3]. The main peculiarities of the experimental behavior have been reproduced, and namely, the narrow hysteresis loops in both magnetic and polarization data as well as the further increase in polarization change with the increase of temperature after the spin transition in magnetic data has already occurred.

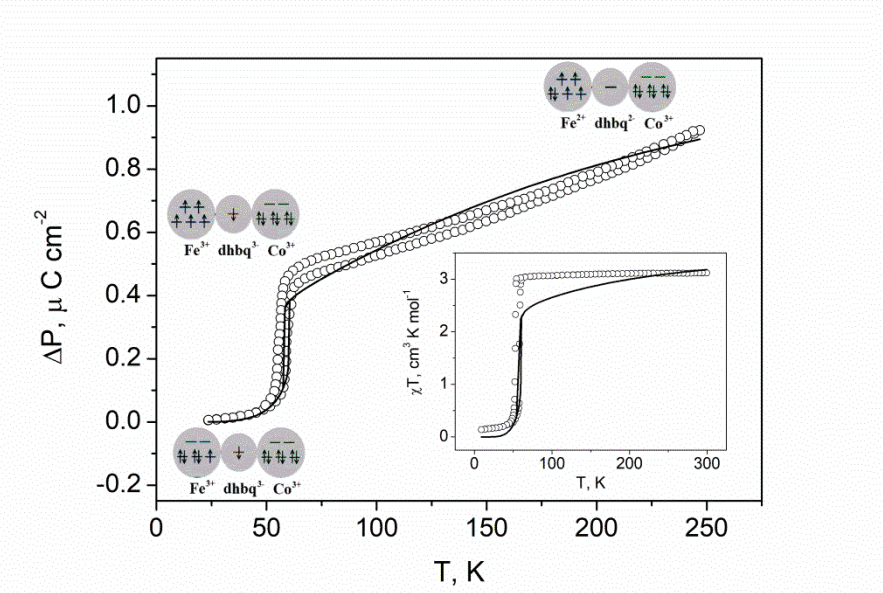


Figure 1. The polarization change as a function of temperature for compound [(Fe(RR-cth))(Co(SS-cth))(μ-dhbq)]$(AsF_6)_3$. Inset: the χT product as a function of temperature for this compound. The circles represent the experimental data [3]. The theoretical curves are calculated in the framework of the presented model.

ACKNOWLEDGEMENTS. The authors are grateful to the National Agency for Research and Development of the Republic of Moldova for financial support (project No. 25.80012.5007.85SE).

[1] V. Hizhnyakov, K. Pae, T. Vaikjarv. *Chem. Phys. Lett.* **525−526** (2012) 64−68.
[2] S. Klokishner, S. Ostrovsky, A. Palii, B. Tsukerblat. *Magnetochemistry* **8** (2022) 24 (13p.).
[3] X. Zhang et al. *J. Am. Chem. Soc.* **145** (2023) 15647−15651.

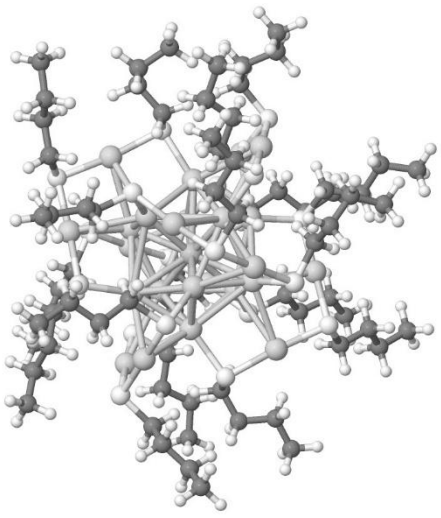
ELECTROCHEMICAL AND SPECTROSCOPIC SIGNATURES OF THE JAHN–TELLER EFFECT IN PLATINUM-MONODOPED $Au_{24}Pt(SR)_{18}$ CLUSTERS

K. Zdunek*, T. Korona, A. Więckowska
Faculty of Chemistry, University of Warsaw
Pasteura 1 St., 02-093 Warsaw, Poland
*E-mail: k.zdunek10@uw.edu.pl

Thiolate-protected gold clusters $Au_{25}(SR)_{18}$ (Au_{25}) can undergo heterometal doping, including platinum incorporation, yielding new electrocatalytic materials with distinguishable properties. In contrast to the Au_{25} form, the $Au_{24}Pt(SR)_{18}$ ($Au_{25}Pt$) cluster (maintaining the 0 charge) exhibits an enhanced Jahn–Teller effect, manifested by the elongation and contraction of selected Au–Pt bonds within the cluster core. Using density functional theory, we describe the structure of this system by analogy to classical distortions in octahedral geometries and rationalize the observed splitting of the superatomic 1P orbitals within a group-theoretical framework.

The stronger Jahn–Teller distortion in the Pt-doped cluster contributes to the increased thermodynamic stability of the $Au_{24}Pt^0$ form relative to the all-gold clusters Au_{25}^- and Au_{25}^0 within the same thiolate environment, which is reflected in its higher oxidation potential. The oxidation and reduction processes of Au_{25} at low (absolute) charge states are expected to follow Nernstian behavior; however, we demonstrate that the Au_{25}^{3+} form is unstable, with a lifetime not exceeding several seconds. Clusters protected by longer-chain alkanethiols (e.g., hexanethiol versus butanethiol) exhibit enhanced stability, and the use of longer ligands favors the formation of $Au_{24}Pt$ species over Au_{25} in the reaction mixture.

Analysis of both experimental and simulated IR spectral shifts indicates a preference for *gauche* conformations in $Au_{24}Pt^0$ clusters relative to *all-trans* configurations, enabling partial exposure of selected atoms within the ligand shell. This structural rearrangement gives rise to distinct catalytic properties compared to Au_{25}, with enhanced reactivity toward electrophilic substrates such as H^+ ions and hydrogen peroxide molecules.



MODELING OF THE VALENCE TAUTOMERIC TRANSFORMATION IN COBALT COMPLEXES: INTERACTION OF MOLECULAR MODES WITH PHONONS

Sophia Klokishner*, Oleg Reu, Serghei Ostrovsky
Moldova State University, Institute of Applied Physics, Chișinău, Republic of Moldova
*E-mail: klokishner@yahoo.com

A theoretical model has been elaborated for the explanation of the valence tautomeric transformation in cobalt compounds with the general formula $[Co(^1Bu_2sq)_2(L)_2]$. The model accounts for electronic states arising from 2 configurations of the complex: **1**. low-spin - $Co^{III}(sq)(cat)$; **2**. high-spin - $Co^{II}(sq)_2$, where the ligand cat contains two paired electrons, while a single electron is located on the sq-ligand. The cooperativity in the model is assured by the interaction accounting for the presence in the vibrational spectra of molecular crystals of phonons along with molecular vibrations. The Hamiltonian of this interaction is obtained by generalization of the approach, suggested for single impurity centers in crystals [1], to crystals containing complexes with labile electronic states, and namely, spin crossover and valent-tautomeric complexes [2]. Since the valence tautomeric transformation is accompanied by electronic density redistribution, the dipole-dipole interaction is included in the model as well. In the frames of the suggested model there are explained quite nicely the magnetic properties of the $[Co(^tBu_2sq)_2(3\text{-tnp})_2]$ and $[Co(^tBu_2sq)_2(2\text{-tnp})_2]$ compounds (Fig.1), for which the dipole-dipole interaction is inactive due to vanishing values of the dipole moments of these complexes calculated with DFT. Then the suggested model is generalized to account for the dipole-dipole interaction, which is relevant for the compound $[Co(^tBu_2sq)_2(btnp)_2]$ possessing non-zero dipole moments in the states of configurations **1** and **2** above mentioned. The energy of dipole-dipole interaction for this compound calculated with the aid of DFT is shown to be comparable to other interactions involved in the model. In the compound $[Co(^tBu_2sq)_2(btnp)_2]$ this interaction suppresses the valence-tautomeric transformation, and the examined compound does not demonstrate a spin transition in the whole temperature range.

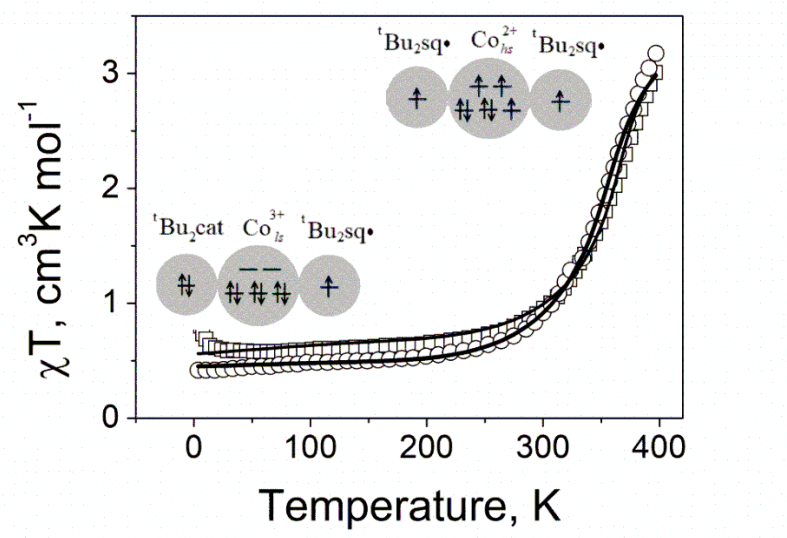


Figure 1. The χT product as a function of temperature for compounds $[Co(^tBu_2sq)_2(3\text{-tnp})_2]$ (squares) and $[Co(^tBu_2sq)_2(2\text{-tnp})_2]$ (circles). The symbols represent the experimental data [3]. The theoretical curves are calculated in the framework of the presented model.

ACKNOWLEDGEMENTS. The authors are grateful to the National Agency for Research and Development of the Republic of Moldova for financial support (project No. 25.80012.5007.85SE).

[1] V. Hizhnyakov, K. Pae, T. Vaikjarv. *Chem. Phys. Lett.* **525−526** (2012) 64−68.
[2] S. Klokishner, S. Ostrovsky, A. Palii, B. Tsukerblat. *Magnetochemistry* **8** (2022) 24 (13p.).
[3] P. Wang et al. *Cryst. Growth Des.* **23** (2023) 2384–2394.

SPIN TRANSFORMATION INDUCED BY THE PROTON TRANSFER IN THE IRON (II) HYDRAZONE CRYSTALLINE COMPOUND $[Fe(HL\text{-}F)_2](AsF_6)_2$

O.S. Reu, S.I. Klokishner*
Moldova State University, Institute of Applied Physics, Chișinău, Republic of Moldova
*E-mail: klokishner@yahoo.com

To explain the observed spin transformation accompanied by the proton transfer inside each iron(II) complex being the structural element of the $[Fe(HL\text{-}F)_2](AsF_6)$ compound [1] the single point DFT calculations (B3LYP functional, triple zeta def2-TZVP basis set in conjunction with the auxiliary basis sets def2-TZVP/C, def2/J [2]) have been performed. Within these calculations the energies of the complex as functions of the total spin value S=0,1 and 2 of the iron(II) ion have been obtained for fixed nuclear configurations, applying the experimental data on the crystal structure of the titled compound at temperatures 25K, 123K, 153K and 220K. At temperatures 25K and 123K for all four complexes A1, A2, A3 and A4 present in the structure of the examined compound the same order of alternation of single point energies complying with the total spin values S=0,1 and 2 of the iron(II) ion has been obtained. The lowest single point energy for all four mentioned complexes corresponds to the total spin value S=0, that is in agreement with the observed vanishing value for the χT product up to 130 K. At 25K in the pairs of complexes A1,A4 and A2,A3 the calculated dipole moments are oppositely directed and have the same magnitude. It is demonstrated that from 8 complexes revealed by X-ray investigations in the unit cell of the crystal 4 complexes are in the *ls*-state at 153K, while the other 4 complexes have already passed to the *hs*-state. The latter result is in agreement with the observed value 1.6 cm^3Kmol^{-1} for the χT product at 153K. For this temperature the DFT calculations also indicate on the presence of four pairs of complexes in the structure with the dipole moments being antiparallel in each pair, so as the total crystal polarization is equal to zero. The performed DFT studies also demonstrate, that at 220 K complexes C1, C2, C3, C4, present in the crystal unit cell have achieved the *hs*-state, and in the pairs of complexes C1,C4 and C2,C3 the dipole moments are directed antiparallel, so as well as for other temperatures the total polarization in the crystal is vanishing. The examination of the spin conversion through single point DFT calculations allowed not only to restore the picture of spin transformation in the titled compound, but also to obtain information about the mutual arrangement of the dipole moments of different complexes present in the crystal structure at various temperatures. Thus, it has been demonstrated that in spite of the fact that the arrangement of dipole moments significantly changes with temperature, it does not lead to the appearance of macroscopic polarization in the crystal at any temperature.

ACKNOWLEDGEMENTS. The authors are grateful to the Ministry of Education and Research of Moldova for financial support (project no. 011201). The authors also express their gratitude to the National Research and Educational Network of Moldova (RENAM) for providing computing resources.

[1] T. Nakanishi, Y. Hori, S. Wu, H. Sato, A. Okazawa, N. Kojima, Y. Horie, H. Okajima, A. Sakamoto, Y. Shiota, K. Yoshizawa, O. Sato, *Angew. Chem. Int. Ed.* **59** (2020) 14781-14787.
[2] Neese, F. Software update: the ORCA program system, version 4.0. *Wiley Interdiscip. Rev.: Comput. Mol. Sci.* **8(1)** (2018) No. e1327

ON THE DOUBLE DEGENERACY OF QUASI-ENERGY LEVELS

I. I. Geru*
Institute of Chemistry, Moldova State University, Chișinău, Republic of Moldova
*E-mail: iongeru11@gmail.com

When the electromagnetic field of large amplitude is perfectly resonant with a transition frequency, the standard perturbation theory fails, and the system requires a non-perturbative treatment. In this case, the behavior of quantum system can be determined using the concept of quasi-energy [1].
In the presence of an external periodical electromagnetic field of large amplitude with the angular frequency ω, the Hamiltonian of the system has the property of time periodicity:

$$\mathbf{H}(\mathbf{x}, t + \tau) = \mathbf{H}(\mathbf{x}, t),\ \tau = 2\pi/\omega \quad (1)$$

where x includes both spatial coordinates and spin variables. The solution of the time-dependent Schrödinger equation has the form

$$\psi(\mathbf{x}, t) = \Phi(\mathbf{x}, t) \exp\left(-\frac{i}{\hbar}\mathcal{E}t\right), \quad (2)$$

where the function Φ(x, t) is periodic in time with the period τ. This function satisfies the equation

$$\boldsymbol{\mathcal{H}}(t)\,\Phi(\mathbf{x}, t) = \mathcal{E}\,\Phi(\mathbf{x}, t), \quad (3)$$

where

$$\boldsymbol{\mathcal{H}}(t) = \mathbf{H}(t) - i\hbar\frac{\partial}{\partial t} \quad (4)$$

and $\mathcal{E}$ is the eigenvalue of the operator $\boldsymbol{\mathcal{H}}(t)$ (the quasi-energy).
The time-translation operators $\boldsymbol{T}_{m\tau}$ (m = 0, ±1, ±2, …), which transform $\psi(\mathbf{x}, t)$ into $\psi(\mathbf{x}, t+m\tau)$, and the time-reversal operator $\boldsymbol{\mathcal{T}} = \mathbf{UKI}_t$ [2] (where **U** is the unitary operator, **K** is the complex conjugation operator, and $\mathbf{I}_t$ transforms t into -t) each commute with the operator $\boldsymbol{\mathcal{H}}(t)$. As for commutator $[\boldsymbol{\mathcal{T}}, \boldsymbol{T}_{m\tau}]$, depending on the ratio $\mathcal{E}/\hbar\omega$, it can be equal to zero or nonzero. Indeed:

$$[\boldsymbol{\mathcal{T}},\ \boldsymbol{T}_{m\tau}]\,\psi(\mathbf{x}, t) = 2i\sin(2m\mathcal{E}/\hbar\omega)\,\boldsymbol{\mathcal{T}}\psi(\mathbf{x}, t),\ (m = 0, \pm1, \pm2, \ldots), \quad (5)$$

where it was taken into account that the functions $\Phi^*(\mathbf{x}, -t)$ and $\Phi^*(\mathbf{x}, -t + m\tau)$ coincide due to their time periodicity. Taking this remark into account, the following equality takes place

$$\mathbf{U}\Phi^*(\mathbf{x}, -t + m\tau)\exp\left(-\frac{i}{\hbar}\mathcal{E}t\right) = \boldsymbol{\mathcal{T}}\psi(\mathbf{x}, t), \quad (6)$$

which was taken into account in (5).
In the absence of additional degeneracy of quasi-energy levels due to the time-reversal symmetry, the wave functions $\boldsymbol{\mathcal{T}}\psi(\mathbf{x}, t)$ and $\psi(\mathbf{x}, t)$ are linearly dependent (*i.e.* $\boldsymbol{\mathcal{T}}\psi(\mathbf{x}, t) = c\psi(\mathbf{x}, t)$, where c is a constant). After substituting $\boldsymbol{\mathcal{T}}\psi(\mathbf{x}, t)$ by $c\psi(\mathbf{x}, t)$ in (5), we obtain:

$$[\boldsymbol{\mathcal{T}},\ \boldsymbol{T}_{m\tau}] = 2i\,c\sin(2\pi m\,\mathcal{E}/\hbar\omega). \quad (7)$$

In Ref. [3], it was shown that if two operators do not commute, but each separately commutes with the time-independent Hamiltonian, then this implies a twofold degeneracy of energy levels. According to (7), the commutator of operators $\boldsymbol{\mathcal{T}}$ and $\boldsymbol{T}_{m\tau}$ is nonzero if the ratio $\mathcal{E}/\hbar\omega$ is an integer or half-integer (the case m = 0 is trivial). By analogy with the two-fold degeneracy of energy levels discussed in Ref. [3], a quantum system under action of a large-amplitude periodic electromagnetic field is characterized by the double degeneracy of quasi-energy levels. This degeneracy arises from the simultaneous presence of time-reversal and time-translation symmetries.

ACKNOWLEDGEMENTS. This research is supported by the research subprogram "Chemical study of secondary metabolites from local natural sources and valorization of their application potential based on broadening molecular diversity with multiple functionality (MetNatVal)" (code 010601) funded by the Ministry of Education and Research of the Republic of Moldova

[1] Ya. B. Zel'dovich, Quasi-energy of quantum system being exposed to periodic action, *JETF* (*ЖЭТФ/ZhETF*) **51(5)**, (1966) 1492-1495.
[2] Ion Geru, Dieter Suter, *Resonance Effects of Excitons and Electrons: Basics and Applications*, Lecture Notes in Physics, Springer-Verlag, Berlin, Heidelberg, **869** (2013) 283 Doi: https://doi.org/10.1007/978-3-642-35807-4.
[3] H. J. Lipkin, *Quantum Mechanics*. North Holland Publishing Company (1973), 588 p.

REACTIVE FILLERS AS A TOOL FOR MICROSTRUCTURE ENGINEERING IN Bi_2Te_3-BASED THERMOELECTRIC COMPOSITES

M. Zhezhu[1*], V. Mehrabyan[1], V. Torosyan[1], D. Vanyan[1], M. Yaprintsev[2], O. Ivanov[2], A. Vasil'ev[1]
[1] *A.B. Nalbandyan Institute of Chemical Physics NAS RA, Yerevan, Armenia;*
[2]*Belgorod State University, Belgorod, Russia*
*E-mail: marina.zhezhu@ichph.sci.am

Bi_2Te_3-based thermoelectric materials remain among the most efficient compounds for near-room-temperature energy conversion [1, 2]. One promising route for further performance enhancement is the introduction of reactive fillers capable of interacting with the matrix during sintering and generating new microstructural features that affect charge and phonon transport [3, 4].
The influence of reactive fillers on the microstructure, carrier concentration, electrical transport, and thermoelectric performance is analyzed and compared in terms of the formation of core–shell inclusions, solid-solution regions, and chemically modified interfaces (see Figure 1). Particular attention is devoted to the recently developed medium-entropy $BiSbSe_{1.5}Te_{1.5}$–$NbTe_4$ system, where the starting quasi-one-dimensional $NbTe_4$ filler undergoes an in situ transformation into an $NbSe_2$-based solid solution during SPS. This transformation is accompanied by pronounced microstructural evolution and modification of the thermoelectric properties.
The results demonstrate that reactive-filler-assisted SPS processing represents a versatile strategy for tailoring the microstructure and transport characteristics of Te- and Se-containing chalcogenides. The proposed approach provides a new pathway for the design of advanced thermoelectric composites through controlled chemical transformation of filler phases during sintering.

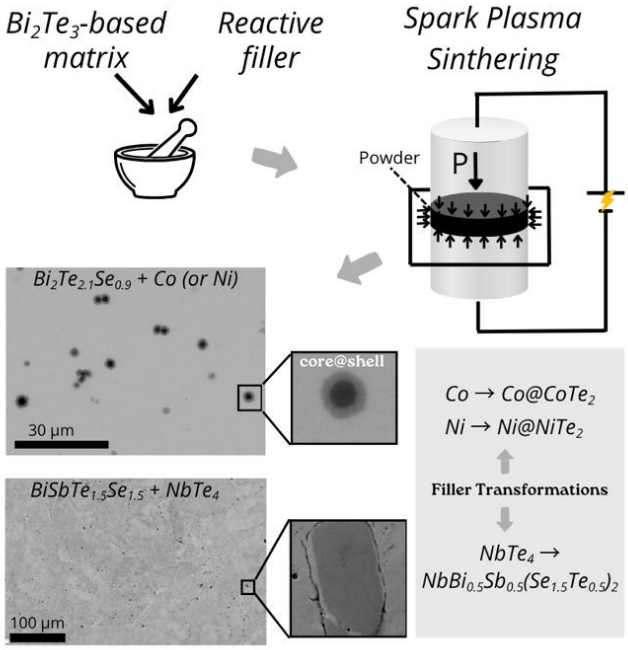


Figure 1. Schematic illustration of microstructural evolution associated with reactive filler transformations during SPS

ACKNOWLEDGEMENTS. This work was supported by the Higher Education and Science Committee of the RA MoESCS Grant No. 25IRF/2-2F001.

[1] M. Darwiche, J. Faraj et al. *Results in Engineering* **24** (2024) 103354.
[2] B. Zhu, X. Liu, et al., *Energy and Environmental Science* **13** (2020) 2106-2114.
[3] M. Zhezhu, O. Ivanov, et al., *J. Alloys and Compounds* **938** (2023) 168564.
[4] M. Zhezhu, A. Vasil'ev, et al. *J. Solid State Chemistry* **305** (2022) 122696.

QUANTUM WELL ENGINEERING FOR HIGH-EFFICIENCY InGaN-BASED RED LEDs

V. P. Sirkeli[1,2,*], S. I. Caragacian[1], Iu. B. Boris[1], D. L. Nika[1]
[1]*E. Pokatilov Laboratory of Physics and Engineering of Nanomaterials, Institute of Applied Physics, Moldova State University, A. Mateevici str. 60, MD-2009, Chisinau, Republic of Moldova;*
[2]*Department of Applied Physics and Computer Science, Faculty of Physics and Engineering, Moldova State University, A. Mateevici str. 60, MD-2009, Chisinau, Republic of Moldova;*
*E-mail: vadim.sirkeli@gmail.com

The realization of efficient red light-emitting diodes (LEDs) based on the InGaN material system remains one of the key challenges for next-generation full-color micro-LED displays. In contrast to blue and green InGaN-based emitters, red LEDs require a substantially higher indium content in the active region, resulting in increased strain, stronger polarization fields, pronounced quantum-confined Stark effect (QCSE), reduced electron–hole wave function overlap, and severe efficiency droop [1-3]. Consequently, the optimization of quantum well (QW) design is crucial for improving both efficiency and spectral stability of long-wavelength InGaN devices.

In this paper, we present a comprehensive numerical investigation of five InGaN-based multiple-quantum-well red LED structures employing different active-region configurations, including conventional rectangular wells, stepped quantum wells, and composition-graded quantum wells incorporating ultrathin high-indium $In_{0.45}Ga_{0.55}N$ insertion layers. Device characteristics were analyzed using a self-consistent simulation framework based on the coupled solution of the Schrödinger, Poisson, and drift-diffusion equations. The influence of QW shape on carrier confinement, transport, recombination processes, current-voltage characteristics, internal quantum efficiency (IQE), wall-plug efficiency (WPE), and electroluminescence spectra was systematically evaluated.

The results demonstrate a strong dependence of LED performance on the quantum well potential profile. The conventional rectangular QW structure exhibits a peak IQE of 53.4% and an efficiency droop of 12.4% at a current density of 100 A/cm². In contrast, an optimized composition-graded quantum well containing a 1 nm $In_{0.45}Ga_{0.55}N$ insertion layer achieves the highest performance, with a peak IQE of 65.6%, wall-plug efficiency of 10.1%, and an efficiency droop of only 3.5%. The optimized structure maintains true red emission, exhibiting an electroluminescence peak shift from 636 nm to 622 nm as the current density increases from 10 to 100 A/cm². Analysis of the energy-band diagrams reveals that the improved performance originates from reduced polarization-induced electric fields, enhanced electron–hole overlap, improved carrier confinement, and suppression of electron leakage.

The obtained results demonstrate that careful quantum-well shape engineering provides an effective route toward simultaneously improving efficiency, reducing droop, and preserving long-wavelength emission in InGaN-based red LEDs. The proposed design strategy offers practical guidelines for the development of high-performance red emitters for future monolithic RGB micro-LED displays and advanced solid-state lighting applications.

ACKNOWLEDGEMENTS. The authors acknowledge the financial support from the Ministry of Education and Research of the Republic of Moldova (research program no. 011208).

[1] C. Altinkaya, R. S. Jalmood, M. A. Najmi, D. Iida, and K. Ohkawa, *Applied Physics Express* **18** (2025) 061001.
[2] V. P. Sirkeli, S. I. Caragacian, Iu. B. Boris, D. L. Nika, *Phys. Solid State* **67** (2025), 655–663.
[3] V. P. Sirkeli, *Semiconductors* **58** (2024), 928-935.

SINGLE - AND TWO - QUANTA PROCESSES IN COUPLED HYBRID SYSTEMS

M. A. Macovei[1,*], T. Mihaescu[2], and A. Isar[2]
[1]*Institute of Applied Physics, Moldova State University, Academiei str. 5, MD-2028 Chișinău, Republic of Moldova;*
[2]*National Institute of Physics and Nuclear Engineering, Reactorului 30, Măgurele-Bucharest, Romania*
*E-mail: mihai.macovei@ifa.usm.md

Recent technological advances with artificial atomic systems have proved their relevance which, actually, growth rapidly nowadays [1-3]. Therefore, here, we shall present our recent theoretical results regarding the non-linear quantum dynamics of a compound sample, consisting from a double quantum dot (DQD) system which is coupled with a leaking single-mode micro-resonator. We shall start with the situation when a continuous microwave field is applied which modulates the DQD's frequency. As a result, the resonances occur when the difference among the qubit's and resonator's frequencies equals to the multiple frequency of the applied field, respectively. We demonstrate that the output cavity electromagnetic field is formed of a single photons flux obeying the sub-Poissonian photon statistics. This was proved via comparison of the resonator's second- and third-order photon correlation functions, respectively [4].

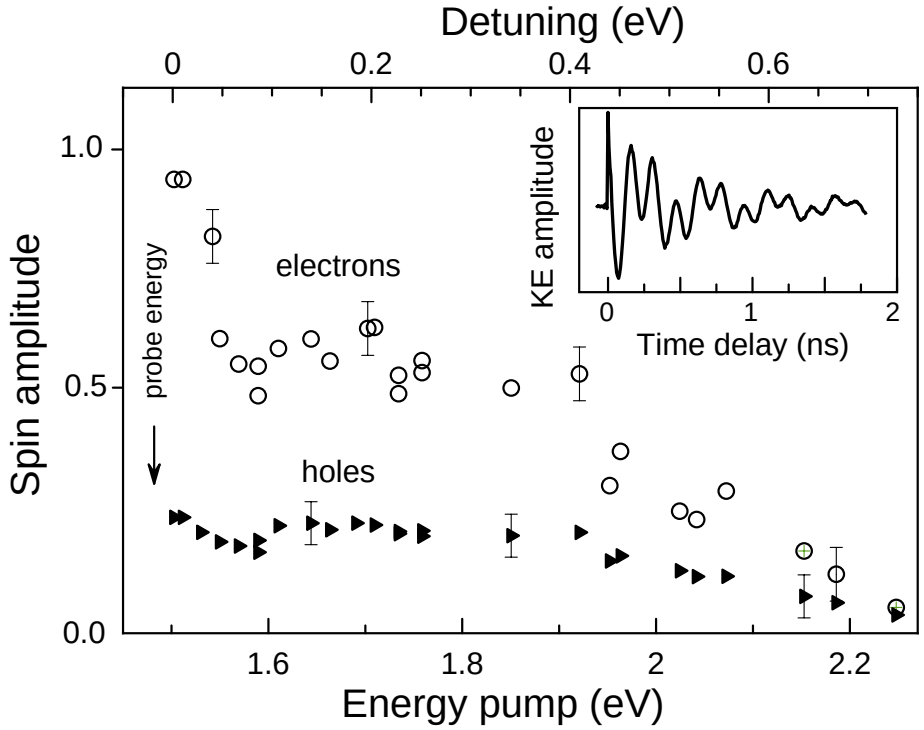
Then, we shall focus on the case when the transition frequency of the DQD equals to the doubled resonator's frequency, respectively, and elucidate the resulting interplay among the involved phonon or photon decay channels. The steady-state quantum dynamics of this complex non-linear system is shown to exhibits a variety of critical behaviors in the relationship among the electrical current through the double quantum dot and the microwave field inside the resonator [5,6].

[1] T. Brandes, Phys. Rep. **408** (2005) 315.
[2] X. Gu, A. Kockum, A. Miranowicz, Y. Liu, F. Nori, Phys. Rep. **718-719** (2017) 1.
[3] G. Burkard, M. J. Gullans, X. Mi, J. R. Petta, Nat. Rev. Phys. **2** (2020) 129.
[4] T. Mihaescu, A. Isar, M. A. Macovei, submitted (2026).
[5] T. Mihaescu, A. Isar, M. A. Macovei, Eur. Phys. J. Plus **140** (2025) 1194.
[6] T. Mihaescu, M. A. Macovei, and A. Isar, Physics **7** (2025) 47.

COHERENT SPIN DYNAMICS OF ELECTRONS AND HOLES PHOTOGENERATED WITH LARGE KINETIC ENERGY IN LEAD HALIDE PEROVSKITE CRYSTALS

E. A. Zhukov*, D. R. Yakovlev, N. E. Kopteva, M. Bayer
Experimentelle Physik 2, Technische Universität Dortmund, 44227 Dortmund, Germany
*E-mail: evgeny.zhukov@tu-dortmund.de

The coherent spin dynamics of electrons and holes are studied in a $FA_{0.9}Cs_{0.1}PbI_{2.8}Br_{0.2}$ perovskite bulk crystal using time-resolved Kerr ellipticity in a two-color pump−probe scheme. The probe photon energy is tuned to the exciton resonance, while the pump photon energy is detuned from it up to 0.75 eV to higher energies. The spin-oriented electrons and holes photogenerated with significant excess kinetic energy relax into states in the vicinity of the band gap, where they undergo Larmor precession in an external magnetic field. At cryogenic temperatures down to 1.6 K, the spin-dephasing time reaches the nanosecond range. During energy relaxation, the carrier spin relaxation is inefficient and only happens when the carriers become localized. In experiments with two pump pulses, all-optical control of the amplitudes and phases of the electron and hole spin signals is achieved in the additive regime by varying the intensities of the pump pulses and the time delay between them.



[1] Evgeny A. Zhukov, Dmitry R. Yakovlev, Erik Kirstein, Natalia E. Kopteva, Oleh Hordiichuk, Maksym V. Kovalenko and Manfred Bayer, *ACS Photonics* **12** (2025) 1698.

COMPLEX DYNAMICS OF INTERACTION BETWEEN CANCER AND IMMUNE SYSTEMS

N. Gubceac[1,2*], N. Ciobanu[1,2], V. Tronciu[1]
[1]*Technical University of Moldova, Chisinau, Republic of Moldova;*
[2]*"Nicolae Testemitanu" State University of Medicine and Pharmacy, Chisinau, Republic of Moldova*
E-mail: natalia.gubceac@fiz.utm.md

In recent decades, studying the dynamics of the interaction between the cancer and immune systems has been a very attractive topic in theoretical and computational biology. An important aspect in cancer biology is how the body's immune system responds to cancer progression. Despite medical advances, there are still some challenges in the prognosis and treatment of these diseases.

In this study, we present a theoretical model that describes the interaction between one (two) cancer center (s) and the immune system [1]. The delay time between the secretion of interleukin and the multiplication of cytotoxic cells was introduced [2]. It influences the dynamics of the investigated system. In case of two cancer centers (Fig. 1), the dynamics of the system is described by eight nonlinear differential equations with delay through the intermediary of precursor cells *R*, tumor cells *Y*, interleukin *I* and cytotoxic lymphocytes *X* as follows

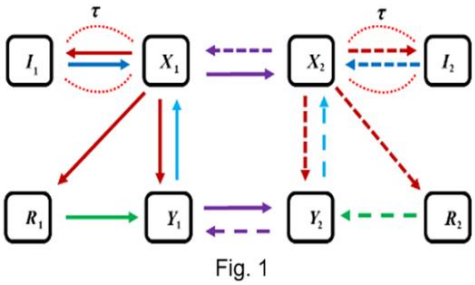


Fig. 1

$$\frac{dR_i}{dt} = R_0\left(1 - R_i - \delta \cdot R_i \cdot Y_i\right),\ \frac{dI_i}{dt} = X_i - \Gamma \cdot I_i,\ \frac{dY_i}{dt} = Y_i - X_i \cdot Y_i - \xi_i \cdot Y_i + \varepsilon_i \cdot \xi_j \cdot Y_j,$$

$$\frac{dX_i}{dt} = G_i \cdot R_i \cdot Y_i + \frac{\alpha \cdot I_i(t-\tau) \cdot X_i(t-\tau)}{1 + \Gamma \cdot \beta \cdot I_i(t) \cdot X_i(t)} - \gamma_i \cdot X_i - X_i \cdot Y_i + \lambda_i \cdot \gamma_j \cdot X_j,\ \text{for } i=1,\ j=2 \text{ and } i=2,\ j=1.$$

We investigate this system by numerical simulations, and found that for certain set of parameters the system exhibits various dynamic behaviors. In particular, changes in the diffusion coefficient of cancer cells between the two tumor centers lead to transitions between different dynamical regimes, such as steady states with stable equilibrium, periodic, quasi-periodic as well as quasi-chaotic oscillations. For low values of the diffusion coefficient (ξ_2) of cancer cells originating from the second tumor center, the concentrations of CTLs and tumor cells converge to a stable stationary state – stable focus (region A). As the diffusion coefficient increases, the system undergoes a transition to stable periodic oscillations via Hopf –bifurcation (region B). A further increase of diffusion coefficient leads to quasiperiodic route to chaotic dynamics (region C). Finally for large ξ_2 the system exhibits quasi-periodic oscillations (region D). As shown in Fig. 2, the bifurcation analysis shows that the instability regions appears through the Hopf bifurcation (green point H in Fig. 2) when the diffusion coefficient of cancer cells is the bifurcation parameter. We found that the instabilities persist over a wide range of the diffusion rate of the intermediate immune population Γ.

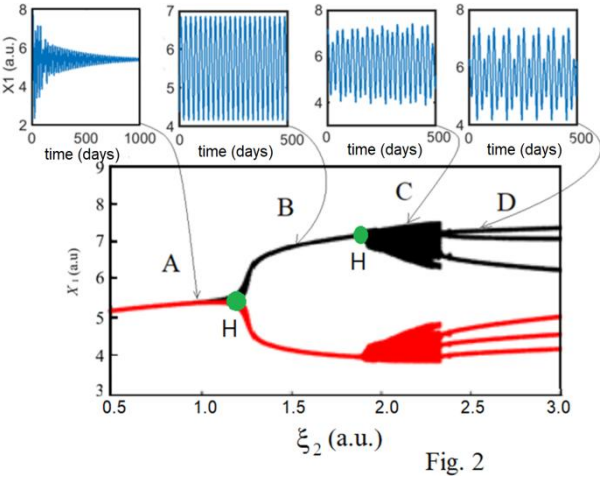


Fig. 2

ACKNOWLEDGEMENTS. This work was supported by the project 02.04.02 Development of technologies and investigation of the properties of layered semiconductor compounds, hybrid nanostructures and laser sources.

[1] V. A. Zaloj, A. Kh. Rotaru, A. E. Barbaroshie et all, *J. Biol. Phys.* **21** (1995) 155–176.
[2] N. Ciobanu, N. Gubceac, V. Tronciu, *Romanian Reports in Physics* (2026) (Accepted for publication).

COOPERATIVE EMISSION AND NONCLASSICAL PHOTON STATISTICS OF THREE ATOMS IN AN EQUILATERAL-TRIANGLE GEOMETRY

A. Rotari[1,*], M. A. Macovei[1]
[1]*Institute of Applied Physics, Moldova State University, Chișinău, Republic of Moldova*
*E-mail: arthurrotari@gmail.com

We investigate the steady-state behavior of three identical two-level emitters coupled via the dipole–dipole interaction, arranged at the corners of an equilateral triangle and immersed in a shared thermal environment. In ensembles containing only a few emitters, cooperativity reorganizes the level structure into collective eigenstates whose radiative and absorptive properties can differ substantially from those of independent atoms, which makes compact geometric configurations a natural testbed for collective spontaneous emission and for the engineering of photon statistics [1]. For the equilateral arrangement, the point-group symmetry of the configuration classifies these collective states and allows the active emission channels to be identified in closed analytical form. Starting from a master equation formulated in the collective basis of the three-atom system, we derive exact expressions for the stationary populations of the collective eigenstates, together with the second- and third-order spatial correlation functions of the spontaneously scattered light [2]. These correlators encode the joint probability of registering photons along distinct spatial directions and therefore serve as sensitive witnesses of the cooperative character of the radiation.

Our analysis reveals that incoherent excitation supplied solely by the thermal reservoir is sufficient for the system to emit streams of single photons exhibiting sub-Poissonian counting statistics, an unambiguous hallmark of nonclassical light. Notably, this behavior persists both in the small-sample (Dicke) limit, where the interatomic separations lie far below the transition wavelength, and in the extended regime, where the distances become comparable to it, demonstrating that the nonclassicality is robust against variations in the spatial scale of the array. Altogether, these findings clarify how geometry, collective coupling, and thermal pumping jointly determine the nonclassical properties of the light radiated by small atomic ensembles.

[1] R. H. Dicke. *Phys. Rev.* **93** (1954) 99.
[2] A. Rotari, M. A. Macovei. arXiv:2602.18269 (2026).

Ab initio RESONANT RAMAN SCATTERING STUDY OF MONOLAYER AND BULK MoS_2

Petru Milev[1,2*], Fulvio Paleari[3], Davide Sangalli[1]
[1]*Istituto di Struttura della Materia-CNR (ISM-CNR), Piazza Leonardo da Vinci 32, 20133, Milan, Italy;*
[2]*Department of Physics ''Aldo Pontremoli'', Università degli Studi di Milano, Via Giovanni Celoria 16, 20133, Milan, Italy;*
[3]*Centro S3, CNR–Istituto Nanoscienze, I-41125 Modena, Italy*
*E-mail: Petru.Milev@mlib.ism.cnr.it

Resonant Raman experiments on monolayer and bulk MoS_2, show a strong enhancement of the signal, at the A_{1g} and E_{2g} phonon modes, due to excitonic effects. However, the shape of the signal differs significantly: monolayer exhibits strong enhancement at the C peak, whereas bulk signal is more enhanced at the A and B excitonic resonances [1,2].

To investigate the physical origins of this difference, we present *ab initio* calculations of Raman spectra with and without excitonic effects. The Raman tensor takes the form of a double-resonant scattering matrix element with excitons as intermediate states coupled by the exciton-phonon interaction, derivable in two ways: within time-dependent adiabatic-GW, assuming coherent phonon motion [3], or from a many-body correlation function [4]. The latter approach has been coded in the Lumen package [5] at independent particle (IP) and Bethe-Salpeter equation (BSE) levels of theory. We discuss details of the implementation, identifying and addressing common computational pitfalls. Specifically, we analyze the impact of damping factors on spectral shapes, convergence behavior regarding number of bands at IP and BSE levels, the roles of intra- and inter-excitonic scattering, and k-grid dependency. We also discuss numerical performance and computational cost. Finally, by comparing with experimental results, we discuss why monolayer, and bulk behave differently [6].

[1]B. R. Carvalho, L. M. Malard, J. M. Alves, C. Fantini, and M. A. Pimenta, *Phys. Rev. Lett.* **114** (2015) 136403.
[2] B. R. Carvalho, L. M. Malard, J. M. Alves, C. Fantini, and M. A. Pimenta, *Phys. Rev. Lett.* **116** (2016) 089904.
[3] Y.-H. Chan, Z. Li, and S. G. Louie, Phys. Rev. B **112** (2025) 024308.
[4] S. Reichardt and L. Wirtz, *Sci. Adv.* **6** (2020) eabb5915.
[5] D. Sangalli et al., Lumen. (May 11, 2026). Zenodo. Doi: https://doi.org/10.5281/zenodo.20121198.
[6] P. Milev, F. Paleari, and D.Sangalli, (*In preparation*).

SUPPRESSION OF THERMAL TRANSPORT IN CUBIC In_2O_3 WITH Pb-Tl DEFECTS

A. Cocemasov[1,*], V. Brinzari[1], D.L. Nika[1]
[1]*Moldova State University, Chisinau, Moldova;*
*E-mail: a.cocemasov@gmail.com

We report on a first-principles density functional theory (DFT) study of the phonon thermal transport properties of cubic In_2O_3 hosting a Pb-Tl diatomic defect (abbr. IPTlO): a Pb atom substituting In at the b-site plus a Tl atom embedded at a nearby vacancy (c-site) [1]. After relaxation, the Pb and Tl atoms form a cage-like configuration enclosed by 12 O and 12 In atoms, expanding the cell volume by 6% and the lattice constant from 10.16 to 10.36 Å relative to pure In_2O_3. Compared with the previously studied Sn_b-Ga_i defect (abbr. ITGO) [2], the Pb-O and Tl-O bonds are up to 51% and 61% softer than the corresponding Sn-O and Ga-O bonds, while the Pb-Tl bond is 48% weaker than the Sn-Ga bond, reflecting markedly stronger rattling of the heavier guest atoms.
Mean square displacement (MSD) calculations confirm this trend: at 300 K the MSD of Pb reaches 0.084 $Å^2$, about 4.7 times larger than that of Sn in ITGO, while Tl also shows enhanced but asymmetric displacements associated with two inequivalent Tl-O bond lengths (2.25 and 2.86 Å). The mode-averaged Grüneisen parameter grows from 1.32 in pristine In_2O_3 to 2.11 in ITGO and 3.06 in IPTlO. The phonon spectrum of IPTlO shows pronounced softening of the acoustic branches and dispersionless low-energy modes (1–10 meV) associated with Pb and Tl, acting as Einstein-like rattlers that interact with acoustic phonons through avoided crossings. These modes broaden the three-phonon scattering phase space (Figure 1a) and sharply shorten the phonon mean free paths, especially for the long-wavelength phonons that dominate heat conduction in the pristine crystal.

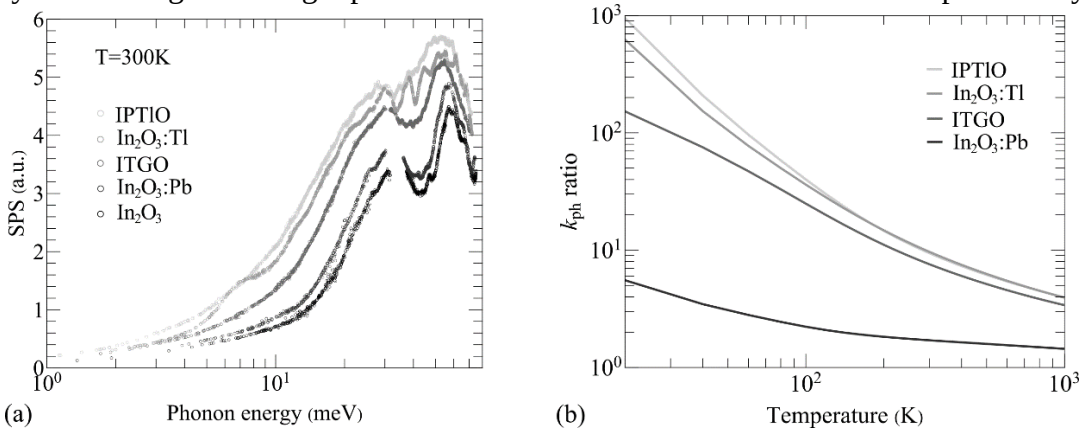


Figure 1. (a) Three-phonon scattering phase space (SPS) at 300K and (b) Ratio of the phonon thermal conductivity of pure In_2O_3 to that of In_2O_3:Pb, In_2O_3:Tl, ITGO and IPTlO as a function of temperature.

As a result, the phonon thermal conductivity, drops to 1.3 $Wm^{-1}K^{-1}$ for IPTlO at room temperature – a factor of ~9.5 lower than in pure In_2O_3 (12.3 $Wm^{-1}K^{-1}$) and stronger than the ~7.7-fold reduction found for ITGO (Figure 1b). The singly-doped In_2O_3:Pb shows only a 1.7-fold reduction, while In_2O_3:Tl is nearly as effective as IPTlO, indicating that Tl doping is mainly responsible for the enhanced phonon scattering; Pb-Tl co-doping nonetheless offers a lower defect formation energy per atom than Tl doping alone. These results demonstrate that heavy, weakly-bonded Pb-Tl rattlers disrupt phonon propagation in cubic In_2O_3 more effectively than the previously studied Sn-Ga pair, offering a promising defect-engineering route toward oxide-based thermoelectric materials with strongly suppressed lattice thermal conductivity.

ACKNOWLEDGEMENTS. The authors acknowledge financial support under the Moldova Government research program no. 011208.

[1] A. Cocemasov, V. Brinzari, D.L. Nika, *Physica B: Condens. Matter* **716** (2025) 417689.
[2] A. Cocemasov, V. Brinzari, D.L. Nika, *J. Phys.: Condens. Matter* **35** (2023) 195701.

GENERATION OF QUANTUM CORRELATIONS IN CONTINUOUS-VARIABLE OPEN QUANTUM SYSTEMS

Alina Stoica[1,2], Aurelian Isar[1,2*]
[1]*Department of Theoretical Physics, National Institute of Physics and Nuclear Engineering, Bucharest-Magurele, Romania*
[2]*Faculty of Physics, University of Bucharest, Romania*
*E-mail: isar@theory.nipne.ro

Hellinger geometric quantum discord and interferometric power are investigated for an open system consisting of two bosonic modes interacting with four different environments: vacuum, squeezed vacuum, thermal and squeezed thermal environment, taking the initial state of the system either a unimodal squeezed state, which presents no correlations, or a squeezed vacuum state. The time evolution of the correlations is investigated in the framework of the theory of open systems, based on completely positive quantum dynamical semigroups, using the Gorini-Kossakowski-Lindblad-Sudarshan master equation. We show that both quantum correlations can be generated from an initial factorized state. For the squeezed vacuum environment, the competition between the influences produced by the squeezing of the initial state and the squeezing of the environment leads to the decreasing, and even destruction of the correlations, or to their enhancement. In the case of an initial squeezed vacuum state in interaction with the squeezed vacuum environment, for specific conditions one can achieve decoherence-free states, while for the interaction with a thermal environment there exist regimes of enhancing or decreasing the considered correlations, depending on the parameters of the open system and environment [1].

[1] Alina Stoica, Aurelian Isar, *European Physical Journal Plus* **141** (2026), 559.

NEGATIVE PARTIAL TRANSPOSE ENTANGLEMENT WITNESSES BASED ON SECOND MOMENTS

Tatiana Mihaescu*
National Institute of Physics and Nuclear Engineering, Reactorului 30, Măgurele-Bucharest, Romania
*E-mail: mihaescu.tatiana@theory.nipne.ro

Continuous-variable quantum systems are naturally described through phase-space methods, where covariance matrices encode the second-order correlations of bosonic modes. While full state tomography is generally costly, many relevant forms of entanglement can already be certified at the level of second moments [1]. In this work, we develop a witness-based framework for detecting negative-partial-transpose (NPT) entanglement in bipartite continuous-variable systems using covariance-matrix data.

From the perspective of convex geometry, the convex and closed sets of physical and separable covariance matrices allow for the formulation of entanglement witnesses. These are represented as positive semidefinite matrices that define separating hyperplanes between separable and entangled states. We then specialize this construction to the partial-transposition criterion [2] and characterize the class of second-moment witnesses capable of detecting NPT entanglement. The resulting conditions can be expressed in terms of symplectic eigenvalues and a Williamson-type canonical form, yielding an algebraic description of all NPT entanglement witnesses directly in covariance-matrix space. This structural result provides a rigorous theoretical tool for classifying non-classical correlations, further streamlining the detection of useful NPT entanglement for advanced quantum tasks such as entanglement distillation. We further discuss how such witnesses may be constructed from incomplete homodyne measurements, leading to a semidefinite-programming detection strategy that avoids full covariance-matrix reconstruction [3].

This approach provides a geometric and computationally accessible method for certifying continuous-variable entanglement from experimentally available second moments, and clarifies the relation between general covariance-matrix witnesses, steering witnesses [4], and NPT entanglement detection [5].

[1] L. Lami, A. Serafini, G. Adesso, New J. Phys. 20 (2018) 023030.
[2] R. Simon, Phys. Rev. Lett. 84 (2000) 2726.
[3] T. Mihaescu, H. Kampermann, G. Gianfelici, A. Isar, D. Bruß, New J. Phys. 22 (2020) 123041.
[4] T. Mihaescu, H. Kampermann, A. Isar, D. Bruß, New J. Phys. 25 (2023) 113023.
[5] T. Mihaescu, in preparation (2026).

PASSIVE QUANTUM COOLING IN OPTOMECHANICAL DEVICES

V. Ceban*, A. Cudreașov, A. Rotari, I. Cebotari
Institute of Applied Physics, Moldova State University, Chișinău, Moldova
*E-mail: victor.ceban@ifa.usm.md

We have investigated the quantum dynamics of an optomechanical device made of a double quantum dot (dQD) placed on a nanomechanical resonator by considering the interaction of the device with the thermal environment. The mechanical resonator interacts with the substrate on which it is deposed, which is represented via a thermal phonon reservoir. The dQD interacts with the thermal electromagnetic environment, represented via a thermal photon reservoir. The quantum dynamics of the open quantum system is expressed by the master equation of the density matrix operator, where the system interaction with its environment is expressed as damping terms defined within the framework of reservoir theory [1]. We were able to numerically solve the system dynamics within the steady-state regime after adapting the reservoir theory to the considered model.

We have identified a quantum cooling effect of the mechanical resonator that occurs passively when the photon environment is slightly cooler than the phonon environment. We show that this effect is specific to dQD and is enabled by the ability of an electron to tunnel between the two sides of the dQD. This effect is different from cooling mechanics with single QDs or other types of two-level systems based on Raman-type transitions, as it does not require an external coherent driving of the system [2].

ACKNOWLEDGEMENTS. We are grateful for the financial support by the Moldavian National Agency for Research and Development (ANCD), Grant for Young Scientists No. 25.80012.5007.35TC.

[1] V. Ceban et al., *J. Phys.: Conf. Ser.* **3239** (2026) 012015.
[2] V. Ceban, M. A. Macovei, *Rom. Rep. Phys.* **70** (2018) 407.

THEORETICAL STUDY OF SHORT PULSE IN DFB LASERS BY RATE EQUATION MODEL

Vasile Tronciu[1,*], Spiridon Rusu[1], Veronica Dobrovolschi[1]
[1]*Department of Physics, Technical University of Moldova, Chisinau, Republic of Moldova*
*E-mail: vasile.tronciu@fiz.utm.md

In this paper, we present the theoretical results of process of generating picosecond optical pulses by a distributed feedback (DFB) laser, emitting at a wavelength of 1070 nm, and operating in the gain - switching regime using the rate equations model. The influence of main parameters as injected current, confinement factor and front facet reflectivity was studied. We conclude that these parameters can result in significant changes of the pulse shape, peak power, and pulse duration. We found the regions of parameters where the pulses are almost symmetric, without a second maximum in the tail. The laser setup is shown in Fig. 1. The parameter J represents the external dimensionless pumping which has a trapezoidal shape. The optical feedback is provided by a Bragg grating that extends over the entire amplification section. The theoretical model is based on rate equations for the Bragg (S_1) and Fabry–Pérot (S_2) modes in a DFB laser. As in the model presented in [1], the Bragg and Fabry–Pérot modes represent two distinct populations of photons that interact with a single population of charge carriers of dimensionless concentration n. Thus, the dynamics of the system shown in Fig. 1 are described by the following equations

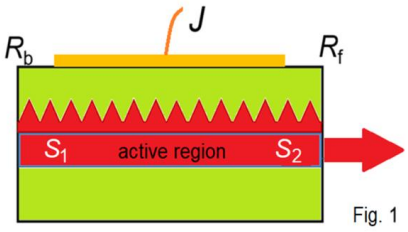


Fig. 1

$$\frac{dS_1}{dt}=\frac{\Gamma_1 g_1 S_1}{1+\varepsilon S_1}-\frac{\tau_0}{\tau_{S,1}}S_1+K_1 n^2,\quad \frac{dS_2}{dt}=\frac{\Gamma_1 g_2 S_2}{1+\varepsilon S_2}-\frac{\tau_0}{\tau_{S,2}}S_2+K_2 n^2,\quad \frac{dn}{dt}=J-R-\frac{\tau_0 c\, g_1 S_1}{1+\varepsilon S_1}+\frac{\tau_0 c g_2 S_2}{1+\varepsilon S_2}.$$

We vary the intensity of the electric current from 0.5 A to 2 A to determine the emergent power as in [2] (black line in Fig. 2, b)). Increasing the current from 0.5 A to 1.56 A results in a monotonous increase in the peak of the emergent power (region A). Subsequently, the increase becomes more rapid, and a current of 2 A yields 4 W (region C). We observe a sudden decrease in pulse duration from 300 ps to 52 ps at a current of 1.62 A (red line in Fig. 2, b)). Panels A, B and C of Fig. 2 show the shape of the pulse at the output of the laser for currents shown in Fig. 2, b). Numerical results obtained in this paper show that, with the basic parameters set to the following values – an injected current of 2 A, a confinement factor of 0.003, and a reflection coefficient of 0.0001 – practically symmetric pulses with a peak power exceeding 15 W and a duration of approximately 20 ps were obtained. It was found that, for currents near 1.6 A, the pulse duration decreases below 15 ps and the peak power decreases below 10 W. The appearance of a second maximum in the pulse tail was found to be correlated with an increase in both the confinement factor, and the reflectivity of the front facet, R_f. We believe that our work provides a good basis for experimental investigations of picoseconds pulses generated by gain-switched DFB lasers. This work was supported by project 02.04.02 Development of technologies and investigation of the properties of layered semiconductor compounds, hybrid nanostructures and laser sources.

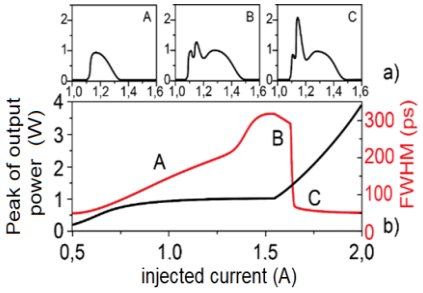


Fig. 2

[1] S. Riecke, H. Wenzel, S. Schwertfeger, K. Lauritsen, K. Paschke, R. Erdmann, R. Erbert, G. Picosecond spectral dynamics of gain-switched DFB lasers. *IEEE Journal of Quantum Electronics*, **47(5)** (2011) 715–722, Doi: https://doi.org/10.1109/JQE.2010.2096501

[2] V.Z.Tronciu, M. Yamada, T. Ohno, S. Ito, T. Kawakami, M. Taneya Self-pulsation in an InGaN laser-theory and experiment. *IEEE Journal of Quantum Electronics*, **39(12)** (2003) 1509-1514, Doi: https://doi.org/10.1109/JQE.2003.819541.

MACHINE LEARNING-BASED OPTIMIZATION OF DFB LASER PARAMETERS FOR SHORT PULSE GENERATION

Vasile Tronciu[1], Sergiu Zaporojan[1], Natalia Gubceac[1], Radu Razvan Slavescu[2]
[1]*Department of Physics, Technical University of Moldova, Chisinau, Republic of Moldova;*
[2]*Department of Computer Science, Technical University of Cluj-Napoca, Cluj-Napoca, Romania.*
E-mail: vasile.tronciu@fiz.utm.md

We present the results of our investigation into the generation of sub-10 ps pulses by DFB lasers. Our contributions are twofold. First, we created a dataset of 36,126 examples by running simulations for a range of parameters, including injected current, optical confinement factor per quantum well, number of quantum wells, and coupling coefficient. Second, we explore Machine Learning (ML) techniques for predicting conditions that are most suitable for laser applications, resulting in high peak power, low full width at half maximum (FWHM), and a higher ratio of pulse energy to total energy. The best results were produced by a Stochastic Gradient Boosting method.

Figure 1 shows the structure of the considered DFB laser. It consists of an active layer of varying multiquantum wells. The injected current applied varies from 150 to 400 mA. The model for direct simulation of the dynamics of gain-switched DFB lasers shown in Fig. 1. It is based on the 1 (time) +1 (space) dimensional traveling wave equations for the slowly varying complex amplitudes E^{+}(z,t) and E^{-}(z,t) of the counter–propagating optical fields within the device and the rate equation for the carrier density N(z,t) [2], [3]

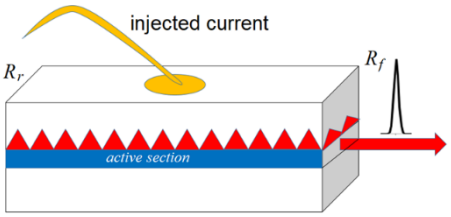


Fig. 1.

$$\frac{n_g}{c_0}\frac{\partial}{\partial t}E^{\pm}(z,t)=\left[\mp\frac{\partial}{\partial t}-i\Delta\beta(N,I)\right]E^{\pm}(z,t)-ikE^{\mp}(z,t),$$

$$\frac{\partial}{\partial t}N=\frac{I}{edWl_A}+\frac{U_F^{'}}{edr_s}\left(\bar{N}-N\right)-\left(AN+BN^2+CN^3\right)-\frac{c_0}{n_g}\Re\sum_{v=\pm}E^{v*}\left[g(N)-D\right]E^{v}.$$

Using the above model, we investigate the generation of short pulses by a DFB laser. It is well known that simulating process behavior is computationally consuming. To address this issue, we fit a ML model (namely, the Stochastic Gradient Booster) able to determine the sweet points in the space of laser parameters. The model predictions show that staying near confinement factor per quantum well 0.003, number of quantum wells between 6 and 8, coupling coefficient 5 - 8 (1/cm), injected current between 390 and 400 (mA) is the optimal region for low FWHM, higher peak of pulse and close to unity ratio between pulse and total energy. A 5-fold cross validation was applied, with R2-score used as a performance metric. Figure 2 shows the results of the numerical simulations of the predicted data for ML. The pulse shapes are almost symmetric, with power peaks between 2.5 and 3.0 W and pulse widths between 10 and 13 ps. The ratio between pulse energy and total energy is around 0.8, indicating that there is no tail in the pulse shape. Thus, the ML method has predicted conditions for parameters where the pulses are suitable for applications. We believe that our work provides a good basis for future experimental realization of a DFB lasers as a sub-ps pulse generator. This work was supported by project 02.04.02 Development of technologies and investigation of the properties of layered semiconductor compounds, hybrid nanostructures and laser sources.

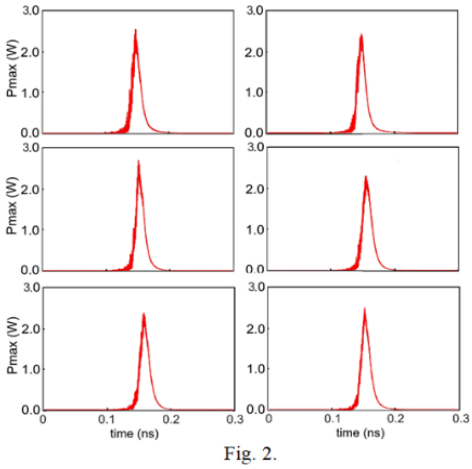


Fig. 2.

[3] G. Genty, L. Salmela, J. M. Dudley, D. Brunner, A. Kokhanovskiy, S. Kobtsev, and S. K. Turitsyn, *Nat. Photonics*, **15(2)** (2021) 91–101, Doi: https://doi.org/10.1038/s41566-020-00716-4.

[4] M. Radziunas and H. J. Wünsche, "Multisection lasers: Longitudinal modes and their dynamics," in Optoelectronic Devices, J. Piprek, Ed. New York, NY, USA: Springer (2005) 121–156,

[5] V. Tronciu, H. Wenzel, M. Radziunas, M. Reggentin, J. Wiedmann, and A. Knigge, *IET Optoelectron.*, **12(5)** (2018) 228–235, Doi: https://doi.org/10.1049/iet-opt.2018.0025.

MODELING OF DYNAMIC EQUILIBRIUM IN THE OXIDANT-ANTIOXIDANT SYSTEM ACCOUNTING FOR THE SYNERGETIC EFFECT OF VITAMINS E, C, AND BIOFLAVONOIDS

O. V. Yaltychenko*, E. Yu. Kanarovskii,
Moldova State University, Institute of Applied Physics, MD-2028, Chișinău, Republic of Moldova
*E-mail: oialt@mail.ru, olga.ialticenco@ifa.usm.md

The paper proposes a graph of dynamic equilibrium in the oxidant-antioxidant system, representing a directed cyclic graph (or network of biochemical reactions), where the nodes are chemical compounds, and the edges are redox reactions. The synergetic effect of vitamins E, C, and bioflavonoids is modeled as a cyclical chain of regeneration of their radicals, ensuring a reduction in oxidative stress. It should be noted that the main targets of the oxidative process in membranes are lipid molecules.

The main components of the system can be divided into the following three key levels (clusters of graph nodes):

1). Level of damage (oxidants – ROS): superoxide anion ($O_2^{\bullet-}$), hydroxyl radical ($OH^{\bullet}$), hydrogen peroxide (H_2O_2) and $HOO^{\bullet}$, as well as lipid radicals $L^{\bullet}$ and $LOO^{\bullet}$.

2). Level of first-line defense (vitamin E): tocopherol (TOH) and tocopheryl ($TO^{\bullet}$).

3). Level of the antioxidant cascade (regeneration cycle): the initial stage with ascorbic acid in the forms of $AscH^{-}$, $Asc^{\bullet-}$, and DHA (dehydroascorbate); the stage with bioflavonoids (FlavOH) and their radical forms ($FlavO^{\bullet}$); and the terminal stage of the regeneration cycle **involving** glutathione (GSH) and NADPH.

Synergetic processes are represented accordingly by a cycle in the graph. The synergy of the three components (vitamins E, C, and flavonoids) consists of the sequential reduction of each other, providing a longer and far more effective neutralization of dangerous free radicals. The graph contains several directed pathways. Interception of the peroxyl lipid radical $LOO^{\bullet}$:

$$LOO^{\bullet} + TOH \rightarrow LOOH + TO^{\bullet}.$$

Tocopherol quenches the lipid radical and is itself converted into a relatively stable and low-reactive tocopheryl radical. This is followed by the first stage of regeneration cycle (C → E), in which vitamin C (water-soluble) restores vitamin E (fat-soluble) at the phase boundary – lipid layer membranes and aqueous phase (cytoplasm or intercellular fluid):

$$TO^{\bullet} + AscH^{-} \rightarrow TOH + Asc^{\bullet-}.$$

In the second stage of the regeneration cycle (bioflavonoids → C) bioflavonoids regenerate the ascorbic acid radical:

$$Asc^{\bullet-} + FlavOH \rightarrow AscH^{-} + FlavO^{\bullet}.$$

The final stage of the reduction reaction cascade terminates at thiol antioxidants, primarily glutathione, the oxidized form of which (GSSG) is regenerated back **to** GSH by glutathione reductase in a process that directly utilizes NADPH from cellular metabolism as an electron donor:

$$FlavO^{\bullet} + GSH \rightarrow FlavOH + GS^{\bullet}.$$

The graph-based modeling clearly demonstrates how the **synergetic effect** based on electron transfer cascade – where bioflavonoids protect vitamin C, and vitamin C protects vitamin E – maintains the overall concentration of free radicals in the system at a minimum (safe) level. The condition for synergy is that the rate of radical quenching by the antioxidant mixture is higher than the sum of the quenching rates of the individual components. Dynamic equilibrium (steady state) is achieved when the influx of oxidants is fully compensated for by the capacity of the antioxidant cascade.

ACKNOWLEDGEMENTS. The research was funded by the Ministry of Education and Research of the Republic of Moldova (subprogram 011201).

PHONON-ASSISTED GENERATION OF ENTANGLED TWO-QUBIT STATES

Elena Cecoi[1*], Viorel Ciornea[1], Aurelian Isar,[2] and Mihai A. Macovei[1]
[1]*Institute of Applied Physics, Moldova State University, Academiei str. 5, Chisinau, Republic of Moldova*
[2] *Horia Hulubei National Institute of Physics and Nuclear Engineering, Reactorului str. 30, P.O.BOX MG-6 Bucharest - Magurele, Romania*
*E-mail: cecoielena@gmail.com

Quantum entanglement and boson-mode cooling are fundamental quantum phenomena for the realization of hybrid quantum technologies. This work investigates the steady-state dynamics of two identical dipole-dipole interacting quantum dots resonantly driven by an external coherent laser field and longitudinally coupled to a single bosonic mode. System evolution is described within the Born–Markov approximation formalism, resulting in a master equation that includes spontaneous emission, coherent pumping, dipole-dipole interaction, boson damping, and thermal phonon effects.
In the dressed-state basis, the diagonalized Hamiltonian enables the derivation of the coupled qubit-boson equations of motion and the numerical analysis of stationary quantum properties. Entanglement is quantified through the concurrence measure, whereas cooling efficiency is attested by evaluating the steady-state mean phonon number. Numerical simulations show that optimal cooling is achieved when the energy separation in the DQD system approaches the boson-mode frequency. Under these resonance conditions, phonon absorption promotes excitation of the collective symmetric state, simultaneously reducing the phonon population and generating entangled two-qubit states [1].

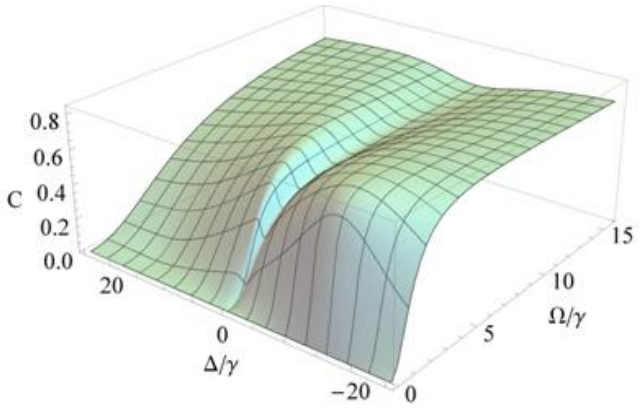


Figure 1. The concurrence C as a function of control parameters [1].

The dependence of the concurrence [2,3] on the normalized pumping parameter is presented in Fig. 1, demonstrating that maximum entanglement is achieved for moderate coherent driving fields. Comparison between the coupled and uncoupled cases shows that interaction with the bosonic mode slightly reduces the maximum concurrence while enabling efficient boson-mode cooling, revealing the close interplay between these two quantum processes. These results provide further insight into the relationship between quantum entanglement and cooling and offer useful guidelines for optimizing hybrid quantum platforms, including semiconductor quantum dots, superconducting qubits, trapped ions, and nanomechanical resonators, for quantum information applications.

[1] E. Cecoi, V. Ciornea, A. Isar, M. A. Macovei, Entanglement of a laser-driven pair of two-level qubits via its phonon environment, *JOSA B* **35**, 1127 (2018).
[2] S. Hill and W. K. Wootters, Entanglement of a pair of quantum bits, *Phys. Rev. Lett.* **78**, 5022 (1997).
[3] W. K. Wootters, Entanglement of formation of an arbitrary state of two qubits, *Phys. Rev. Lett.* **80**, 2245 (1998).

MODELING OF MULTICENTER CORE-SHELL NANOCLUSTERS

E. Yu. Kanarovskii*, O. V. Yaltychenko
Moldova State University, Institute of Applied Physics, MD-2028, Chișinău, Republic of Moldova
*E-mail: kanarovskii@gmail.com, evghenii.canarovschii@ifa.usm.md

Currently, within the physics of composite nanomaterials and nanostructures, theoretical and experimental research into single- and multi-center cluster nanosystems is significantly expanding. Multi-center nanoclusters (MNCs) possess a richer variety of physical and structural properties than single-center ones. This ensures their high application potential, successfully exploited in opto- and nanoelectronics, materials science, chemistry, and medicine. MNCs are inherently superclusters whose centers (nodes) consist of single-center molecular nanoclusters or core-shell nanoparticles, interconnected by their ligand shells either directly or via linker molecules. For MNCs, a prominent feature is the geometric configuration of their centers. The proposed model describes the dynamics of electron localization (EL) in MNCs under an external low-frequency electric field, accounting for various configurations of centers (linear, planar, and spatial). This model treats the MNC as composed of N centers, each having a core and a ligand shell, while a shared electron tunnels through barriers formed by the ligand shells of the centers. Accordingly, the model, along with a weak tunnel coupling between the nearest neighboring MNC centers, includes a strong electron-vibrational interaction with the local vibrational modes of the ligand shells of the centers. The model construction is based on a Holstein-type Hamiltonian in the node representation. The model Hamiltonian includes an alternating electric field with a frequency Ω and a field strength amplitude $\mathbf{E}$ as an external factor. It also accounts for a number of internal factors: electronic states localized at the MNC nodes with energies ε_m (the index m labels the nodes) and wave functions ψ_m (Wannier-type), tunneling between nodes (parameter V_{mn}), vibrational modes of the ligand environment at each of the MNC nodes (parameters q_m and ω_m), electron-vibrational interaction (parameter g_m). The wave function $\Psi(t)$ of the shared electron in the MNC was taken as a superposition of localized wave functions ψ_m with coefficients $c_m(t)$. As a result of the modeling, a system of differential equations (DEs) was obtained for the probability amplitudes $c_m(t)$ of finding the electron at different MNC nodes. Also, the method of slowly varying amplitudes was used to eliminate the vibrational degrees of freedom from the model DE system. Ultimately, the solutions of this system determine the nonlinear dynamics of electron localization in MNCs. For MNCs with equivalent centers, the model system of DEs has a minimal set of model parameters. The numerical simulation results for different MNCs (trimers, tetramers, pentamers) with various configurations of the centers show the existence of three characteristic EL regimes. Two of them are periodic regimes – the intermediate center transparency regime and the intermediate center partial filling regime – whereas the third is the locking regime at one of the MNC centers. Overall, the model allows for identifying these EL regimes, the conditions for switching between them, and comparing their features for MNCs with different configurations and numbers of centers. An analysis of several series of computational experiments with various model parameters shown that the external electric field is an effective control factor in implementing, switching, and tuning different EL regimes in MNCs, which are characterized by the shape of the time dependence, the duration of EL at the MNC centers, and the duration of inter-center switching of EL. It should also be noted that the dynamics of the electron density distribution within the MNC determines changes in its dipole moment in both direction and magnitude, thereby influencing the physical properties of the matrix into which MNCs of this type are embedded. Thus, the model is applicable for simulating the control of the optical and electronic properties of nanostructured materials containing MNCs. In general, the obtained model system of DEs is a flexible simulation tool since it can be easily modified to simulate the core-shell MNCs with non-equivalent centers by using an extended set of the specified model parameters. Moreover, the model is naturally expanded to include the additional external fields or the matrix effects.

ACKNOWLEDGEMENTS. The research was funded by the Ministry of Education and Research of the Republic of Moldova (subprogram 011201).

A DFT-TB2J INSIGHT INTO THE MAGNETIC BEHAVIOR AND INTRACHAIN INTERACTIONS OF THE 1D Co(II) PIVALATE COORDINATION POLYMER WITH HEXAMETHYLENETETRAMINE

Yu. Chumakov*, E. Beleaev, S. G. Baca
Institute of Applied Physics, Moldova State University, Chisinau, Republic of Moldova
*E-mail: yurii.chumakov52@gmail.com

One-dimensional Co(II)-based coordination polymers with multidentate ligands are promising materials for molecular electronics and single-chain magnets due to their tunable magnetic anisotropy and unique architectures. Developing these materials with targeted properties relies on controlling the correlation between crystal structure and magnetic exchange interactions. In this context, quantum chemical modeling based on density functional theory (DFT) serves as a powerful tool for predicting and understanding the magnetic properties of complex coordination compounds. Specifically, combining DFT [1] with the TB2J [2] approach allows for an accurate, first-principles evaluation of microscopic magnetic exchange parameters in low-dimensional spin systems.

In this work, the magnetic interaction parameters within the Heisenberg model for the one-dimensional coordination polymer $\{[Co_2(piv)_4(hmta)_2][Co_2(piv)_4(dmso)]\}_n$ (**1**, where Hpiv = pivalic acid, hmta = hexamethylenetetramine) (Fig. 1) were systematically investigated. Spin-dependent band structure calculations showed that one spin channel has a large band gap, while the other has a narrower one. The DFT-TB2J approach revealed that the magnetic behavior of **1** is highly sensitive to the coordination environments of the cobalt centers and bridging ligands, which directly regulate the electronic density of states and the resulting exchange pathways. Consequently, the compound exhibits coexisting ferromagnetic and antiferromagnetic intrachain interactions. These are modulated by structural features that effectively shift the relative energies of the cobalt d-orbitals, leading to the distinct magnetic behavior of **1**. Finally, the force theorem approach was employed to evaluate the magnetic anisotropy energy of the investigated system.

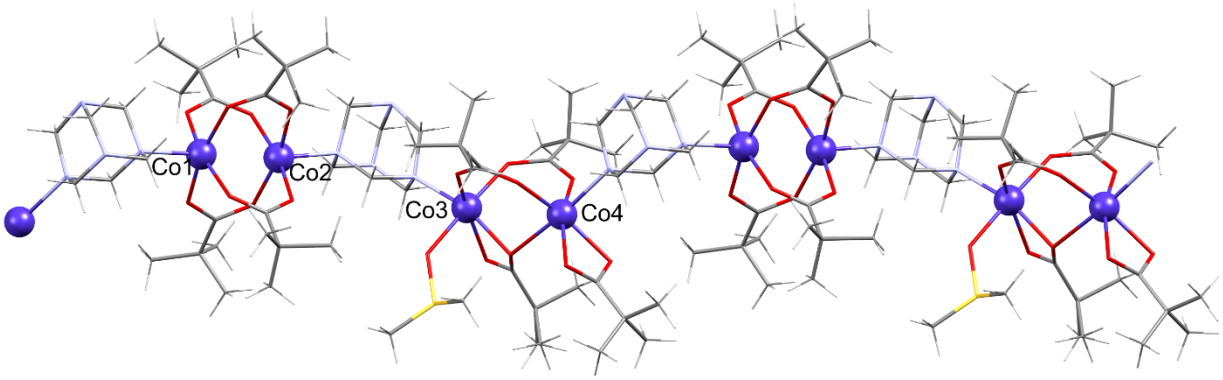


Figure 1. Structure of $\{[Co_2(piv)_4(hmta)_2][Co_2(piv)_4(dmso)]\}_n$ (**1**).

ACKNOWLEDGEMENTS. The authors are grateful subprogram 011202 financed by the Ministry of Education and Research of the R. Moldova and the Moldovan National Agency for Research and Development (NARD) (project 25.80012.5007.87SE).

[1] J. M. Soler, E. Artacho, J. D. Gale, A. Garcia, J. Junquera, P. Ordejon, D. Sanchez-Portal, *J. Phys.: Condens. Matter.* **14** (2002) 2745.
[2] X. He, N. Helbig, M. J. Verstraete, E. Bousquet, *Comput. Phys. Commun*. **264** (2021) 107938.

MONO- AND TETRASULFO-DERIVATIVES OF ZINC PHTHALOCYANINE AND THEIR CHITOSAN-BASED COMPOSITIONS

Ş. Robu*, V. Stegariov, I. Lungu, M. Diru, T. Potlog
Laboratory of Organic/Inorganic Materials for Optoelectronics,
Institute of Applied Physics, Moldova State University;
*E-mail: s.v.robu@mail.ru

Sulfonated phthalocyanines represent an important class of water-soluble macrocyclic compounds with potential applications in photodynamic therapy, optoelectronics, and functional hybrid materials. In this work, mono- and tetrasulfonated derivatives of tetraaminomethylene zinc phthalocyanine were synthesized and characterized, and their incorporation into chitosan-based matrices was investigated.

The sulfonation of zinc phthalocyanine derivatives was performed according to the procedure reported in the literature by treatment with 10% oleum for monosulfonation and 20% oleum for tetrasulfonation. Amino-functionalized derivatives were obtained using hydroxymethylphthalimide as an intermediate precursor. Subsequent hydrolysis of mono- and tetra-(o-carboxybenzamidomethylene) zinc phthalocyanine sulfonates was carried out in 10% hydrochloric acid solution for 4 h, yielding the target products with an isolated yield of 82%.

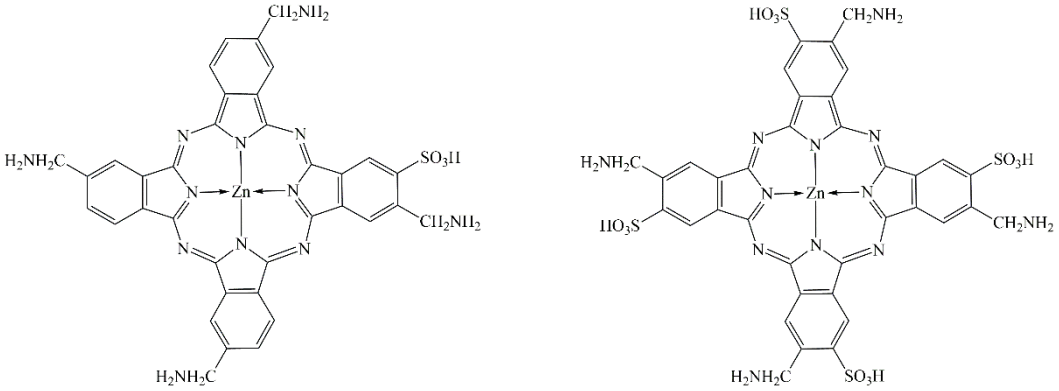


Figure 1. Chemical structures of (left) monosulfonated tetraaminomethylene zinc phthalocyanine and (right) tetrasulfonated tetraaminomethylene zinc phthalocyanine.

The synthesized compounds were characterized by FTIR and UV–Vis spectroscopy. FTIR spectra exhibited characteristic absorption bands at 1300–1360 cm^{-1} corresponding to sulfonic groups (–SO_3H), while the absorption bands observed in the 3100–3300 cm^{-1} region were assigned to primary amino groups, confirming the successful functionalization of the phthalocyanine macrocycle. Electronic absorption spectra revealed the characteristic Q-band of zinc phthalocyanines in the 670–680 nm region, indicating preservation of the conjugated π-electron system after sulfonation. The formation of composite systems with chitosan and nanostructured metal or metal-oxide additives resulted in modifications of the absorption profile, including a bathochromic shift of the Q-band toward longer wavelengths.

The observed spectral behavior suggests enhanced light-harvesting capability in the red and near-infrared spectral regions, which is advantageous for the development of photosensitive materials intended for biomedical and photonic applications. The results obtained demonstrate that sulfonated zinc phthalocyanines and their chitosan-based composites are promising platforms for the design of functional photoactive systems.

ACKNOWLEDGEMENTS. This work was supported by the Ministry of Education and Research of the Republic of Moldova through the Moldova State University research subprogram #011209.

[1] Lacey, H. T. (1956). U.S. Patent No. 2,761,868. Washington, DC: U.S. Patent and Trademark Office.

TWO DIPOLE-DIPOLE INTERACTING EMITTERS IN A MODERATELY STRONG LASER FIELD

A. S. Cudreasov[1,*], M. A. Macovei[1]
[1]*Institutul de Fizică Aplicată, Unviersitatea de Stat din Moldova, Academiei 5, MD-2028 Chișinău, Republic of Moldova*
*E-mail: alexander.cudreasov@gmail.com

The resonance fluorescence features of an ensemble of two closely packed and moderately laser-driven two-level emitters under non-resonant conditions are investigated. The regime of choice is the Dicke limit, when the distance between any two-level emitters is smaller than their emission wavelength, such that the dipole-dipole interactions are not negligible anymore. Under the secular approximation, the collective resonance fluorescence spectrum consists of 5 spectral lines, of which 4 are sidebands symmetrically located around the generalized Rabi frequency with respect to the central peak line, and are distinguishable if the dipole-dipole coupling strength is larger than the collective spontaneous decay rate [1]. Thus, it becomes possible for the emitter number within the ensemble to be measured from the spontaneously scattered collective resonance fluorescence spectrum.

[1] A. S. Cudreasov, P. Bardetski, and M. A. Macovei, "Two Dipole-Dipole Interacting Emitters in a Moderately Strong Laser Field," in 7th International Conference on Nanotechnologies and Biomedical Engineering, ICNBME 2025, IFMBE Proceedings, vol. 134, edited by V. Sontea, I. Tiginyanu, and S. Railean, Springer, Cham, pp. 49–55 (2025). Doi: https://doi.org/10.1007/978-3-032-06494-3_6

MODELING BLOOD FLOW IN STENOSED ARTERIES: PRESSURE LOSSE

I. M. Cernica*
Institute of Applied Physics, Moldova State University, Chisinau, Republic of Moldova
*E-mail: ion_cernica@yahoo.com

Arterial stenosis is a serious cardiovascular condition caused by atherosclerosis and is widespread, particularly in Western countries. According to the 2023 statistical report by the American Heart Association, the mortality rate from heart disease in the United States was 295 deaths per 100.000 inhabitants [1].

The aim of modeling the physiological processes of blood flow in stenosed arteries is to provide methods and calculation formulas for the pressure losses. Blood is assumed to be an incompressible fluid undergoing quasi-steady turbulent flow through an artery with rigid, smooth walls, while the arterial stenosis behaves like a circular orifice plate of the same diameter (Figure 1).

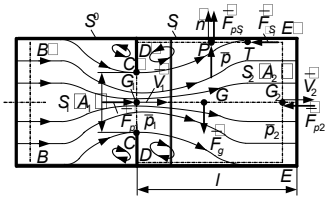


Figure 1. Sudden narrowing of a stenosed artery.

Substituting the expression for $\bar{p}_1 - \bar{p}_2$ given by the momentum theorem for a stream tube [2] into the generalized Bernoulli equation [2, 3], where $\alpha_1 = \alpha_2 \cong 1,$ and taking into account that for liquids $\bar{V}_1 A_1 = \bar{V}_2 A_2 = Q,$, we obtain

$$\Delta\bar{p}_{r,1-2} = \frac{1}{2}\rho\bar{V}_2^{\,2}\left(\frac{st_A}{1-st_A}\right)^2 + \varphi\tau_w = \frac{1}{2}\rho\bar{V}_1^{\,2}st_A^{\,2} + \varphi\tau_w, \tag{1}$$

where $st_A = 1 - A_1/A_2$ is the degree of arterial stenosis, and $\varphi = A_1/A_2$ is the shape factor of the affected artery. Neglecting the wall shear stresses [2], relation (1) becomes

$$\Delta\bar{p}_{r,1-2} = \frac{1}{2}\rho\bar{V}_2^{\,2}\left(\frac{st_A}{1-st_A}\right)^2 = \frac{1}{2}\rho\bar{V}_1^{\,2}st_A^{\,2}. \tag{2}$$

The pressure loss can also be calculated with the Darcy-Weisbach equation

$$\Delta\bar{p}_{r,1-2} = \lambda\frac{l}{d}\frac{\rho\bar{V}_2^{\,2}}{2}. \tag{3}$$

Equating (2) and (3) and solving for the Darcy coefficient yields

$$\lambda = \frac{4}{\varphi}\left(\frac{st_A}{1-st_A}\right)^2, \tag{4}$$

For a carotid artery with diameter $d = 10$ mm and length $l = 250$ mm affected by stenosis of a certain severity $st_A = 0.50$ the resistance coefficient λ=0.04 is practically 2.5 times higher than in an unaffected artery. Assuming a blood density of ρ = 1050 kg/m^3 and a flow velocity of V = 0.2 m/s, the pressure loss in the carotid artery $\Delta\bar{p}_{r,1-2} = 21$ Pa, is nearly three times greater than in an unaffected artery $\left(\Delta\bar{p}_{r,1-2} = 6.813 \text{ Pa}\right).$ Although this value is small compared to normal blood pressure, it is sufficient to exacerbate the stenosis.

[1] American Heart Association. ,,Report: cardiovascular diseases caused 1 in 3 global deaths in 2023". WHO.int, 2025.
[2] D. Gh. Ionescu. Introduction to Fluid Mechanics, 2nd edition (in Romanian), 2005, 594 p. ISBN 973-31-2256-4.
[3] I. M. Cernica. Fundamentals of Fluid Mechanics (in Romanian), 2021, 948 p. ISBN 978-9975-87-886-9.

MODELING BLOOD FLOW IN STENOSED ARTERIES: BLOOD FLOW RATE

I. M. Cernica*
Institute of Applied Physics, Moldova State University, Chisinau, Republic of Moldova
*E-mail: ion_cernica@yahoo.com

The primary goal of all treatment methods is to restore blood flow to physiological levels, while ensuring that the resulting pressure drop remains within physiological limits.
Consider an artery with an initial diameter d that narrows to a diameter d_s due to the formation of an atherosclerotic plaque (Figure 1). It is assumed that the blood flow is turbulent and quasi-steady, and that the arterial walls are rigid and smooth.

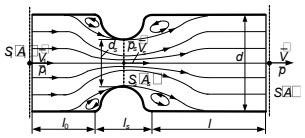


Figure 1. Quasi-steady turbulent flow in a stenosed blood vessel.

We establish a formula for the blood flow rate through the stenosed artery, starting from the generalized Bernoulli equation [1, 2] and the continuity equation:

$$\frac{\rho\bar{V}_1^2}{2}+\bar{p}_1=\frac{\rho\bar{V}^2}{2}+\bar{p}+\zeta_s\frac{\rho\bar{V}_s^2}{2}+\frac{\rho\left(\bar{V}_s-\bar{V}\right)^2}{2}+\lambda\frac{l}{d}\cdot\frac{\rho\bar{V}^2}{2}, \tag{1}$$

$$Q=\bar{V}_sA_s=\bar{V}A. \tag{2}$$

Here ζ_s is the local resistance coefficient of the constriction.

Expressing the velocities $\bar{V}_c$ and $\bar{V}$ in terms of the blood flow rate Q yields

$$Q=\mu A\sqrt{2\Delta\bar{p}/\rho}, \tag{3}$$

in which the proportionality coefficient μ has the expression

$$\mu=\frac{1}{\sqrt{1+\dfrac{\zeta_s+st_A^{\,2}}{\left(1-st_A\right)^2}+\lambda\dfrac{l}{d}}}. \tag{4}$$

As a first approximation, the local resistance coefficient can be estimated with the orifice plate formula [1] $\zeta_s=\left(A/\left(\varepsilon A_s\right)-1\right)^2$, For an artery with a severity degree of $st_A = 0.50$, the values obtained are $\varepsilon=0.676$ and $\zeta_s=0.068.$ If we further assume $\lambda=0.04$ and $l/d=25,$ then relation (4) yields $\mu=0.553$, meaning that the blood flow rate is 34.4% lower than in an unaffected artery.
The same assumptions give the minimum diameter of the cylindrical lumen

$$d_{\min}=\frac{d}{\sqrt[4]{1+\dfrac{2\Delta p}{\rho}\dfrac{1}{V^2}}}, \tag{5}$$

Thus, for a carotid artery with a diameter of d = 10 mm – carrying blood with a density of ρ = 1050 kg/m^3 at a mean velocity $V=0.2\ \mathrm{m/s},$ and a pressure difference $\Delta p=p-p_s$=54.4 Pa – calculation using equation (5) yields a value of $d_{\min}=0.007265$ m. A reduction in the artery's diameter by 2.735 mm results in a 47.22% decrease in the arterial cross-sectional area, corresponding to moderate stenosis ($st_A \approx 0.53$). Below this value the lumen is completely occluded by the external pressure p_{ext} When such a blockage occurs in a coronary artery the heart ceases to function.

[1] D. Gh. Ionescu. Introduction to Fluid Mechanics, 2nd edition (in Romanian), 2005, 594 p. ISBN 973-31-2256-4.
[2] I. M. Cernica. Fundamentals of Fluid Mechanics (in Romanian), 2021, 948 p. ISBN 978-9975-87-886-9.

THE PEIERLS STRUCTURAL TRANSITION IN QUASI-ONE-DIMENSIONAL TTT2I3 ORGANIC CRYSTALS WITH CONSIDERIND INTERCHAIN INTERACTION

S. C. Andronic*, I. I. Sanduleac
Technical University of Moldova, Chisinau, Republic of Moldova;
*E-mail: silvia.andronic@mt.utm.md

We investigate the Peierls structural transition in quasi-one-dimensional organic crystals of tetrathiotetracene-iodide, TTT2I3, within a three-dimensional (3D) theoretical framework for different carrier concentrations. The proposed physical model incorporates the two main hole-phonon interaction mechanisms. The first interaction describes the deformation potential and the second one is of polaron type. In addition, carrier scattering by structural defects is included, as it plays a crucial role in describing the phase transition. The renormalized phonon spectrum is calculated in the random phase approximation for different temperatures applying the method of Green functions. Computer simulations for renormalized phonon spectrum, $\Omega(q_x)$, for different temperatures are presented in two cases: 1) when the interaction between TTT chains is neglected ($q_y = 0$, $q_z = 0$) and 2) when the interaction between TTT chains is taken into account ($q_y = \pi$, $q_z = \pi$). Numerical simulations are performed for several values of the dimensionless Fermi wave vector, k_F, corresponding to different carrier concentrations. The results demonstrate that the structural transition is of the Peierls type and is highly sensitive to the iodine concentration. It was observed that with a decrease of the carrier concentration the Peierls critical temperature increases. Also, one can see that the interchain interaction reduces the transition temperature. The theoretical predictions are in good agreement with the experimental values reported in the literature [1, 2], confirming the validity of the proposed three-dimensional model.

[1] V. F. Kaminskii, M. L. Lhidekel', R. B. Lyubovskii et all. *Phys. Status Solidi A*, **44** (1977) 77.
[2] I. F. Shchegolev, E. B. Yagubskii. *Plenum Press*, **2** (1982), 385.

INDIRECT POPULATION OF AN EMPTY OPTICAL CAVITY VIA COLLECTIVE ATOMIC EFFECTS

S. Cârlig*, V. Ciornea, C. Gherman, M. A. Macovei
Institute of Applied Physics, Moldova State University, Republic of Moldova
*E-mail: carligsergiu@gmail.com

Coupled optical cavity architectures represent a flexible platform for investigating light–matter interactions and coherent excitation transfer in composite quantum systems. In this work, we theoretically analyze the steady-state dynamics of a system consisting of two optical cavities coupled through bidirectional photon exchange, each of which may contain an ensemble of real or artificial two-level atoms, fig. 1 [1]. The atoms are coherently pumped by external laser fields and interact with independent electromagnetic reservoirs, which introduce dissipative processes such as spontaneous emission, atomic dephasing, and cavity photon losses.

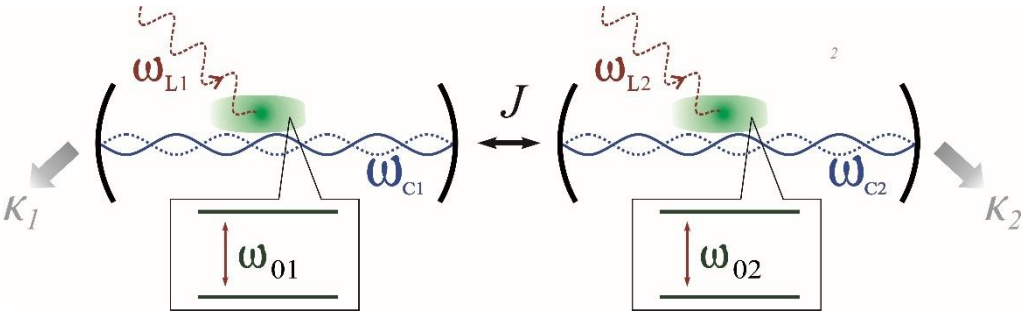


Figure 1. The schematic setup depicting two coupled-cavities, each containing a multi-atom two-level ensemble that is coherently pumped with an externally applied laser field. Both the cavities and the atomic subsystems interact with the corresponding electromagnetic environmental vacuum reservoirs, resulting in dissipative effects. The laser frequencies are denoted by ω_{L1} and ω_{L2}, while the atomic transition frequencies are ω_{01} and ω_{02}. The resonance frequencies of the cavity modes are ω_{C1} and ω_{C2}, respectively. J is coupling constant between cavities, and $\kappa_{1,2}$ – each cavity loss rates.

The system is studied within the dressed-state formalism, in the regime where the Rabi frequencies exceed the collective spontaneous emission and cavity decay rates. Under the secular approximation, the master equation and the corresponding equations of motion are derived, allowing the analytical determination of the steady-state mean photon numbers in the two cavities.

Special attention is devoted to an asymmetric configuration in which only the first cavity contains a coherently pumped atomic ensemble, while the second cavity is completely empty. The results demonstrate that excitations generated in the first cavity can be efficiently transferred to the second cavity exclusively through the inter-cavity interaction. This transfer is enhanced by cooperative effects among the emitters. In particular, the mean photon number in the initially empty cavity is proportional to the square of the number of pumped atoms in the first cavity, providing a signature of Dicke-like collective behavior.

The obtained results highlight the possibility of indirectly populating an optical resonator and offer perspectives for controlling excitation transport in multi-cavity quantum systems. The investigated model may be relevant to the development of quantum optical platforms, quantum thermodynamics, and the study of cooperative processes in the high-frequency domain.

[1] S. Carlig. *Physics of the Solid State* **67(10)** (2025) 873–878.

ATOMIC STRUCTURE AND STRUCTURAL DISORDER VS. DEVICE EFFICIENCY IN KESTERITE MONOGRAIN SOLAR CELLS

G. Gurieva[1,*], K. Ernits[2], A. Manjon Sanz[3], D. Sheptyakov [4], M. Avdeev[5], N. Siminel[6], M. Kirkham[3], D. Meissner[2,7], S. Schorr[1,8]
[1]*Helmholtz-Zentrum Berlin für Materialien und Energie, Berlin, Germany;*[2]*Crystalsol O¨U, Tallinn, Estonia;* [4]*Neutrons Scattering Division, Oak Ridge National Lab, Oak Ridge, Tennessee, USA;* [4]*Laboratory for Neutron Scattering and Imaging, Paul Scherrer Institut, Villigen, Switzerland;* [5]*Australian Nuclear Science and Technology Organisation, Lucas Heights, NSW, Australia;* [6]*Institute of Applied Physics, Academy of Sciences of Moldova, Chisinau, Moldova;* [7]*Department of Materials and Environmental Technology, Tallinn University of Technology, Tallinn, Estonia;* [8]*Freie Universität Berlin, Institute of Geological Sciences, Berlin, Germany*
*E-mail: galina.gurieva@helmholtz-berlin.de

Quaternary chalcogenides, especially kesterite-type $Cu_2ZnSn(S,Se)_4$ (CZTSSe), have gained a lot of attention as emerging absorber material for photovoltaic (PV) applications. PV devices, reaching a power conversion efficiency of 16.6% [1], are based on an off-stoichiometric CZTSSe absorber layer [2]. Deviations from stoichiometry in CZTSSe are possible due to the flexibility of the kesterite-type structure to accept intrinsic point defects (vacancies, anti-sites, interstitials) [3]. These point defects, occuring in high concentrations up to 10^{20} cm^{-3}, can be discussed as the materials' structural disorder. A special kind of this disorder is the Cu/Zn disorder (Cu_{Zn} and Zn_{Cu} anti-sites in Cu-Zn planes) always present in kesterite-type compounds [4]. The formation of point defects is creating energy levels within the band gap, which can affect conductivity, charge carrier concentrations and optical properties setting the material's electrical conductivity, recombination dynamics, and device limits [5]. Thus, knowledge about intrinsic point defect scenario and control of defect processes in PV materials is essential for realizing high-efficiency solar cells and related optoelectronic devices.
We have developed a methodology to determine the type and concentration of intrinsic point defects from diffraction data [6]. Here we have applied mainly neutron diffraction which allows to distinguish the electronic similar elements copper and zinc in the structural analysis. On the other hand, neutron diffraction requires large sample volumes. We have used CZTSSe monograins (single crystals of 50-100 μm size) as samples in the neutron powder diffraction experiments, which are later on fixed in a polymer matrix to form a flexible solar cell. Thus, kesterite monograins offer the unique possibility to correlate structural disorder in kesterite-type absorbers with device performance parameters of the monograin layer solar cell [7].
In this work, we investigate how the purity of the synthesis precursors [8], thermal and mechanical processing [7], and cation and anion stoichiometry [9] influence the atomic structure, structural disorder, and, consequently, the efficiency and stability of CZTSSe monograin solar cells. Finally, we aim to provide a deeper understanding of the factors underlying the exceptional performance of the CZTSSe monograin solar cell that currently holds the world-record efficiency for this technology.

[1] NRL chart
[2] J. Zhou et al., *Nano Energy* **89** (2021) 106405.
[3] S. Schorr et al., *J. Phys. En.* **2** (2020) 012002.
[4] S. Schorr, *Sol. En. Mat. Sol. Cells* **95** (2011) 1482.
[5] J.S. Park et al., *Nat. Rev. Mat.* **3** (2018) 194.
[6] S. Schorr et al., in: Advanced characterization techniques for thin film solar cells, ed. by D.Abou-Ras, T.Kirchartz, U.Rau, Wiley, 2016
[7] G. Gurieva et al., *Sol. En. Mat. Sol. Cells* **248** (2022) 112009.
[8] G. Gurieva et al., *Phys. Rev. Mat.*, **9**, (2025), 075403/1-10.
[9] G. Gurieva et al., *Faraday Discuss.*, **xx**, (2026), 1–15.

FROM $Cu_2ZnSiSe_4$ TO $Cu_2ZnGeSe_4$: EVOLUTION OF VIBRATIONAL PROPERTIES WITH Ge INCORPORATION

V. Rotaru[1,2,*], G. Gurieva[3], P. Vidal Fuentes[1], A. Pérez-Rodríguez[1,4], V. Izquierdo Roca[1], S. Schorr[3,5], M. Guc[1]

[1]*Catalonia Institute for Energy Research (IREC), 08930 Barcelona, Spain;*
[2]*Facultat de Fisica, Universitat de Barcelona (UB), 08028 Barcelona, Spain*
[3]*Helmholtz-Zentrum Berlin für Materialien und Energie (HZB), 14109 Berlin, Germany*
[4]*Departament d'Enginyeria Electrònica i Biomèdica, IN2UB, Universitat de Barcelona, 08028 Barcelona, Spain*
[5]*Freie Universität Berlin, Institute of Geological Sciences, 12249 Berlin, Germany*
*E-mail: vrotaru@irec.cat

$Cu_2ZnGe_xSi_{1-x}Se_4$ (CZGSiSe) solid solutions are promising materials for sustainable thin-film photovoltaic applications due to their tunable properties. In this system, the crystal structure evolves from kesterite $Cu_2ZnGeSe_4$ (CZGSe) to wurtz-kesterite $Cu_2ZnSiSe_4$ (CZSiSe) [1], providing an opportunity to investigate the relationship between composition, structure, and lattice dynamics.

In this work, we study the vibrational properties of CZGSiSe solid solutions by multiwavelength Raman spectroscopy and investigate the lattice dynamics of wurtz-kesterite CZSiSe using *first-principles calculations*. Particular attention is given to the effects of Ge/Si substitution on the Raman spectra and to the vibrational fingerprint of CZSiSe in its recently established wurtz-kesterite structure. Previous Raman studies on CZSiSe were interpreted assuming a wurtz-stannite structure; therefore, an updated description of its vibrational properties is required for the correct scientific interpretation of the results.

Raman spectra of a series of CZGSiSe powder samples have been measured employing the 442, 532 and 785 nm excitation wavelengths, covering excitation energies both above and below the band-gap range of the solid solutions. *First-principles calculations* of the electronic ground state of wurtz-kesterite CZSiSe were performed within density functional theory using the Perdew-Burke-Ernzerhof functional revised for solids, as implemented in the CASTEP code. Phonon densities of states and vibrational mode frequencies were calculated and used to support mode assignment.

The Raman spectra exhibit continuous and systematic evolution with increasing Si content, independent of the excitation wavelength. Whereas the end-member compounds show their characteristic Raman signatures, the intermediate compositions display predominantly two-mode behavior, typical of complex semiconductor solid solutions. Additional Raman bands are observed in the 220-260 cm^{-1} range and are attributed to vibrational modes specific to the solid-solution compositions. Theoretical results provide insight into the nature of the vibrational modes of wurtz-kesterite CZSiSe and enable reliable assignment of the experimentally observed features.

Analysis of the composition-dependent Raman spectra reveals distinct spectral regions dominated by modes associated with the parent compounds. Based on these trends, a Raman-spectroscopy methodology is proposed for rapid and non-destructive determination of the Ge/(Ge+Si) ratio in CZGSiSe solid solutions. The results contribute to a deeper understanding of the composition-dependent lattice dynamics across CZGSiSe solid solutions and wurtz-kesterite CZSiSe.

[1] G.Gurieva, D.M.Többens, A.Manjon Sanz, V.Rotaru, C.Hennig, M.Kirkham, M.Guc, S.Schorr, *J. Mater. Chem. A,* **14(3)** (2026) 1770-1781.

INTRINSIC POINT DEFECTS IN ALKALI-DOPED KESTERITE-TYPE SEMICONDUCTORS AND THEIR INFLUENCE ON SOLAR CELL PERFORMANCE

H. Prell[1,2,*], G. Gurieva[2], M. Rusu[2], M Grossberg-Kuusk[3], M. Kauk-Kuusik[3], S. Schorr[1,2]
[1]*Freie Universität Berlin, Berlin, Germany;* [2]*Helmholtz-Zentrum Berlin für Materialien und Energie GmbH, Berlin, Germany;* [3]*Tallinn University of Technology, Tallinn, Estonia*
*E-mail: Henrik.Prell@helmholtz-berlin.de

Kesterite-type $Cu_2ZnSn(S,Se)_4$ (CZTSSe) semiconductors combine non-toxic, earth-abundant elements with a direct, composition-tunable bandgap and a high optical absorption coefficient, making them promising absorber materials for low-cost, sustainable photovoltaics. Although power conversion efficiencies exceeding 16% have recently been achieved [1], device performance remains limited by open-circuit voltage losses associated with intrinsic point defects, cation disorder, and band tailing. Among the proposed approaches to mitigate these limitations, alkali metal doping has emerged as a promising strategy for tailoring defect chemistry and improving optoelectronic properties [2].

This work investigates the effects of alkali metal incorporation in off-stoichiometric CZTSSe bulk monograin and polycrystalline powder samples synthesized from elemental precursors using different alkali-salts to evaluate the mechanisms and extent of alkali incorporation and their influence on intrinsic point defects. Monograin solar cells are subsequently fabricated using Monograin technology [3] to correlate absorber properties with photovoltaic performance.

Structural characterization is performed using X-ray diffraction and neutron diffraction combined with Rietveld refinements and average neutron scattering length analysis [4] to determine lattice parameters, atomic positions, cation distributions, and the type and concentration of intrinsic point defects. Phase purity, homogeneity, and chemical composition are assessed by electron microprobe analysis, while the optical bandgap is determined by diffuse reflectance UV-Vis-NIR spectroscopy. Kelvin probe and photoelectron yield spectroscopy provide complementary information on surface potential variations and electronic structure, enabling determination of the hole concentration and the Fermi level position relative to the valence band maximum.

Particular emphasis is placed on Cu/Zn disorder [5] and the development of intrinsic point defects resulting from alkali-metal treatment, and on their correlation with chemical composition, bandgap energy, electronic properties, and photovoltaic performance. By establishing structure-property relations between alkali-induced defect chemistry and device performance, this work provides insights into defect engineering strategies for improving CZTSSe absorbers and advancing high-efficiency kesterite solar cells.

[1] NLR (2026). *Best Research-Cell Efficiency Chart*. U.S. DOE. www.nlr.gov/pv/cell-efficiency, 09.07.2026
[2] Y. E. Romanyuk et al., *Journal of Physics: Energy*, **1 (**2019) 044004.
[3] D. Meissner, et al., *Sol. Energy Mater. Sol*. Cells, **252** (2023) 112160.
[4] S. Schorr, C. Weidenthaler (Eds.), Crystallography in Materials Science, *Walter de Gruyter*, (2021) 128-133.
[5] S. Schorr, *Solar Energy Materials and Solar Cells*, **95**(6) (2011) 1482-1488.

DISORDER-CONTROLLED MAGNETISM IN POLAR ANTIFERROMAGNETS $M_2Mo_3O_8$

L. Prodan[1,*], I. Filippova[2], D. Croitori[2], S. Moldovanu[2], O. G. Grendal[3,4], S. Shova[5], A. Tsirlin[6], I. Kézsmárki[1], V. Tsurkan[1,2]

[1] *Institute of Physics, University of Augsburg, Augsburg, Germany;* [2]*Institute of Applied Physics, Moldova State University, Chişinău, Republic of Moldova;* [3]*NTNU Norwegian University of Science and Technology, Trondheim, Norway;* [4]*European Synchrotron Radiation Facility ESRF, Grenoble, France;* [5]*"Petru Poni" Institute of Macromolecular Chemistry, Romanian Academy, Iasi, Romania;* [6]*Felix Bloch Institute for Solid-State Physics, Leipzig University, Leipzig, Germany*

*E-mail: lilian.prodan@uni-a.de

Antiferromagnetic materials are promising candidates for ultrafast and energy efficient spintronic devices. The interplay of electronic correlations, broken inversion symmetry, and site-selective chemical substitution in ternary molybdenum oxides $M_2Mo_3O_8$ makes them an attractive platform for realizing unconventional phenomena of relevance for fundamental research and quantum technologies [1-3]. To exploit and manipulate their functionality, it is essential to understand how their properties can be tuned by chemical substitution and external stimuli.

Here, we investigate the effect of controlled, site-selective substitution of magnetic ions by non-magnetic Zn ions on the crystal structure, magnetic, and thermodynamic properties of $Co_{2-y}Zn_yMo_3O_8$ and $Fe_{2-y}Zn_yMo_3O_8$. We revealed site-occupancy behavior in the two systems leading to modification of the intra-layer and inter-layer exchange interactions, [Fig.1(a)], and the competing magnetic anisotropies associated with the octahedral and tetrahedral (M^{2+}) sites as well. In $Co_{2-y}Zn_yMo_3O_8$, robust antiferromagnetic order persists up to substitution y=0.55, while strong magnetic disorder emerges at y=0.66 [4]. In contrast, $Fe_{2-y}Zn_yMo_3O_8$ undergoes a transition from an antiferromagnetic to a ferrimagnetic state already at $y\geq0.2$. For $y\geq1.3$, the long-range magnetic order is almost suppressed. Our results demonstrate that the atomic-scale control of chemical composition enables systematic tuning of magnetic states (Fig. 1), with chemical disorder acting as an effective microscopic control factor. We discuss the correlation between the site-selective substitution, crystal structure, and magnetic properties, and show how the magnetic order and exchange interactions are governed by the changes in the site occupancy. These findings establish the chemical disorder in $M_2Mo_3O_8$ not merely as an uncontrolled perturbation, but a powerful design parameter for engineering of functional magnetic materials.

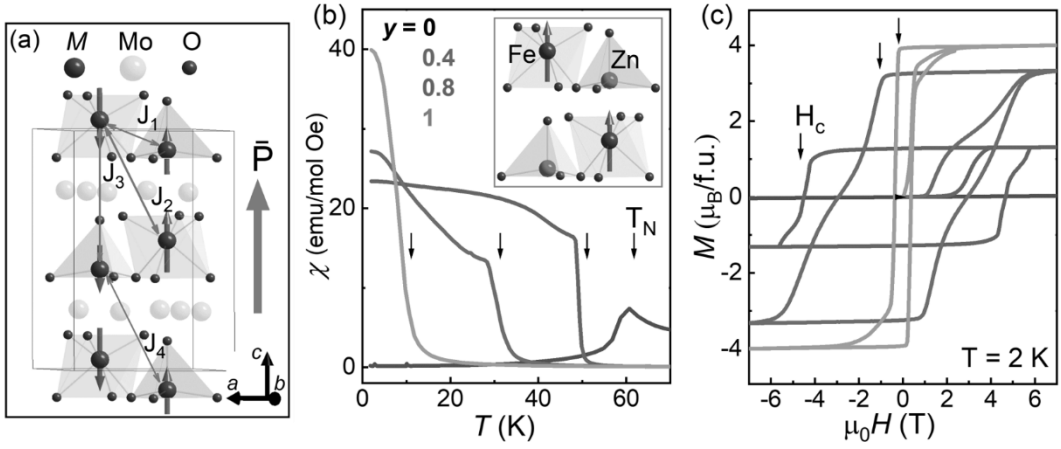


Figure 1. (a) Crystal structure (polar space group $P6_3mc$) and ground-state spin arrangement in $M_{2-y}Zn_yMo_3O_8$ (M = Fe and Co). (b) Temperature dependence of the low-field magnetic susceptibility χ, and (c) of the isothermal magnetization hysteresis loops measured for $Fe_{2-y}Zn_yMo_3O_8$. The inset in (b) illustrates the occupancy of Zn and magnetic ions on the tetrahedral and octahedral crystallographic sites.

[1] S.-W. Cheong, F.-T. Huang. *npj Quantum Mater.* **10** (2025) 38.
[2] S. Ghara, *et al*., *Nat. Commun.* **14** (2023) 5174.
[3] D. Szaller, *et al*., *Phys. Rev. B.* **111** (2025) 184404.
[4] L. Prodan, et al., *Phys. Rev. B.* **106** (2022) 174421.

INSIGHTS INTO THE PHOTOLUMINESCENT AND STRUCTURAL PROPERTIES OF THE BINUCLEAR COMPLEX [Eu_2(*o*-MBA)$_6$(phen)$_2$]

V. Ghenea[1,2,*], I. Culeac[1], E. Melnic[1], I. Cojocaru[1], V. Verlan[1], A. Siminel[1], I. Bulhac[3], A. Buzdugan[2], A.-G. Pantazi[4,5], M. Enachescu[4,5]

[1]*Institute of Applied Physics, Moldova State University, Chisinau, Republic of Moldova;* [2]*Department of Microelectronics and Biomedical Engineering, Technical University of Moldova, Chisinau, Republic of Moldova;* [3]*Institute of Chemistry, Moldova State University, Chisinau,* [4]*Center for Surface Science and Nanotechnology, National University of Science and Technology POLITEHNICA Bucharest, Romania;* [5]*Academy of Romanian Scientists, Bucharest, Romania*

*E-mail: vladislav.ghenea@ifa.usm.md

Optical properties of Eu(III)-based luminescent materials are strongly influenced by the local coordination environment. In this work, the binuclear complex [Eu_2(o-MBA)$_6$(phen)$_2$], containing o-methylbenzoate (o-MBA) and 1,10-phenanthroline (phen) ligands, was investigated through complementary spectroscopic and structural approaches to establish correlations between photoluminescence behavior and crystal structure [1].

Single-crystal X-ray diffraction confirmed that both Eu^{3+} ions possess comparable nine-coordinate environments within a triclinic crystal structure. Hirshfeld surface analysis revealed an uneven distribution of intermolecular interactions, indicating a distorted crystal field around the metal centers [2]. Photoluminescence spectra registered between 15 and 300 K show characteristic emission bands of Eu^{3+} with multiple narrow components (Fig.1) [3]. The integrated emission of the intensity of the complex exhibits moderate quenching over the temperature range 80–300 K. Analysis of Stark splitting of the $^5D_0 \rightarrow {}^7F_J$ transitions indicated a low-symmetry coordination environment, with the $^5D_0 \rightarrow {}^7F_1$ transition resolved into three nearly equally spaced components, while the hypersensitive $^5D_0 \rightarrow {}^7F_2$ transition displaying multiple al least six Stark components [4]. These results support the existence of two crystallographically independent Eu^{3+} sites with highly similar coordination geometries.

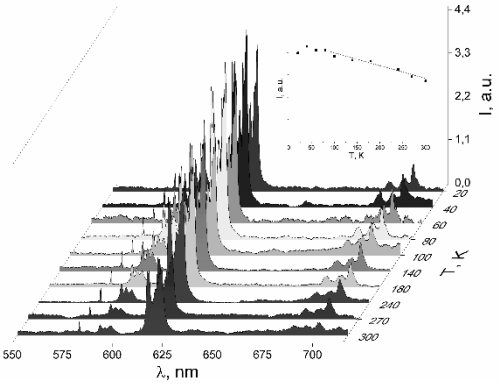


Figure 1. PL emission spectra of [Eu_2(o-MBA)$_6$(phen)$_2$] powder sample for different temperatures under excitation λ_{ex} = 405 nm.

The emission spectrum at 300 K exhibits a color purity of ~97%, with chromaticity coordinates located in the pure red region. Estimation of the crystal-field parameters obtained from analysis of the Stark splitting of $^5D_0 \rightarrow {}^7F_{1,2}$ transitions correlate with C_i local symmetry and indicates a substantial rhombic contribution comparable to the axial crystal-field component [5].

The complex appears to be a promising candidate for red-emitting materials in optoelectronics applications.

ACKNOWLEDGEMENTS. This research was funded by the Ministry of Education and Research of the Republic of Moldova (subprograms 011201, 011202, 010602), as well as by the Romanian Ministry of Investments and European Projects and the Ministry of Research, Innovation and Digitalization under the projects HICONNECTS - contract no. G 2024-68867/16.10.2024, POCIDIF-SMIS 2021+ code 315746, and 14ACMOS - contract no. G 2025-54059/390013/12.05.2025, POCIDIF-SMIS 437 2021+ code 338315.

[1] Culeac et al. *Front. Nanotechnol.*, **8** (2026) 1875127.
[2] Spackman et al. *J. Appl. Crystallog.*, **54** (2021) 1006-1011;
[3] Bunzli, *Inorg. Chim. Acta.*, **139** (1987) 219-222;
[4] Culeac et al. *Journal of Luminescence*, **276** (2024) 120854;
[5] Binnemans et al. *Chem. Phys. Lett.*, **245** (1995) 75-78;

STRUCTURAL CHIRALITY AND FUNCTIONALITY IN INCOMMENSURATE MODULATED TETRAGONAL TUNGSTEN BRONZES

O. Grendal[1,*], C. R. Zeiger[2], R. S. Dragland[2], R. Sjøkvist[1], R. Beanland[1], D. Meier[2], M. Senn[3]
[1]*Department of Physics, University of Warwick, Gibbert Hill Road, Coventry CV4 7AL, United Kingdom;* [2]*Department of Materials Science and Engineering, NTNU Norwegian University of Science and Technology, Sem Sælandsvie 12, 7491 Trondheim, Norway;* [3] *Department of Chemistry, University of Warwick, Gibbert Hill Road, Coventry, CV4 7AL, United Kingdom*
*E-mail: olag.grendal@gmail.com

Chirality is a crucial and fundamental concept in natural sciences having great implications in fields ranging from cosmology to particle physics, including chemistry, medicine and biology [1]. In solid-state physics chirality is closely linked to optical activity [2] and is gaining increasing interest due to topics like magnetic skyrmions [3], chiral quantum optics [4] and even enabling negative refraction and thus making of "perfect" lenses [5]. Following from this is a growing interest in direct external-field control of chirality, *i.e. ferrochirality*, as this would enable direct control of chirality-related phenomena and functionality. A ferrochiral material need to possess an achiral to chiral phase transition and show "switchable" chirality in the chiral phase. Such materials are rare, and an unambiguous direct switching of chirality has so-far not been demonstrated. However, promising work using laser radiation for controlling chirality have been performed [6].

Here we present an in-depth structural characterization of two new potential ferrochiral materials. The incommensurate modulated structure of the two tetragonal tungsten bronze materials $K_4Bi_2Nb_{10}O_{30}$ (KBN) and $Rb_4Bi_2Nb_{10}O_{30}$ (RBN) are solved, and their functional properties characterized. The incommensurate modulated structures are described by superspace group $P42_12(00\gamma)q00$ with an unusual helical displacement of Bi^{3+} atoms along the *c*-direction of the average cell, as shown in Fig. 1. $P42_12$ is one of the 43 *non-enantiomorphic* Sohncke space group, and the structure is thus chiral due to the chirality of the Bi^{3+} helix in the structure. The order parameter of the achiral to chiral phase transition is shown to transform as the irreducible representation Λ_5 (*i.e.* the order parameter is the chirality itself), with a second order parameter transforming as Γ_1^-. The Γ_1^- mode induces piezoelectricity, that we have experimentally verified. Finally, through group theory and invariant analysis, we propose that combining symmetry breaking share strain (transforming as Γ_5^+) and an electric field (transforming as Γ_5^-) can be used as a conjugate field to switch the chirality through its link with the piezoelectric properties of the materials. This would then be a way of demonstrating chiral switching and provide solid evidence for ferrochirality in these materials.

[1] E. Bousquet, M. Fava, Z. Romestan, F. Gómez-Ortiz, E. E. McCabe, A. H Romero. J. Phys. Condens. Matter, **37**, (2025)
[2] A. M. Glazer, K. Stadnicka. J. Appl. Crystallogr, **19**, (1986)
[3] S. Mühlbauer, B Binz, F. Jonietz, C. Pfleiderer, A. Rosch, A. Neubauer, R Georgii, P Böni. Sci., **323**, (2009)
[4] P. Lodahl, S. Mahmoodian, S. Stobbe, A. Rauschenbeutel, P. Schneeweiss, J. Volz, H. Pichler, P. Zoller. Nat., **541**, (2017)
[5] J. B. A. Pendry. Sci., **306**, (2004)
[6] T. Hayashida, K Kimura, T. Kimura. J. Phys. Chem. Lett., **13**, (2022)

[Eu(DBM)$_3$Phen] SUBLIMATED THIN FILMS FOR OPTOELECTRONIC DEVICES

I. Culeac[1], V. Verlan[1], V. Ghenea[1], I. Bulhac[2], I. Cojocaru[1,*],
A.-G. Pantazi[3], M. Enachescu[3]
[1]*Institute of Applied Physics, Moldova State University, Chișinău, Republic of Moldova;*
[2]*Institute of Chemistry, Moldova State University, Chișinău, Republic of Moldova;*
[3]*Center for Surface Science and Nanotechnology, University Politehnica of Bucharest, Romania.*
*E-mail: ion.cojocaru@ifa.usm.md

Lanthanide organic coordination compounds remain a research hotspot because of their high potential for optoelectronic and photonic applications. Specifically, Eu(III) complexes are excellent materials for displays technology and electro-luminescence devices, usually fabricated by vacuum deposition of thin films on indium-tin-oxide (ITO)-coated glass substrates. Luminescent thin films for optoelectronic applications require high optical transmission, homogeneity, as well as photochemical long-term stability. We report here on new comparative photoluminescence (PL) and emission photostability measurements in [Eu(DBM)$_3$(Phen)] powder samples and sublimated thin films, obtained by deposition in vacuum on the glass substrates.

For thin films deposition the complex powder was heated in the vacuum to a temperature of ~200ºC and completely sublimed (thickness ~ 30 nm). AFM image of the sublimated thin-film illustrating a medium surface roughness, caused by a non-ideal process during film preparation (Fig. 1).

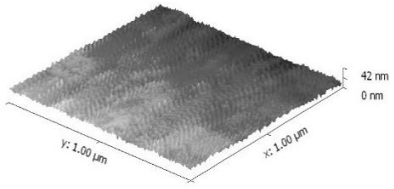


Figure1. AFM image of the sublimated film [Eu(DBM)$_3$Phen].

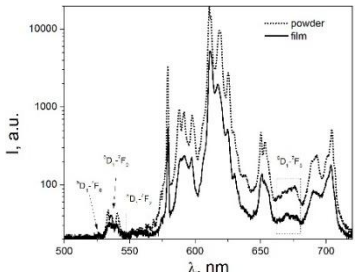


Figure 2. PL spectra of the [Eu(DBM)$_3$Phen]: powder and sublimated film samples.

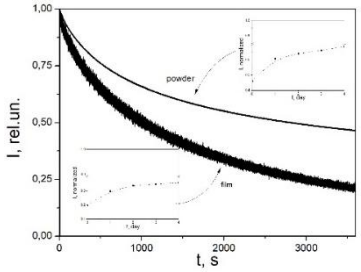


Figure 3. PL photodegradation under continuous irradiation with the excitation beam 405 nm.

Thin films of the [Eu(DBM)$_3$(Phen)] display a red-orange photoluminescence emission (405 nm laser excitation), typically for ternary Eu(III) complexes, with similar character of the emission bands for two sample morphologies - the powder samples and sublimated films ones (Fig. 2). The PL spectra are characterized by narrow emission bands, determined by radiative transitions from the first resonant level $^5D_0$ to the ground state multiplet ^7F_J (J = 0-4). The intrinsic quantum yield, estimated from the PL decay kinetics, was found to be approximately 28% for the powder samples and 26% for the thin films, in good agreement with values reported for related Eu(III) complexes. In addition, the Judd–Ofelt intensity parameters, radiative transition probabilities, branching ratios, and radiative lifetimes were evaluated.

The PL photostability was investigated in an air under continuous irradiation by excitation beam 405 nm (Fig. 3). The complex shows a considerable PL degradation both in thin films as well as in powder samples, with subsequent partial recovery under storing in the dark. Inserts in Fig. 3 illustrate partial recovery of the PL emission after secession of the excitation. It can be concluded that the [Eu(DBM)$_3$(Phen)] complex, although subjected to degradation, displays moderate UV-light stability in powder samples while lower stability is registered in thin sublimated films, although it keeps emissive after ~ 60 min of near-UV irradiation 405 nm.

ACKNOWLEDGEMENTS. This research was funded by the Ministry of Education and Research of the Republic of Moldova (subprograms 011201, 010602).

SYNTHESIS AND SPECTROSCOPIC PROPERTIES OF ZN(II)/CD(II) SCHIFF BASE COMPLEXES

V. Ghenea[1,2*], I. Culeac[1], I. Bulhac[3], L. Cuba[3]
[1]*Institute of Applied Physics, Moldova State University, str. Academiei 5, Chisinau MD-2028, Republic of Moldova;* [2]*PhD School, Technical University of Moldova, bd. Stefan cel Mare 168, Chisinau MD-2004, Republic of Moldova;* [3]*Institute of Chemistry, Moldova State University, str. Academiei 3, Chisinau MD-2028, Republic of Moldova*
*E-mail: vladislav.ghenea@ifa.usm.md

This study reports the synthesis and detailed comparative spectroscopic characterization of d^{10} transition metal coordination compounds, $[ZnL^1(CH_3COO)_2]\cdot 2H_2O$ and $[CdL^1(CH_3COO)_2]\cdot 3H_2O$, featuring a Schiff base ligand (L^1) derived from isonicotinic hydrazide and o-phthalaldehyde. Infrared (IR) spectroscopy reveals distinct coordination modes: bidentate bridging acetates in the Cd(II) complex ($\Delta\nu = 128$ cm^{-1}) compared to monodentate acetates in the Zn(II) complex ($\Delta\nu = 301$ cm^{-1}), accompanied by ligand modifications such as ν(C=O) shift due to metallocycle formation in Zn(II).

Under 405 nm excitation, both complexes exhibit intense green-yellow emission (Zn(II): $\lambda_{max} \approx 507$ nm [2]; Cd(II): $\lambda_{max} \approx 530$ nm) absent in the free ligand, attributed to coordination-enhanced ligand-centered fluorescence from rigidified structures suppressing nonradiative decay [3,4].

The Zn(II) complex exhibits higher intensity, narrower band ($\lambda_{max} \approx 507$ nm), relative to the Cd(II) complex ($\lambda_{max} \approx 530$ nm) (Fig.1), attributed to enhanced structural rigidity, reduced vibrational coupling, and considerable suppression of radiationless decay rates upon metal coordination [5], with CIE coordinates (Zn: x=0.2785, y=0.5604; Cd: x=0.3286, y=0.4555) (Fig.2) suitable for green emitters in optoelectronic devices [6]. These trends align with literature reports on d^{10} systems, where Zn(II) complexes often outperform Cd(II) analogs in emission brightness. These complexes emerge as promising materials for green-emitting components in RGB digital displays, white-light emitters, and luminescent sensors.

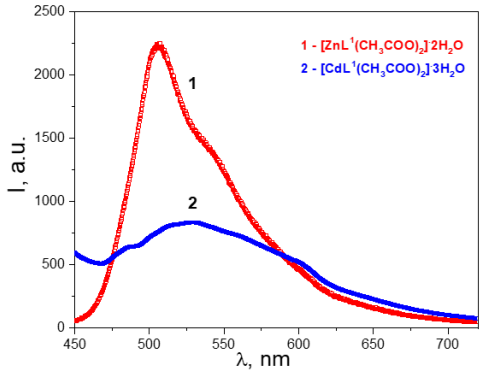


Figure 1. Emission spectra of Zn(II) and Cd(II) complexes.

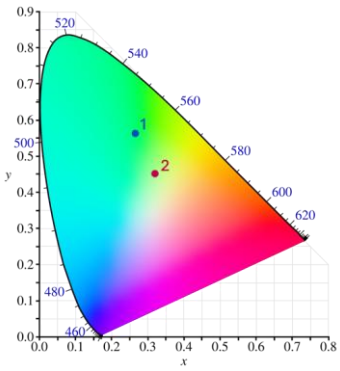


Figure 2. Cromaticity plot for colour coordinates of Zn(II) complex (1) and Cd(II) complex (2).

ACKNOWLEDGEMENTS. This research was funded by the Ministry of Education and Research of the Republic of Moldova (subprograms 011201 and 010602).

[1] Barbieri et al. *Chemical Communications* (2008) 2185-2193;
[2] Diana and Panunzi Molecules, **25** (2020) 4984;
[3] Korolenko et al. *Journal of Luminescence*, **237** (2021) 118156-118168;
[4] Kokina et al. *Dalton Transactions*, **52** (2023) 7429-7446;
[5] Majumder et al. *Polyhedron*, **25** (2006) 1753-1762.
[6] Bulhac et al. *Studia Universitatis Moldaviae*, **186** (2026) – *to be published*.

FEATURES OF ZEEMAN SPLITTING IN UNIAXIALLY DEFORMED BISMUTH WIRES

E. Condrea*
Technical University of Moldova, Institute of Electronic Engineering and Nanotechnologies, MD-2004, Chisinau, Republic of Moldova
*E-mail: elcondrea@gmail.com; elena.condrea@iien.utm.md

The question of how extreme conditions of uniaxial strain and high magnetic fields may affect the parameters of the anisotropic crystalline materials was the main subject of our experimental investigations. Under strain, the parameters of the anisotropic crystalline materials change differently depending on the direction of the magnetic field relative to the crystallographic axes. In this case, it is particularly important to determine the deformation characteristics of the material in the elastic range, in which the parameters of the used sample are reproduced. Since the electronic characteristics of materials are determined by their energy structure, the ability to track changes in the energy spectrum during deformation will allow us to identify a correlation between structure and revealed deformation properties.

Analysis of previously conducted magnetoresistance (*MR)* measurements of Bi wires in the geometric configuration with a magnetic field directed perpendicular to the wire axis and corresponding directed along the binary axis revealed the appearance of the doublet structures of the Shubnikov-de Haas oscillations at strong deformations that had previously been neglected as a modulation of the quantum oscillations. However, as Shoenberg [1] points out, it is possible to experimentally observe the spin splitting of energy levels in the magnetic field under favorable circumstances on the quantum oscillations with small quantum numbers near the quantum limit.

A doublet structure of oscillations is due to increases of the spin splitting above the cyclotron energy at strong deformation and high magnetic field. Usually, the magneto-oscillatory phenomena at high ratio $\boldsymbol{B/T}$ can reveal detailed information about electronic structure that is not evident at higher temperatures or lower fields. By high $\boldsymbol{B/T}$ one mean field high enough and temperatures low enough such that $\boldsymbol{h\omega_c >> k_BT.}$ The investigated samples must be clean enough to assure the additional condition $\boldsymbol{h\omega_c >> k_B\, T_D}$ (in our case, we determined a decrease in the Dingle temperature $\boldsymbol{T_D}$ during deformation). When both of these conditions are satisfied appearance of the doublet structures is the direct consequence of the high harmonic content of the Shubnikov-de Haas oscillations and quantitative information on the $\boldsymbol{g}$-factor and spin polarization can be obtained from experimental measurements as indicated in [1]. Our qualitative estimates of the g-factor for electrons are consistent with the results on deformed Bi samples presented by the authors in [2].

[1] D. Shoenberg. Magnetic oscillations in metals / Translated from English. edited by M. I. Kaganov. - Moscow: Mir, 1986. - 680 p.
[2] Yuki Fuseya, Zengwei Zhu, Benoıt Fauquue,Woun Kang, Bertrand Lenoir, and Kamran Behnia. *Phys. Rev. Lett*. **115** (2015) 216401.

OBSERVATION OF RESONANT PHOTOLUMINESCENCE FROM DEEP ENERGY CONTINUUM OF LAYER SEMICONDUCTOR InSe

D. P. Dvornikov[1,*], A.V. Siminel[2]
[1]*Ghitu Institute of Electronic Engineering and Nanotechnologies, Technical University of Moldova, Chisinau, Rep. of Moldova;*
[2]*Institute of Applied Physics, Moldova State University, Chisinau, Republic of Moldova.*
[*]E-mail: dmitri.dvornikov@iien.utm.md

The layered semiconductor InSe is considered a promising material for modern microelectronics and nanophotonics due to its bandgap tuning (from 1.26 eV to 2.0 eV) and *direct-to-indirect* bandgap structure crossover when transitioning from bulk crystal to monolayers, high charge mobility in thin layers, and high photosensitivity in the near IR range. Due to its two-dimensional nature and specific structure of the valence band, InSe exhibits unique optical properties, which are manifested, among others, in the features of the photoluminescence spectra.

The observation of hot photoluminescence of InSe caused by transitions from states located deep in the conduction and valence bands at distances comparable with the semiconductor's fundamental band gap value is reported. At excitation of InSe samples by 405 nm linearly polarized light directed along the c-axis, two distinct emission lines were observed in the 2.4–2.5 eV range (Fig.1). With increasing temperature, the intensity of the 2.45 eV line decreases and at temperatures above 100 K it disappears completely. The position and intensity of this line vary significantly between samples and the corresponding analogue is absent in the absorption. This apparently indicates that it is associated with defects or impurities, which, however, have the specificity that their levels are located deep in the region of the continuous spectrum, exceeding the edge of intrinsic absorption by an amount of the order of the band gap. As for the 2.53 eV line, its position and intensity remain constant in all samples within the experimental error. As the temperature increases above 77 K, a relatively weak broadening is observed without a significant decrease in intensity up to room temperature, while the integrated intensity at 300 K is only about 2.5 times lower than at liquid nitrogen temperature. The 2.53 eV line observed in the emission completely correlates with the corresponding peak deep in the region of InSe intrinsic absorption [1]. The resonant behavior of 2.53 eV line undoubtedly indicates the exciton nature of the observed radiation. The type of critical point in the band structure of the semiconductor with which this exciton is associated can be more consistently interpreted in terms of the formation deep within the conduction-valence band energy continuum of semiconductors with a layer structure (such as InSe and GaSe) of exciton states with an ultra-high binding energy of about 320 meV [2], the so-called hyperbolic excitons. This phenomenon is directly related to the specific anisotropy of the effective masses and band structure of the layered crystals.

[1] I. Savchuk, N. P. Gavaleshko, G. D. Delevsky, Z. D. Kovalyuk. *Ukr. J. Phys.* **17(9)** (1972) 1548-1552.
[2] V.K.Subashiev, Le-khac-Binh; L.S. Chertkova. *Solid State Comm.* **9(6)** (1971) 369-372.

STRUCTURAL, VIBRATIONAL AND OPTICAL PROPERTIES OF $Ag_2(Zn,Cd)(Sn,Ge)S_4$ THIN FILMS SUBJECTED TO THERMAL ANNEALING

V. Batîr[1,*], I. Anefnaf [2], S. Aazou[3], N. Curmei[1], L. Dermenji[1], Z. Sekkat[4], E. Arushanov[1] and M. Guc[5]

[1]*Moldova State University, Institute of Applied Physics, Academiei Str. 5, MD-2028 Chisinau, Republic of Moldova;* [2]*CEMHTI (UPR 3079, CNRS) Université d'Orléans 1 AV. de la Recherche Scientifique, France;* [3]*Department of Chemistry, Faculty of Sciences, Mohammed V University in Rabat, Morocco;* [4]*Chair of Optical Sciences and Photonics, University Mohammed VI Polytechnic, Benguerir, Morocco;* [5]*Catalonia Institute for Energy Research (IREC), C/Jardins de les Dones de Negre 1, Sant Adria` de Beso`s, Barcelona 08930, Spain*

*E-mail: batir.valentin@usm.md

Quaternary Ag-based chalcogenides Ag_2ZnSnS_4 (AZTS), Ag_2ZnGeS_4 (AZGS), Ag_2CdSnS_4 (ACTS) and Ag_2CdGeS_4 (ACGS) are being explored as wide-gap analogues of the kesterite absorber Cu_2ZnSnS_4, in which the larger Ag^+ cation is expected to raise the formation energy of the Cu_{Zn} antisite defects responsible for the open circuit voltage deficit of Cu-based kesterite solar cells [1]. Additionally, literature value of the AZTS optical gap is ~1.5 eV [2], while the wurtz-kesterite ACTS phase exhibits a gap near 1.93 eV [3], making these compounds attractive for tandem, indoor and semitransparent applications.

Chemical spray pyrolysis was employed to deposit AZTS, AZGS, ACTS and ACGS thin films (150–800 nm), owing to its low cost and simplicity. Since post-deposition annealing strongly governs stoichiometry and phase formation, understanding this process is essential for optimizing quaternary chalcogenide photovoltaic performance.

EDS analysis showed that annealing shifts most cation ratios further from unity relative to as-deposited films. In AZTS, AZGS and ACGS, both the Ag/(II+IV) and II/IV ratios increase, indicating growing cation imbalance. ACTS behaves differently: its Ag/(Cd+Sn) ratio decreases toward unity, while Cd/Sn still increases, making it the only compound approaching more balanced stoichiometry. Overall, annealing enhances non-stoichiometry in most investigated films.

Raman spectroscopy showed the presence of the quaternary phase only in the as-deposited AZTS sample, while the other films were characterized by the presence of binary and ternary secondary phases. For the AZTS sample, a dominant Raman peak was detected at 342 cm^{-1}, accompanied by weaker peaks located at 220, 264 and 371 cm^{-1}. The main peak at 342 cm^{-1} is close to 338 cm^{-1} A-mode reported for magnetron sputtered AZTS films [2], confirming the kesterite-related vibrational signature, with a slight upshift relative to the literature value.

UV-Vis transmission measurements and Tauc-plot analysis performed before and after annealing gave optical gaps significantly lower than reported values. These downshifts likely arise from the presence of SnS and Ag_2GeS_3 secondary phases, exhibiting gaps of 1.07 eV [4] and 1.30 eV [5], respectively, close to values obtained for the investigated samples. This conclusion is supported by Raman measurements, which indicate the quaternary phase only in the as-deposited AZTS sample, while EDS analysis suggests compositional off-stoichiometry.

[1] J. Li, D. Wang, X. Li, et al. *Adv Sci*. **5** (2018) 1700744.
[2] C. Ma, H. Guo, K. Zhang, et al. *Materials Letters*. **186** (2017) 390-393.
[3] E.M. Heppke, S. Berendts, and M. Lerch. *Zeitschrift für Naturforschung B*. **75** (2020) 393-402.
[4] J. Vidal, S. Lany, M. d'Avezac, et al. *Appl Phys Lett*. **100** (2012) 032104.
[5] A.H. Reshak, S. Auluck, M. Piasecki, et al. *Spectrochimica Acta Part A: Molecular and Biomolecular Spectroscopy*. **93** (2012) 274-279.

RADIATIVE PROPERTIES OF NANOSIZED ZnO:Ag POWDERS

N. Nedeoglo[1,*], T. Goglidze[1], E. Goncearenco[2], V. Sirkeli[1], D. Nedeoglo[1]
[1]*Faculty of Physics and Engineering, Moldova State University, Chișinău, Republic of Moldova;*
[2] *National Institute for Lasers, Plasma and Radiation Physics, Bucharest-Măgurele, România*
*E-mail: natalia.nedeoglo@usm.md

Photoluminescence (PL) spectra of a series of ZnO:Ag powders with various concentrations of doping impurity (between 102 and 252 mg of $AgNO_3$ salt), obtained by chemical deposition from aqueous solution, have been studied in the wavelength range between 360 and 750 nm under various excitation energies. Ultraviolet (UV) emission with maximum at 380 nm is attributed to Ag_{Zn} acceptor-bound excitons, violet (400 – 450 nm) and yellow-orange (560 – 600 nm) emission are due to recombination of non-equilibrium charge carriers within donor-acceptor pairs (Fig. 1). Al_{Zn}, Ga_{Zn}, In_{Zn} substitutional defects and Li_i, Zn_i interstitial atoms may be the donors. V_{Zn} native defects or V_{Zn}-based associative centres and Ag_{Zn} substitutional defects may be the acceptors. As excitation energy decreases, self-absorption of the short-wavelength violet emission and energy transmission to the centers of the long-wavelength yellow-orange emission (570 nm) is observed. The UV band position, unchanged under UV excitation from 250 to 350 nm, shifts to 370 nm under excitation with visible light of 580 nm (Fig. 1, inset).

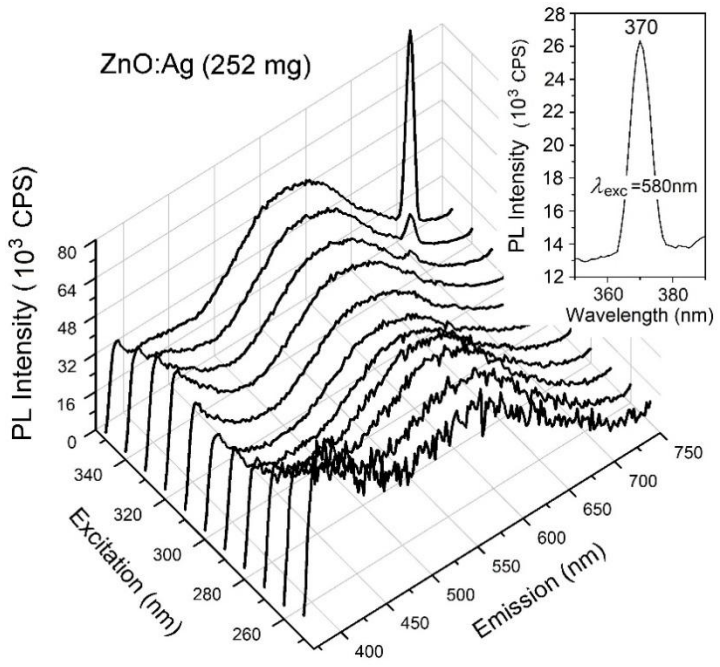


Figure 1. PL spectra of ZnO:Ag powder. λ_{exc}=(250–350) nm. T=300 K. Inset: λ_{exc}=580 nm.

PL excitation spectra between 300 and 700 nm of excitation wavelength have been registered for all PL band maxima. Of particular note is the appearance of PL excitation bands at wavelength value exceeding that for corresponding PL band (Fig. 2). Thus, anti-Stokes luminescence occurs, when PL spectrum shifts towards short-wavelength region relative to PL excitation spectrum, i. e. emitting photon energy is higher than that of absorption photon, the difference being equal to the phonon energy. The presence of several maxima in PL excitation spectrum for every PL band indicates excitation by subsequent resonance energy transmissions to luminescence center from several sensitization centers, so-called cooperative sensitization. In II-VI semiconductors, namely Ag and Cu are sensitization centers. With increasing PL band maximum wavelength, the PL excitation bands also shift towards long-wavelength region.

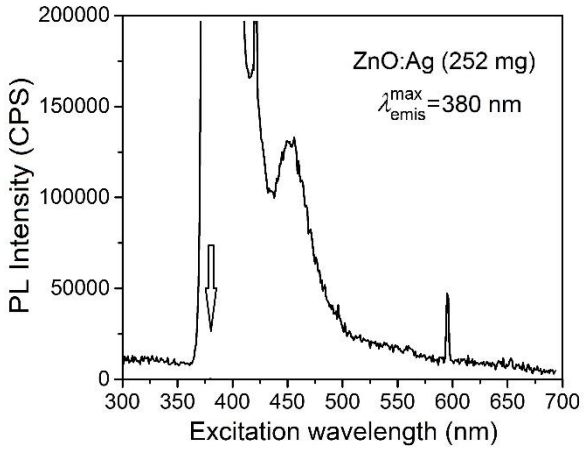


Figure 2. PL excitation spectrum for ZnO:Ag nanopowder. T = 300 K.

ACKNOWLEDGEMENTS. The presented study is carried out within projects 011207 and 011208 by Ministry of Education and Research of the Republic of Moldova.

EFFECT OF SYNTHESIS ATMOSPHERE ON STRUCTURAL AND TRANSPORT PROPERTIES OF $(Ag_xCu_{1-x})_2ZnSnS_4$ SOLID SOLUTIONS

V. Batîr[1,*], D. Usenco[1], N. Curmei[1], L. Dermenji[1], K. G. Lisunov[1,2], E. Arushanov[1]
[1]*Moldova State University, Institute of Applied Physics, Academiei Str. 5, MD-2028 Chisinau, Republic of Moldova;*
[2]*Lappeenranta University of Technology, PO Box 20, FIN-53851 Lappeenranta, Finland*
*E-mail: batir.valentin@usm.md

Kesterite-type compounds like Cu_2ZnSnS_4 (CZTS) attracted attention owing to their favorable photovoltaic properties and the abundance and low toxicity of their elements. However, the efficiency of kesterite based solar cells remains limited by deep intrinsic defects, mainly Cu_{Zn} antisites, creating a defect acceptor band within the material band gap. Partial Cu substitution by Ag has been proposed to suppress this disorder [1]. The synthesis atmosphere is also expected to strongly affect defect chemistry and charges transport, motivating the present study.

Here, we investigate the effect of the synthesis atmosphere on the cationic ratios and on the resistivity, $\rho(T)$, of $(Ag_xCu_{1-x})_2ZnSnS_4$ thin films, prepared by chemical spray pyrolysis under four atmospheres: CO_2 (S1 sample), N_2 (S2 sample), Ar (S3 sample) and air (S4 sample). The composition of samples was determined by X-ray Fluorescence (XRF), while $\rho(T)$ dependence was measured within $T \sim 20$ - 290 K.

XRF analysis revealed an insignificant variation of ratio Ag/(Ag+Cu) ≈ 0.21 - 0.25, for S1 - S4 samples. Also, the ratio (Ag+Cu)/(Zn+Sn) ≈ 0.87 - 0.98 indicates a nearly stoichiometric, slightly Cu-poor lattice for all atmospheres, while Zn/Sn varies noticeably with synthesis conditions from ~ 0.94 to ~ 1.27 values. These trends indicate that the atmosphere modifies the relative Zn/Sn incorporation without strongly affecting the overall Ag/Cu balance.

The resistivity of all films exhibits a strongly activated character. Within the higher-temperature intervals $\Delta T_n \approx 256$ - 286 K, 125 - 154 K, 132 - 156 K and 89 - 116 K for S1, S2, S3 and S4, respectively, ln(ρ/T) follows the nearest-neighbor hopping (NNH) law, with activation energies $E_a \approx$ 126, 57, 55 and 37 meV, respectively. Within the lower-temperature intervals $\Delta T_M \approx 172$ - 219 K, 129 - 168 K, 125 - 152 K and 74 - 97 K, the data instead follow the Mott law of the variable-range hopping (VRH) conduction, $\ln(\rho T^{-1/4}) \propto (T_0/T)^{1/4}$ [2], from which the width of the density of localized states (DOS) is estimated as $W \approx$ 199, 109, 98 and 61 meV for S1 - S4, respectively. In the rectangular approximation of the DOS, the acceptor concentration ratio $N/N_c \approx$ 0.20, 0.20, 0.21 and 0.10, while the ratio of the localization radius $a/a_0 \approx$ 1.26, 1.25, 1.27 and 1.12, for S1 - S4 samples.

The synthesis atmosphere thus strongly influences the hopping transport parameters: the CO_2-deposited film (S1) exhibits the largest E_a and W values, consistent with the highest disorder and carrier localization, whereas the air-deposited film (S4) shows the lowest values of these parameters, suggesting the least disordered acceptor band among the series. The DOS widths obtained here, $W \approx$ 61 - 199 meV, considerably exceed those reported for Ag-free CZTS single crystals, $W \approx$ 12 - 25 meV [3], likely reflecting the additional cationic disorder introduced by Ag incorporation and the polycrystalline nature of the sprayed films. The mechanism responsible for the atmosphere-dependent transport behavior of the $(Ag_xCu_{1-x})_2ZnSnS_4$ solid solutions will be discussed in detail during the presentation.

ACKNOWLEDGEMENTS. This work was supported by the National Agency for Research and Development of the Republic of Moldova under the project 25.80012.5007.33TC.

[1] A. Guchhait, Z. Su, Y.F. Tay, et al. *ACS Energy Lett*. **1** (2016) 1256–1261.
[2] B.I. Shklovskii, and A.L. Efros, Electronic properties of doped semiconductors (Springer, Berlin, 1984).
[3] E. Lähderanta, M. Guc, M.A. Shakhov, et al. *Journal of Applied Physics*. **120** (2016) 035704.

SYNTHESIS AND CRYSTAL GROWTH OF ALTERMAGNET CANDIDAT $Fe_{2-x}Zn_xMo_3O_8$: COMPOZITION AND STRUCTURAL ANALYSIS

L. Prodan[1], I. Filippova[2], D. Croitori[2], S. Moldovanu[1], S. Shova[3], O. Grendal[4,5], V. Tsurkan[1,2,*]
[1]*Institute of Physics, University of Augsburg, Germany;* [2]*Institute of Applied Physics, Moldova State University, Republic of Moldova;* [3]*"Petru Poni" Institute of Macromolecular Chemistry, Romanian Academy, Romania,* [4]*NTNU Norwegian University of Science and Technology, Norway;* [5]*European Synchrotron Radiation Facility ESRF, France.*
*E-mail: vtsurkan@yahoo.co.uk

We report on synthesis and single-crystal growth of ternary molybdenum iron oxides $Fe_{2-x}Zn_xMo_3O_8$ with substitution of Fe by Zn. These antiferromagnetic materials with strong electronic correlations and polar crystal structure manifest a large number of unconventional physical phenomena [1-3] due to concurrent broken time- and space-inversion symmetry and are considered recently as potential altermagnet candidates [4,5].

Synthesis of pure and Zn –substituted polycrystalline powder was performed by conventional solid state method in closed quartz ampolules at 1000 ºC. As starting materials, high-purity binary oxides MoO_2, FeO and ZnO were used. At least three repeated sinterings were necessary to reduce the amount of non-reacted oxides below 5 %. The single-crystal growth was performed by the chemical transport reactions using the synthetisized powder and anhydrous $TeCl_4$ as the transport agent. The growth was done in the temperature gradient of 50°C with the hot end of the quartz ampoule at 950°C. Single crystalline samples with dimension up to 7-9 mm in the *ab*-plane have been obtained after one-month transport (Fig. 1).

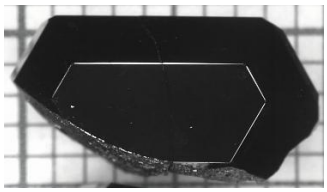


Figure 1. Optical image of as-grown $Fe_{2-x}Zn_xMo_3O_8$ single crystal on a mm greed (x_N = 0.1).

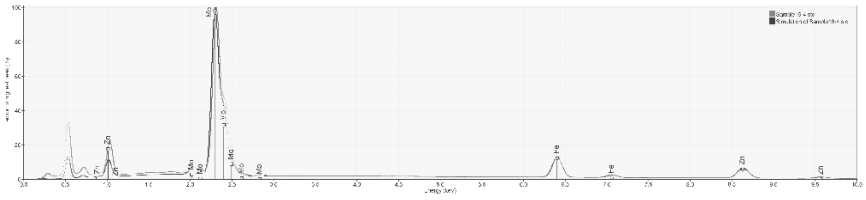


Figure 2. Raw and quantized EDS spectra for single crystalline sample with nominal substitution x_N = 1.0.

Structural analysis of polycrystals was done using high-resolution XRD data collected at the ID22 beamline of the European Synchrotron Radiation Facility (ESRF, Grenoble) utilizing the multi-analyzer detector setup. The structural refinement was done by Jana2006 program. The analysis revealed the simultaneous presence of Zn on both tetrahedral and octahedral sites that was not considered in previous studies of this system.

The composition of as grown single crystals was analyzed by EDS using SEM "TESCAN VEGA" with Si(Li) detector. The quantification of the EDS data was done by NIST DTSA-II-Neptune program (Fig.2). The composition analysis established significant deviations of the real concentration of Zn in samples compared to nominal one x_N, particularly high for the substitution level x <1.0. These data are in agreement with our earlier finding for related $Co_{2-x}Zn_xMo_3O_8$ system [3].

The above results demonstrate that the realistic modelling the substitutional disorder in $M_2Mo_3O_8$ (M = Fe, Co, Mn) must take into account the real concentration of Zn and the presence of Zn ions on both, tetrahedral and octahedral sites.

[1] S. Ghara, *et al*., *Nat. Commun.* **14** (2023) 5174.
[2] D. Szaller, *et al*., *Phys. Rev. B* **111** (2025) 184404.
[3] L. Prodan, *et al*., Phys. Rev. B **106** (2022) 174421.
[4] S.-W. Cheong and F.-T. Huang, *npj Quantum Materials* **9** (2024) 13.
[5] Chen *et al*, Nature **640** (2025) 349.

PROSPECTS OF CHEMICAL VAPOR TRANSPORT FOR SINTERING OF $ZnO_{1-x}Se_x$ ALLOYS

I. Inculet[1], M. A. Koltsov[2], S. Moldovanu[1], N. Spalatu[2], G. V. Colibaba[1,*]
[1]*Moldova State University, Institute of Applied Physics, Chisinau, Moldova*
[2]*Tallinn University of Technology, Department of Materials and Environmental Technology, Estonia*
*E-mail: GKolibaba@yandex.ru

$ZnO_{1-x}E_x$ (E = S, Se, Te) ternary alloys have emerged as promising multifunctional semiconductors due to their tunable band gap, environmental compatibility, and wide applicability in optoelectronic, photocatalytic, and spintronic devices. [1–3]. These material systems also demonstrate versatility in synthesis, as it has been successfully fabricated via pulsed laser deposition, metalorganic chemical vapor deposition, non-alkoxide sol-gel routes, as well as co-precipitation method [1, 4–6]. However, for many methods, corresponding coatings have relatively low structural perfection and conductivity. Magnetron sputtering is a relatively simple and cost-effective method to produce thin films, but ceramic targets with high uniformity and density are required for this technology. Recently, chemical vapor transport (CVT) has been successfully used to sintering ZnO ceramics [7], and ZnO_xS_{1-x} alloys [8]. CVT ceramic targets can be operated at high magnetron power, contributing to high structural perfection and conductivity of thin films [8, 9]. The development of CVT technology for $ZnO_{1-x}Se_x$ ceramics and thin films with controllable electrical properties is of great interest.

The sintering of $ZnO_{1-x}Se_x$ alloys (x = 0 – 50 %) by the CVT method using ZnO:Ga_2O_3 (1 mol%) + ZnSe mixed micropowders and HCl + H_2 as a transport agent has been developed. CVT ceramics were sintered in sealed quartz chambers at 950 °C for 24 h. For comparative analyses, classical ceramic samples sintered in a vacuum under the same conditions were also obtained. To characterize the synthesized composites, XRD, SEM, EDX and Hall measurements were carried out.

The advantages of the CVT sintering method are as follows: (i) low sintering temperature ~950°C, instead of conventional temperatures of about 1500°C; (ii) the use of simple micropowders as a source of material (particle size of 10–100 μm); (iii) minimal losses of the sintered material, including chalcogenides; (iv) minimal deviation of the ceramics diameter; (v) higher conductivity (by 1–2 orders of magnitude) due to better solubility of Ga impurity and stoichiometric deviation (oxygen / selenium vacancies and interstitial zinc).

ACKNOWLEDGEMENTS. This work was supported by the Ministry of Education, Culture and Research of Moldova under the project No. 011201 (Functional 2D and 3D oxychalcogenic materials, metals and polymers with advanced magnetic, photoelectric, optical and bioactive properties for applications in spintronics, optoelectronics and biomedicine) in collaboration with project No. 26.00208.5007.10/PD (Engineering highly conductive semiconductors based on complex chemical transport reactions)

[1] S. Polivtseva et al. *ACS Appl. Energy Mater.* 1 (2018) 6505
[2] L-Y. Lin et al., *Chin. Phys. Lett.* 33 (2016) 107801
[3] O. Aguilar-Martinez et al., *Renewable Energy*. 113 (2017) 43e51
[4] K. Lee et al., *Curr. Appl. Phys.* 19 (2019) 14
[5] J. Mena Arenas et al. *J. Phys.: Conf. Ser.* 1247 (2019) 012002
[6] P. Verma et al. *Physica B.* 404 (2009) 3894
[7] G.V. Colibaba et al. *J. Eur. Ceram. Soc*. 41 (2021) 443
[8] G.V. Colibaba et al. *Phys. Solid State*. 67 (2025) 961
[9] G.V. Colibaba et al. *Physica Scripta*. 99 (2024) 105967

COMPARATIVE ANALYSIS OF ENERGY TRANSFER AND RADIATIVE RECOMBINATION PROCESSES IN $ZnIn_2S_4$ AND $CdIn_2S_4$ SINGLE CRYSTALS STUDIED BY LUMINESCENCE SPECTROSCOPY

V. Pintea[1], E. Arama[2], T. Shemyakova[3,*]
[1]*Technical University of Moldova, Chisinau, Republic of Moldova*
[2]*„Nicolae Testemitanu" State University of Medicine and Pharmacy, Chisinau, Republic of Moldova*
[3]*Institute of Applied Physics, State University of Moldova, Chisinau, Moldova*
*E-mail: tatiana.shemyakova@ifa.md

This work presents a comparative analysis of the photoluminescence, cathodoluminescence, and X-ray induced luminescence properties of single crystals of ternary semiconductor compounds $ZnIn_2S_4$ and $CdIn_2S_4$. The influence of the excitation method on the position of the emission maxima, the full width at half maximum (FWHM) of the luminescence bands, and the mechanisms of energy transfer to the luminescence centers are analyzed. The experimental results show that X-ray excitation involves the entire volume of the crystal, in contrast to photoluminescence and cathodoluminescence, where the excitation processes are confined to more restricted regions. It was established that the differences between the spectral parameters of the two compounds are determined by the particularities of the electronic structure, the distribution of crystal defects, and the nature of the divalent cation. The comparative analysis demonstrates that structural defects act not merely as nonradiative recombination centers but are also actively involved in the energy transfer to the luminescence centers.

Comparison of the spectral characteristics of the $ZnIn_2S_4$ and $CdIn_2S_4$ single crystals shows that, although the two materials belong to the same class of ternary sulfide compounds and exhibit similar crystal structures, their luminescence properties are significantly influenced by the nature of the divalent cation. Substitution of the Zn^{2+} ion by Cd^{2+} leads to changes in the crystal lattice parameters, in the distribution of the electronic states, and in the position of the defect-related energy levels, which is directly reflected in the spectral parameters of the emission. An important criterion for the comparative analysis is the position of the emission band maximum. For the $CdIn_2S_4$ single crystals, the X-ray luminescence spectrum at room temperature shows an energy maximum located at approximately 2.00 eV, with a spectral structure characterized by a broad band. In the case of the $ZnIn_2S_4$ single crystals, the position of the emission maximum is different, indicating a change in the energy of the radiative recombination processes as a result of the change in the nature of the metal ion in the cation sublattice. The shift in the position of the emission bands can be explained by the differences between the electronic configurations of the Zn^{2+} and Cd^{2+} ions, as well as by their influence on the energy band structure of the semiconductor.

Based on the experimental results, a general model of the charge carrier generation and transport, as well as a radiative recombination mechanism are proposed, capable of describing the luminescence processes in both investigated materials. The proposed energy transfer model accounts for the experimental differences observed among photoluminescence, cathodoluminescence, and X-ray luminescence, as well as for the specific features of the emission spectra of the two compounds studied. The results obtained show that tailoring the chemical composition through the substitution of Zn^{2+} ions with Cd^{2+} ions is an effective way of tuning the luminescent properties. This is a finding of practical importance for the development of materials for X-ray detectors, scintillator screens, and other optoelectronic applications. These findings contribute to the understanding of the fundamental luminescence mechanisms in ternary sulfides and may help to optimize materials for X-ray detectors and scintillator screens.

STRUCTURAL, OPTICAL AND ELECTRICAL PROPERTIES OF $(ZnO)_k \cdot Ga_2O_3$ CERAMICS AND THIN FILMS

D. Rusnac[1], N. Spalatu[2], G.V. Colibaba[1,*]
[1]*Moldova State University, Institute of Applied Physics, Chisinau, Moldova*
[2]*Tallinn University of Technology, Department of Materials and Environmental Technology, Estonia*
*E-mail: GKolibaba@yandex.ru

High-power magnetron sputtering is one of the most reproducible methods for the deposition of ZnO thin films with high structural perfection [1]. ZnO-based alloys are of high practical interest due to the variation of chemical, optical and electrical properties [2]. The aim of the present work is to investigate the structural, optical and electrical properties of $(ZnO)_k \cdot Ga_2O_3$ alloys deposited by magnetron sputtering.

$(ZnO)_k \cdot Ga_2O_3$ ceramic alloys (k = 6 – 200) have been obtained by conventional sintering in air at 1050°C for 48 h [3]. To characterize the synthesized composites, XRD, SEM, EDX and Hall measurements were carried out. Thin films of $(ZnO)_k \cdot Ga_2O_3$ were deposited on glass substrates by DC magnetron sputtering, employing the obtained ceramic samples as sputtering targets. High-purity Ar (99.998%) at a pressure of 4×10^{-6} atm was used as the working gas. The substrate-target distance, sputtering current density, and substrate temperature were 5 cm, 40 mA/cm^2, and 100–250 °C, respectively. The resulting films had a thickness of about 500 nm. No post-deposition annealing treatment was applied to any of the films. XRD, SEM, EDX and Hall measurements of obtained coatings were also carried out.

The solubility limit of Ga in ZnO is about 6 at% (k = 67). This concentration corresponds to thin films with the lowest resistivity (5×10^{-4} Ω·cm) and the highest figure of merit (1.5×10^{-2} Ω^{-1}). Increasing the Ga_2O_3 content promotes an increase in the density of $ZnGa_2O_4$ inclusions. This also leads to an increase in the band-gap from 3.3 to 4.4 eV and in the resistivity of thin films to 10^4 Ω·cm.

ACKNOWLEDGEMENTS. This work was supported by the Ministry of Education, Culture and Research of Moldova under the project No. 011201 (Functional 2D and 3D oxychalcogenic materials, metals and polymers with advanced magnetic, photoelectric, optical and bioactive properties for applications in spintronics, optoelectronics and biomedicine) in collaboration with project No. 26.00208.5007.10/PD (Engineering highly conductive semiconductors based on complex chemical transport reactions)

[1] G.V. Colibaba et al. Effect of chlorine on the conductivity of ZnO:Ga thin films. *Journal of Materials Science: Materials in Electronics*. 32 (2021) 18291
[2] G.V. Colibaba. Low-temperature CVT sintering of n-$ZnFe_2O_4$ and n-$Fe_2O_3 \cdot (ZnO)_k$ alloys with controllable stoichiometric deviation and conductivity. *Ceramics International.* 51 (2025) 48823
[3] G.V. Colibaba et al. Low-temperature sintering of highly conductive ZnO:Ga:Cl ceramics by means of chemical vapor transport. *Journal of the European Ceramic Society.* 41 (2021) 443

LOW-TEMPERATURE SINTERING OF $Zn_kIn_2O_{k+3}$ COMPOUND OXIDES BY CHEMICAL VAPOR TRANSPORT

G.V. Colibaba[1,*], S. Moldovanu[1], D. Rusnac[1], N. Spalatu[2]
[1]*Moldova State University, Institute of Applied Physics, Chisinau, Moldova;*
[2]*Tallinn University of Technology, Department of Materials and Environmental Technology, Estonia*
*E-mail: GKolibaba@yandex.ru

The production of coatings based on complex oxides $Zn_kIn_2O_{k+3}$, which are characterized by higher chemical resistance compared to ZnO and lower cost compared to In_2O_3, is of great practical interest.

These ternary alloys are promising multifunctional semiconductors due to their tunable band gap, environmental compatibility, and wide applicability in optoelectronics and photo catalysis. However, the synthesis of such compounds at low temperatures is difficult. The most typical temperatures for sintering $Zn_kIn_2O_{k+3}$ are in the range of 1200-1550°C [1]. Magnetron sputtering is a relatively simple and cost-effective method to produce thin films, but ceramic targets with high uniformity are required for this technology. Chemical vapor transport (CVT) has been successfully used to sintering ZnO [2], ITO [3], and various compound oxides, for example $ZnFe_2O_4$ [4]. CVT ceramic targets can operate at high magnetron power, which improves the structural perfection and conductivity of thin films [5]. Halogens dissolved in the ceramics promote better incorporation of impurities into the crystal lattice of coating [6]. The development of low-temperature CVT technology for $Zn_kIn_2O_{k+3}$ ceramic targets with high uniformity and conductivity is of great interest.

The sintering of $Zn_kIn_2O_{k+3}$ compound oxides (k = 3–11) by the CVT using ZnO + In_2O_3 + SnO_2 (as dopant) mixed micropowders and HCl as a transport agent has been developed. CVT ceramics were sintered in sealed quartz chambers at 950°C for 24 h. Classical ceramic samples sintered in air under the same conditions were also obtained for comparative analyses. XRD, SEM, EDX and Hall measurements were carried out to characterize the synthesized composites.

kZnO×ITO ceramics sintered in air at 1050°C are predominantly a mixture of ZnO + In_2O_3 + SnO_2. The resistivity of such materials is relatively high, exceeding 10^6 Ω·cm, even at a relatively high Sn impurity concentration of up to 4 at%. The use of HCl in the synthesis of such complex oxides has a remarkable effect. This allows to obtain a material consisting of a pure $Zn_kIn_2O_{k+3}$ phase and the almost complete dissolution of the SnO_2 dopant. The high homogeneity of the obtained material, effective Sn doping, the presence of residual Cl impurity, and the stoichiometric deviation caused by the presence of hydrogen in the sintering medium (Zn and In excess) reduce the resistivity of these ceramics by 4 orders of magnitude.

ACKNOWLEDGEMENTS. This work was supported by the Ministry of Education, Culture and Research of Moldova under the project 25.80013.5007.10RE (Strategic vision for the development of scalable thin-film technologies in niche photovoltaic markets) in collaboration with project No. 26.00208.5007.10/PD (Engineering highly conductive semiconductors based on complex chemical transport reactions).

[1] T. Moriga, et al. Phase relationships and physical properties of homologous compounds in the Zinc Oxide–Indium Oxide system. *J. Am. Ceram. Soc.* 81 (1998) 1310
[2] G.V. Colibaba. Sintering highly conductive ZnO:HCl ceramics by means of chemical vapor transport reactions. *Ceram. Int*. 45 (2019) 15843
[3] G.V. Colibaba et al. Low-Temperature CVT sintering of In_2O_3:Sn ceramics. *Phys. Solid State*. 67 (2025) 879
[4] G.V. Colibaba. Low-temperature CVT sintering of n-$ZnFe_2O_4$ and n-Fe_2O_3·$(ZnO)_k$ alloys with controllable stoichiometric deviation and conductivity. *Ceram. Int*. 51 (2025) 48823
[5] G.V. Colibaba et al. Effect of chlorine on the conductivity of ZnO:Ga thin films. *Journal of Materials Science: Materials in Electronics*. 32 (2021) 18291
[6] G.V. Colibaba et al. ZnO thin films co-doped with III-valence metals and halogens: theory and experiment. *Physica Scripta* 99 (2024) 105967

QUANTUM NEMATIC TRANSITION IN THE $EuMe_2Pn_2$ COMPOUNDS

A. Nateprov[1,*], Yu. Goryunov[2]
[1]Institut of Applied Physics, Moldova State University, Chisinau, Moldova,
[2]Zavoisky Phys-Tech Institute, FRC Kazan Scientific Center of RAS, Kazan, Russia
*E-mail: Alexandr.Nateprov@phys.asm.md

Relative recently, magnetic layered systems have attracted attention as spin nematics [1], which exist in a specific region of the T-H diagram [2,3]. We have studied the magnetic properties of compounds $EuMe_2Pn_2$ (Me = Zn, Cd, Fe; Pn = P, As, Sb) by ESR. At the temperature decreasing well before the antiferromagnetic order we have observed an increasing of lineswidth and a decreasing of the resonance fields, which in our case is very good described by the Landau theory of magnetic fluctuations. However, the paramagnetic temperature $\boldsymbol{\theta}_{c\text{-}w}$ obtained from the temperature dependence of the ESR signal intensity, has the positive sign. We believe that such behaviour of $\boldsymbol{\theta}_{c\text{-}w}$ is connected with the proximity to the quantum critical point and with the relevant instability of magnetic and crystal structures. So, the intermetalic pnictides have the trigonal $CaAl_2Si_2$-type structure (space group $P\bar{3}m1$) or the tetragonal $ThCr_2Si_2$-type structure (space group I4/mmm) and it causes the instability of Me_2Pn_2-layers and, a competition between nonmagnetic $4f^6$ and magnetic $4f^7$ states of Eu. Eu -ions have nonintegral valence, g-factor substantially not equal 2.0 and spins are stacked in layers by various means.

Comparison of the behavior of the Curie paramagnetic temperature and the antiferromagnetic odering temperature with the changes in the composition of those compounds indicates on the presence of quantum critical point in those ternary systems. With an increase in the lattice constant and a change of the concentration of free electrons, the transition temperature T_A into the nematic phase became lower than the Neel temperature ($T_A \sim \boldsymbol{\theta}_{c\text{-}w} < T_N$) and the situation returns to the normal case. Thus, a quantum phase transition takes place in the $EuMe_2Pn_2$ ternary systems.

1. A.F. Andreev, I.A. Grishchuk, *J. Exp. Theor.Phys.*, **60**(2), 267 (1984)
2. G. Beaudin, L.M. Fournier, A.D. Bianchi, M. Nicklas, M. Kenzelmann, M. Laver, W. Witczak-Krempa. *Phys. Rev.B*, 105, 035104 (2022)
3. Ya. Yu. Matyunina, O. A. Kosmachev, Yu. A. Fridman, *Phys. of Metals and Metallography*, **125**(5), 463 (2024)

FEATURES OF BI_2S_3 CRYSTAL GROWTH

G.V. Colibaba[1,*], M.A. Koltsov[2], N. Spalatu[2]
[1]*Moldova State University, Institute of Applied Physics, Chisinau, Moldova;*
[2]*Tallinn University of Technology, Department of Materials and Environmental Technology, Tallinn, Estonia.*
*E-mail: GKolibaba@yandex.ru

Bismuth sulfide (Bi_2S_3, bismuthinite) is an orthorhombic (Pnma) semiconductor with a direct bandgap of about 1.3 eV, a quasi-one-dimensional ribbon-like crystal structure, and earth-abundant, comparatively non-toxic constituents – features that have motivated investigation across a broad range of applications, from photovoltaics and thermoelectrics to sodium-ion batteries, electrocatalytic CO_2 reduction, gas sensing, photothermal cancer therapy, and solid lubricant coatings [1–3]. The growth of dense, high-quality single crystals remains challenging due to sulfur volatility.

We present a systematic study of Bi_2S_3 crystal growth by physical vapor transport (PVT), chemical vapor transport (CVT), and the Bridgman method, supported by thermodynamic calculations of phase equilibria. Of the six transport agents evaluated (Cl_2, Br_2, I_2, HCl, HBr, HI), HI provides the densest growth medium and high mass transport efficiency, increasing the mass transport rate tenfold compared with PVT. Nevertheless, vapor-grown crystals remain impractically small and elongated. Bridgman growth yields large ingots, but with porosity of up to 30 vol.% due to sulfur volatilization during solidification. We demonstrate four strategies for minimizing porosity: deviation from stoichiometry, halogen doping, Sn doping, and reduced growth chamber conicity. A method for reducing the porosity below 1% and increasing the grain size to 5 mm is proposed.

ACKNOWLEDGEMENTS. This study was funded by Estonian Research Council project PSG689 (Bismuth Chalcogenide Thin-Film Disruptive Green Solar Technology for Next-Generation Photovoltaics) and by the Ministry of Education, Culture and Research of Moldova under the projects 25.80013.5007.10RE (Strategic vision for the development of scalable thin-film technologies in niche photovoltaic markets) and 26.00208.5007.10/PD (Engineering highly conductive semiconductors based on complex chemical transport reactions)

[1] V. Panwar et al. Ultrahigh Photo-Responsivity and Detectivity in 2D Bismuth Sulfide Photodetector for Vis–NIR Radiation. *Small* 20 (2024) 2309428
[2] M. Koltsov et al. Development of Bi_2S_3 thin film solar cells by close-spaced sublimation and analysis of absorber bulk defects via in-depth photoluminescence analysis. *Solar Energy Materials and Solar Cells* 254 (2023) 112292
[3] K. Biswas et al. Tellurium-Free Thermoelectric: The Anisotropic n -Type Semiconductor Bi_2S_3. *Advanced Energy Materials* 2 (2012) 634

SYNTHESIS OF ACZTS THIN FILMS IN DIFFERENT GAS ATMOSPHERES

L. Dermenji[1], V. Batîr[1,*], N. Curmei[1], V. Zalamai[2], G. Gurieva[3],
D. Podgornîi[1], D. Usenco[1] and E. Arushanov[1]
[1]*Moldova State University, Institute of Applied Physics, Academiei Str. 5, MD-2028 Chisinau, Republic of Moldova;* [2]*National Center for Materials Study and Testing, Technical University of Moldova, 78 31 August 1989 str., MD 2004, Chisinau, Republic of Moldova;* [3]*Helmholtz-Zentrum Berlin für Materialien und Energie, Department Structure and Dynamics of Energy Materials, Hahn-Meitner-Platz 1, D-14109 Berlin, Germany;*
*E-mail: batir.valentin@usm.md

Interest in kesterites Cu_2ZnSnS_4 (CZTS) and kesterite solid solutions is driven by their prospects as materials for solar cells. One such material is the kesterite solid solution $(Cu_{1-x}Ag_x)_2ZnSnS_4$ (ACZTS). In this work, we analyze the effect of the synthesis gas atmosphere on the resulting ACZTS thin films. The synthesis was performed by spray pyrolysis method. Air, CO_2, N_2 and Ar were used as gas atmospheres.

XRD spectra recorded on annealed samples showed that the crystal lattice belongs to space group $I\bar{4}$, with lattice constants $a = b = 5.446$ (Å), $c = 10.823$ (Å) for thin films obtained in CO_2, and $a = b = 5.462$ (Å), $c = 10.847$ (Å) for N_2. The unsplit peak at 47° of 2Θ angle, indicates that the Ag content in thermally annealed samples, does not exceed 0.3 value of the ratio C[Ag]/(C[Ag]+C[Cu]) [1].

The composition of the obtained samples was determined from XRF spectral analysis. For investigated samples, the ratios C[Cu+Ag]/(C[Zn]+C[Sn]) = 0.9 and C[Zn]/C[Sn] = 1.1 were obtained. The annealed samples showed stoichiometric ratios close to those set in the precursors. The spread in composition between annealed and non-annealed samples may result from a non-uniform distribution across the substrate surface [2].

The transmittance and reflectance spectra of the thin films were also studied before and after annealing. From these measurements, the absorption coefficient $\alpha(\lambda)$ and the optical band gap E_g were estimated. The following E_g values were obtained: 1.61/1.46, 2.17/1.47, 2.27/1.58 and 2.34/1.39 for CO_2, Air, Ar and N_2, before/after annealing, respectively. The spectra show that for the CO_2 samples the E_g value is minimal and closest to that expected for single crystals, unlike the samples obtained in the other gas atmospheres.

The specifics of thin-film deposition allow for the presence of both secondary phases and amorphous state of the target compound, which usually changes E_g, toward higher values [3]. However, after annealing, recrystallization removes most of the secondary phases and orders the structure, as confirmed by the XRD spectra and by E_g values of the annealed samples.

ACKNOWLEDGMENTS. This work was supported by the National Agency for Research and Development of the Republic of Moldova under the project 25.80012.5007.33TC and by the Ministry of Education and Research of the Republic of Moldova under research sub-programme 011201.

[1] W. Gong, T. Tabata, K. Takei, et al. *Phys Status Solidi C*. **12**, (2015) 700–3.

[2] L. Dermenji, N. Curmei, M. Guc, et al. *Surf Engin ApplElectrochem*. **52**, (2016) 509–14.

[3] J. Yang, J. Xu, D. Miao, et al. *Physica B: Condensed Matter*. **623**, (2021) 413375.

DESIGN AND SYNTHESIS OF A COPPER (II) COMPOUND WITH N-(4-METHOXYPHENYL)-2-[1-(PYRIDIN-2-YL)ETHYLIDENE]HYDRAZINE-1-CARBOTHIOAMIDE

Aliona Pîntea[1,*], Roman Rusnac[1], Victor Tsapkov[1], Sergiu Shova[2], Aurelian Gulea[1]
[1]*Laboratory of "Advanced Materials in Biopharmaceutics and Technic", Institute of Chemistry, Moldova State University, Chisinau, Republic of Moldova;*
[2]*"Petru Poni" Institute of Macromolecular Chemistry, Alea Grigore Ghica voda 41-A, 700487 Iasi, Romania*
*E-mail: pintea.aliona@usm.md

The *p*-anisidine group ($N^{(4)}$-substituted) present in the ligand structure serves to modulate the lipophilicity of the organic skeleton [1]. By coordinating these ligands to the copper(II) ion, the objective is to reduce the systemic toxicity of the free ligand through the prior fixation of the metal center, while simultaneously generating a new stable chemical entity capable of efficiently penetrating cell membranes and inducing apoptosis via redox-active pathways or the generation of reactive oxygen species [1, 3].
The present study aims to determine the coordination mode of the N-(4-methoxyphenyl)-2-[1-(pyridin-2-yl)ethylidene]hydrazine-1-carbothioamide ligand to the copper(II) ion. To achieve the final result, the syntheses of both the ligand and the coordination compound were performed according to the descriptions in the specialized literature [1, 2], yielding a single crystal that allowed the structural characterization of the coordination compound presented in Figure.

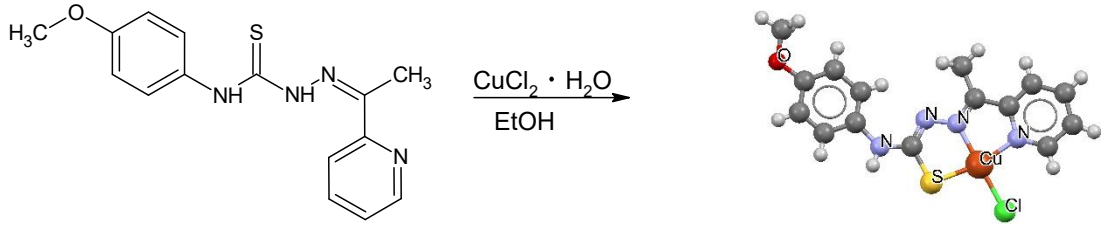


Figure. Structural formula of the ligand and the coordination compound obtained

A new copper(II) coordination compound based on an organic ligand from the heterocyclic thiosemicarbazone class was successfully synthesized and characterized. The data obtained via FT-IR and NMR spectroscopy confirm the tridentate behavior of the ligand, which coordinates through the set of N, N, S donor atoms after deprotonation into its thiol form. The evaluated biological properties show that chelation of the copper(II) ion in the ligand structure amplifies the biological effect, making this coordination compound a promising candidate for further extensive studies.

[1] D.X. West, S.B. Padhye & P.B. Sonawane, Structural and biological studies of thiosemicarbazone complexes of copper(II). *Coord. Chem. Rev.* **123(1-2)** (1993) 49-71.
[2] T.S. Lobana, R. Sharma, G.Bawa & S. Khanna, Transition metal complexes of thiosemicarbazones: positions and prospects. *Coord. Chem. Rev.* **253(7-8)** (2009) 977-1055.
[3] E.W. Ainscough, A.M. Brodie, J.D. Ranford & J.M. Secondary, Cytotoxicity of copper(II) complexes of 2-acetylpyridine thiosemicarbazones. *J. Inorg. Biochem.* **70(3-4)** (1998) 175-185.

SYNTHESIS AND MAGNETIC PROPERTIES OF HEXANUCLEAR {Fe_4Ln_2} CLUSTERS BASED ON CARBOXYLATE AND AMINO-POLYALCOHOL LIGANDS

Daniel Podgornii[1*], Jan van Leusen [2], Victor Ch. Kravtsov [1], Yurii Skourski [3], Paul Kögerler [2], Svetlana G. Baca [1]

[1]*Institute of Applied Physics, Moldova State University, Chisinau, Republic of Moldova.;* [2]*Institute of Inorganic Chemistry, RWTH Aachen University, Germany.;* [3]*Dresden High Magnetic Field Laboratory, Helmholtz-Zentrum Dresden Rossendorf, Germany*

*E-mail: danya.podgornii@gmail.com

Polynuclear Fe–Ln clusters are attractive systems in molecular magnetism due to the combination of magnetic exchange interactions between Fe(III) centers and the strong magnetic anisotropy of lanthanide ions. Herein, we report the synthesi and magnetic investigation of a series of heterometallic $[Fe_4Ln_2O_2(piv)_4(Hteed)_2(NO_3)_4]\cdot 2MeCN$ clusters (Hpiv = pivalic acid; $teedH_4$ = *N′,N′,N″,N″*-tetrakis(hydroxyethyl)ethylenediamnie; Ln = Pr(**1**), Nd(**2**), Gd(**3**), Tb(**4**), Dy(**5**), Ho(**6**)).

The compounds were obtained from the trinuclear precursor $[Fe_3O(piv)_6(H_2O)_3]\cdot$Hpiv, H_4teed, lanthanide nitrates, and auxiliary ligands in acetonitrile under ultrasonic irradiation. Mild reaction conditions reproducibly afforded the desired hexanuclear species, demonstrating the suitability of H_4teed for the assembly of heterometallic Fe–Ln clusters.

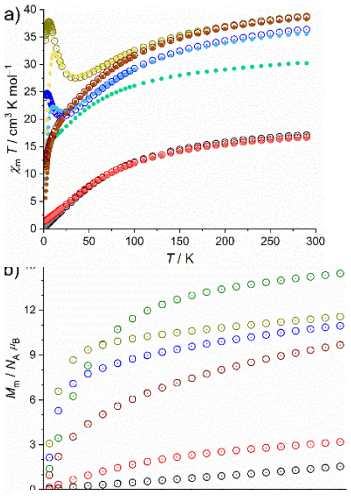


Figure 1. (a) SQUID data of 1–**6** shown as $\chi_m T$ vs. T curves at 0.1 T (open symbols) and 1.0 T (full symbols); b) molar magnetizations M_m vs. applied magnetic fields B at 2.0 K; color code: black (**1**), red (**2**), green (**3**), blue (**4**), yellow (**5**), brown (**6**).

The magnetic properties of compounds **1–6** were investigated by *dc* and *ac* susceptibility measurements. At 290 K, the χ_mT values are lower than those expected for non-interacting Fe(III) and Ln(III) ions, indicating predominant antiferromagnetic exchange interactions within the clusters. Upon cooling, χ_mT decreases for all compounds, consistent with antiferromagnetic coupling and, for the anisotropic lanthanides, depopulation of crystal-field-split m_j states [1,2]. Compounds **4** (Tb) and **5** (Dy) exhibit shallow minima followed by low-temperature maxima in the χ_mT (T) curves, suggesting additional weak ferromagnetic Fe–Ln interactions. Field-dependent magnetization measurements at 2 K show rapid initial increases followed by a gradual approach to saturation. The observed magnetization values are largely determined by the lanthanide ions, while the contribution of the {Fe_4} fragment remains strongly suppressed due to antiferromagnetic exchange. Analysis of the magnetic data suggests antiferromagnetic interactions within the Fe4 unit, with estimated exchange parameters of $J_{side} \approx -7$ to -4 cm^{-1} and $J_{diag} \approx +1$ cm^{-1} [1]. AC susceptibility measurements revealed slow magnetic relaxation for compounds **5** (Dy) and **6** (Ho), whereas compounds **1–4** showed no significant out-of-phase signals above 1.9 K. For compound 5, frequency-dependent χ'' signals were observed below 5 K and could be described by a generalized Debye model [3]. The relaxation process is dominated by quantum tunneling of magnetization (QTM), with a characteristic relaxation time of approximately 2×10^{-5} s [2].

To further probe the low-temperature magnetic behavior, high-field magnetization measurements were performed on compounds 4–6. At 1.5 K, all three compounds display open hysteresis-like magnetization curves characteristic of slow relaxation phenomena. The effect is most pronounced for the Dy analogue (**5**), followed by the Ho (**6**) and Tb (**4**) compounds. These results indicate that the incorporation of anisotropic lanthanide ions leads to slow magnetic relaxation, although only weak single-molecule magnet behavior is observed in this family of clusters [2,4].

ACKNOWLEDGMENTS. This study was supported by the subprogram 011202 financed by the Ministry of Education and Research of R. Moldova and the research project "MultiClust" (01DK25013 and 25.80013.5007.07GER) financed by the German Federal Ministry of Education and Research (BMBF) and the National Agency for Research and Development (NARD)

[1] H. Lueken, *Magnetochemie*, Teubner Verlag, Stuttgart, 1999.

[2] J. D. Rinehart and J. R. Long, *Chem. Sci.*, 2011, **2**, 2078.

[3] R. Werner, S. Ostrovsky, K. Griesar and W. Haase, *Inorg. Chim. Acta*, 2001, **326**, 78.

[4] H. Weihe and H. U. Güdel, *J. Am. Chem. Soc.*, 1997, **119**, 6539.

SYNTHESIS AND XRD STUDY OF SOME α-HEXYLCINNAMALDEHYDE THIOSEMICARBAZONES

A. Ciursin[1,*], R. Rusnac[1], G. Ghilețchii[2], S. Vatavu[2], A. Gulea[1]
[1]*Laboratory of Advanced Materials in Biopharmaceutics and Technics, Institute of Chemistry, Moldova State University, 60 Mateevici Street, MD-2009 Chisinau, Republic of Moldova;*
[2]*Physics of Semiconductors and Devices Lab, Faculty of Physics and Engineering, Moldova State University, 2009 Chisinau, Republic of Moldova*
*E-mail: ciursin.andrei@usm.md

Thiosemicarbazones represent an important class of organic compounds that have attracted significant attention owing to their diverse biological activities, including antioxidant, antibacterial, antifungal, and anticancer activity. A contemporary strategy in thiosemicarbazone research involves the incorporation of specific structural fragments or the functionalization of naturally occurring compounds. Such modifications frequently result in reduced toxicity while maintaining or even enhancing the biological potential of these derivatives. In this context, a series of thiosemicarbazones derived from α-hexylcinnamaldehyde was synthesized and investigated in the present study.

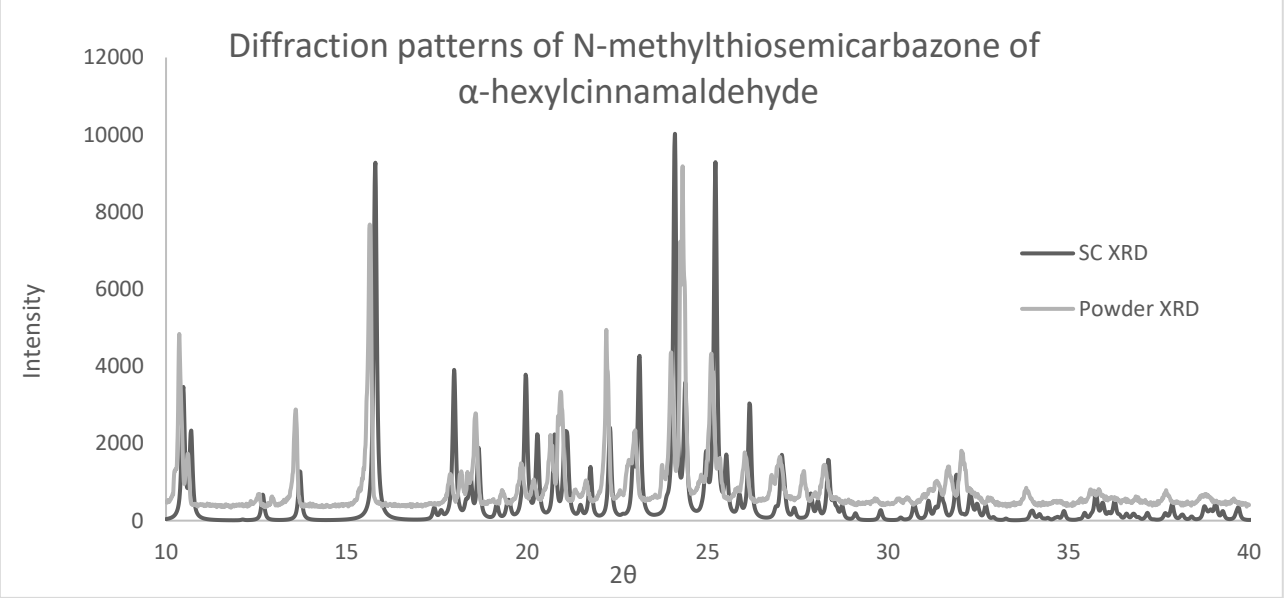


Figure. X-ray diffraction patterns of N-methylthiosemicarbazone of α-hexylcinnamaldehyde

To obtain the desired thiosemicarbazones, 4-allylthiosemicarbazide and 4-methylthiosemicarbazide were condensed with α-hexylcinnamaldehyde. The reactions were carried out under reflux in ethanol for approximately 6 h, using glacial acetic acid as a catalyst. In both cases, upon completion of the reaction, as determined by thin-layer chromatography, a solid precipitated upon cooling. The resulting products were isolated by filtration and washed with cold ethanol. The structures of the synthesized compounds were confirmed by NMR and FTIR spectroscopy, as well as by single-crystal X-ray diffraction analysis. Furthermore, powder X-ray diffraction (PXRD) patterns were recorded and compared with those simulated from the single-crystal diffraction data. An example of this comparison is presented in the figure, where the diffraction peaks obtained in both cases are observed to be in nearly perfect agreement.

In conclusion, two α-hexylcinnamaldehyde-derived thiosemicarbazones were successfully synthesized and structurally characterized by NMR, FTIR, and X-ray diffraction techniques. The excellent agreement between the experimental and simulated PXRD patterns confirmed the phase purity of the synthesized compounds and the representativeness of the single-crystal structures for the bulk materials.

SYNTHESIS OF NOVEL MOLECULAR HYBRIDS: 2-(1-ETHYL-2-OXOINDOLIN-3-YLIDENE)HYDRAZONO)-THIAZOLIDIN-4-ONE AND ITS DERIVATIVE BY KNOEVENAGEL CONDENSATION

A. S. Batanov[1,*], N. S. Sucman[1], S. Shova[2], G. Balan[3], E. C. Gorincioi[1], F. Z. Macaev[1]
[1]*Moldova State University, Institute of Chemistry, Chisinau, Moldova*
[2]*Petru Poni Institute of Macromolecular Chemistry, Iasi, Romania*
[3]*Nicolae Testemitanu State University of Medicine and Pharmacy, Chisinau, Moldova*
*E-mail: tci21batanov.alexandr@gmail.com

Thiazolidinone is a well-studied biologically important heterocycle containing sulfur and nitrogen heteroatoms and a carbonyl group at the 2, 4, or 5 positions. 4-Thiazolidinone has been shown to exhibit a large number of biological activities, such as antimicrobial, antituberculosis, antiviral, anti-inflammatory, antidiabetic, anticancer, anticonvulsant, FSH agonist, and CFTR inhibitor [**Error! Bookmark not defined.**].

Using pharmacophore hybrid approach, we considered that, hybridization of two different bioactive fragments, of isatine (**1**) and 4-thiazolidinone with complementary pharmacophoric functions and different mechanisms of action could show potential synergistic effects.

Target compound (**3**) was synthesized in several steps. Firstly, thiosemicarbazone of N-ethylisatin was obtained *via* condensation of N-ethylisatin (**1**) with thiosemicarbazide. In the second step, the reaction of thiosemicarbazone group with monochloroacetic acid in the presence of potash results in the formation of a 4-thiazolidinone ring. The obtained molecular hybrid (**2**) contains an active methylene group that undergoes Knoevenagel condensation with the carbonyl group of anisaldehyde, affording compound (**3**) (Figure 1, A). Structures of the newly synthesized compounds (**2**) and (**3**) were established by modern physicochemical methods. Amino-imino tautomerism was attested in DMSO-d_6 solution for compound **(2)**, by the presence of two singlets at δ 11.69 ppm and 12.51 ppm in the ^{1}H NMR spectrum, which may identify 2-imino-4-thiazolidinone fragment [1]. Presence of the only imine isomer has been confirmed in the ^{1}H NMR spectrum of **(3)**, the corresponding proton resonating at δ 13.06 ppm. The structure of compound **(3)** was definitely confirmed by single crystal X-ray diffraction analysis (Figure 1, B), which has proven that it crystallizes in the triclinic centrosymmetric space group $P\bar{1}$. Compound (**3**) has shown promising effects in preliminary bioassays on pathogens causing intrahospital infections.

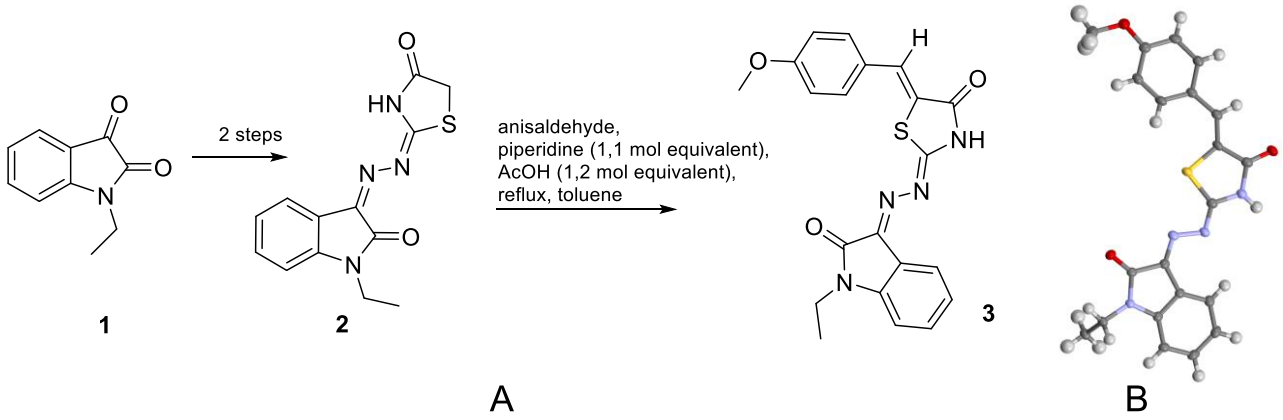


Figure 1. Scheme of synthesis of (2Z,5Z)-2-((E)-(1-ethyl-2-oxoindolin-3-ylidene)hydrazono)-5-(4-methoxybenzylidene)thiazolidin-4-one **(3)** and crystal structure of compound **(3)**.

ACKNOWLEDGEMENTS. This research is supported by the research subprogram MetNatVal (code 010601) funded by the Ministry of Education and Research of the Republic of Moldova.

[1] S. Nirwan, V. Chahal, R. Kakkar. Journal of Heterocyclic Chemistry **56** (2019) 1239.

MULTICOMPONENT MATRICES FOR CORNEAL REGENERATION WITH INSULIN/ GLUCOSE SENSITIVE FLUORESCENCE

A. Chiaburu[1,*], A. Besliu[1], I. Coretchi[1], I. Casian[1], A. Casian[1], E. Pavlovschi[1], I.-R. Tigoianu[2], B.-I. Ciubotaru[2], M.-F. Zaltariov[2]

[1]*Nicolae Testemitanu State University of Medicine and Pharmacy, Chisinau, Republic of Moldova;*
[2]*Petru Poni Institute of Macromolecular Chemistry, Iaşi, Romania.*
*E-mail: kiaburu@yahoo.com

Dysregulated blood glucose can trigger a variety of ocular complications such as retinal ischemia and glaucoma. Corneal damage develops in 40%–70% of cases. Hyperglycemia in diabetes damages the corneal epithelial layer, which can lead to permanent vision impairment. Current mainstream therapies include tissue adhesives, bionic gels and corneal transplantation.

In this study we report a series of chitosan-gelatin-starch multicomponent matrices incorporating kaempferol formulations with natural deep eutectic solvents in different molar ratios (1:1, 2:1, 1:2). The starting eutectic mixtures were characterized by FTIR and NMR spectroscopy. The influence of the addition of kaempferol-eutectic solvents to the polymeric blends matrix was investigated by FTIR, mechanical, optical and thermal analyses. The polymeric blend films showed sensing detection of glucose and insulin by means of fluorescence spectroscopy. The glucose presence promoted the increase of emission maximum at 438 nm and the calculated LOD and LOQ were found to be 100 μg/ml and 1.7μg/ml, respectively. The insulin presence determined an opposite effect producing the quenching of the fluorescence. The advantages lie in the simultaneous possibility to monitor the glucose level during the regeneration of cornea by application of kaempferol-based multicomponent matrices.

ACKNOWLEDGEMENT. „This work was supported by a grant of the Ministry of Research, Innovation and Digitization, CNCS – UEFISCDI, project PN-IV-PCB-RO-MD-2024-0372, within PNCDI IV".

SYNTHESIS AND CHARACTERIZATION OF A MULTIFUNCTIONAL THERMOSTABLE CONDUCTIVE NANO-SIZED OLIGOMER BASED ON ORTHO-PHENYLENEDIAMINE AND CATECHOL

Ramil Rzayev[1,2,*], Natalia Sucman[1], Bakhtiyar A. Mammadov[2], Rena Akhmedova[2], Fliur Macaev[1]
[1]*Institute of Chemistry of the Moldova State University, Chișinău, Republic of Moldova;*
[2]*Institute of Polymer Materials, Azerbaijan National Academy of Sciences, Azerbaijan Republic;*
[*]Email: ramilrzayev81@gmail.com

The rapid development of modern electronics, energy storage devices, biosensors, and high-temperature aerospace components has created substantial demand for advanced multifunctional materials. Conductive polymers and oligomers represent promising candidates for these applications because they combine electrical conductivity, structural tunability, and mechanical flexibility. However, the industrial implementation of traditional conductive polymers, such as polyaniline, polypyrene, and polythiophene, remains constrained by their intrinsic thermal instability, limited solubility, and difficulties in processing at elevated temperatures [1–6] .

To overcome these limitations, nano-sized oligomeric frameworks should integrate aromatic diamines and dihydroxy benzenes. Ortho-phenylenediamine (o-PDA) offers high thermal stability, rigidity, and cross-linking potential through its aromatic backbone and two reactive amine groups. Catechol (1,2-benzenediol, 1,2-BD) contributes strong electron-donating properties, increased redox activity, and hydrogen-bonding capability, which together enhance charge transport and functional diversity in the conjugated system [7–10].

In this study, we synthesized a thermostable, conductive nanosized oligomer from o-PDA and 1,2-BD through oxidative chemical polymerization. We characterized its chemical structure, molecular weight, and nanoscale morphology using FTIR, NMR, and XRD. Thermal stability was assessed with TGA/DTA.

The FT-IR spectrum of the synthesized compound exhibits a broad absorption band at 3550–2585 cm^{-1}, attributed to the overlapping O–H (approximately 3350 cm^{-1}) and N–H (approximately 3220 cm^{-1}) deformation vibrations. The peak at 1566 cm^{-1} is assigned to the C=N deformation absorption band, while the absorption at 1490 cm^{-1} corresponds to C=C deformation vibrations of the aromatic rings. The band at 1282 cm^{-1} is attributed to C–N stretching vibrations. The signal near 1085 cm^{-1} is characteristic of electron delocalization within the coupled system. The absorption band in the range of 860 to 670 cm^{-1} is associated with out-of-plane C–H vibrations of the aromatic ring.

The ^{1}H NMR spectrum (DMSO-d6) confirmed the structure of the oFDA–1,2-BD oligomer. Signals observed in the aromatic region (δ = 6.36–7.95 ppm) correspond to aromatic fragments generated by oxidative copolycondensation of ortho-phenylenediamine and catechol units. Signals detected in the aliphatic region (δ = 0.79–1.14 ppm) indicate the presence of protons from the long alkyl chain of dodecylamine, which served as a surfactant. The thermogravimetric analysis (TGA-DTG) diagram indicates that oligo-(oFDA-1,2-BD) exhibits moderate thermal stability. Cleavage of the main and side chains commences at approximately 275°C. The XRD analysis has proved the semi-crystalline structure of synthesized oligomers. Furthermore, mass analysis of the oligomer of oligo-(oFDA-1,2-BD) was performed using MALDI. Accordingly, although the synthesized substance mainly consists of amine and catechol dimers, peaks corresponding to tetramers and pentamers can also be seen in the reaction mixture.

The synthesized compounds are black powders that dissolve in polar organic solvents. These materials exhibit paramagnetic behavior and function as high-density semiconductors. Because they contain amine-functional hydroxyl groups, they can form complexes with heavy metal ions and participate in electron and ion exchange reactions

[1] R. S. Rzayev, B. A. Mammadov, Y. A. Abdullayev, E. A. Ismayilova, and R. A. Ibrahimova. Processes of Petrochemistry and Oil Refining 23 (2022) 495–503.
[2] R. Rzayev, N. Sucman, I. Geru, et al. ChemistrySelect 10 (2025) e202401279.
[3] A. M. Grancarić, I. Jerković, V. Koncar, C. Cochrane, F. M. Kelly, D. Soulat, and X. Legrand. Journal of Industrial Textiles 47 (2018) 612–642.
[4] A. K. Poddar, S. S. Patel, and H. D. Patel. Polymers for Advanced Technologies 32 (2021) 4616–4638.
[5] R. Rzayev, N. Sucman, E. Monaico, I. Geru, A. Nicolescu, C. Deleanu, V. Batır, B. Mammadov, R. Akhmedova, and F. Macaev. Chemistry Journal of Moldova 21 (2026) 112–121.
[6] R. Rzayev, N. Sucman, E. V. Monaico, A. Nicolescu, et al. Journal of Polymer Research 33 (2026) 243.
[7] R. H. Sestrem, D. C. Ferreira, R. Landers, M. L. A. Temperini, and G. M. do Nascimento. European Polymer Journal 46 (2010) 484–493.
[8] B. P. Lee, H. Birkedal, and H. Lee. Frontiers in Chemistry 8 (2020) 212.
[9] E. Faure, C. Falentin-Daudré, C. Jérôme, J. Lyskawa, D. Fournier, P. Woisel, and C. Detrembleur. Progress in Polymer Science 38 (2013) 236–270.
[10] H. Zhang, T. Zhao, B. Newland, W. Liu, W. Wang, and W. Wang. Progress in Polymer Science 78 (2018) 47–55.

CRYSTAL ENGINEERING OF Co(II/III) CLUSTER-BASED COORDINATION POLYMERS

E. Beleaev*, S. G. Baca
Institute of Applied Physics, Moldova State University, Chisinau, Republic of Moldova;
*E-mail: ecaterina.beleaev@ifa.usm.md

Cluster-based coordination polymers (CCPs) represent an important class of functional materials due to their structural diversity and remarkable physicochemical properties. These characteristics render them prominent candidates for applications in catalysis, molecular magnetism, gas adsorption, sensors and materials science. Within this field, cobalt CCPs are particularly attractive due to the ability of cobalt ions to adopt multiple oxidation states and varied coordination geometries, which facilitates the assembly of diverse polymeric architectures.

As part of our ongoing research on the preparation of CCPs with 3d metals [1-4], we report herein the rational design and synthesis of a series of cobalt-based CCPs. These materials were engineered using dinuclear cobalt carboxylate building blocks, derived from cobalt isobutyrate or pivalate, in combination with distinct classes of auxiliary nitrogen- and oxygen-donor ligands: N-bridging spacers (hexamethylenetetramine, pyrazine, 4,4′-dipyridylsulfide, 4,4′-dipyridine), chelating aminoalcohols (diethanolamine, triethanolamine) and functional aromatic co-ligands (4,4′-dihydroxybiphenyl, 3-pyridine sulfonic acid).

This presentation will discuss the specific synthetic conditions, including the effects of temperature, solvent media, and component ratios, that govern the crystallization process. By systematically varying the steric hindrance and coordination profiles of the auxiliary ligands, precise control over the self-assembly process was achieved, leading to the formation of Co(II)/Co(III) cluster-based coordination polymers with diverse architectures. We will examine how these parameters influence the formation of Co CCPs, driving the structural diversity from one-dimensional (1D) chains to three-dimensional (3D) frameworks. Furthermore, the correlation between synthetic parameters, cluster core formation, and ultimate framework topology will be analyzed. This work provides insights into the rational development of advanced coordination materials with tailored structural features and promising functional properties.

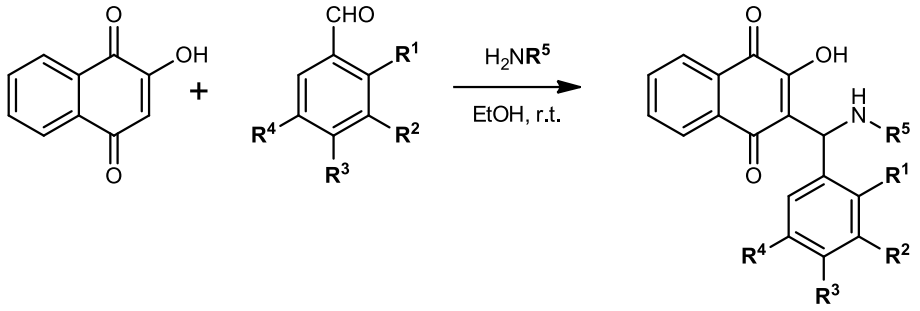
ACKNOWLEDGEMENTS. The authors are grateful for the project 25.80012.5007.87SE supported by the Moldovan National Agency for Research and Development (NARD).

[1] E.S. Beleaev, J. van Leusen, V.Ch. Kravtsov, D. Brüx, Yu. Chumakov, P. Kögerler, S.G. Baca. *Solid State Sci*. **176** (2026) 108288. Doi: https://doi.org/10.1016/j.solidstatesciences.2026.108288.
[2] S. Baca, P. Kögerler. *Chemistry* **3(1)** (2021) 314-326. Doi: https://doi.org/10.3390/chemistry3010023
[3] D. Podgornii, J. van Leusen, V.Ch. Kravtsov, P. Kögerler, S.G. Baca. *CrystEngComm*. **23(30)** (2021) 5153-5156. Doi: https://doi.org/10.1039/d1ce00777g.
[4] M. Darii, I.G. Filippova, J. Hauser, S. Decurtins, S.-X. Liu, V.Ch. Kravtsov, S.G. Baca. *Crystals* **8(2)** (2018) 100-1-100-11. Doi: https://doi.org/10.3390/cryst8020100.

NOVEL BIOACTIVE AMINONAPHTHOQUINONES: DESIGN, SYNTHESIS AND SPECTROSCOPIC STUDIES

D. Feldman[1,*], A. Simion[2], E. Gorincioi[1], N. E. Dina[2], F. Z. Macaev[1]
[1] *Moldova State University, Institute of Chemistry, Chisinau, Republic of Moldova;*
[2] *National Institute for Research and Development of Isotopic and Molecular Technologies, Cluj-Napoca, Romania*
*E-mail: cbf.21.feldman.danil@gmail.com

Modern medicinal chemistry faces the dual challenge of generating structurally diverse bioactive compounds while maintaining synthetic efficiency, atom economy, and alignment with green-chemistry principles. Here, we report a novel series of aminonaphthoquinone Mannich bases synthesized through a one-pot, single-step reaction at room temperature using readily available reagents and green solvents. Lawsone (2-hydroxy-1,4-naphthoquinone), a naturally occurring compound and established pharmacophore, was selected as the starting scaffold and systematically functionalized to afford a structurally diverse set of biologically active derivatives.



Scheme: Synthesis of the Lawsone Mannich bases

Lawsone Mannich bases were synthesized according to the general procedure described in the literature [1], (Scheme). A suspension of 2-hydroxy-1,4-naphthoquinone (1.7 mmol) in 5 ml ethanol and the respective amine (1.8 mmol) were stirred at room temperature for 10 minutes until the total dissolution of the naphtoquinone occurred and a color change was observed that corresponded to the formation of lawsonate solution. The aldehyde (2 mmol) was added and the mixture was stirred at room temperature in the dark for 12 hours. The resulting precipitate was filtered, washed with ethanol and diethyl ether to obtain the final compound.

In addition to solution NMR and FT-IR spectroscopy, which were used to confirm molecular structure, solid-state NMR spectroscopy was employed to probe the local structural and electronic environments of the synthesized compounds. The solid-state measurements provided information on intermolecular interactions, including hydrogen bonding and π–π stacking, as well as substituent-dependent electronic effects that may be averaged or obscured in solution. Such insight is particularly relevant for quinone-based pharmacophores, whose cytotoxic activity is often associated with redox cycling and reactive oxygen species generation.

Acknowledgements: This work was supported through the "Nucleu" Program within the National Research Development and Innovation Plan 2022–2027, Romania, carried out with the support of MEC, project no. 27N/03.01.2023, component project codes PN 23 24 01 02 and PN 23 24 01 05. The research was also supported through a grant from the Ministry of Education and Research, CNCS -UEFISCDI and NARD of Moldova, project number PN-IV-PCB-RO-MD-2024-0011, within PNCDI IV, and through a grant from the Ministry of Education and Research of Moldova, project Chemical study of secondary metabolites from local natural sources and valorization of their application potential basing on broadening molecular diversity with multiple functionality (MetNatVal) (code 010601).

[1] Neves, A.P.; Barbosa, C.C.; Greco, S.J.; Vargas, M.D.; Visentin, L.C.; Pinheiro, C.B.; Mangrich, A.S.; Barbosa, J.P.; Costa, G.L.D. Novel Aminonaphthoquinone Mannich Bases Derived from Lawsone and Their Copper(II) Complexes: Synthesis, Characterization and Antibacterial Activity. *J. Braz. Chem. Soc.* **20** (2009) 712–727.

NMR SPECTROSCOPY AS A TOOL FOR STRUCTURAL ELUCIDATION OF OLIGOMERS OBTAINED BY OXIDATIVE POLYCONDENSATION OF AROMATIC AMINES WITH DIHYDROXYBENZENES

N. Sucman[1,*], R. Rzayev[1], I. Geru[1], F.Macaev[1]
[1]*Laboratory of Organic Synthesis, Institute of Chemistry, Moldova State University, Chisinau, Republic of Moldova*
*E-mail: natalia_sucman@yahoo.com

Oxidative polycondensation of aromatic amines with dihydroxybenzenes represents an attractive approach for the synthesis of functional oligomeric materials with potential applications in electronics, catalysis, and sensing [1-4]. However, elucidation of the molecular structure of these products remains challenging because of their heterogeneous composition, multiple possible coupling pathways, and limited solubility. Consequently, the structural characterization of polymers of this type is predominantly based on FTIR spectroscopy. The application of NMR spectroscopy has been reported only in a limited number of studies and is generally restricted to ^{1}H and, less commonly, ^{13}C NMR experiments. In this work, nuclear magnetic resonance (NMR) spectroscopy was employed as the principal technique for structural elucidation of oligomers obtained by the oxidative polycondensation of *p*-phenylenediamine, *o*-phenylenediamine, and *o*-toluidine with resorcinol, catechol, and hydroquinone.

Comprehensive structural analysis was performed using one- and two-dimensional NMR techniques, including ^{1}H, ^{13}C, DEPT, COSY, NOESY, ^{1}H-^{13}C-HSQC and HMBC, ^{15}N-^{1}H HSQC and HMBC NMR experiments. The proposed structural models were further supported by FTIR spectroscopy, EPR spectroscopy, elemental analysis, and MALDI-TOF mass spectrometry, providing complementary information on functional groups, paramagnetic centers, elemental composition, and molecular weight. The presentation will include both previously published results [5-7] and new, as yet unpublished, data.

Comparative analysis of the obtained oligomers revealed significant differences in the preferred coupling pathways depending on both the aromatic amine and the dihydroxybenzene isomer. Based on the combined spectroscopic and analytical data, plausible mechanisms of oxidative polycondensation were proposed for each reaction system, explaining the formation of the observed structural fragments and oligomer architectures.

ACKNOWLEDGEMENTS. This research was supported by the Moldovan National Agency for Research and Development (Project Nr. 25.80012.5007.72SE).

[1] A. Yusif, R. Ramil, J. Autschbach. *Journal of Computational Chemistry* **43**(2022) 1313-1319.
[2] Amer, T. Mokrani, L Jewell, DA. Young, HCM Vosloo. *Tetrahedron Lett* **57** (2014) 426-430.
[3] F. Godarzi, H. Shi, J. Arjomandi. *Synth Met* **274** (2021) 116722.
[4] J. Sapana, C. Narendra Pal Singh, C. Sampath, A. Radhamanohar, S. Manda, C. Narendra Singh, R. Abbas. *Biomedical Materials & Devices* **1** (2023) 351–365.
[5] R. Rzayev, N. Sucman, I. Geru, E. Monaico, B. Mammadov, E. Ibadov, F. Macaev. *ChemistrySelect* **10** (2025) e01279.
[6] R. Rzayev, N. Sucman, E. Monaico, I. Geru, A. Nicolescu, C. Deleanu, B. Valentin, B. Mammadov, R. Akhmedova, F. Macaev. *Chemistry Journal of Moldova* **1** (2026) 112-124.
[7] R. Rzayev, N. Sucman, E. Monaico, A. Nicolescu, I. Geru, C. Deleanu, E. İbadov, B. Mammadov, F. Macaev. *Journal of Polymer Research* **33** (2026) 243.

MECHANISTIC INSIGHTS INTO THE SYNERGISTIC AND ANTAGONISTIC RADICAL-SCAVENGING DYNAMICS OF RESVERATROL-ASCORBIC ACID COMBINATIONS

N. Bolocan[1,*], Elena Gorincioi[1], Crina Vicol[1], Alic Barba[1], Gheorghe Duca[1]
[1]*Institute of Chemistry, Moldova State University, Chisinau, Republic of Moldova*
*E-mail: natalia.bolocan@sti.usm.md

Combining natural antioxidants often yields non-linear radical-scavenging outcomes, where the net effect can significantly surpass or impair individual activities. This study investigates the kinetic and mechanistic interaction between trans-resveratrol and L-ascorbic acid when reacting with the 2,2-diphenyl-1-picrylhydrazyl (DPPH) radical. By systematically adjusting molar ratios, we identified distinct zones of synergy and antagonism, with peak synergistic efficiency occurring at an equimolar (1:1) ratio. Spectroscopic examination via ^{13}C NMR revealed that the oxidative dimerization of resveratrol into trans-*δ*-viniferin plays a central role in driving this enhanced cooperative response.

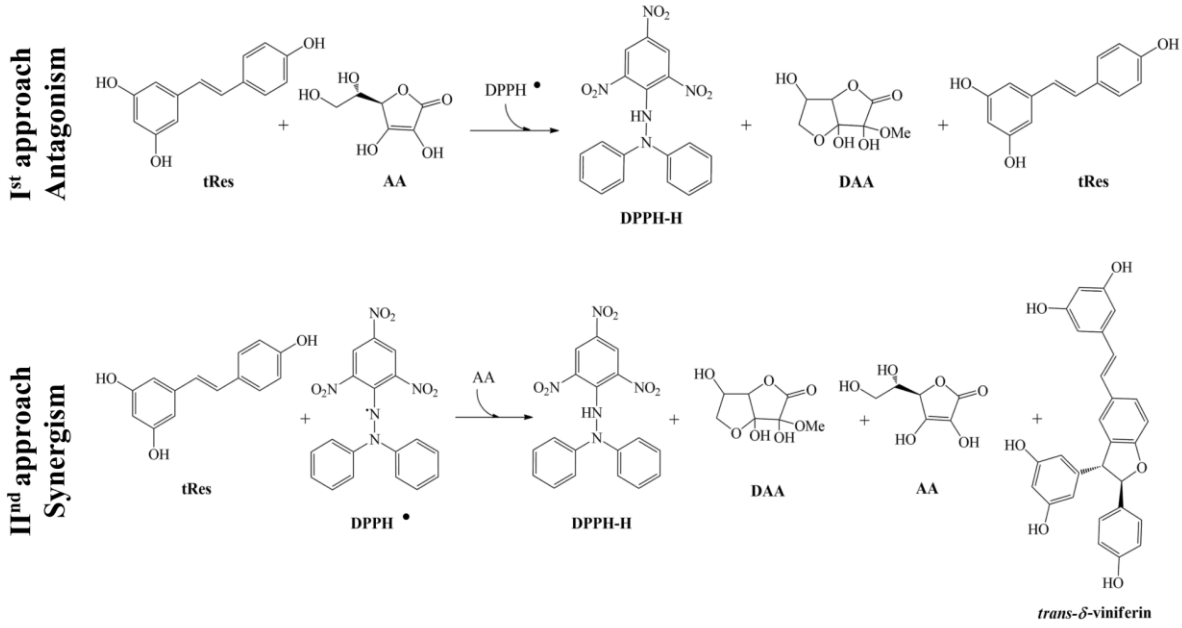


Figure 1. Different reaction products and antioxidants interactions generated under the I[st] and II[nd] approaches of performing the reaction.

Complementary Density Functional Theory calculations showed that L-ascorbic acid (AA) regenerates both *trans*-resveratrol radical (tRes$^{\bullet}$) and *trans-δ*-viniferin radicals by the hydrogen atom transfer (HAT) pathway that requires less energy than the reaction of AA with DPPH$^{\bullet}$, and therefore the synergism can be, theoretically, attributed to this regeneration. The regenerated tRes and *trans-δ*-viniferin would then be again included into the process of DPPH$^{\bullet}$ quenching, thus increasing the overall antioxidant activity of the mixture.

These findings elucidate the molecular crosstalk in multi-antioxidant matrices and offer design rules for optimizing stable, highly active antioxidant formulations

[1] E. Gorincioi, C. Vicol, N. Bolocan, C. Cimpoiu, A. Barba, S. Nica, Gh. Duca. Acta Chimica Slovenica (2025) 18;72(4):654-665. doi: 10.17344/acsi.2025.9292. PMID: 41408802.

OPTIMIZED THERMOACCUMULATION AS A CONDITION *SINE QUA NON* FOR ENSURING SUSTAINABLE DEVELOPMENT

Iurie Bosneaga*
Institute of Applied Physics, Moldova State University, 5 Academiei str., Chisinau, MD2028, Republic of Moldova
*E-mail: iubosneaga@gmail.com

Natural thermoaccumulation is the foundation of the developed (advanced) life on Earth. Thermal inertia is based predominantly on the exceptional (unique, out of the ordinary) water thermoaccumulation properties. Nowadays optimal artificial thermoaccumulation becomes the condition *sine qua non* for ensuring sustainable development. We apply thermodynamic approach for optimization. As it comes from the thermodynamic analysis, the main parameter for optimization should be the increment (gain) of free energy ΔG (Gibbs's energy) which is a function of the realized process. We sustain that this gain of free energy ΔG is a universal integral parameter which finally characterizes the result of any activity, inclusively can serve as a numerical criterion of sustainability. Respectively, *Sustainability Index S* is introduced for the numerical appreciation of the development:

$$S = \Delta G_{renewable} / (\Delta G_{fossil} + \Delta G_{renewable}) \quad (1)$$

We demonstrate that this approach ensures a breakthrough in Econophysics, contributing to its transformation into exact science. The possibilities of global extensive development are mainly exhausted. Respectively, imperative (mandatory) intensive development imposes development of science (especially of applied science), elaboration and implementation of cutting-edge technologies (of carbon-neutral energy generation, nanotechnologies and nanomaterials, AI, optimal artificial thermoaccumulation, etc.).

Thermoaccumulation is an indispensable component of energy-efficient systems. It refers to accumulation of both - high-potential, and low-potential thermal energy – usually as secondary energy, or "waste" heat. Intermittence of renewables (especially, of solar radiation), daily and seasonal temperature variations - these are additional arguments for thermoaccumulation development.

In this material we analyze and substantiate mainly some optimal (in our opinion) solutions for low-potential thermal energy accumulation.

From large amount nomenclature of such thermoaccumulators we especially highlight two - most important - types of thermoaccumulators: related to accumulation of natural ("winter") cold and summer heat, plus the secondary energy ("waste heat") accumulation, coming from the thermal machines (heat engines). Both mentioned types of thermoaccumulators have extremely large potential field of application and - respectively - can drastically change (improve) energy problems solving. For both cases we propose efficient principles and constructions for thermoaccumulation.

Intelligent application of the advanced low temperature (cold) accumulators permits realization of the competitive advantages for the relatively high latitudes' countries - with continental climate. We develop non-traditional thermal machines, based on the frozen water (ice) expansion. Unique property of the frozen water to expand by approximately 9% ensures obtaining of the additional high-potential energy during freezing process, the quantity of which is a strong function of the operating pressure. Large-scale application of the low-temperature thermoaccumulation decisively improves the economy indices for many related technologies.

SPECTROSCOPIC STUDY OF ALUMINUM AND SILICON CHLOROPHTHALOCYANINES

T. Potlog[1,*], I., Lungu[1], R. Tigoianu[2,*], A. Airinei[2]
[1]*Institute of Applied Physics, Moldova State University, Chisinau, Republic of Moldova*
[2]*„P. Poni" Institute of Macromolecular Chemistry, Iasi, Romania*
*E-mail: tpotlog@gmail.com

Photosensitizers are crucial compounds in various photophysical applications, particularly in photodynamic therapy (PDT) and photovoltaics. Phthalocyanines represent an important class of highly conjugated macrocyclic compounds that have attracted considerable scientific interest due to their remarkable optical, electronic, and photophysical properties. Among these, phthalocyanines, specifically aluminum chlorophthalocyanine (AlClPc) and silicon chlorophthalocyanine (SiClPc), stand out due to their unique electronic structures, durable stability and efficient light-harvesting capabilities. The photophysical characteristics of the investigated AlClPc and SiClPc in DMSO solution were examined using UV–Vis absorption and fluorescence spectroscopies. The absorption spectra of AlClPc and SiClPc demonstrate intense Q-bands, which facilitate the efficient absorption of light in the visible region, typically around 600-700 nm. The new bands in the absorption spectrum of AlClPc and SiClPc in the regions of 705, 740, and 770 nm indicate the formation of aggregates. The fluorescence spectrum of AlClPc typically shows a significant emission peak in the range of 670-700 nm, although specific peaks can vary based on solvent and environmental factors. SiClPc also exhibits fluorescence emission with peaks slightly shifted compared to AlClPc, generally in the same 670-720 nm region. The fluorescence emission primarily occurs in the same spectral region as the absorption, but often at a longer wavelength due to Stokes shift. Upon flash photoexcitation, the AlClPc molecules absorb photons, promoting electrons from the ground state (S_0) to an excited singlet state (S_1). The energy absorbed leads to the formation of a short-lived excited state, which can undergo various pathways. Comparing the fluorescence spectra of AlClPc and SiClPc highlights the interplay of their electronic structures and how the central metal influences their photophysical properties. Another parameter that measures the efficiency of fluorescence is the fluorescence quantum yield. AlClPc exhibit a higher fluorescence quantum yield than SiClPc in certain conditions or environments, which affect its utility in applications like photodynamic therapy. This difference can be attributed to internal conversion and intersystem crossing rates that differ for Al and Si complexes, influencing energy relaxation pathways. Flash photoexcitation of solutions of AlClPc in DMSO leads within the laser flash time to the appearance of the triplet states AlClPc, which is characterized by a broad difference spectrum with a maximum at ~490 nm and bleaching in the region of the AlClPc ground state absorption bands as well as it was previously observed in DMSO solutions of others phthalocyanines [1]. The triplet states of these photosensitizers generate reactive oxygen species (ROS), including singlet oxygen, crucial for the therapeutic efficacy in biological environments.

So, these compounds exhibit remarkable photophysical properties, such as strong light absorption in the visible region, significant singlet oxygen generation, and long-lived excited states, making them ideal candidates for applications in PDT.

ACKNOWLEDGEMENTS. This work was supported by the Ministry of Education and Research of the Republic of Moldova through the Moldova State University research subprogram #011209.

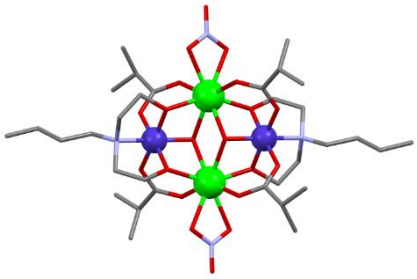
[1] T. Potlog, I. Lungu, A. Airinei, R. Tigoianu. Photophysical Properties of Substituted Zinc Phthalocyanine-Dextran Systems. *ChemPhotoChem*, **9** (2025), e2400385.

FROM BUTTERFLIES TO WHEELS: EVOLUTION OF NUCLEARITY AND TOPOLOGY IN HETEROMETALLIC Co-La CLUSTERS DIRECTED BY AMINO-ALCOHOL AND CARBOXYLATE LIGANDS

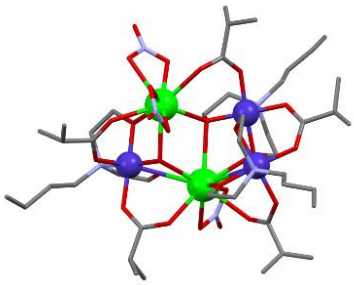
D. Stati[1,*], V.Ch. Kravtsov[1], P. Kögerler[2], S.G. Baca[1]
[1]*Institute of Applied physics, Moldova State University, Chisinau, Republic of Moldova;*
[2]*Institute of Inorganic Chemistry, RWTH Aachen University, Aachen, Germany*
*E-mail: dumitru.stati@ifa.usm.md

The design and synthesis of heterometallic 3d–4f clusters have attracted significant attention in coordination chemistry and materials science over the past few decades. The co-assembly of transition metals and lanthanides within a single molecular framework offers a powerful strategy for generating synergistic properties that are inaccessible in homometallic systems. Understanding how systematic variations in reaction conditions and ligand-to-metal ratios influence the evolution of molecular architecture - from simple oligomers to massive wheel-like topologies remains a key objective in crystal engineering.

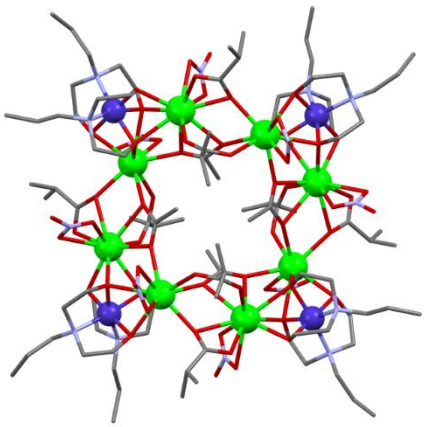
Herein, we report the systematic synthesis and structural characterization of three new heterometallic Co-La clusters, demonstrating an evolution of nuclearity directed by the versatile coordination of *N*-butyldiethanolamine ($bdeaH_2$) and isobutyrate (ib^-) ligands. The series includes the tetranuclear $[Co_2La_2(\mu_3\text{-}OH)_2(ib)_4(bdea)_2(NO_3)_2]\cdot 2MeCN$ (**1**), the pentanuclear $[Co_3La_2(\mu_3\text{-}OH)(ib)_5(bdea)_3(NO_3)_3]\cdot 1.5MeCN$ (**2**), and the dodecanuclear $[Co_4La_8(ib)_8(bdea)_8(MeCO_2)_4(NO_3)_8]\cdot 8MeCN$ (**3**) clusters (Figure). All clusters were comprehensively characterized by elemental analysis, FT-IR spectroscopy, ESI-MS spectrometry, and single-crystal and powder X-ray diffraction studies. Cluster **1** features a planar, C_i-symmetric "butterfly" $\{Co_2La_2\}$ core, where the La^{III} and Co^{III} ions are bridged by μ_3-OH groups. Pentanuclear cluster **2** exhibits greater structural complexity and comprises a $\{Co_3La_2\}$ core, which is formed through the fusion of heterometallic triangular units. Further structural expansion yields the dodecanuclear assembly **3**, which exhibits distinctive wheel-like architecture. In **3**, an eight-membered, saddle-shaped La^{III} octagon is decorated by four peripheral Co^{III} vertices and stabilized by internal μ_3-acetate bridges Continuous shape measures analysis (SHAPE) confirms distorted octahedral environments for the Co^{III} centers across the series, while the La^{III} ions transition from eight- to ten-coordinate geometries. This series highlights the structure-directing role of the deprotonated $bdea^{2-}$ scaffold in assembling high-nuclearity heterometallic frameworks with tunable topologies.



1



2



3

ACKNOWLEDGEMENTS. The authors are grateful for the subprogram 011202 financed by the Ministry of Education and Research of R. Moldova and the bilateral project "MultiClust" (01DK25013 and 25.80013.5007.07GER) supported by the German Federal Ministry of Education and Research (BMBF) and the National Agency for Research and Development (NARD).

A NEW COBALT(II) COORDINATION POLYMER BASED ON DINUCLEAR PIVALATE BUILDING UNITS AND PYRAZINE LINKERS

E. Beleaev[1,*], V. Ch. Kravtsov[1], S. G. Baca[1]
[1]*Institute of Applied Physics, Moldova State University, Chisinau, Republic of Moldova;*
*E-mail: ecaterina.beleaev@ifa.usm.md

The rational design of coordination polymers relies on the judicious selection of metal centers and bridging ligands capable of directing framework assembly. Cobalt(II) ions are attractive building blocks due to their variable coordination geometries and magnetic properties. Pivalate ligands readily support the formation of stable multinuclear cobalt units, while pyrazine acts as a rigid μ_2-bridging spacer that efficiently connects metal-containing secondary building units into extended architectures. Consequently, cobalt–pivalate–pyrazine systems represent a promising platform for the development of coordination polymers with diverse topologies and useful properties. A new coordination polymer, $\{[NaCo_2(N_3)(piv)_4(pyz)]\cdot H_2O\}_n$ (**1**) (where Hpiv = pivalic acid, pyz = pyrazine), has been synthesized under hydro(solvo)thermal conditions. X-ray structural analysis reveals that **1** crystallizes in the orthorhombic space group *Imcm* with the following unit cell parameters a = 11.7771(9), b = 15.5394(15), c = 18.7693(11) Å, and V = 3435.0(5) Å ^{3}. The structure of **1** exhibits a polymeric architecture in which adjacent $[Co_2(N_3)(piv)_4]$ building units are interconnected by pyrazine ligands acting as μ_2-bridging linkers into 1D polymeric zig-zag chains (Fig. 1). These chains are further linked by Na^+ ions into a 3D framework. The coordination environment of the Co(II) ion is described as a distorted N_2O_4 octahedron defined by two nitrogen atoms (one from pyz ligand and the other from the azide group) and four oxygen atoms from two bridging and one chelating piv ligands. The Co–O bond distances are in the range of 2.022(5) – 2.167(5) Å and the Co–N bond distances are 2.091(7) and 2.143(7) Å, confirming the Co(II) oxidation state. The Co(II)·Co(II) separation is 3.348(1) Å across the bridging azide and 7.095(1) Å through the pyz ligand.

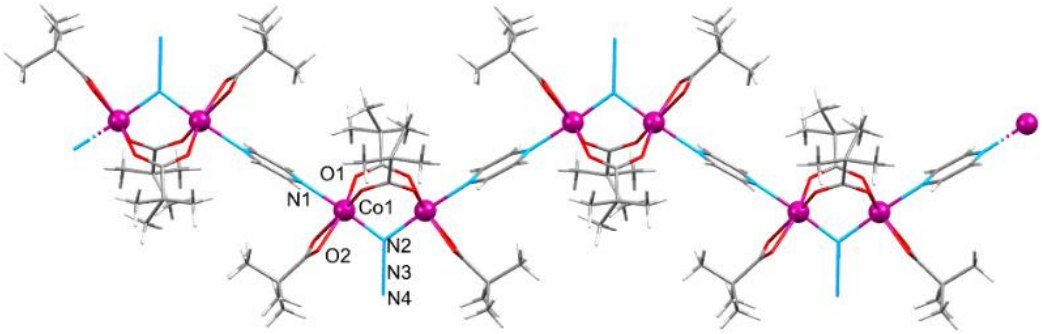


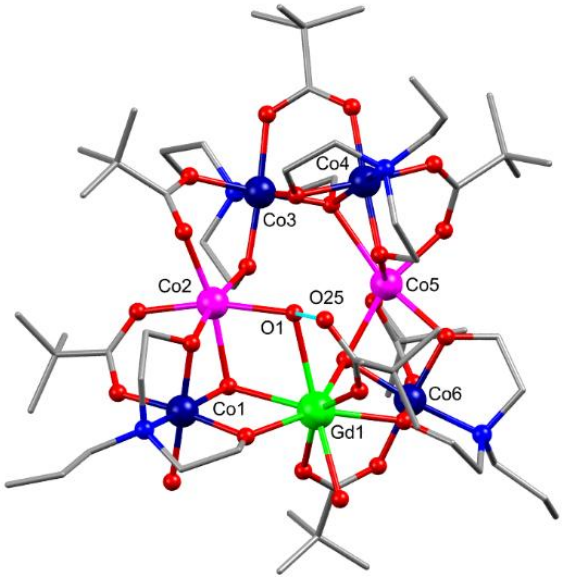
Figure 1. View of the 1D zig-zag chain in **1**.

ACKNOWLEDGEMENTS. The authors are grateful for the subprogram 011202 financed by the Ministry of Education and Research of R. Moldova and the project 25.80012.5007.87SE supported by the Moldovan National Agency for Research and Development (NARD).

A HEPTANUCLEAR HETEROMETALLIC $\{Co^{III}_4Co^{II}_2Gd^{III}\}$ PIVALATE CLUSTER SUPPORTED BY *N*-BUTYLDIETHANOLAMINE LIGANDS

E. Beleaev[1,*], D. Brüx[2], J. van Leusen[2], P. Kogerler[2], S. G. Baca[1]
[1]*Institute of Applied Physics, Moldova State University, Chisinau, Republic of Moldova;*
[2]*Institute of Inorganic Chemistry, RWTH Aachen University, Aachen, Germany*
*E-mail: ecaterina.beleaev@ifa.usm.md

The design and synthesis of 3d-4f coordination clusters represent an active area of research in modern coordination chemistry and molecular magnetism, due to their intriguing structural diversity and potential applications as single-molecule magnets and magnetocaloric materials. A new mixed-valent, heptanuclear heterometallic coordination cluster, $[Co^{III}_4Co^{II}_2Gd(OH)_3(piv)_7(bdea)_4(H_2O)_2](NO_3)\cdot 0.5CH_3CN$ (**1**) (where Hpiv = pivalic acid, H_2bdea = *N*-butyldiethanolamine), has been synthesized and characterized by elemental analysis, IR spectroscopy, and ESI-MS spectrometry. Single-crystal X-ray diffraction analysis shows that **1** crystallizes in the triclinic space group $P\bar{1}$ with the following unit cell parameters: a = 15.5652(6), b = 15.6873(6), c = 20.5739(9) Å, α = 79.076(4), β = 71.984(4), γ = 75.691(4)˚, and V = 4594.2(3) Å^3. The structure of **1** consists of a cationic $[Co_6Gd(OH)_3(piv)_7(bdea)_4(H_2O)_2]^+$ cluster unit with a mixed-valence $\{Co^{III}_4Co^{II}_2Gd^{III}\}$ core, accompanied by a NO_3^- counteranion and half of an acetonitrile solvate molecule. The core features a wheel-like motif, wherein a central Gd^{III} ion is surrounded by six peripheral Co ions in their respective oxidation states (Fig.). Cluster **1** comprises four Co^{III} (Co1, Co3, Co4, and Co6) and two Co^{II} (Co2 and Co5) atoms, three μ_3-OH groups, seven piv^- ligands, four doubly deprotonated $bdea^{2-}$ ligands, and two coordinated water molecules. The Co^{III} centers are six-coordinate and display distorted octahedral NO_5 coordination environments. Specifically, the coordination sphere of each Co^{III} ion includes one oxygen atom provided by a μ_3-OH group, alongside two oxygen atoms and one nitrogen atom from a chelating $bdea^{2-}$ ligand. The octahedral environment of the Co1 atom is completed by an oxygen atom from a piv^- ligand and one coordinated water molecule, whereas the coordination spheres of the remaining Co3, Co4, and Co6 atoms are completed by two oxygen atoms from different bridging piv^- moieties. The Co^{III}–O and Co^{III}–N bond distances are in the ranges of 1.852(6)–1.948(7) Å and 1.956(9)–2.000(8) Å, respectively. The two Co^{II} ions are also six-coordinate and adopt a distorted O_6 octahedral geometry, coordinated by a μ_3-OH group, oxygen atoms from three $bdea^{2-}$ ligands, and two oxygen atoms from different bridging piv^- moieties, with Co^{II}–O bond distances ranging from 1.990(7) to 2.196(7) Å. The eight-coordinate Gd^{III} center possesses an O_8 donor set and adopts a distorted triangular dodecahedral geometry (*TDD-8*) with a deviation value of 1.319 calculated by the SHAPE program. Its coordination sphere is occupied by three μ_3-OH groups, two oxygen atoms from two distinct $bdea^{2-}$ ligands, two oxygen atoms from monodentate and bridging piv^- ligands, and one coordinated water molecule. The Gd^{III}–O bond distances range from 2.288(7) to 2.541(7) Å. Finally, the magnetic properties of **1** will be discussed in correlation with these structural features.



Acknowledgements: The authors are grateful for the bilateral project "MultiClust" (01DK25013 and 25.80013.5007.07GER) supported by the German Federal Ministry of Education and Research (BMBF) and the National Agency for Research and Development (NARD) of R. Moldova.

NEW HEXANUCLEAR {Co_3Tb_3} NANOCLUSTER CONSTRUCTED BY METHYLDIETHANOLAMINE AND PIVALATE LIGANDS

E. Beleaev[1,*], D. Brüx [2], J. van Leusen[2], P. Kögerler[2], S. G. Baca[1]
[1]*Institute of Applied Physics, Moldova State University, Chisinau, Republic of Moldova;*
[2]*Institute of Inorganic Chemistry, RWTH Aachen University, Aachen, Germany*
*E-mail: ecaterina.beleaev@ifa.usm.md

In recent decades, nanoscale homo- and heterometallic coordination clusters incorporating magnetic transition-metal and/or lanthanide ions have attracted considerable interest owing to their potential as building blocks for next-generation functional materials. Such systems have found applications in diverse fields, including molecular magnetism, magnetic sensing, spintronics, magnetocaloric refrigeration, catalysis, and energy-related technologies. A new coordination compound $[Co_3Tb_3(OH)_4(piv)_6(mdea)_3(H_2O)_3]\cdot(NO_3)_2\cdot 0.15H_2O\cdot 1.75MeCN$ (**1**), (Hpiv = pivalic acid, $mdeaH_2$ = methyldiethanolamine), has been prepared and characterized by elemental analysis, IR spectroscopy and ESI-MS spectrometry. X-ray structural analysis shows that **1** crystallizes in the monoclinic $P2_1/n$ space group, with the unit cell parameters: a = 9.79640(10), b = 24.2848(4), c = 31.1489(4)Å, β = 92.3360(10)° and V = 7404.28 Å^3. The molecular structure consists of three Co^{III} and three Tb^{III} metal ions assembled into a {Co_3Tb_3} metallic hemicubane-type topology (Fig. 1). The metallic core is supported by four μ_3-hydroxy ligands that bridge the metal centers and stabilize the cluster framework. The Tb(III) ions are further connected to the Co^{III} centers through six bridging carboxylates. Three $mdea^{2-}$ ligands act as chelating donors through the amino nitrogen and bidentate bridges connecting the metal centers through the hydroxylic groups located on their branches. The coordinated water molecules complete the coordination sphere of each Tb^{III} atom. Magnetic data of **1** (Fig. 2) show a $\chi_m T$ value of 35.5 cm^3 K mol^{-1} at 300 K and 1.0 T, which is well within the expected range of 35.3-36.5 cm^3 K mol^{-1} for three non-interacting Tb^{III} and three low spin Co^{III} centers; note that the latter make a small temperature independent paramagnetic (TIP) contribution. Upon cooling the compound, the $\chi_m T$ values essentially decrease due to thermal depopulation of the m_J states of the Tb^{III} centers, although minor exchange interactions between the Tb^{III} centers cannot be excluded. In addition, the plot of molar magnetization M_m vs. applied magnetic field B of the powder sample, i.e. statistically oriented crystallites, confirms the presence of three Tb^{III} centers within the compound since the M_m values at higher fields are roughly half of the saturation values due to the distinct magnetic anisotropy of these centers.

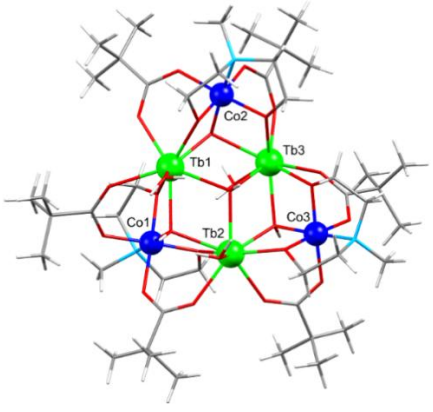


Figure 1. Structure of $[Co_3Tb_3(OH)_4(piv)_6(mdea)_3(H_2O)_3]$ cluster in **1**.

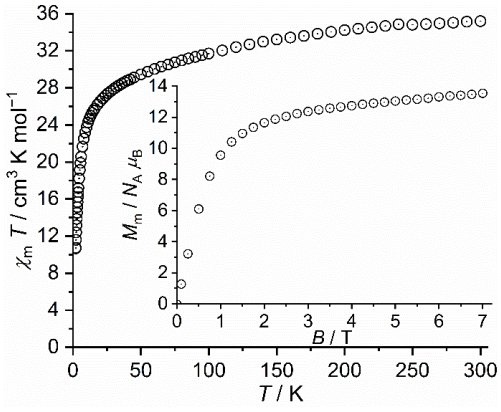


Figure 2. Magnetic data of **1** $\chi_m T$ vs. T at 1.0 T; inset: M_m vs. B at 2.0 K.

ACKNOWLEDGEMENTS. The authors are grateful for the bilateral project "MultiClust" (01DK25013 and 25.80013.5007.07GER) supported by the German Federal Ministry of Education and Research (BMBF) and the National Agency for Research and Development (NARD) of R. Moldova, and Scholarship program offered by World Scholars Fund (FMS), 2026.

SYNTHESIS AND CHARACTERISATION OF A NOVEL Cu(II) SEBACATE WITH 2,2'-BIPYRIDINE

P. Cebotaru[1,*], O. Cuzan[1], S. Shova[2], V. Lozan[1]
[1]*Institute of Chemistry, Moldova State University, 3, Academiei str., MD-2028 Chisinău, Republic of Moldova;*
[2] *"Petru Poni" Institute of Macromolecular Chemistry, 41A, Grigore Gica Voda Alley, Iasi, Romania*
*E-mail: paulacebotaru@gmail.com

The class of polycarboxylic acids play an important role in the synthesis of coordination polymers due to their versatile binding properties. One-, two- or three-dimensional polymers can manifest a wide range of properties such as sorption, catalytic and magnetic properties [1].
The new complex with the composition $\{[Cu(C_{10}H_{16}O_4)(C_{10}H_8N_2)]\cdot 3H_2O\}_n$, where, $C_{10}H_8N_2$ represents 2,2'-bipyridine, and $\{C_{10}H_{16}O_6\}^{2-}$ the bideprotonated sebacic anion, was isolated and comprehensively characterized. The compound was synthesized by heating at 60°C in water/ethanol mixture. The crystalline product was isolated in two weeks and analysed by elemental analysis, IR spectroscopy and X-ray diffraction analysis. The compound crystalizes in the triclinic *P*-1 group and its structure represents a 1D coordination polymer formed by the sebacate anions and Cu^{2+} metal centres anchored with the bipyridine moiety. The Cu^{2+} ion is by two nitrogen atoms from the 2,2'-bipyridine ligand and two oxygen atoms provided by sebacate dianions (Figure 1).

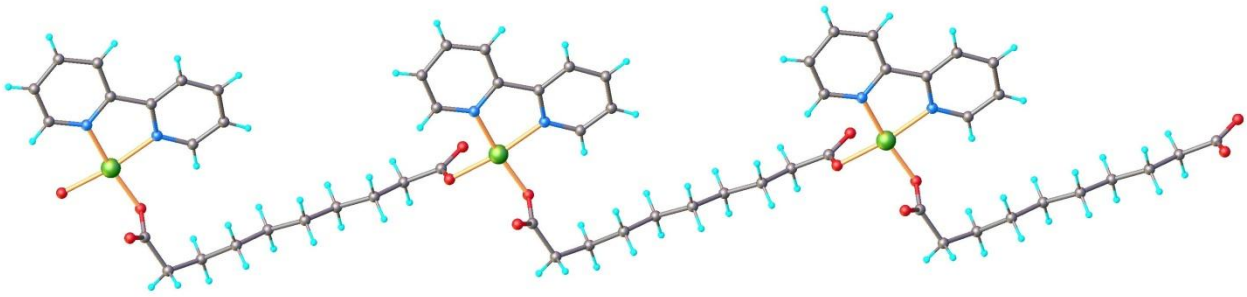


Figure 1. Partial view of 1D coordination polymer $[Cu(C_{10}H_{16}O_4)(C_{10}H_8N_2)]_n$.

ACKNOWLEDGEMENTS. This work was supported by the Research Subprogram SSMCCLP (code 010602).

[1] O. Cuzan, S. Shova, G. Novitchi, V. Lozan. *Inorganica Chimica Acta* **553** (2023) 121526.

CRYSTAL STRUCTURE OF 1D COORDINATION POLYMER CATENA-(BIS(μ_2 -4,4'-OXYDIANILINE)-(μ_2-PHENANTHROLINE)-CADMIUM (II) PERCHLORATE)

N. Craciun*, V. Ch. Kravtsov, M.S. Fonari
Institute of Applied Physics, Moldova State University, Chisinau, Republic of Moldova
E-mail: nicoletacaimac@gmail.com

The relationship between ligand geometry and resulting network topology is crucial for rational design of coordination networks and Metal-Organic Frameworks (MOFs). The incorporation of flexible ligands introduces conformational freedom that can lead to dynamic structural behavior and responsive properties. These materials can exhibit breathing effects, guest-dependent structural changes, or temperature-induced phase transitions [1]. The inclusion of photoactive organic molecules as components of coordination polymers allows to obtain functional materials showing photoluminescent properties such as fluorescence emission [2]. However aromatic diamine ligands were significantly less exploited in comparison with the pyridine-type ligands due to the poorer donor ability of the amine groups towards the metal centres. In continuation of our recent study demonstrated the possibilities of 4,4′-methylenedianiline as a suitable mediator to construct 1D and 2D coordination networks [3] herein we report the synthesis and crystal structure of new coordination polymer using the underexplored 4,4′-oxydianiline (oda). Compound $\{[Cd(phen)_2(oda)_2](ClO_4)_2\}_n$ (**1)** was obtained by solvothermal reaction between cadmium perchlorate and 4,4'-oxydianiline in the presence of phenanthroline (phen). The final product represents a linear 1D coordination polymer with the composition $\{[Cd(phen)_2(oda)](ClO_4)_2\}n$. **1** crystallises in the monoclinic $P2_1/n$ space group with unit cell parameters *a* 12.3172(11), *b* 17.5397(14), *c* 17.0703(14) Å, *β* 107.285(10) °, *V* 3521.3(5) Å^3, Z 4. The Cd(II) octahedral coordination geometry with the N_6-set of donor atoms is formed by two bidentate-chelate phen residues and two bidentate-bridging oda ligands. The Cd-N distances are in the range 2.31-2.47 Å. The outer-sphere perchlorate anions participate in the NH…O(ClO_4) hydrogen bonds and CH…O(ClO_4) short contacts that stabilise the crystal lattice. In the crystal, the parallel chains run along *a* crystallographic axis, with the metal-metal separation in the chain corresponding to the unit cell parameter *a*=12.3172(11) Å.

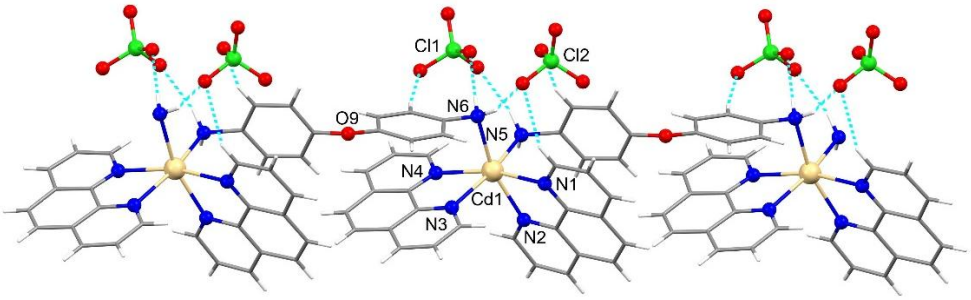


Figure 1. Fragment of 1D coordination polymer $\{[Cd(phen)_2(oda)_2](ClO_4)_2\}_n$ **1**

The conformation of the oda ligand in **1** differs from the crystalline pure form. The quantitative and qualitative distribution of intermolecular interactions was evaluated using Hirshfeld surface analysis. Further work is addressing to the structural diversity and functional applications of oda ligand with other metal salts.

ACKNOWLEDGMENTS. The authors thank the subprogram **011202** financed by the Ministry of Education and Research of R. Moldova.

[1] M. Shivanna, A. A. Bezrukov, V. Gascón-Pérez, K. Otake, S. Sanda, D. J. O'Hearn, Q.-Y. Yang, S. Kitagawa, M. J. Zaworotko, *ACS Appl. Mater. Interfaces* **14** (2022) 39560-39566.
[2] M. Kou, X. Zhai, W.-. Duan, P. Zhang, J. Martí-Rujas, F. Guo, *Inorg. Chim. Acta* **494** (2019) 154-159.
[3] N. Craciun., E. Melnic, A.V. Siminel, N.V. Costriucova, D. Chisca, M.S.Fonari, *Inorganics* **13** (2025) 90.

CRYSTAL AND ELECTRONIC STRUCTURE OF MACROCYCLIC TRINUCLEAR COMPLEX OF Co(II)

O. Danilescu[1,3,*], I. Bulhac[1], M. Cocu[1], P. Bourosh[2], Yu. Chumakov[2]
[1]*Moldova State University, Institute of Chemistry, Chisinau, Republic of Moldova;*
[2]*Moldova State University, Institute of Applied Physics, Chisinau, Republic of Moldova;*
[3]*Technical University of Moldova, Chisinau, Republic of Moldova*
[*]E-mail: olgadanilescu@gmail.com

A macrocyclic trinuclear Co(II) coordination compound, $[Co_3(H_6L)(H_2O)_6](ClO_4)_6 \cdot 8H_2O$ (**1**), was successfully prepared from a 15-dentate macrocyclic Schiff base ligand obtained by the condensation of 2,6-diacetylpyridine and malonic acid dihydrazide using a template synthesis method. The chemical composition, molecular structure, and crystal structure of macrocyclic complex were determined and confirmed by single-crystal X-ray diffraction, IR spectroscopy, and elemental analysis.

The X-ray analysis established that the investigated compound crystallizes in the monoclinic space group $P2_1/m$. The central atom (Co1, Co2) in macrocyclic complex is heptacoordinated, with the coordination geometry of the Co(II) ion being a centrosymmetric pentagonal bipyramid. The coordination environment of $[CoN_3O_4]$ is the Schiff base-type macrocyclic ligand and the oxygen atoms of the water molecules coordinated in the apical positions.

The macrocyclic complex has an ionic crystal structure consisting of the complex cation $[Co_3(H_6L)(H_2O)_6]^{6+}$, ClO_4^- anions and molecules of crystallization water in a molar ratio of 1:6:8. In the crystal of compound **1**, the $[Co_3(H_6L)(H_2O)_6]^{6+}$, which act as proton donors, ClO_4^- anions, crystallization and coordinated water molecules, and =NH groups are linked by a complex network of hydrogen bonds.

The isotropic exchange parameters between Co(II) ions were calculated using the Heisenberg model from Density Functional Theory (DFT) and it was observed both week ferro- and antiferromagnetic coupling. The calculated spin-polarized DOS and projected DOS (Figure 1) revealed that in studied complex both spin-up and spin-down spin channels are the spin-gapless channels.

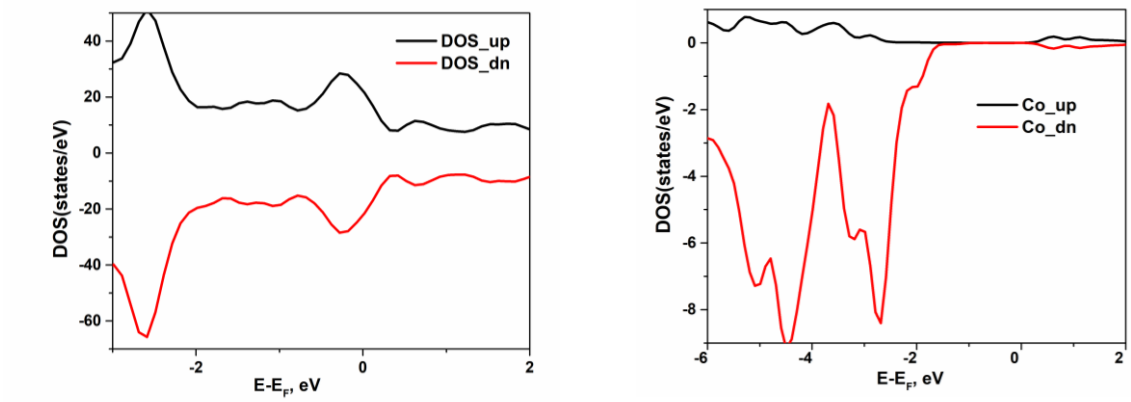


Figure 1. Spin-up and spin-down DOS and projected DOS of $[Co_3(H_6L)(H_2O)_6](ClO_4)_6 \cdot 8H_2O$.

The spin-up and spin-down states of Co(II) ions are delocalized and such hybridization between metals and ligands atoms could provide the magnetic exchange between ions.

ACKNOWLEDGEMENTS. The authors are grateful for the research subprograms 011202 and 010602, financed by the Ministry of Education and Research of R. Moldova.

[1] X. He, N. Helbig, M. J. Verstraete, E. Bousquet. *Comput. Phys. Commun*. **264** (2021) 107938.
[2] Soler J. M., Artacho E., Gale J.D., Garca A., Junquera J., Ordejon P., Sanchez-Portal D. *J. Phys.: Condens. Matter.* **14** (2002) 2745.

TUNING THE PHOTOLUMINESCENCE PERFORMANCE OF Cd(II) POLYMERS THROUGH POLYMORPHISM

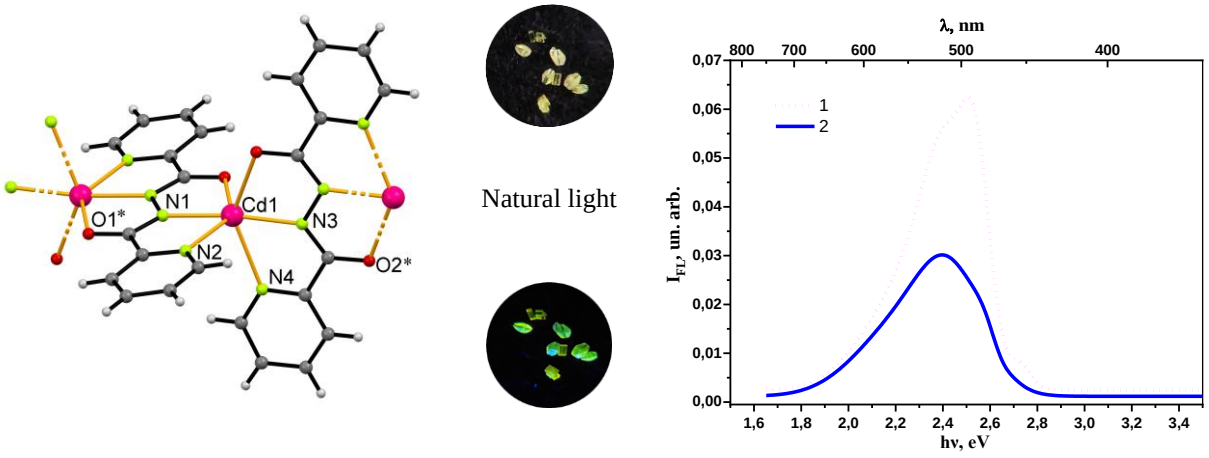
O. Danilescu[1*], I. Bulhac[1], P. Bourosh[2], O. Kulikova[2], Yu. Chumakov[2]
[1]*Moldova State University, Institute of Chemistry, Chisinau, Republic of Moldova*
[2]*Moldova State University, Institute of Applied Physics, Chisinau, Republic of Moldova*
[*]E-mail: olgadanilescu@gmail.com

In recent years, coordination polymers (CPs) are an attractive area of research in coordination chemistry and crystal engineering due to their intriguing topological architectures and various applications. Herein, we present solvothermale method for the synthesis of Cd(II) CPs based on the *N,N'*-bis(picolinoyl)hidrazine (H_2L) [1]. The crystals of discrete polymorphous CPs, $\{[Cd(L)]\cdot 0.5H_2O\}_n$ (**1**) and $\{[Cd(L)]\cdot H_2O\}_n$ (**2**), were obtained by template assembly of *o*-phtalaldehyde, picolinic acid hidrazide and $Cd(NO_3)_2\cdot 4H_2O$.

The photoluminescence (PL) study was performed on both samples and luminescence excitation was carried out by pulse nitrogen laser (337.1 nm) at a temperature of 300 K. PL study of the polymorphs **1** and **2** revealed that the PL activity of these polymorphs are significantly different, with notable enhancements observed, particularly for **1**, upon illumination with visible light.

The results of the photoluminescence study demonstrated that the both polymorphs emit yellow-green fluorescence, with the maximum located at 2.5 eV (500 nm) for **1** and 2.4 eV (520 nm) – for **2**, respectively. PL suitable for the production of screens and viewing devices, since the yellow-green region is the most comfortable and optimal for the human eye and allows for better visual perception.

The density of states (DOS) was calculated for studied compounds to get insight on behavior of PL spectra. It was shown that the PL maximum arises from the ligand-to-ligand $\pi \rightarrow \pi^*$ charge transfers.



a) b) c)

Figure 1. View of the coordination environment of the Cd(II) ion in **1** and **2** with partial numbering scheme (a); Images of **1** (bipyramid) and **2** (prisme) under natural and UV (365 nm) lights (b); Solid-state emission plots (λ_{ex} = 337 nm) for compounds **1** and **2** (c).

Our results overall highlight the potential of polymorphic design as a promising avenue for fine-tuning the photoluminescence properties of crystalline CPs, thereby opening avenues for their utilization in the optoelectronic industry.

ACKNOWLEDGEMENTS. The authors are grateful for the subprograms financed by the Ministry of Education and Research of R. Moldova: 011201, 011202 and 010602.

[1]. S. Shao, D. Zhu, Y. Song, X.Z. You, S.S.S. Raj, H.-K. Fun. N,N'- Bis(picolinoyl)hydrazine. *Acta Cryst., Section C*, **C55** (1999) 1841-1843. Doi: https://doi.org/10.1107/S0108270199009890

PHOTOLUMINESCENCE PROPERTIES AND DFT CALCULATIONS OF ISOMORPHIC ONE-DIMENSIONAL COORDINATION POLYMERS OF ZN(II) AND CD(II) BASED ON A DIHYDRAZONE LIGAND WITH TERMINAL N-DONOR PYRIDINE FRAGMENTS

Yu. Chumakov[2,*], M. Cocu[1], I. Bulhac[1], V. Kravtsov[2], P. Bourosh[2],
O. Kulikova[2], O. Danilescu[1]
[1] *Moldova State University, Institute of Chemistry, Chisinau, Republic of Moldova;*
[2] *Moldova State University, Institute of Applied Physics, Chisinau, Republic of Moldova*
[*]E-mail: yurii.chumakov52@gmail.com

Two new one-dimensional coordination polymers (CP) of Zn(II) and Cd(II) were synthesized and characterized by X-ray diffraction: $\{[Zn(L)(H_2O)]\cdot 5H_2O\}_n$ (**1**) and $\{[Cd(L)(H_2O)]\cdot H_2O\cdot 0.75EtOH\}_n$ (**2**) (H_2L = 2,6-diacetylpyridin-bis(isonicotinoylhydrazone)). The heptacoordinated (N_4O_3) complexes **1** and **2** are formed by three N atoms and two O atoms of the bis-deprotonated ligand in the basal plane of the pentagonal bipyramid, as well as the O atom of the water molecule and the N atom of the terminal pyridine fragment of another organic ligand at the vertices of the bipyramid. This axial coordination of the nitrogen atoms resulted in the formation of one-dimensional coordination polymers in both compounds, as a *zig-zag* like chains. The intermolecular interactions in polymers **1** and **2** were analyzed by Hirshfeld surface and two-dimensional fingerprint diagrams. The supramolecular architecture of CP **2** affect the photoluminescent properties: the intensity of the PL spectrum of **2** is more than 100 times lower compared with the ligand. The quenching of PL intensities in **2** might be caused by disordered water and ethanol molecules, observed in the crystals, suppressing the photoluminescence through nonradiative pathways.

The DFT calculations [1] showed that a decrease in the number of electron states in the top of the valence band may hinder the electron-hole recombination process. The similarity of the electronic structures of compounds **1** and **2** might lead to similarities in their photoluminescence spectra (Figure 1).

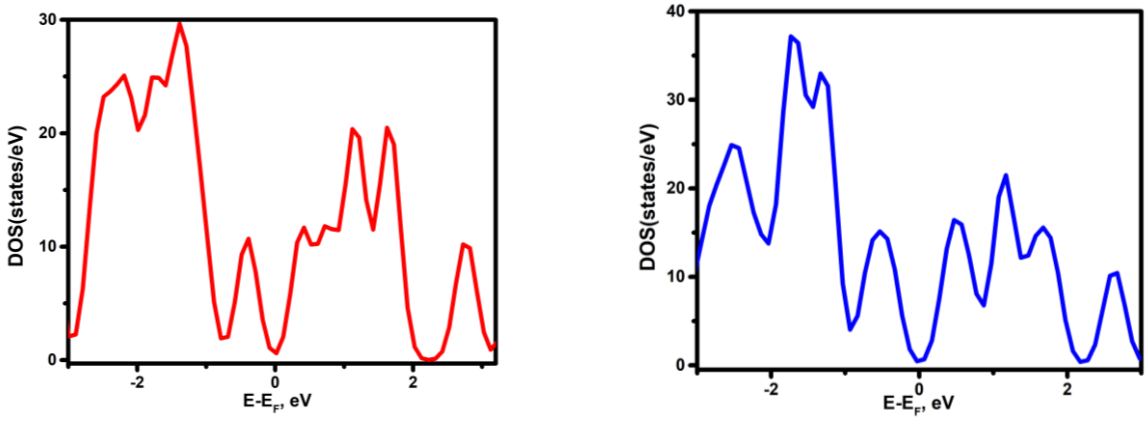


Figure 1. DOS for $\{[Cd(L)(H_2O)]\cdot H_2O\cdot 0.75EtOH\}_n$ (a) and $\{[Zn(L)(H_2O)]\cdot 5H_2O\}_n$ (b).

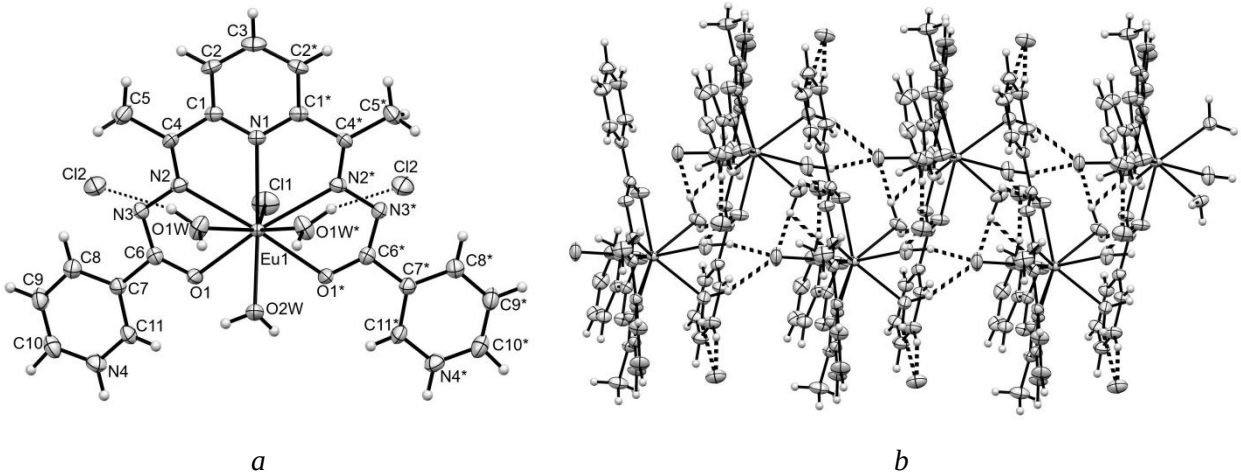
ACKNOWLEDGEMENTS. The authors are grateful to project, financed by the ANCD, „Synthesis, structural analysis and design of coordination polymers of zinc(II) and cadmium(II) with photoluminescent properties", 25.80012.5007.74SE., as well as authors thank for support provided within the subprograms, financed by the Ministry of Education and Science of the Republic of Moldova: 011201, 011202 and 010602.

[1] J.M. Soler, E. Artacho, J.D. Gale, A. Garca, J. Junquera, P. Ordejon, D. Sanchez-Portal. *J. Phys.: Condens. Matter.* **14** (2002) 2745.

MONONUCLEAR Eu(III) COMPLEX OF 2,6-DIACETYLPYRIDINE BIS(NICOTINOYLHYDRAZONE): SYNTHESIS AND CRYSTAL STRUCTURE

I. Bulhac[1,*], E. Melnic[2], V. Ghenea[2,3], O. Danilescu[1,3], I. Culeac[2]
[1]*Moldova State University, Institute of Chemistry, 3 Academiei str.,Chisinau, R. Moldova;*
[2]*Moldova State University, Institute of Applied Physics, 5 Academiei str., Chisinau, R. Moldova;*
[3]*Technical University of Moldova, 168 Stefan cel Mare bd., Chisinau, Republic of Moldova*
*E-mail: ionbulhac@yahoo.com

Polydentate hydrazone ligands are promising building blocks for lanthanide coordination compounds due to their structural versatility and photophysical potential [1]. However, the coordination chemistry of 2,6-diacetylpyridine bis(nicotinoylhydrazone) (H_2L) with lanthanides has not been extensively studied [2]. Herein, we report the synthesis a new mononuclear Eu(III) complex with H_2L and its structural and Hirshfeld surface analyses. This compound with the formula $[Eu(H_2L)(H_2O)_3Cl]Cl_2$ was obtained *via* the reaction of $EuCl_3$, 2,6-diacetylpyridine and nicotinic hydrazide in ethanol at 100 °C for 24 h in a programmable laboratory oven. The compound crystalizes in the centrosymmetric orthorhombic space group *Pnam*, unit cell parameters: a = 7.3343(3) Å, b = 14.0432(3) Å, c = 25.4811(6), $\alpha = \beta = \gamma$ =90°, V = 2624.50(14) Å^3. The coordination environment of the Eu^{3+} center is defined by a pentadentate duble zwitterionic H_2L ligand, which coordinates through two imine nitrogen atoms, one pyridine nitrogen atom, and two carbonyl oxygen atoms (ONNNO). Three coordinated water molecules and one chloride ion also contribute to the nine-coordinate metal centre. The coordination of the organic ligand to the Eu^{3+} ion generates four five-membered chelate rings. The resulting coordination polyhedron can be described as a distorted tricapped trigonal prism with an O_5N_3Cl donor set (Figure 1). The positive charge of the complex cation $[Eu(H_2L)(H_2O)_3Cl]^{2+}$ is balanced by two chloride counterions located in the outer coordination sphere. The Eu–O bond lengths range from 2.386 to 2.491 Å, the Eu–N bond lengths from 2.531 to 2.543 Å, while the Eu–Cl bond length is 2.822 Å. The crystal structure shows supramolecular ribbons forming and being stabilised by O–H···O, O–H···Cl and N–H···Cl hydrogen bonds, as well as π–π stacking interactions between adjacent pyridine rings (Cg···Cg = 3.741 Å). Hirshfeld surface analysis indicates that the crystal packing is dominated by H···H (43.5%), Cl···H/H···Cl (26.8%), and C···C (8.3%) interactions, which govern the supramolecular arrangement.



a *b*

Figure 1. Molecular structure (**a**) and fragment of crystal structure (**b**) of the coordination compound.

ACKNOWLEDGEMENTS. This research was funded by the Ministry of Education and Research of the Republic of Moldova (subprograms 010602, 011202, 011201).

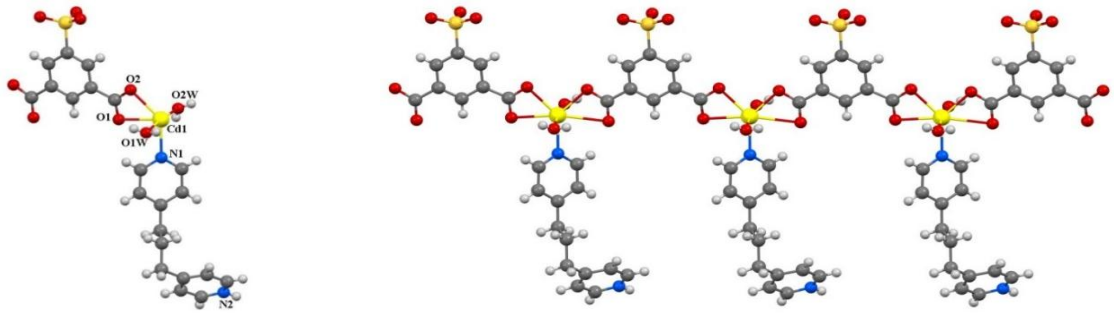
[1] V. Lozovan, G. Borodi, I. Perhaţia, A. Turza, A. M.V. Brânzanic, A. Pîrnău, L. E. Mureşan. Journal of Molecular Structure **1322** (2025) 140397.

[2] O.Danilescu, P. Bourosh, O.V. Kulikova, Yu.Chumakov, I.Bulhac, L.Croitor. *Inorganic Chemistry Communications* **146** (2022) 110199.

A NOVEL ONE-DIMENSIONAL CADMIUM(II) COORDINATION POLYMER: SYNTHESIS AND STRUCTURAL CHARACTERIZATION

A. A.Vitiu*, P.N. Bourosh
Institute of Applied Physics, Moldova State University, 5, Academei str., Republic of Moldova
*E-mail: vitiualiona@gmail.com

In recent years, significant attention has been devoted to the rational design and synthesis of metal–organic frameworks (MOFs) and coordination polymers with well-defined network architectures, driven by their potential as advanced functional materials for a wide range of applications [1]. The selection of suitable ligands plays a pivotal role in stabilising the topology and physicochemical properties of coordination networks [2]. Despite the fact that the coordination chemistry of multicarboxylate–sulfonate ligands has received comparatively limited attention, 5-sulfoisophthalic acid (H_3sipa) is considered to be a promising building block owing to its multiple coordination sites, rigid and symmetric geometry, and the presence of both carboxylate and sulfonate functionalities. Collectively, these factors facilitate the formation of high-dimensional coordination frameworks and diverse supramolecular architectures. A wide variety of one-, two-, and three-dimensional coordination architectures have been successfully assembled using additional rigid and flexible bipyridine-type ligands, such as 4,4′-bipyridine (bpy), 1,2-bis(4-pyridyl)ethane (bpe), and 1,3-bis(4-pyridyl)propane (bpp) [3]. More recently, the construction of increasingly complex supramolecular and coordination frameworks has been achieved through a strategy that combines rigid benzenepolycarboxylate ligands as fundamental building blocks with auxiliary ligands, including bpp for exemple, which promote framework extension and enhance structural diversity [4]. The reaction of Cd(II) ions with 1,3-bis(4-pyridyl)propane and monosodium 5-sulfoisophthalate in a mixed C_2H_5OH-H_2O – DMF solvent system afforded an open one-dimensional coordination polymer with formula $\{[Cd(sipa)(Hbpp)(H_2O)_2]\cdot 2H_2O\}_n$. The crystal structure expand through the $sipa^{3-}$ ligand, which functions as a bridging linker, connecting neighboring Cd(II) centers into an infinite linear coordination chain. Notably, the coordinated bpp ligand undergoes *in situ* protonation, giving rise to the monoprotonated species $Hbpp^+$. The coordination surrounding of the metal centre is defined by an NO_6 donor set. The nitrogen atom originates from the protonated $Hbpp^+$ ligand, whereas the oxygen atoms are complete the basal plane of the polyhedron are provided by two $sipa^{3-}$ ligands. The axial positions are occupied by two coordinated water molecules, completing the coordination polyhedron. It has been established that both the coordinated and crystallization water molecules participate in the hydrogen bonding system that binds the coordination polymers in the crystal.



a) b)

Figure 1. a) The mode of coordination of ligands to Cd(II) in 1; b) Fragment of 1D coordination polymer $[Cd(sipa)(Hbpp)(H_2O)_2]_n$.

ACKNOWLEDGEMENTS. The authors are grateful to the Ministry of Education and Research of Moldova for financial support (project no. 011202).

[1] Ch. Zhang, Y. Yan, L. Sun, Z. Liang, J. Li. *CrystEngComm*, **18** (2016) 4102-4108.
[2] J-R. Li, R. J. Kuppler, H.-C. Zhou. *Chem. Soc. Rev.*, **38** (2009) 1477-1504.
[3] F.H. Allen. *Acta Crystallogr., Sect. B: Struct. Sci.*, **58** (2002) 380-388.
[4] Q - Liua, Li Xu. *CrystEngComm*, **7(12)** (2005) 87-89.

DESIGN AND CHARACTERIZATION OF A NEW CADMIUM(II) METAL–ORGANIC FRAMEWORK

Silvia Melnic,[1,2] Dana Bejan,[3] Sergiu Shova,[1] Vasile Lozan[1]
[1]*Moldova State University, Institute of Chemistry, Chisinau, Republic of Moldova*
[2] *"Nicolae Testemitanu" State University of Medicine and Pharmacy, Faculty of Pharmacy, Chisinau, Republic of Moldova;*
[3]*Centre of Advanced Research in Bionanoconjugates and Biopolymers, "Petru Poni" Institute of Macromolecular Chemistry of the Romanian Academy, Iasi, Romania*
*E-mail: silmel_sm@yahoo.com

Metal–organic frameworks (MOFs) based on cadmium(II) ions have been extensively investigated because of their rich coordination chemistry and ability to form structurally diverse porous networks. These materials combine high crystallinity with tunable architectures, making them attractive for applications ranging from molecular recognition and sensing to catalysis and adsorption.

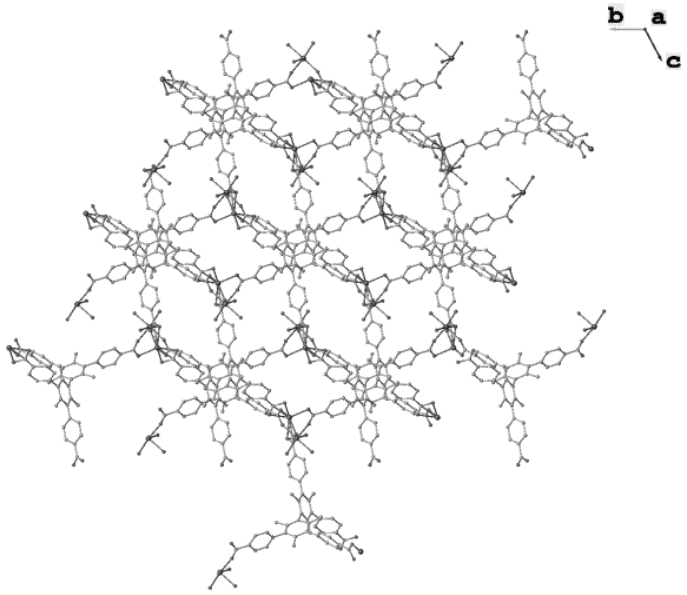


Figure 1. View of 3D Cd-MOF along axis *a*

In this study, we report the synthesis, crystal structure, thermal stability, and sorption properties of a novel cadmium(II) metal–organic framework (Cd-MOF) constructed from 3,3′,5,5′-tetrakis(4-carboxyphenyl)-2,2′,4,4′,6,6′-hexamethyl-1,1′-biphenyl (H_4L). The MOF was synthesized via a solvothermal reaction between H_4L and $Cd(NO_3)_2 \cdot 4H_2O$. Single-crystal X-ray diffraction analysis revealed that the compound forms a three-dimensional coordination network in which cadmium(II) ions act as nodes and L^{4-} ligands serve as polydentate linkers. The compound crystallizes in the triclinic crystal system, space group P1. Thermogravimetric analysis demonstrated that the framework is thermally stable up to approximately 400 °C. Furthermore, the MOF exhibits permanent porosity with a BET specific surface area exceeding 411 m^2/g.

ACKNOWLEDGEMENTS. This study is a part of subprogram SSMCCLP code 010602, Institute of Chemistry, Moldova State University.

CRYSTAL PACKING-DIRECTED LUMINESCENCE IN POTASSIUM COORDINATION POLYMERS BASED ON POSITIONAL ISOMERS OF CHLORONITROBENZOIC ACID

A. Gorobet [1,*], M. E. Crisan [2], P. N. Bourosh [1], O. V. Kulikova[1], L. Croitor [1]
[1] *Institute of Applied Physics, Moldova State University, Chisinau, Republic of Moldova;*
[2] *"Coriolan Dragulescu" Institute of Chemistry, Timisoara, Romania*
*E-mail: anastasia.gorobet@ifa.usm.md

The relationship between crystal packing and luminescence was investigated using two potassium coordination polymers assembled from the positional isomers 2-chloro-4-nitrobenzoic acid (2Cl4NBH) and 2-chloro-5-nitrobenzoic acid (2Cl5NBH). Despite differing only in the position of the nitro substituent, the ligands give rise to coordination polymers with markedly different crystal architectures and photoluminescent properties.

Single-crystal X-ray diffraction shows that the 2Cl4NB ligand forms a three-dimensional coordination framework, while the 2Cl5NB analogue adopts a two-dimensional layered structure. Hirshfeld surface [1] analysis further differentiates the two crystal packings. The 3D polymer is dominated by K···O/O···K contacts (24.0%), whereas the 2D analogue exhibits a lower contribution from coordination-related contacts (16.6%) together with a substantially higher contribution of O···H/H···O interactions (29.9%) (Figure 1), highlighting the greater involvement of hydrogen bonding in stabilizing the layered structure.

Both coordination polymers exhibit room temperature solid-state photoluminescence, with main emission maxima at ca. 410–420 nm. Compared with the corresponding free ligands, coordination enhances the emission intensity in both compounds; however, the enhancement is considerably greater for the 3D polymer (Figure 1). This behavior is attributed to the higher structural rigidity imparted by the extended three-dimensional coordination framework, which more efficiently restricts structural flexibility and reduces non-radiative relaxation pathways than the layered 2D architecture.

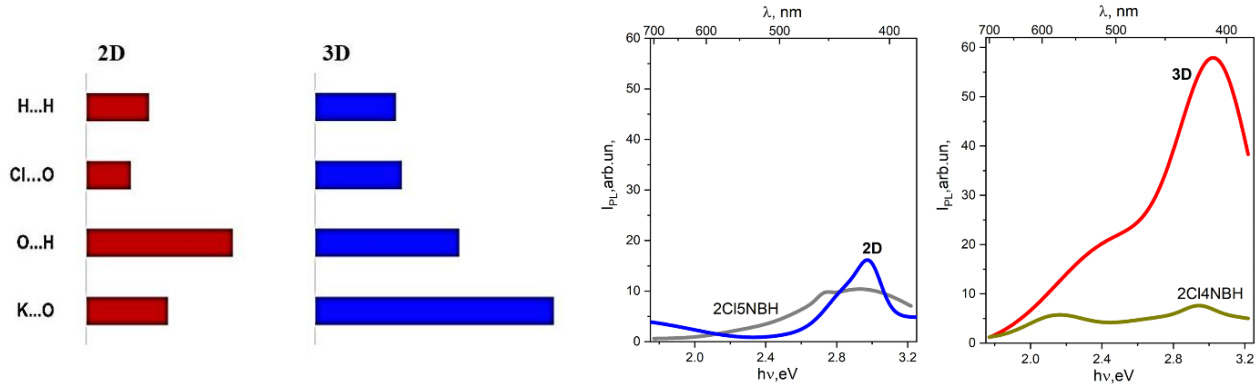


Figure 1. Comparison of the dominant intermolecular interactions obtained from Hirshfeld surface analysis (left) and room temperature solid-state photoluminescence spectra of the coordination polymers and corresponding ligands (right).

The correlation between crystal dimensionality, intermolecular interactions, and emission intensity demonstrates that crystal packing plays a decisive role in controlling the photophysical behavior of these potassium coordination polymers. Positional isomerism therefore provides a viable strategy for tuning the luminescent response of coordination materials.

ACKNOWLEDGMENT. The authors from RM are grateful for the subprograms financed by the Ministry of Education and Research of R. Moldova 011202 and 010602.

[1] F. L. Hirshfeld, *Theor. Chim. Acta*, **44** (1977) 129–138.

THE COORDINATION COMPOUND OF Mn(II) DERIVED FROM 5-(4-CARBOXY-5-METHYL-1*H*-1,2,3-TRIAZOL-1-YL)ISOPHTHALIC ACID

V. Gorinchoy[1,*], G. Roman[2], S. Shova[2], V. Lozan[1]
[1]*Institute of Chemistry, Moldova State University, 3, Academiei str., Chisinău MD 2028, Republic of Moldova;* [2] *"Petru Poni" Institute of Macromolecular Chemistry, 41A, Grigore Gica Voda Alley, Iasi, Romania*
**E-mail:* oviorina@gmail.com*; viorina.gorincioi@sti.usm.md;*

By solvothermal reaction between manganese chloride with the H_3L ligand, where L = 5-(4-carboxy-5-methyl-1*H*-1,2,3-triazol-1-yl)isophthalic acid [1], were isolated single crystals with the composition $\{[Mn_2L_2(H_2O)_6]\cdot DMF\cdot 2H_2O\}_n$.

The crystallographic study has shown that the investigated compound represents a dinuclear manganese coordination compound. The compound crystallizes in the monoclinic space group $P2_1/c$, with unit cell parameters: a=13.0703(4), b=18.7664(5), c=8.6779(3) Å, β=100.635(3)°. The manganese(II) ions have an octahedral environment; the coordination number of six is provided by two oxygen atoms from carboxylate groups, one nitrogen atom from the triazole ring, and three oxygen atoms from three water molecules (Figure 1).

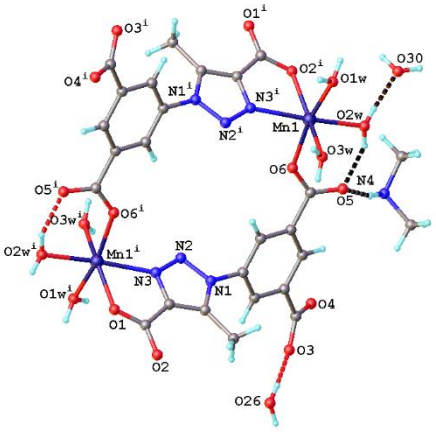


Figure 1. The crystal structures of coordination compound $\{[Mn_2L_2(H_2O)_6]\cdot DMF\cdot 2H_2O\}_n$

In the IR spectrum of **1**, a broad absorption band appearing at 3206 cm^{-1} corresponds to the stretching $\nu_{(O-H)}$ vibrations of the water molecules. The characteristic vibration modes of $\nu_{(C-H)}$ for the $-CH_3$ group appear at 2809 cm^{-1}. The peaks at 1608 and 1472 cm^{-1} correspond to characteristic absorptions for the asymmetric $\nu_{as}(COO^-)$ and symmetric $\nu_s(COO^-)$ stretching vibrations of C=O bond, whereas the very strong band at 1559 cm^{-1} has been attributed to the characteristic stretching vibrations of the phenyl ring. The absorption band appearing at 1375 cm^{-1} confirms the presence of the triazole ring in the structure of the dimeric compound, the strong band at 1178 cm^{-1} has been attributed to the vibration of $\nu_{(C-C)}$. The peak at 1122 cm^{-1} belongs to the $\nu_{(C-N)}$ stretching vibrations and the peak at 1024 cm^{-1} belongs to the $\nu_{(C-O)}$ stretching vibrations.

ACKNOWLEDGEMENTS. This research was supported by the subprogram SSMCCLP (code 010602).

[1] M. Dascălu, A.-L. Chibac-Scutaru, G. Roman. *Journal of Molecular Liquids* **386** (2023) 122457.

DINUCLEAR COPPER(II) COMPLEX WITH 5-CHLOROSALICYLIC ACID

V. Gorinchoy[1,*], S. Melnic[2], O. Cuzan[1], S. Shova[3]
[1]*Institute of Chemistry, Moldova State University, 3, Academiei str., MD 2028 Chisinau, Republic of Moldova;* [2]*State University of Medicine and Pharmacy "Nicolae Testemitanu", Chisinau, Republic of Moldova;* [3]*"Petru Poni" Institute of Macromolecular Chemistry, 41A, Grigore Gica Voda Alley, Iasi, Romania*
**E-mail:* oviorina@gmail.com*; viorina.gorincioi@sti.usm.md;*

The novel heterodinuclear complex $\{[CuBa(5–ClSalH)_4(DMA)_4]\}_n$ (**1**) was synthetized and characterized by IR spectroscopy and X-Ray single-crystal diffraction. The blue single crystals of **1** were obtained *via* the solvothermal synthesis method starting from copper(II) nitrate trihydrate and barium chlorosalicylate.

The IR spectrum characterization and bands assignment was made in comparison to the barium 5-chlorosalicylate and in accordance with literature data [1]. The band at 3230 cm^{-1} is attributed to the ν(OH) stretching vibrations of the phenolic OH group; the intense band at 1290 cm^{-1} and the shoulder at 1221 cm^{-1} are assigned to the ν(C–O) stretching vibrations of the phenolic OH and COOH groups, respectively [1]. The band characteristic of the C–Cl halogen group stretching vibrations can be observed in the 791–674cm^{-1} range. The IR spectrum of complex **1** contains bands characteristic of $\nu_{as}(COO^-)$ vibrations at 1592 cm^{-1} and $\nu_s(COO^-)$ vibrations at 1361cm^{-1}. The difference between the wavenumbers of the $\nu_{as}(COO^-)$ and $\nu_s(COO^-)$ absorption bands $\Delta\nu(\nu_{as} - \nu_s) \approx 231$ cm^{-1} indicates a bidentate bridging coordination mode.

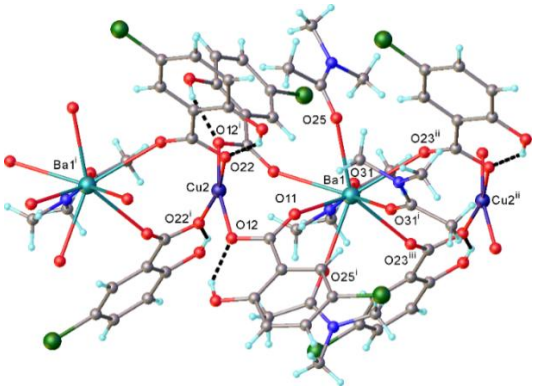


Figure 1. View of the molecular structure of the complex $\{[CuBa(5–ClSalH)_4(DMA)_4]\}_n$.

The X-ray diffraction study has shown that the investigated compound represents a Cu–Ba heterodinuclear 1D-coordination polymer along axis *b* (Figure 1). The compound crystallizes in the monoclinic space group P–1, with unit cell parameters: *a*=23.0355(7), *b*=9.00285(17), *c*=24.8376(6) Å, β=93.638(2)°.

The Cu:Ba:5–ClSalH:DMA ratio in **1** is 1:1:4:4; where the 5–$ClSalH^-$ anion is monodeprotonated and coordinates solely through the carboxylic group, while the OH group remains protonated and does not participate in coordination. Carboxylic groups from two 5–$ClSalH^-$ anions coordinate to Cu(II) and Ba(II) ions in μ_2–η_2 bridging mode. The tetrahedral environment of the copper atom is provided by four oxygen atoms from four carboxylic groups of the 5–$ClSalH^-$ anions. The Ba(II) ion has a coordination number equal to eighth, provided by eigth oxygen atoms: four from 5–$ClSalH^-$ ligands and four from DMA molecules.

ACKNOWLEDGEMENTS. The authors thank the research subprogram SSMCCLP (code 010602) for the financial support of this work.

[1] V.V. Gorinchoy, Y.A. Simonov, S.G. Shova, V.N. Shofranskii, K.I. Turte. *Journal of Structural Chemistry*, **50(6)** (2009) 1143–1148.

CRYSTAL STRUCTURE OF ZINC(II) PENTANUCLEAR CLUSTER BASED ON BENZOTRIAZOLE

V. Avdeev*, M.S. Fonari, P. Bourosh
Institute of Applied Physics, Moldova State University, Chisinau, Republic of Moldova
E-mail: mrvikrd59@gmail.com

Polynuclear complexes of transition metals are the focus of attention in the development of new hybrid materials, as these compounds stimulate the development of bioinorganic chemistry, solid-state physics, and materials science. The judicious choice of ligand is very important. In this regard, the polydentate benzotriazole (HBtz), with a favourable arrangement of coordination centres, can provide versatile coordination modes depending on the metal, and reaction conditions, and is extensively employed for the synthesis of organic–inorganic hybrid materials. Known examples of Zn-Btz **polynuclear clusters** are characterised by high stability and are widely used as secondary building units (SBU) in MOF construction and as effective catalysts [1-3]. A new compound, $[Zn_5(Btz)_6(CH_3COO)_3(OH)(H_2O)_2]\cdot 6.5H_2O$, was obtained in solvothermal reaction conditions from zinc acetate and benzotriazole (Hbtz). Crystal data: monoclinic, space group $P2_1/n$ with unit cell parameters a 17.195(3), b 16.821(3), c 19.977(2) Å, β 101.45(2)°, V 5662.8(2) Å^3, Z 4. Each cluster resides in the general position, with five Zn atoms located at the centre (Zn1) and at the vertices (Zn2-Zn5) of virtual tetrahedron (Fig. 1). The distances from the central to the peripheral Zn atoms are in the range 3.55 – 3.66 Å. Cluster neutrality is provided by six monodeprotonated Bzt ligands, three acetate and one hydroxide anion. The central zinc atom, Zn1, has a distorted octahedral geometry with the N_6 set of donor atoms from six Btz ligands. One of the peripheral zinc atoms (Zn5) also has a distorted octahedral geometry, with the N_3O_3 donor set formed by three Btz ligands and complemented by one hydroxide anion and two aqua ligands. The remaining three zinc atoms (Zn2-Zn4) have a tetragonal pyramidal N_3O_2 geometry from three Btz and one acetate ligand.

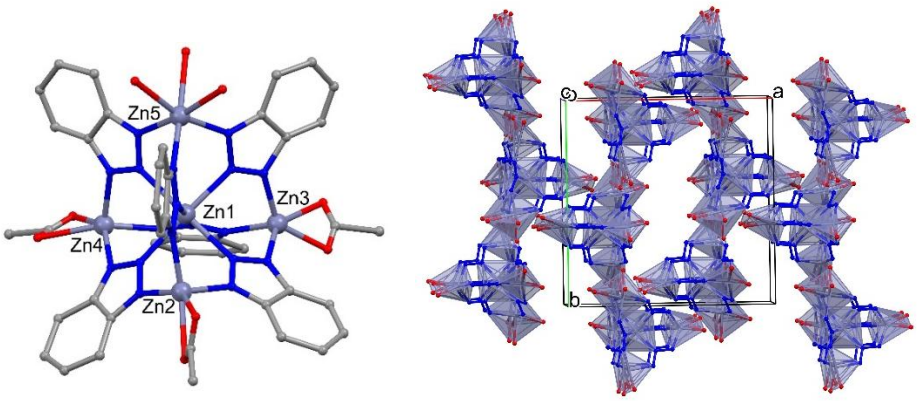


Figure 1. View of (a) pentanuclear cluster $[Zn_5(Btz)_6(CH_3COO)_3(OH)(H_2O)_2]$ (H-atoms are omitted) and (b) packing of clusters (C, H-atoms and solvent molecules are omitted).

The cluster is characterized by approximately equal trans-annular C...C distances of ~14.9 Å. The packing of these large particles in the crystal creates pores (accounting for ~ 21 % of the unit cell volume) filled with solvent molecules. Further research is aimed at exploring the structural diversity and functional applications of the Hbtz ligand in combination with other transition metal salts.

ACKNOWLEDGMENT. The authors thank the subprogram 011202 financed by the Ministry of Education and Research of R. Moldova.

[1] Q. Lio, N. Hoefer, G. Berkbigler, Z. Cui, T. Liu, C. A. Co, W. D. McComb, *Inorg. Chem*. **61** (2022) 18710–18718.
[2] Y. Lan, S. Li, H. Jiang, Q. Xu, *Chem. Eur. J.* **18** (2012) 8076–8083.
[3] X. Xue, G.-T. Li, Y.-H. Peng, L. Wu, B.-L. Wu, *J. Coord. Chem.* **64** (2011) 1953–1962.

3D COORDINATION POLYMERS OF LANTHANIDES WITH 5-(4-CARBOXYPHENYL)-1-PHENYL-1H-PYRAZOLE-3-CARBOXYLIC ACID

E. Neguta[1,*], S. Shova[2], G. Roman[2], A. Siminel[3], Y. Chumakov[3], V. Lozan[1]
[1]*Institute of Chemistry, Moldova State University, Chișinău, Republic of Moldova;*
[2]*"Petru Poni" Institute of Macromolecular Chemistry, Iași, Romania;*
[3]*Institute of Applied Physics, Moldova State University, Chișinău, Republic of Moldova;*
*E-mail: elena.neguta@sti.usm.md, neguta26elena@gmail.com

The chemistry of coordination polymers is of particular interest due to their wide range of applications derived from catalytic, magnetic, and sorption properties. The design of organic ligands, especially polycarboxylic ones, is essential for the formation of metal-organic frameworks with targeted structures [1]. This study presents the synthesis and characterization of four lanthanide complexes (Eu, Gd, Tb, Ho) obtained using a hybrid ligand with a central pyrazole ring: 5-(4-carboxyphenyl)-1-phenyl-1H-pyrazole-3-carboxylic acid (H_2L), which are highly relevant for the development of novel porous coordination polymers.

Experimental methods: Four isostructural coordination polymers were synthesized via the solvothermal method (in DMF or DEF, in the presence of HNO_3, at 120 °C for 72 h): $\{[Eu(HL)(L)]\cdot 20H_2O\}_n$ (**1**) [2], $\{[Gd(HL)(L)]\cdot 0.5H_2O\}_n$ (**2**), $\{[Tb(HL)(L)]\cdot 28H_2O\}_n$ (**3**), and $\{[Ho(HL)(L)]\cdot 32H_2O\}_n$ (**4**). The compounds were characterized by single-crystal and powder X-ray diffraction, FT-IR spectroscopy, thermogravimetric analysis (TG), and luminescence spectroscopy.

Crystal Structure: X-ray diffraction analysis revealed that all polymers **1-4** crystallize in the tetragonal system, adopting the $P\bar{4}n2$ space group. The ligand exhibits a tridentate coordination profile featuring simultaneously chelating and bridging carboxylate groups, leaving the nitrogen atom uncoordinated. Eight oxygen atoms derived from four individual ligand molecules saturate the metal coordination sphere, yielding a robust three-dimensional coordination network.

IR Spectroscopy and Thermal Analysis: FT-IR spectra confirmed the structural composition, highlighting bands at 3442-3448 cm^{-1} (O-H stretching vibrations of water), 1690-1650 cm^{-1} and 1450-1440 cm^{-1} (asymmetric and symmetric vibrations of carboxylate groups), and 1353-1265 cm^{-1} (vibrations specific to the pyrazole ring). The TG analysis indicated a primary weight loss step between 30 and 320 °C, corresponding to the complete elimination of water molecules, followed by thermal decomposition of the polymeric framework up to 700 °C.

Luminescence Properties: Tests utilizing a pulsed nitrogen laser (337.1 nm) revealed that polymers **1** (Eu) and **3** (Tb) exhibit relatively long relaxation processes in the visible region. Polymer **3** displayed four narrow, intense bands in the spectral range from blue to red. In comparison, polymer **4** (Ho) and the free H_2L ligand exhibited only broad, unstructured bands with post-illumination lifetimes below the system's resolution threshold (< 20 ns).

Electronic Structure and DFT Calculations: DFT modeling reveals that polymers **1**, **2**, and **4** exhibit a spin-gapless metallic character, with emissions driven by the antenna effect. Conversely, polymer **3** acts as a novel spin-gapless semiconductor featuring a unique band structure. This specific electronic architecture facilitates its complex emission profile via simultaneous ligand-to-ligand and ligand-to-metal energy transfers.

ACKNOWLEDGEMENTS. This work was funded by the Research Subprogram SSMCCLP (code 010602).

[1] S. Kitagawa, R. Kitaura, S. Noro. *Angewandte Chemie International Edition* **43** (18) (2004) 2334-2375.
[2] E. Neguta, G. Roman, S. Shova, V. Lozan. *The 10th International Conference on Materials Science and Condensed Matter Physics* (2024) 121.

SYNTHESIS AND STRUCTURAL CHARACTERIZATION OF A SERIES OF Cu(II) COMPLEXES WITH 2-SALICYLIDENHYDRAZON-THIAZOLIDIN-4-ONE AND MONO- OR BIDENTATE AMINES

M. Mînăscurtă[1,*], T. Jovmir[1], S. Shova[2], V. Lozan[1]
[1]*Institute of Chemistry, Moldova State University, 3, Chișinău, Republic of Moldova;*
[2]*"Petru Poni" Institute of Macromolecular Chemistry, Iași, Romania*
[*]E-mail: 2004.16mariaminascurta@gmail.com

The interaction of 2-salicylidenehydrazone-thiazolidin-4-one (H_2L) with Cu(II) salts in the presence of H_2O yields a coordination compound with square geometry [$CuL \cdot H_2O$] [1].

The aim of this work is to study the reactivity of [$CuL \cdot H_2O$] towards a series of amines that can act as ligands with various denticities, such as ammonia, α,α'-dipy, o-phen, γ,γ'-dipy, ethylenediamine, diazabicyclooctane (DABCO) and hexamethylenetetramine. The reactions with the first four amines, carried out in different solvents, led to the obtaining of respective four coordination compounds of Cu(II) ***1***-***4***, in which the initial water molecule was substituted by the amine. The structures for ***1***-***4*** has been resolved by X-ray diffraction method (see Fig. 1-4). The rest of the amines behave differently: ethylenediamine destroys the original compound, while DABCO and hexamethylenetetramine do not interact with [$CuL \cdot H_2O$], even if the amines are taken in tenfold excess on heating.

The X-ray study revealed that in ***1*** the copper ion is tetracoordinated with square coordination geometry, the initial water molecule being substituted by an ammonia molecule.

In ***2*** and ***3*** the central copper ion is pentacoordinated, having a distorted tetragonal pyramid geometry of the coordination polyhedron. Both amines act as bidentate chelates, occupying the apical and basal positions of the pyramid.

Compound ***4*** represents a dimer due to trans-bidentate coordination of γ,γ'-dipy ligand, thus linking two copper ions. The geometry of the coordination polyhedron is a square pyramid, where the apical position is completed by a solvent molecule (DMF).

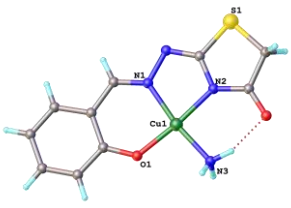


Fig. 1. [$CuL \cdot NH_3$] (***1***)

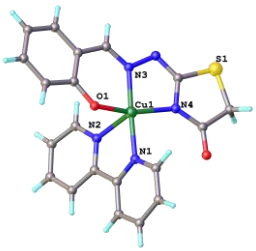


Fig. 2. [$CuL \cdot$α,α'-dipy] (***2***)

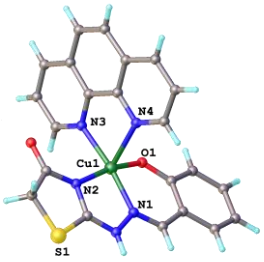


Fig. 3. [$CuL \cdot$o-phen] (***3***)

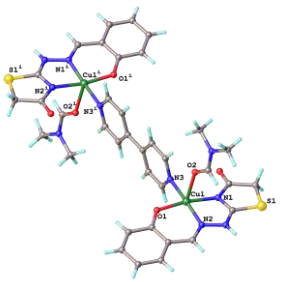


Fig. 4. [$(CuL/DMF)_2 \cdot$ γ,γ'-dipy] (***4***)

The obtained results confirm the plasticity of the coordination sphere of Cu(II) complexes.

ACKNOWLEDGEMENTS. This work was funded by the Research Subprogram SSMCCLP (code 010602).

[1] M. Mînăscurtă, T. Jovmir, S. Șova, V. Lozan. In: *Integrare prin cercetare şi inovare: conferința științifică națională cu participare internațională. Ştiinţe Exacte şi ale naturii.* Chișinău, 6-7 noiembrie 2025. Chișinău: CEP USM (2025) 714-721. Doi: https://doi.org/10.59295/spd2025e.93

EFFICIENT SYNTHESIS OF TRANS-DIOXIMES THROUGH THE CONDENSATION OF PYRIDINE AND *γ*-PICOLINE WITH DICHLOROGLYOXIME

D. Ureche[1,*], P. Bourosh[2], I. Bulhac[1]
[1]*Modova State University, Institute of Chemistry, Chisinau, Republic of Moldova;*
[2]*Moldova State University, Institute of Applied Physics, Chisinau, Republic of Moldova*
*E-mail: d.ureche@yahoo.com

Following the condensation reaction to dichlorglyoxime of pyridine and *γ*-picoline in a molar ratio of 1:2 in ethanol and dimethylformamide (DMF) medium, the synthesis of two novel coordination agents of the vic-dioxime class was achieved. The new coordination agents were subjected to elemental analysis, FT IR spectroscopy and single-crystal X-ray diffraction.

The IR spectra of compounds **1** and **2** contain many common bands. Thus, in the IR spectra, $\nu(OH)_{oxime}$ absorption bands are present in the region 3288 and 2728 cm^{-1} in **1** and 3278 and 2592 cm^{-1} in **2** that participate in the formation of intermolecular hydrogen bonds. In the spectrum of compound **2**, the absorption bands $\nu_{as}(CH_3)$ at 2994 cm^{-1} and $\nu_s(CH_3)$ at 2845 cm^{-1} are present.

The ν(C=N) absorption bands in both compounds are observed in the region 1638 cm^{-1} (**1**) and 1633 cm^{-1} (**2**), both of which are of high intensity [1]. For the aromatic rings, several absorption bands corresponding to the vibrations ν(C=C) are characteristic: 1602, 1497, 1425 cm^{-1} in **1** and 1554, 1509, 1467 cm^{-1} in **2**. Non-planing deformation strips $\delta(CH)_{nonpl.}$ characteristic of the monosubstituted aromatic ring at 708 cm^{-1} in **1** and those characteristic of the aromatic ring *p*-substituted at 811 cm^{-1} in **2** [2]. The ν(N-O) absorption bands manifest themselves at 922 cm^{-1} in **1** and 933 cm^{-1} in **2** [3].

The X-ray study established the crystal structure of two new ionic organic compounds (proligands) of the class of vic-dioximes with the molecular formulas $[DPyH_2]Cl_2$ (**1**) and $[D\gamma PicH_2]Cl_2 \cdot H_2O$ (**2**). Compound **1** crystallizes in the $P2_1/n$ spatial group, and compound **2** – in the $P2_1/c$ spatial group of the monoclinic crystal system. Both compounds are novel coordinating agents of the dioxime class, namely they are trans-dioximes. Both compound **1** and compound **2** are ionic centrosymmetric, formed from the cation $[DPyH_2]^{2+}$ for **1** and $[D\gamma PicH_2]^{2+}$ for **2** (Figures), and the positive charge formally located on the nitrogen atom of the pyridinium (or picolinium) cation is stabilized by electron delocalization in the aromatic *π* system of the heterocycle, while the electrical neutrality of the compound is ensured by two chloride anions (Cl^-), bonded by bdrogen bonds with the organic cation, which electrostatically compensates for the positive charge. In the case of compound **2**, there is another molecule of crystallizing water in the outer sphere.



(a) (b)

Figure. Crystal structure of cations in compounds **1** (a) and **2** (b).

The interatomic distances between C1 – N2 are equal to 1.449 Å for **1** and 1.447 Å for **2**, the distances C1 – N1 – 1.272 Å for **1** and 1.262 Å for **2** and the distances N1 – O1 are equal to 1.368 Å for **1** and 1.363 Å for **2**.

Acknowledgments: The results reported in this paper were obtained within two research subprograms entitled: "Synthesis and studies of new materials based on complex combinations with polyfunctional ligands and having useful application in medicine, biology and technology" (code: 010602) and "Design and fabrication of intelligent materials with advanced magnetic, adsorption, luminescent and biologically active properties" (code 011202).

[1] L.J. Bellamy. Infrared spectra of complex molecules. New York, USA. Wiley, (1958).
[2] K. Nakanishi, Infrared Absorption Spectroscopy. Nankodo, Tokyo, (1962); Mir, Moscow, (1965).
[3] A. Gordon and R. Ford, The Chemist's Companion, A Handbook of Practical Data. Techniques and References (Wiley, New York, 1972; Mir, Moscow, 1976).

SYNTHESIS AND CHARACTERIZATION OF A TRINUCLEAR HETEROMETALLIC {$CeCu_2$} CLUSTER WITH PIVALATE AND TRIETHANOLAMINE LIGANDS

O. Capbătut[1,*], D. Brüx[2], J. van Leusen[2], P. Kogerler[2], S. G. Baca[1]
[1]*Institute of Applied Physics, Moldova State University, Chisinau, Republic of Moldova*
[2]*Institute of Inorganic Chemistry, RWTH Aachen University, Aachen, Germany*
[*]E-mail: olga.capbatut@ifa.usm.md

Carboxylate-based ligands, such as pivalate, are particularly advantageous in coordination chemistry due to their flexible coordination modes, while polyfunctional amines, such as triethanolamine, can serve simultaneously as chelating and bridging units. The interplay between these complementary ligands often drives the self-assembly of well-defined heterometallic cores under appropriate synthetic conditions.

Herein, we report the synthesis, structural characterization, and magnetic properties of a new trinuclear heterometallic cluster, $[CeCu_2(piv)(H_2tea)_3(NO_3)_2]NO_3 \cdot CH_3CN \cdot H_2O$ (**1**), (where Hpiv = pivalic acid, H_3tea = triethanolamine). Compound **1** was characterized by elemental analysis, IR spectroscopy, and ESI mass spectrometry. Single-crystal X-ray analysis revealed that **1** crystallizes in the triclinic *P*-1 space group with the following unit cell parameters: a = 10.8682(4), b = 11.1731(4), c = 17.4841(5) Å, α = 78.402(3), β = 78.351(3), γ = 87.145(3)°, and V = 2036.84(13) Å^3. The structure of **1** is composed of a $[CeCu_2(piv)(H_2tea)_3(NO_3)_2]^+$ cation, a balancing NO_3^- anion, and lattice acetonitrile and water molecules. Within the cationic unit, the Ce(III) ion and two Cu(II) ions are held together by one bridging pivalate and three mono-deprotonated H_2tea^- ligands (Fig. 1). Notably, a single oxygen atom from one H_2tea^- ligand acts as a μ_3-bridge, simultaneously linking the Ce(III) ion to both Cu(II) ions. The coordination sphere of the Ce(III) atom is completed by two bidentate nitrate anions. The two Cu(II) sites exhibit different coordination environments. The Cu1 center is five-coordinate with a NO_4 donor set, comprising one nitrogen atom and two oxygen atoms from a chelating H_2tea^- ligand, one oxygen atom from a neighboring H_2tea^- ligand, and one pivalate oxygen atom**.** The Cu1–O bond distances are in the range of 1.910(3) - 2.389 Å, while Cu1–N distance is 2.061(4) Å. In contrast, Cu2 is six-coordinate with a distorted NO_5 geometry, defined by one nitrogen and three oxygen atoms from an H_2tea^- ligand, one oxygen atom from another H_2tea^- ligand, and the remaining pivalate oxygen atom. The Cu2–O bond distances range from 1.907(3) to 2.389(4) Å, and the Cu2–N bond distance is 2.038(4) Å**.** The ten-coordinate Ce(III) ion adopts a bicapped square antiprismatic geometry, with the Ce–O bond distances varying between 2.369(3) and 2.751(4) Å, and the Ce–N bond distance of 2.848(4) Å.

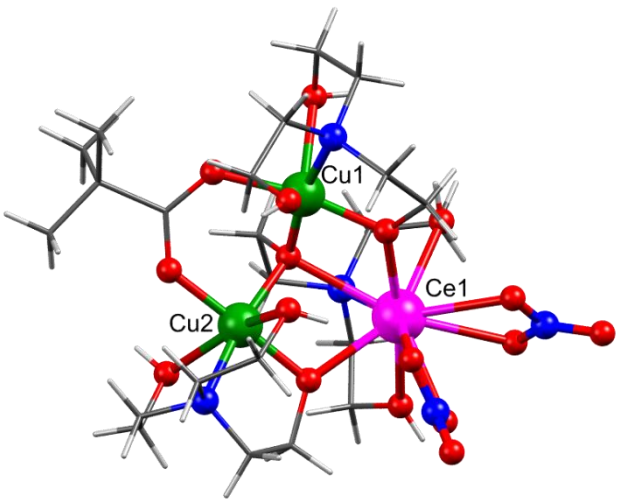


Figure 1. Structure of the cationic complex $[CeCu_2(piv)(H_2tea)_3(NO_3)_2]$.

ACKNOWLEDGMENTS. The authors are grateful for the subprogram 011202 financed by the Ministry of Education and Research of R. Moldova and the bilateral project "MultiClust" (01DK25013 and 25.80013.5007.07GER) supported by the German Federal Ministry of Education and Research (BMBF) and the National Agency for Research and Development (NARD) of R. Moldova.

A DODECANUCLEAR Mn(II, III) CLUSTER BASED ON ISOBUTYRIC AND 1,1,1-TRIS(HYDROXYMETHYL)PROPANE LIGANDS

R. Derivolcova, O. Capbătut*, V. Ch. Kravtsov, S. G. Baca
Institute of Applied Physics, Moldova State University, Chisinau, Moldova
E-mail: olga.capbatut@ifa.usm.md

Polynuclear manganese compounds continue to attract considerable interest due to their remarkable structural diversity and promising properties. Within this field, high-nuclearity manganese clusters featuring adaptable metal-oxygen cores can be strategically engineered through deliberate ligand selection. Focusing on oxygen-donor frameworks is a particularly powerful approach, opening new avenues for expanding the boundaries of crystal engineering and structural chemistry.

As a continuation of our work on the synthesis of high-nuclearity Mn(II,III) clusters [1, 2], a new dodecanuclear compound, $[Mn_{12}(\mu_4\text{-}O)_2(ib)_{10}(thmp)_4(MeO)_2(MeOH)_2]\cdot 2MeOH$ (**1**) (where Hib = isobutyric acid, thmp = 1,1,1-tris(hydroxymethyl)propane), was prepared by the reaction of the hexanuclear cluster $[Mn_6O_2(ib)_{10}(H_2O)_2(EtOH)(hmta)]$ (hmta = hexamethylenetetramine) with 1,1,1-tris(hydroxymethyl)propane. Single-crystal X-ray diffraction analysis showed that **1** crystallizes in the monoclinic $P2_1/n$ space group with the following unit cell parameters: a = 13.6985(10), b = 15.9499(8), c = 22.4880(13) Å, β = 92.200(6)°, and V = 4909.8(5) Å^3. The cluster resides around center of symmetry, thus has C_i molecules symmetry. The asymmetric unit of the crystal contains six manganese atoms, one μ_4-bridging oxygen atom, five isobutyrate ligands, two thmp^{3-} ligands, one deprotonated and one neutral methanol ligand, along with one solvate methanol molecule. The mixed-valent $\{Mn^{III}_4Mn^{II}_8\}$ core is stabilized by two central μ_4-oxide atoms (O1) and the oxygen atoms of the thmp^{3-} ligands. The peripheral coordination sphere is completed by ten chelating and bridging isobutyrate ligands, two methoxide groups, and two coordinated methanol molecules (Fig. 1). The manganese ions exhibit different oxidation states, which are well-supported by Bond Valence Sum (BVS) calculations. The four Mn^{III} centers (Mn1, Mn2, and their symmetry-equivalent sites) display a characteristically elongated octahedral geometry due to the Jahn-Teller effect. The eight Mn^{II} ions adopt more distorted six-coordinate (Mn3, Mn4, Mn5, and their symmetry-equivalent sites) and five-coordinate (Mn6 and its symmetry-equivalent site) geometries. In the crystal, solvent methanol molecules attached to the cluster via O–H···O = 2.711 Å hydrogen bonds.

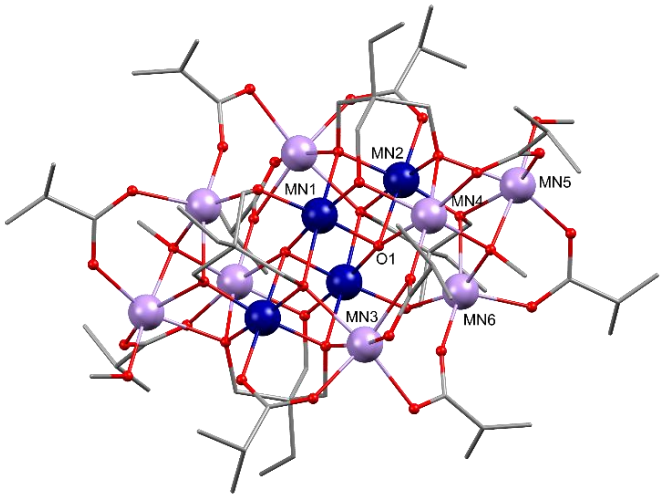


Figure 1. Structure of the $[Mn_{12}O_2(ib)_{10}(thmp)_4(MeO)_2(MeOH)_2]$ cluster in **1**.

ACKNOWLEDGMENTS. The authors are grateful for the financial support from subprogram 011202, financed by the Ministry of Education and Research of the R. Moldova, and the bilateral project "MultiClust" (01DK25013 and 25.80013.5007.07GER).

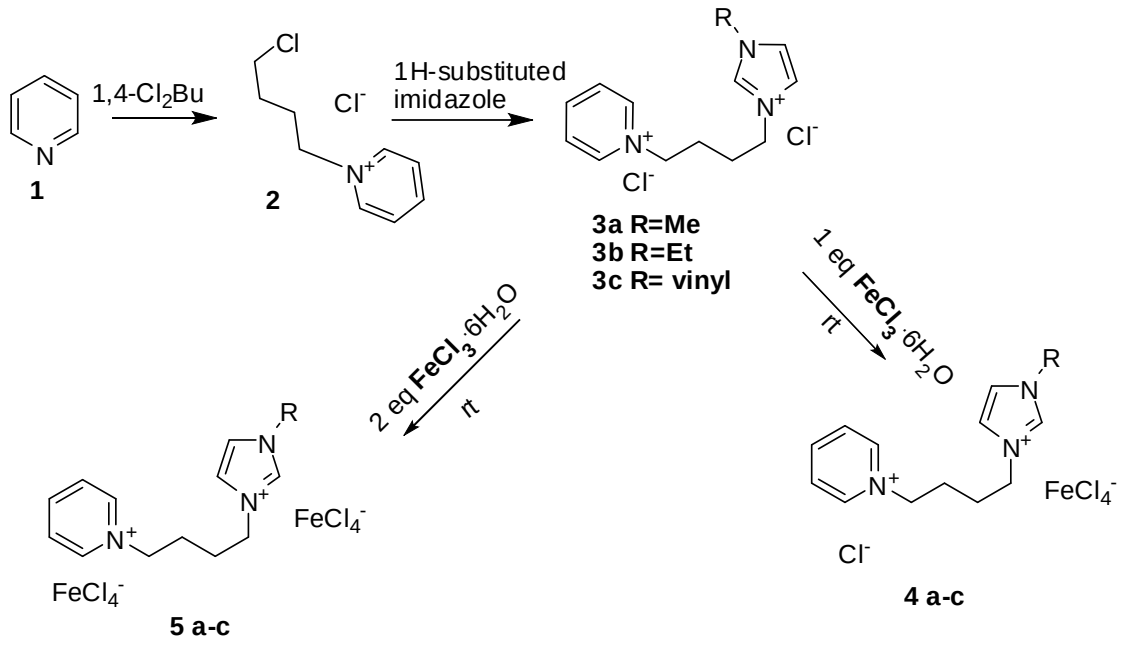
[1] M. Darii, J. van Leusen, V.Ch. Kravtsov, Y. Chumakov, K. Krämer, S. Decurtins, Sh.-X. Liu, P. Kögerler, S. G. Baca. *Cryst Growth Des*. **23(9)** (2023) 6944.
[2] M. Darii, V.Ch. Kravtsov, K. Krämer, J. Hauser, S. Decurtins, S.-X. Liu, M. Affronte, S.G. Baca, *Cryst Growth Des*. **20(1)** (2020) 33.

PREPARATION OF TETRACHLOROFERRATES(III) IONIC LIQUIDS CONTAINING IMIDAZOLIUM AND PYRIDINIUM CATIONS

M. Ceabanova[1,*], E. Stîngaci[1], N. Sucman[1], V. Pogrebnoi[1], M. Neamtu[2], F.Z. Macaev[1]
[1]*Institute of Chemistry, Moldova State University, Chisinau, Republic of Moldova;*
[2]*Alexandru Ioan Cuza" University, Iași, Romania*
*E-mail: marina.ceabanova@sti.usm.md

Over the past decade, the issue of wastewater treatment has intensified due to an increase in the amount of pollutants and the complexity of their structure; most of these pollutants do not occur naturally and are recalcitrant to oxidation, including pharmaceutical compounds. The Fenton oxidation method is the most widely used for the oxidation of organic compounds [1]. The aim of this work is to synthesize asymmetric imidazolium and pyridinium ionic liquids (ILs), prepare tetrachloroferrates(III) based on them, and select the optimal synthesis method. The Fenton oxidation method is the most widely used for the oxidation of organic compounds, including pharmaceuticals [1]. Imidazolium and pyridinium ILs **3 a–c** were synthesized according to the procedure [2]. Upon mixing with one equivalent of iron(III) chloride, compounds **4 a–c** were isolated, and with two equivalents, crystalline compounds **5 a–c** were obtained.

Scheme



Research is currently underway to investigate the possibility of using these substances as photosensitizers in the Fenton oxidation process and the results of this research will be published in other papers.

ACKNOWLEDGEMENT. This research was supported by the Moldovan National Agency for Research and Development project number 25.80013.5107.23ROMD and the Romanian Ministry of Education and Research, CNCS - UEFISCDI, project number PN-IV-PCB-RO-MD-2024-0011, within PNCDI IV.

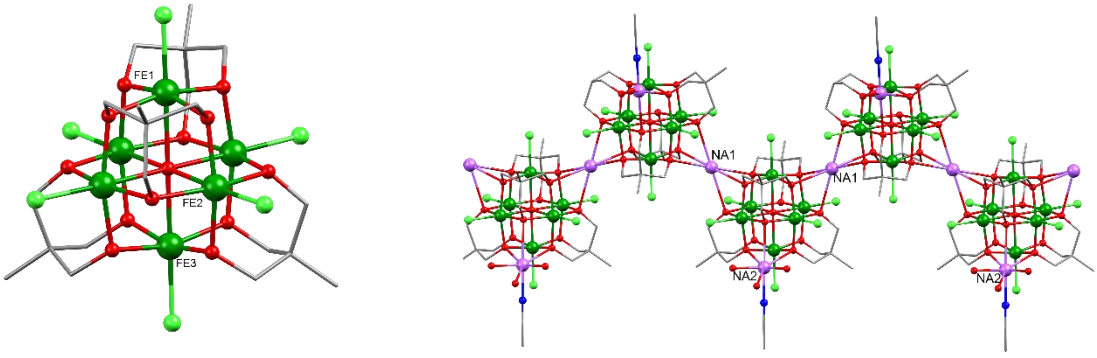
[1] N. De la Cruz, J. Giménez, S. Esplugas, D. Grandjean, L.F. de Alencastro, C. Pulgarín. *Water research*. **46(6)** (2012) 1947-1957.
[2] Jui-Cheng Chang, Wen-Yueh Ho, I.-Wen Sun, Yung-Liang Tung, Meng-Chin Tsui, Tzi-Yi Wu, Shih-Shin Liang. *Tetrahedron*. **66(32)** (2010) 6150–6155.

A 1D COORDINATION POLYMER BASED ON HETEROMETALLIC OXO-CENTERED {Na_2Fe_6} CLUSTERS: SYNTHESIS AND STRUCTURAL CHARACTERIZATION

A. Trofaila*, V. Ch. Kravtsov, S. G. Baca
Institute of Applied Physics, Moldova State University, Chisinau, Republic of Moldova
*E-mail: s.trofaila1@gmail.com

In recent years, cluster-based coordination polymers (CBCPs) have attracted significant attention due to their predictable topologies, high structural robustness, and diverse applications in catalysis, gas separation, and molecular magnetism. Unlike conventional frameworks with single-metal nodes, CBCPs utilize discrete polynuclear metal clusters as secondary building units (SBUs). This strategy allows for the precise tuning of framework properties, providing a high density of active sites and strong cooperative electronic effects. Among these systems, oxo-centered iron clusters supported by multidentate polyalcohol ligands are of particular interest, as they offer unique platforms for studying complex magnetic interactions and mimicking the active centers of iron-containing enzymes [1].

As a continuation of our work on the preparation of CBCPs [2,3], we herein report the synthesis and crystallographic characterization of a new one-dimensional (1D) coordination polymer, $\{[Na_2Fe_6O(thme)_4Cl_6(CH_3CN)(H_2O)_2]\cdot x(solv)\}_n$ (**1**). Compound **1** was prepared by an ultrasonic-assisted self-assembly reaction of iron(III) chloride hexahydrate with 1,1,1-tris(hydroxymethyl)ethane (H_3thme), and sodium azide in acetonitrile. Single-crystal X-ray diffraction revealed that **1** crystallizes in the tetragonal $I4_1/amd$ space group with the following unit cell parameters: $a = b$ =14.5126(8), c = 41.473(3) Å, and V = 8734 Å^3. The structure is built upon a hexanuclear {$Fe_6(\mu_6$-O} cluster core, in which six Fe(III) ions surround a central μ_6-oxo atom, stabilized by four fully deprotonated thme^{3-} ligands (Fig. 1a). Each Fe(III) center adopts a slightly distorted octahedral coordination geometry completed by the central μ_6-oxo atom, four bridging alkoxo oxygen atoms, and one terminal chloride ligand. BVS calculations confirm the +3 oxidation state of all iron centers, and continuous shape measures (SHAPE) quantify the distortion of the octahedral coordination sphere (OC-6 = 0.829–0.998). The Fe–O bond distances range from 1.980(6) to 2.263(10) Å, whereas the Fe–Cl bond lengths fall within the narrow range of 2.266(6)–2.284(4) Å. These hexanuclear units are further interconnected by sodium ions (Na1–O, 2.714–2.827 Å), extending the structure into 1D cluster-based coordination chains (Fig. 1b). The other sodium anion (Na2) is attached to the periphery of the hexanuclear unit, providing a charge balance.



(a) (b)

Figure 1. (a) Structure of {$Fe_6O(thme)_4Cl_6$} core and (b) a view of 1D chain formed in **1**.

ACKNOWLEDGMENTS. The authors are grateful for the subprogram 011202 financed by the Ministry of Education and Research of R. Moldova and the bilateral project "MultiClust" (01DK25013 and 25.80013.5007.07GER).

[1] S. Baca, P. Kögerler, *Chemistry* **3(1)** (2021) 314.
[2] D. Podgornii, J. van Leusen, V.Ch. Kravtsov, P. Kögerler, S.G. Baca, *CrystEngComm.* **23(30)** (2021) 5153.
[3] S.G. Baca, T. Secker, A. Mikosch, M. Speldrich, J. van Leusen, A. Ellern, P. Kögerler. *Inorg. Chem.* **52(8)** (2013) 4154.

MOLECULAR STRUCTURE OF A NEW 1D COBALT(II) COORDINATION POLYMER BASED ON SEBACIC ACID AND 4,4'-BIS(1H-IMIDAZOL-1-YLMETHYL)BENZENE

I. Voda[1,*], V. Druta[1], S. Shova[2], V. Lozan[1]
[1]*Institute of Chemistry, Moldova State University, Chisinau, Republic of Moldova;*
[2]*„Petru Poni" Institute of Macromolecular Chemistry, Iasi, Romania*
*E-mail: iravoda@gmail.com

Metal-organic frameworks (MOFs), previously referred to as coordination polymers, have emerged at the forefront of scientific research and public interest. This prominence is driven by their exceptional capacity for binding neutral guest molecules, which enables applications in gas separation and storage [1].

A new compound with chemical formula **{[Co($C_{10}H_{16}O_4$)BIX]·($C_{10}H_{18}O_4$)$_{0.5}$·H_2O}$_n$** was synthesized using hydrothermal techniques, where **$C_{10}H_{16}O_4$ =** deprotonated form of sebacic acid and **BIX** = 4,4'-bis(1H-imidazol-1-ylmethyl)benzene. The compound structure was determined by X-ray analysis showing a new one-dimensional polymer chain (*Figure 1*). The coordination number of the metal center is 5 with a distorted trigonal bipyramidal surrounding. The two carboxylic groups of the acid dianion have different roles: one coordinates Co(II) ion in a monodentate way, while the second has a bidentate chelating effect upon a neighboring metal ion. Two **BIX** molecules with a *syn* conformation coordinate the next Co(II) ion forming another chain ring and thus the polymer chain propagates in one direction. In each ring formed by **BIX** molecules there is a half of protonated sebacic acid inclusion molecule per structural unit. There are also crystallization water molecules in the crystal lattice.

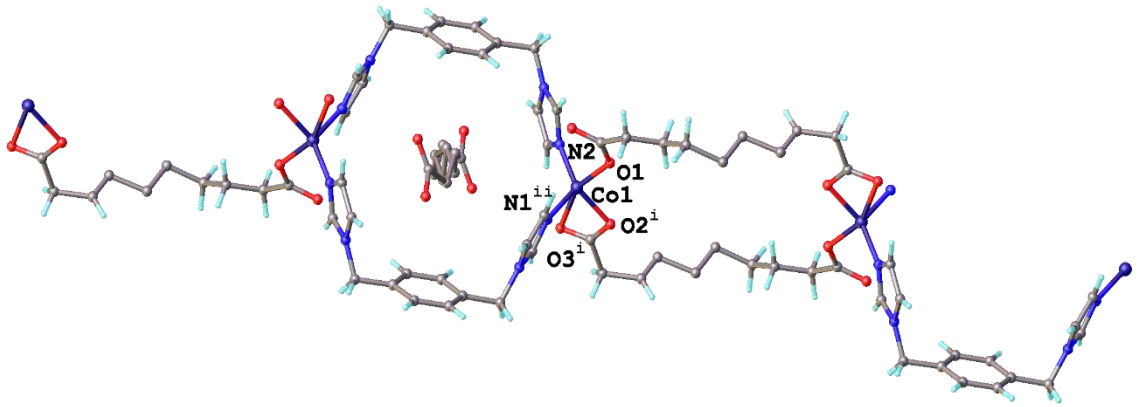


Figure 1. Polymeric structure of 1D-{[Co($C_{10}H_{16}O_4$)BIX]·($C_{10}H_{18}O_4$)$_{0.5}$·H_2O}$_n$

Thermogravimetric measurements of the compound haven't shown a clear removal of sebacic acid inclusion molecules from the channels. Thermal decomposition of the network occurs between 160 - 500 °C (87,94 %), after crystallization water molecules removal below 120 °C. The final residue is CoO (12,15 %) formed at 500 °C.

ACKNOWLEDGEMENTS. This work was funded by the Research Subprogram SSMCCLP (code 010602).

[1] O. M. Yaghi, L. Guangming, L. Hailian. *Nature* **378** (1995) 703-706.

SYNTHESIS AND LUMINESCENT PROPERTIES OF Zn(II) COORDINATION COMPOUNDS BASED ON 1,5-*BIS*(3,5-DI-TERT-BUTYL-SALICYLALDEHYDE)CARBOHYDRAZONE

Natalia Talmaci[1,*], Diana Dragancea[1,2], Sergiu Shova[3]
[1]*Moldova State University, Institute of Chemistry, 3, Academiei str., Chisinau, R. Moldova*
[2]*"C. D. Nenitzescu" Institute of Organic and Supramolecular Chemistry of the Romanian Academy, Bucharest, Romania*
[3]*"Petru Poni" Institute of Macromolecular Chemistry of the Romanian Academy, Aleea Grigore Ghica Vodă 41-A, RO-700487 Iasi, Romania*
*E-mail: natalia.talmaci@ichem.md

A growing field of coordination chemistry is the synthesis and study of coordination compounds of interest for their functional properties, including luminescence. This interest is related to applications in modern molecular electronics, especially in the production of organic light-emitting diodes (OLEDs).

Thus, two coordination compounds $[Zn_2(HL)(CH_3COO)(CH_3OH)_2]\cdot H_2O$ (**1**) and $[Zn_2(HL)((CH_3)_3CCOO)(CH_3OH)_2]\cdot H_2O$ (**2**) were obtained from the reaction of the 1,5-*bis*(3,5-di-tert-butyl-salicylaldehyde)carbohydrazone ligand H_4L with $Zn(CH_3COO)_2\cdot 2H_2O$ and $Zn((CH_3)_3CCOO)_2$ in methanol. The compounds were characterized by single-crystal X-ray diffraction, which established a new coordination mode for carbohydrazone ligands. The H_4L ligand adopts a new conformation, never seen before in the literature, in which the OH group of a salicylic aldehyde fragment is twisted at 180º towards the azometine bond. The asymmetric unit of compound **1** and the ligand coordination mode are shown in Figure A. As a result, the ligand coordinates simultaneously to 3 zinc ions through donor atoms ONO, NN, and O.

The photoluminescent properties of solid samples **1** and **2**, as well as the free ligand H_4L, were investigated at room temperature. For the free ligand, no emission was detected upon excitation. Both compounds exhibit characteristic luminescence with maxima at 468 nm for **1** (λ_{ex} = 410 nm) and 464 nm (λ_{ex} = 370 nm) for **2**, respectively (Figure B).

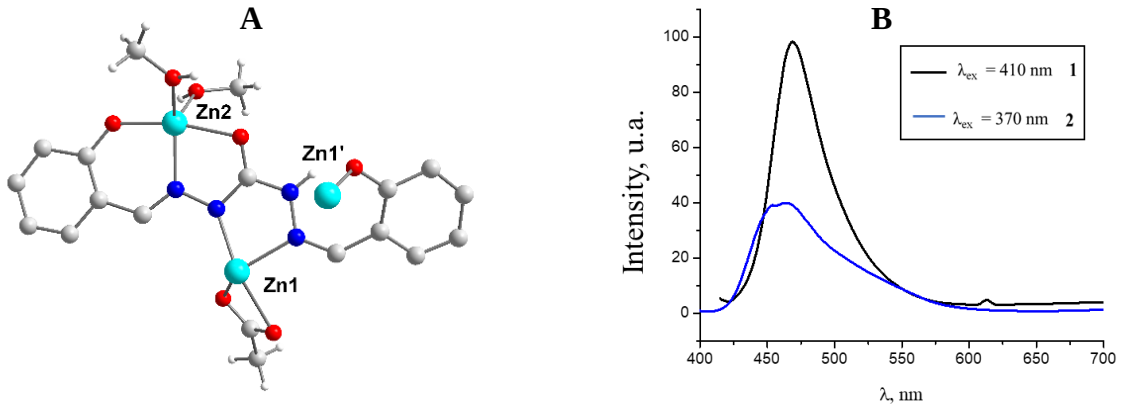


Figure 1. The asymmetric unit of compound **1 (A)** and Solid-state fluorescence spectra of compounds **1**,**2** at room temperature

For Zn(II) compounds, no emission from MLCT/LMCT excited states is expected, since the Zn(II) ion is difficult to oxidize or reduce due to its stable d^{10} configuration. Thus, the emission observed in the complexes is attributed to the intraligand $\pi\rightarrow\pi^*$ transition.

The formation of Zn(II) chelates increases the rigidity of the ligands and thus reduces the energy loss through thermal vibrational motion. These measurements show that the studied compounds exhibit luminescence, which can be used in the field of optical sensors or emission devices.

ACKNOWLEDGEMENTS. The authors are grateful to the scientific subprogram 010206 of the Institute of Chemistry of MSU, financed by the Ministry of Education and Research and ANSP.

SYNTHESIS AND CHARACTERIZATION OF COORDINATION COMPOUNDS OF Cu(II) AND Bi(III) WITH SOME BENZOYLHYDRAZONES AND AMINOPOLYCARBOXYLATE LIGANDS

B. Mindrescu[1], N. Popa[1], S. Shova[2], I. Bulimestru[1,*]
[1]*Moldova State University, Chisinau, Republic of Moldova;* [2]*Petru Poni Institute of Macromolecular Chemistry, Iasi, Romania*
*E-mail: ion.bulimestru@usm.md

In the context of intensified research on the identification of new versatile agents, interest in salicylaldehyde benzoylhydrazones and their metal complexes has increased considerably [1]. It has been demonstrated that the coordination of benzoylhydrazones to metallic ions considerably increase the affinity of the resulted complexes for biological targets [2].

Considering this, the research was focussed on the synthesis and characterization of several homometallic Cu(II) and heterometallic Cu(II)-Bi(III) coordination compounds, based on benzoylhydrazones (HL) of 3-methoxy, 4-hydroxy and 5-bromosalicylic aldehydes as Cu(II) chelating agents, along with aminopolycarboxylates (APC) as Bi(III) ligands (here APC stays for ethylenediaminetetraacetate ($edta^{4-}$), cyclohexane-1,2-diaminetetraacetate ($cdta^{4-}$) and diethylenetriaminepentaacetate ($dtpa^{5-}$)). Notably, when homometallic Cu(II) complexes with $edta^{4-}$ and $cdta^{4-}$ are concerned, as well as for $dtpa^{5-}$-based Cu(II)-Bi(III) heterometallic analogues, the molar ratio between the „cationic" copper(II)-benzoylhydrazone and „anionic" copper(II) or bismuth(III)-APC moieties was found to be equal to 2:1. Noteworthy, in heterometallic compounds containing $edta^{4-}$ and $cdta^{4-}$ ligands, with the same benzoylhydrazones, this ratio is always 1:1. The general formulas of the complexes can be given as $\{Cu(HL)\}_2Cu(APC)\cdot nH_2O$, $Cu(HL)\}_2Bi(dtpa)\cdot nH_2O$ and $Cu(HL)Bi(APC)\cdot nH_2O$.

The differences in the IR spectra of the free Schiff bases and the ones of the corresponding homo are heterometallic complexes with the same benzoylhydrazones, demonstrated that the ligands are coordinated to the metal ions. The values of $\Delta = \nu_{as}(COO) - \nu_{sim}(COO)$ higher than 200 cm^{-1} made possible the assumption that COO groups of APC ligands are predominantly coordinated in a monodentate mode, while values lower than 200 cm^{-1} demonstrate their bidentate or bidentate-bridging nature.

The molecular structure of $[Cu(L)Bi(cdta)(H_2O)_2]\cdot H_2O$ was determined by single crystal X-ray diffraction (here HL is benzoylhydrazone of 4-hydroxysalicylaldehyde). The structure is formed of separate heterobimetallic units, generated on the basis of bridging oxygen atoms of the carboxylate groups of $[Bi(cdta)(H_2O)_2]^-$ entities. The Bi(III) ions have a coordination number of eight, with the coordination sphere consisting of the set of 2N+4O atoms of the $cdta^{4-}$ ligand and oxygen atoms of two water molecules. The Cu(II) ions have a distorted square-planar geometry, coordinating tridentately a monodeprotonated benzoylhydrazone and complete their coordination sphere to four by bridging oxygen atoms of carboxylate groups of the $[Bi(cdta)]^-$ entity.

The research was carried out within the framework of project 010602 "Synthesis and study of new materials based on complex compounds with polyfunctional ligands and with useful properties in medicine, biology and technology".

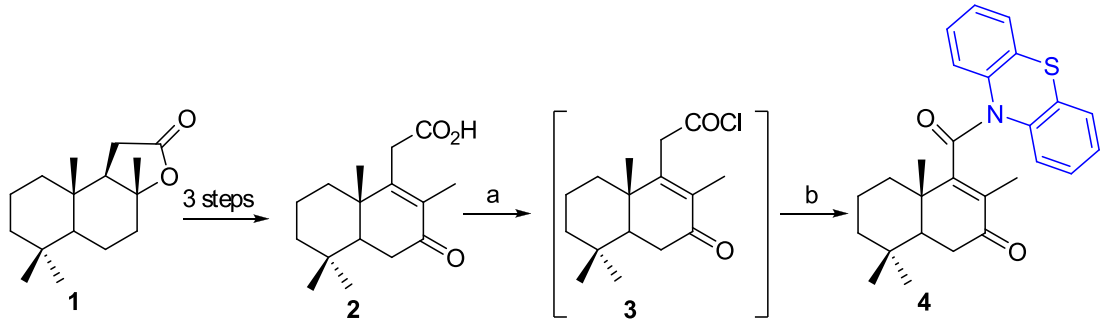
[1] M.M. Shakdofa, M.H.Shtaiwi, N. Morsy, T.M.A. Andel-Rassel. Metal complexes of hydrazones and their biological, analytical and catalytic applications: A review. *Main Group Chemistry,* **13** (2014) 187- 218.
[2] E. W. Ainscough, A. M. Brodie, W. A. Denny, G. J. Finlay, S. A. Gothe, J. D. Ranford Citotoxicity of salicylaldehyde benzoylhydrazone analogs and their transition metal complexes: quantitative structure-activity relationships. *Journal of Inorganic Biochemistry,* **77** (1999) 125-133.

SYNTHESIS AND X-RAY ANALYSIS OF *N*-(13,14,15,16-TETRANORLABD-7-OXO-8-EN-11-OYL)PHENOTHIAZINE

L. Lungu[1,*], A. Ciocârlan[1], S. Shova[2], A. Arîcu[1]
[1]*Institute of Chemistry, Moldova State University, Chisinau, Republic of Moldova;*
[2]*"Petru Poni" Institute of Macromolecular Chemistry, Iasi, Romania*
*E-mail: lidia.lungu@sti.usm.md

Phenothiazine-based molecular hybrids incorporating natural terpenoid scaffolds represent a promising class of compounds with potential biological activity. The incorporation of a natural terpene framework is expected to contribute to favourable biocompatibility while expanding the structural diversity of phenothiazine derivatives.

In the present study, an efficient synthetic approach was developed using commercially available (+)-sclareolide **1**, obtained from the natural labdane diterpene (-)-sclareol, extracted from renewable resources. The natural origin of the diterpene scaffold is expected to contribute to the high biological properties and low toxicity of the targeted hybrid.



Reagents and conditions: **a**. $(COCl)_2$, C_6H_6, r.t., 1h, Δ, 1h; **b**. Phenothiazine, CH_2Cl_2, r.t., 24h, 70%.
Scheme. Synthesis of molecular hybrid 4.

The important intermediate 13,14,15,16-tetranorlabd-7-oxo-8-en-12-oic acid **2**, was prepared in three steps from commercially available (+)-sclareolide **1** [1]. The desired tetranorlabdane phenothiazine hybrid **4** was obtained by acylation of phenothiazine with the acyl chloride **3** (generated *in situ* from acid **2**) under the conditions described in the Scheme. The structures of the synthesized compounds were confirmed by ATR-FTIR, ^1H and ^{13}C NMR spectroscopy, as well as by single-crystal X-ray diffraction analysis.

The absolute configuration of the hybrid **4** was determined by single-crystal X-ray diffraction analysis. The ORTEP representation confirms the molecular geometry and the connectivity of all atoms, with thermal ellipsoids shown at the 50% probability level.

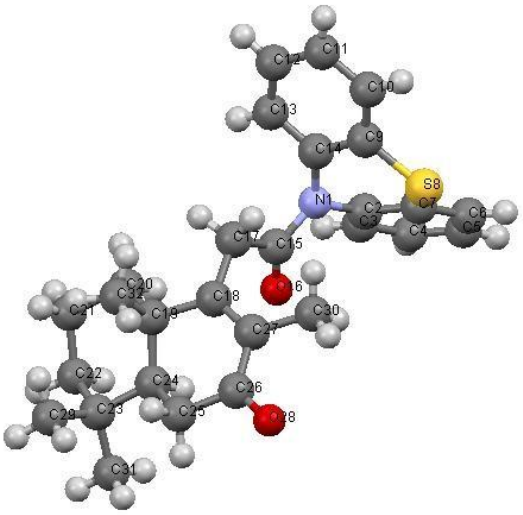


Figure 1. X-ray molecular structure of hybrid **4**.

Acknowledgements: This research was supported by the Institutional Research Program of the Moldova State University (MSU), subprogram code 010601, Chisinau, Republic of Moldova.

[1] A. Ciocarlan, L. Lungu, S. Blaja, I. Dragalin, A. Aricu. *Chemistry Journal of Moldova*. **15(2)** (2020) 69-77.

COMPUTATIONAL MODELING OF MB ADSORPTION ON THE PAH-AC SURFACE

Iolanta Balan[1], Raisa Nastas[1,*]
[1]*Institute of Chemistry, Moldova State University, Chisinau, MD-2028, Republic of Moldova*
*E-mail: ibalan02@yahoo.com

Methylene Blue (MB) is a cationic dye ($C_{16}H_{18}ClN_3S$) frequently used as an adsorbate to evaluate the treatment and pollutant removal efficiency of various porous and composite materials [1].

In this study, Density Functional Theory (DFT) was employed to investigate the adsorption of methylene blue (MB) on polyallylamine hydrochloride (PAH) and activated carbon (AC) complex (Figure 1). The calculations were performed to determine the optimized molecular geometries, adsorption energies, and charge transfer between the interacting species, providing detailed insight into the adsorption mechanism at the molecular level. These theoretical results contribute to a better understanding of the interactions governing dye adsorption and offer valuable information for the design and optimization of efficient adsorbent materials for wastewater treatment.

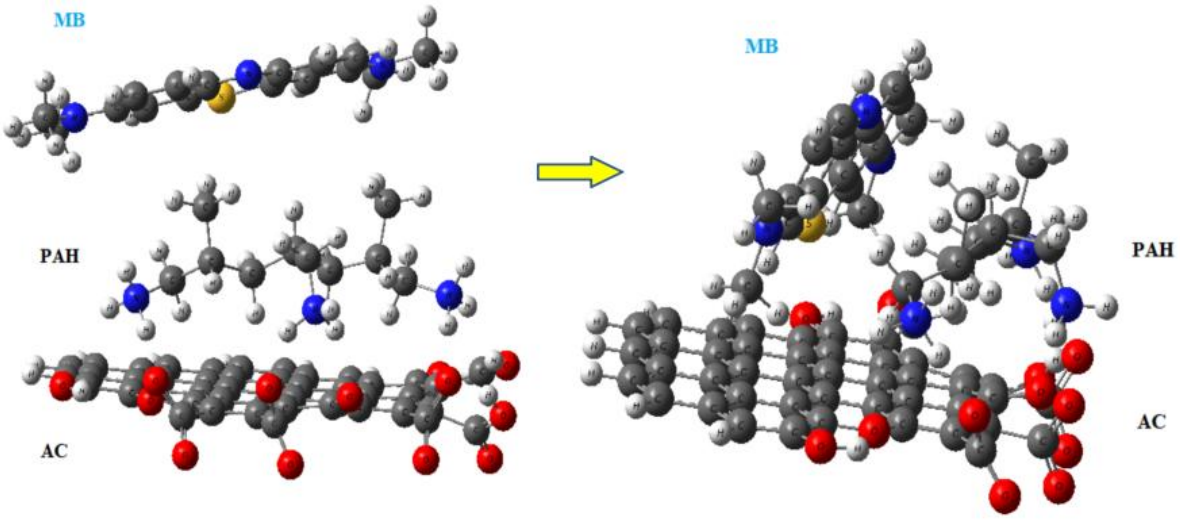


Figure 1. The adsorption of MB on PAH-AC complex.

Accordingly, the MB–PAH–AC complex, in which the functional groups of PAH and AC were protonated/deprotonated to reflect acidic solution conditions (Figure 1), was optimized using the DFT/wB97XD method with the 6-31+G(d,p) basis set implemented in the Gaussian 09 software package [2].

The calculated adsorption energy of MB on the PAH–AC complex is 658.8 kcal/mol, indicating a strong interaction between the adsorbate and the adsorbent. Mulliken population analysis revealed a net charge transfer of 0.22 e^- from the PAH–AC complex to the MB molecule upon adsorption, suggesting the presence of significant electronic interactions that contribute to the stability of the adsorption complex.

ACKNOWLEDGEMENTS. This work was supported by the Republic of Moldova Minister of Education and Research subprogram "ECOAQUA" (code 010603) of the Institute of Chemistry of Moldova State University https://ichem.md/en/ECOAQUA

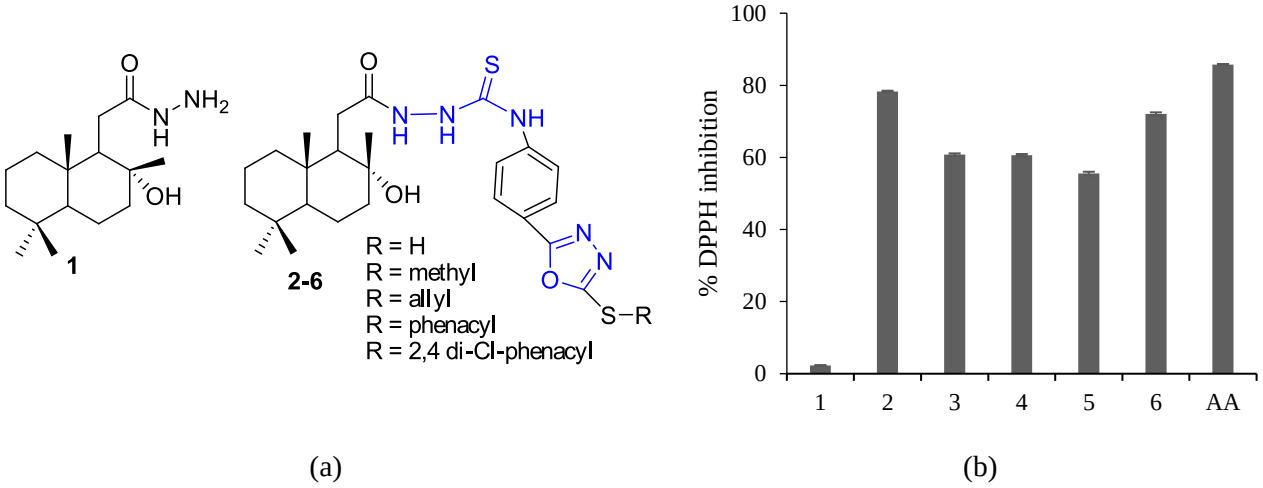
[1] D. Dimbo, M. Abewaa, E. Adino, A. Mengistu, T. Takele, A. Oro, M. Rangaraju, *Results in Engineering*, Volume 21, 2024, 101910, pp. 1-11. Doi: https://doi.org/10.1016/j.rineng.2024.101910
[2] M.J. Frisch, G.W. Trucks, H.B. Schlegel, G.E. Scuseria, M.A. Robb, et al., Gaussian, Inc.: Wallingford, 2009. https://gaussian.com/glossary/g09/

DESIGN AND ANTIRADICAL ACTIVITY OF A NOVEL MOLECULAR HYBRID BASED ON A HOMODRIMANE SCAFFOLD INCORPORATING THIOSEMICARBAZIDE AND OXADIAZOLE UNITS

L. Lungu*, C. Vicol, V. Pogrebnoi, A. Ciocârlan, A. Arîcu
[1]*Institute of Chemistry, Moldova State University, Chisinau, Republic of Moldova*
*E-mail: lidia.lungu@sti.usm.md

The synthesis of molecular hybrids combining distinct pharmacophoric units is an important strategy in modern medicinal chemistry for the development of novel bioactive compounds. Among them, terpeno–heterocyclic hybrids based on the homodrimane scaffold have attracted considerable attention due to their diverse biological activities. Numerous homodrimane derivatives incorporating benzothiazole, benzimidazole, thiadiazole, and other heterocyclic moieties have been reported with promising biological properties [1].

In this study, a novel homodrimane derivatives containing thiosemicarbazide and oxadiazole moieties **2-6** and its precursor **1**, both synthesized from commercially available (+)-sclareolide, were evaluated for antiradical activity. The structures of the synthesized compounds were confirmed by ATR-FTIR and ^{1}H, ^{13}C and ^{15}N NMR spectroscopies.



(a) (b)

Figure 1. Chemical structures of the six synthesized compounds (a) and their antiradical activity (b), expressed as the percentage of inhibition of the DPPH• at the molar ration of 0.5 mol LL/mol DPPH, in comparison with ascorbic acid (AA) (*b*).

The DPPH assay, a widely used method for evaluating antiradical activity, demonstrated that the newly synthesised compounds exhibited markedly enhanced antiradical activity compared with the parent compound **1**, which showed no free radical scavenging activity. Among the tested derivatives, **2** displayed the highest activity, scavenging approximately 80% of the DPPH• at a molar ratio of 0.5 mol LL/mol DPPH, a value comparable to that of ascorbic acid (AA; ≈85%). Compound **6** exhibited the second-highest activity, scavenging approximately 70% of the DPPH radical, followed by **3** and **4** (≈60% each), whereas **5** showed a moderate scavenging activity of approximately 55%.

ACKNOWLEDGEMENTS. Authors are grateful for the funding offered by the National Agency for Research and Development of the Republic of Moldova under the project 25.80012.5007.28TC.

[1] L. Lungu, A. Ciocarlan, I. I. Mangalagiu, A. Aricu. *Pharmaceuticals*, **18** (2025) 1411.

CRYSTAL STRUCTURES OF TWO MIXED-LIGAND COPPER(II) COORDINATION COMPOUND WITH METHYL *N*'-[(2-HYDROXYPHENYL)METHYLIDENE]-*N*-(PROP-2-EN-1-YL)CARBAMOHYDRAZONOTHIOATE

P. N. Bourosh[1], V. Ch. Kravtsov[1], I. S. Kravchuk[2], V. O. Graur[2,*], A. S. Cotovaia[2], O. S. Garbuz[3], A. P. Gulea[2]

[1]*Institute of Applied Physics, Moldova State University, Chișinău, Republic of Moldova;*

[2]*Laboratory of Advanced Materials in Biopharmaceutics and Technics, Institute of Chemistry, Moldova State University, Chișinău, Republic of Moldova;*

[3]*Laboratory of Systematics and Molecular Phylogenetics, Institute of Zoology, Moldova State University, Chișinău, Republic of Moldova*

*E-mail: vasilii.graur@usm.md

Copper(II) coordination compounds of thiosemicarbazones and isothiosemicarbazones represent a group of substances with promising biological activity. Introducing of some *N*-heteroaromatic bases into the inner sphere leads to the modification of their structure and biological properties.

The aim of this work is the determination of crystal structures of copper(II) coordination compounds: $[Cu(4\text{-Pic})(L)(NO_3)]_n$ (**1**) and $[Cu(3,4\text{-Lut})(L)NO_3]_n$ (**2**) (4-Pic – 4-methylpyridine, 3,4-Lut – 3,4-dimethylpyridine, HL – methyl N'-[(2-hydroxyphenyl)methylidene]-N-(prop-2-en-1-yl)carbamohydrazonothioate). Both of them are linear 1D coordination polymers. The molecular structure of monomeric units (Figures 1a and 1b) in these polymers are similar. In both structures the mono-deprotonated ligand L^- coordinates with copper(II) atoms in a tridentate NNO manner.

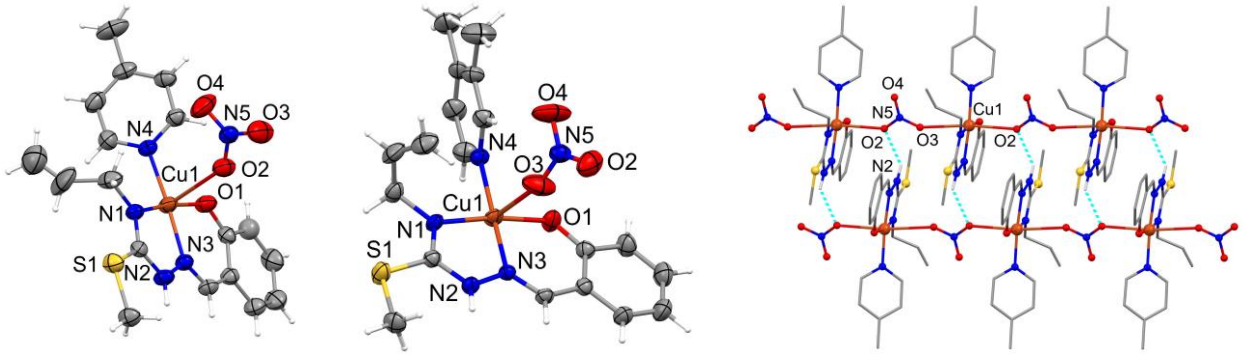


Figure 1. Molecular structures of formula units in **1** (a) and **2** (b) as well as the example of hydrogen bonded coordination polymer chains in **1** (c).

The nitrate anions bridge the neighboring copper(II) atoms, forming the linear 1D coordination polymer (Figure 1c) with Cu1···Cu1 separation of 7.4715(9) and 7.3112(6) Å in **1** and **2**, respectively. This results in a square bipyramidal metal atom environment with nitrate anions in the vertexes of bipyramid. The Cu1-O2 and Cu1-O3 distances equal 2.692(2) and 2.702(3) Å in **1**, and 2.860(3) and 2.763(2) Å in **2**. The Cu-O/N distances in the base of coordination bipyramid are essentially shorter and fall in the region 1.895-2.006 Å. The copper(II) atom deviates from the mean plane of the four donor atoms at the base of the bipyramid by 0.008 and 0.033 Å in **1** and **2**, respectively. In the crystal, **1** and **2** the neighboring linear coordination polymers are linked in the same way into double chains by N2-H···O2 hydrogen bonds which equals 2.883(3) Å and 2.908(4) Å, respectively.

Both complexes manifest antiradical activity towards ABTS cation radicals that exceeds the activity of trolox which is used as standard antioxidant drug.

ACKNOWLEDGEMENTS. This work was fulfilled with the financial support of the subprograms 010602, 010701, and 011202 of the institutional projects.

ANTIOXIDANT ACTIVITY OF IONIC LIQUIDS FORMED BY CARNITINE AND FOOD ACIDS: A COMPUTATIONAL STUDY

Iolanta Balan*, Mikhail Gorbaciov, Natalia Gorinchoy, Olga Moroz
Institute of Chemistry, Moldova State University, Chisinau, MD-2028, Republic of Moldova
*E-mail: ibalan02@yahoo.com

This study presents a quantum-chemical investigation (by the ROHF method) of the antioxidant activity of ionic liquids formed by the interaction between protonated carnitine and the anions of selected food acids [1-2]. The antioxidant activity of these ionic liquids was evaluated using the ferric reducing antioxidant power (FRAP) assay, which is based on the reduction of the ferric complex $[Fe(III)(TPTZ)_2]^{3+}$ by antioxidant compounds.

The SCF-ROHF calculations(*) revealed that the spatial distribution of the unpaired electron density in the $[Fe(III)(TPTZ)_2]^{3+}$ complex (Fig. 1) is predominantly localized on one of its terminal pyridyl rings. At the same time (Fug. 2) for both the resulting products (which describe the interactions of the complex $[Fe(III)(TPTZ)_2]^{3+}$ with an anion of gentisic acid and with the ionic pair formed by protonated carnitine and an anion of gentisic acid) the electron density of the considered unpaired electron is localized on the structural fragments describing their former gentisic acid anions. These findings indicate that the antioxidant activity originates from the food acid anion and is preserved after the formation of the ionic liquid. Thus, the studied ionic liquids retain the antioxidant capacity of the corresponding food acid anions.

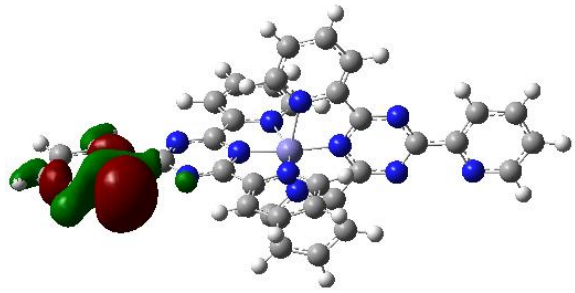


Figure 1. The spatial distribution of the unpaired electron density in the complex $[Fe(III)(TPTZ)_2]^{3+}$.

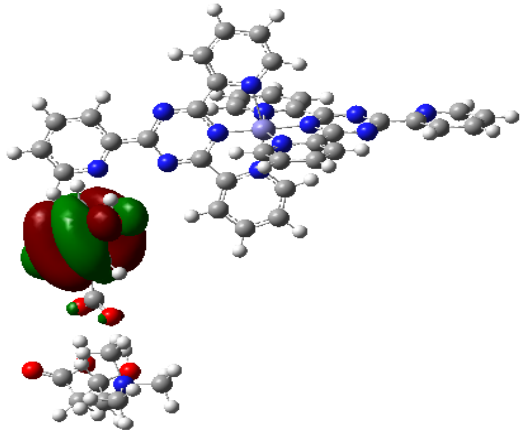


Figure 2. The spatial distribution of the unpaired electron density in the resulting products: $[Fe(III)(TPTZ)_2]^{3+}$ -protonated carnitine - anion of gentisic acid.

The geometric and electronic structure calculations of all studied molecular systems were performed by the restricted open-shell Hartree Fock method ROHF using the 6-31G(d) basis set for atomic orbitals. All calculations were performed considering the solvent (water) based on the IEFPCM option of the Gaussian09 software package [3].

ACKNOWLEDGEMENTS. This work was supported by the Republic of Moldova Minister of Education and Research subprogram "ECOAQUA" (code 010603) of the Institute of Chemistry of Moldova State University https://ichem.md/en/ECOAQUA

[1] K. Czerniak, J. Pernak, *Chemistry Select*, **6** (2021) 1994-2001. Doi: https://doi. org/10.1002/slct.202100420
[2] M. Gorbachev, N. Gorinchoy, I. Balan, *Chemistry Journal of Moldova*, **17(1)** (2022) 24-30. Doi: http://doi.org/10.19261/cjm.2021.919
[3] M.J. Frisch, G.W. Trucks, H.B. Schlegel, G.E. Scuseria, M.A. Robb, et al., Gaussian, Inc.: Wallingford, 2009. https://gaussian.com/glossary/g09/

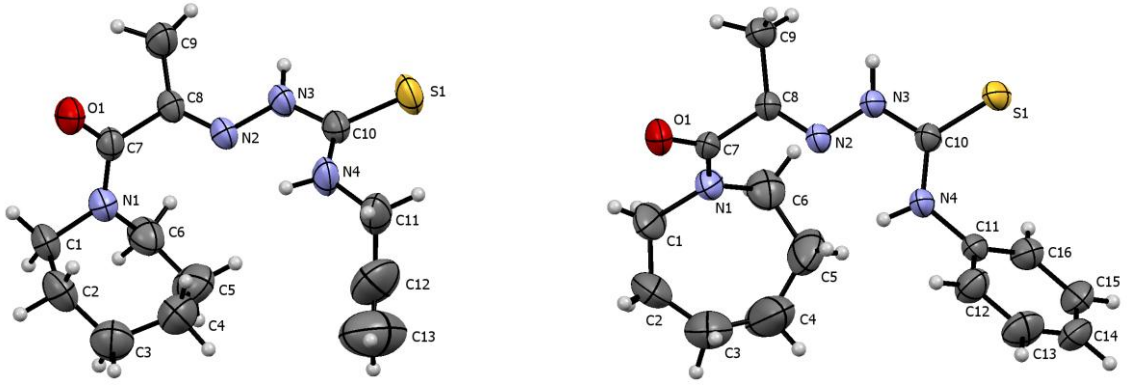
CRYSTAL STRUCTURES OF TWO SUBSTITUTED PYRUVAMIDE THIOSEMICARBAZONES

E. I. Melnic[1], P. N. Bourosh[1], I. I. Graur[2,*], V. O. Graur[2], O. S. Garbuz[3],
V. I. Tsapkov[2], A. P. Gulea[2]
[1]*Institute of Applied Physics, Moldova State University, Chișinău, Republic of Moldova;*
[2]*Laboratory of Advanced Materials in Biopharmaceutics and Technics, Institute of Chemistry, Moldova State University, Chișinău, Republic of Moldova;*
[3]*Laboratory of Systematics and Molecular Phylogenetics, Institute of Zoology, Moldova State University, Chișinău, Republic of Moldova*
*E-mail: ulchina.ianina@usm.md

Pyruvamide thiosemicarbazones represent a class of bioactive compounds whose activity depends on their structure. Modification of the substituents in these substances can lead to an enhance of different biological properties, including antioxidant and antiproliferative properties.

The aim of this work is the determination of crystal structures of two substituted pyruvamide thiosemicarbazones, namely 2-[1-(azepan-1-yl)-1-oxopropan-2-ylidene]-N-(prop-2-en-1-yl)hydrazine-1-carbothioamide (**HL^1**) and 2-[1-(azepan-1-yl)-1-oxopropan-2-ylidene]-N-phenylhydrazine-1-carbothioamide (**HL^2**).

Single-crystal X-ray diffraction study indicates that the thiosemicarbazone **HL^1** crystallizes in the triclinic *P*–1 space group and the thiosemicarbazone **HL^2** crystallizes in the monoclinic $P2_1/c$ space group. Structural analysis shows that the thiosemicarbazone fragment is nearly planar in both cases and they adopt an *E*-configuration along N3-C10 bond. This configuration is stabilized by N(4)–H···N(2) intramolecular hydrogen bonds.



a **b**

Figure 1. The view of molecules **HL^1** (a) and **HL^2** (b) with numbering scheme. Thermal ellipsoids are drawn at the 50% probability level.

Both thiosemicarbazones show antiradical activity towards ABTS cation radicals and antiproliferative activity towards THP-1 human leukemia cell line. The calculated IC_{50} values towards $ABTS^{\bullet+}$ are 3.9±0.2 μM (**HL^1**) and 12.0±0.1 μM (**HL^2**). The calculated IC_{50} values towards THP-1 cell line are 3.9±0.4 μM (**HL^1**) and 0.18±0.01 μM (**HL^2**). Thus, the substituent at the N4 atom in the thiosemicarbazide fragment affects the bioactivity. Both thiosemicarbazones surpass Trolox (standard antioxidant) by their antiradical activity. **HL^2** shows better antiproliferative activity that exceeds the activity of both **HL^1** and doxorubicin, a standard anticancer drug with IC_{50} towards THP-1 cell line of 0.32±0.06 μM.

ACKNOWLEDGEMENTS. This work was fulfilled with the financial support of the subprograms 010602, 010701, and 011202 of the institutional projects.

CRYSTAL STRUCTURES OF A PYRUVAMIDE THIOSEMICARBAZONE AND ITS NICKEL(II) COORDINATION COMPOUND

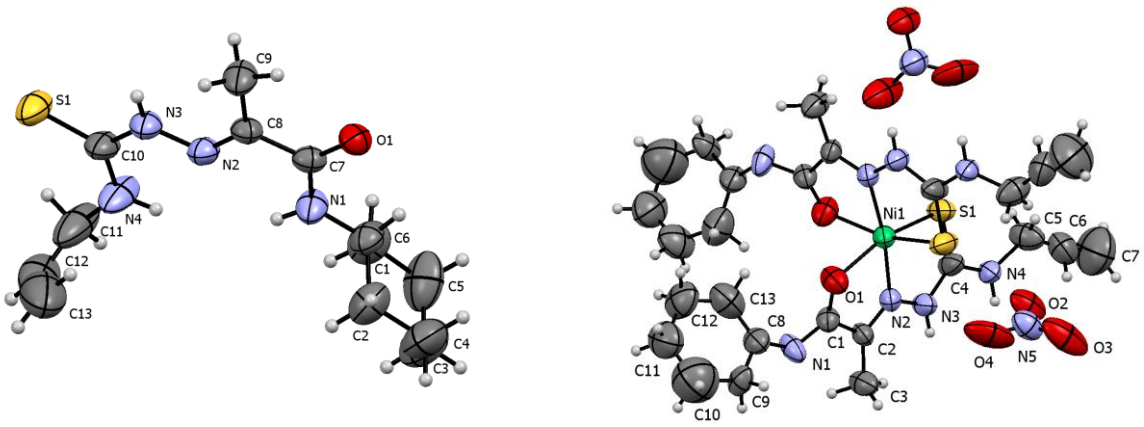
E. I. Melnic[1], P. N. Bourosh[1], I. I. Graur[2,*], V. O. Graur[2], O. S. Garbuz[3], V. I. Tsapkov[2], A. P. Gulea[2]

[1]*Institute of Applied Physics, Moldova State University, Chișinău, Republic of Moldova;*
[2]*Laboratory of Advanced Materials in Biopharmaceutics and Technics, Institute of Chemistry, Moldova State University, Chișinău, Republic of Moldova;*
[3]*Laboratory of Systematics and Molecular Phylogenetics, Institute of Zoology, Moldova State University, Chișinău, Republic of Moldova*
*E-mail: ulchina.ianina@usm.md

Among pyruvamide thiosemicarbazones, that are derivatives of naturally occurring pyruvic acid, there are substances with promising bioactivity. In many cases their coordination to some 3d metal ions leads to an increase of bioactivity that hugely depends on the nature of substituents in thiosemicarbazone ligand, nature of the central metal ion and the structure of complex.

The aim of this work is the determination of crystal structures of N-cyclohexyl-2-{2-[(prop-2-en-1-yl)carbamothioyl]hydrazinylidene}propanamide (**HL**) and bis(N-cyclohexyl-2-{2-[(prop-2-en-1-yl)carbamothioyl]hydrazinylidene}propanamide)nickel(II) nitrate ($[Ni(HL)_2](NO_3)_2$, **1**).

Single-crystal X-ray diffraction study indicates that the thiosemicarbazone **HL** crystallizes in the monoclinic $P2_1/c$ space group and adopts an *E*-configuration along N3-C10 bond. The tridentate **HL** ligand in its *Z*-configuration coordinates to the nickel center through O, N, and S donor atoms. Compound **1** crystallizes in the orthorhombic *Pbcn* space group. The Ni(1) center adopts a distorted octahedral geometry, coordinated by two **HL** ligands through $O_2N_2S_2$ donor sets. The Ni–O, Ni–N, and Ni–S distances are 2.090, 2.018, and 2.378 Å, respectively. Each ligand forms two fused five-membered NiSCNN and NiNCCO metallacycles.



a **b**

Figure 1. The view of molecules **HL** (a) and $[Ni(HL)_2](NO_3)_2$ (**1**) (b) with numbering scheme. Thermal ellipsoids are drawn at the 50% probability level.

Both thiosemicarbazone **HL** and its nickel(II) coordination compound **1** show antiradical activity towards ABTS cation radicals. **HL** exhibits a moderate antiradical activity with IC_{50} value of 84.2±4.5 μM. Meanwhile, its coordination to the nickel(II) ions leads to a huge increase of antiradical properties with IC_{50} = 8.6±0.3 μM. It makes complex **1** ten-times more active than **HL** and four-times more active than trolox, a standard antioxidant used as a reference drug.

ACKNOWLEDGEMENTS. This work was fulfilled with the financial support of the subprograms 010602, 010701, and 011202 of the institutional projects.

KAEMPFEROL-BASED BIOCOMPOSITES: PREPARATION, CHARACTERIZATION AND APPLICATION IN CORNEAL HEALING

A. Besliu[1], A. Chiaburu[1], I. Casian[1], A. Casian[1], I. Coretchi[1], A. Sulaiman[1], D. Peptanariu[2], M.-F. Zaltariov[2], B.-I. Ciubotaru[2]
[1]*Nicolae Testemitanu State University of Medicine and Pharmacy, Chisinau, Republic of Moldova;*
[2]*Petru Poni Institute of Macromolecular Chemistry, Iaşi, Romania.*
*E-mail: alina.besliu@usmf.md

Corneal blindness is the second most common form of blindness following cataracts worldwide. Corneal transplantation is currently the only treatment option available. However, it increases the chance of developing bacterial keratitis, which can impair the healing process and possibly result in transplant failure. Another major issue with corneal transplantation is the challenge of re-epithelialization, while the occurrence of postoperative immune rejection is still as high as 50% for inflammatory and vascularized beds [1]. Since the cornea is a thin tissue, the inclusion of a physical carrier in corneal restoration materials may result in a reduction in mechanical qualities, biocompatibility, or optical performance (the human cornea's light transmittance is approximately 87%). The optimal scaffold for tissue engineering should have appropriate mechanical qualities, high optical clarity, and immunologic tolerance. Recent advances in corneal tissue engineering have attempted to use cell- and matrix-based approaches both able to mimic the structure and the function of the cornea.

Our strategy was to develop new hybrid composites using multicomponent matrices based on natural biopolymers (chitosan, gelatin, glycerol and starch) as suitable substrates for corneal constructs. While glycerol possesses strong antimicrobial properties and acts as a plasticizer for biocomposite matrices, also increasing the corneal surface wettability, chitosan can promote cell phenotypes used in corneal keratinocytes, and starch can improve intraocular transparency of gelatin matrix. More than that the challenges related to neovascularization and fibrosis due to the extreme inflammation is essential to be neutralized to promote corneal repair and regeneration.

Therefore, kaempferol formulations with natural deep eutectic solvents which ensure the compatibilization with the multicomponent matrix, reduce brittleness and ensure wettability were prepared and mixed together with the polymeric solutions at a concentration of 60%. The resulting matrices as standing transparent films were investigated from structural, mechanical, dielectric, optical and biological perspectives with the aim of developing and selecting the best materials' formulations to support corneal regeneration.

ACKNOWLEDGEMENT. „This work was supported by a grant of the Ministry of Research, Innovation and Digitization, CNCS – UEFISCDI, project PN-IV-PCB-RO-MD-2024-0372, within PNCDI IV".

[1] Y. Liu, X. Liu, M. Wu, P. Ji, H. Lv, L. *International Journal of Biological Macromolecules* **121** (2019) 233–238.

GOLD NANOPARTICLE-CONJUGATED PHTHALOCYANINES (AuNPs)

Victor Suman[1, 2,*]
[1] *Doctoral School of Natural Sciences, Moldova State University, 60 A. Mateevici Str., MD-2009 Chisinau, Republic of Moldova;*
[2] *D. Ghitu Institute of Electronic Engineering and Nanotechnologies, Technical University of Moldova, Academiei Str. 3/3, MD-2028 Chisinau, Republic of Moldova*
*E-mail: victor.suman@iien.utm.md

Phthalocyanines are well-established photosensitizers in photodynamic therapy (PDT), owing to their strong absorption in the red and near-infrared spectral regions, high singlet oxygen generation efficiency, and excellent photostability. Recent advances have focused on the covalent conjugation of phthalocyanines, particularly zinc phthalocyanines, with a wide range of bioactive molecules to improve their selectivity, therapeutic efficacy, and multifunctionality. Such conjugates combine the efficient generation of reactive oxygen species (ROS) with targeted delivery and controlled release, resulting in enhanced treatment precision and reduced toxicity toward healthy tissues.

Conjugation with chemotherapeutic agents and gold nanoparticles (AuNPs) has attracted considerable attention because these hybrid systems exhibit receptor-mediated cellular uptake, pH-responsive behavior, and synergistic therapeutic effects capable of overcoming multidrug resistance. Furthermore, targeting moieties such as chitosan, chondroitin sulfate, tannic acid, sodium citrate, and carbohydrates have been employed to exploit receptor-mediated endocytosis, thereby enhancing cellular internalization and improving therapeutic performance. In addition to their photodynamic activity, these multifunctional conjugates possess intrinsic fluorescence properties, enabling image-guided therapy through simultaneous diagnostic imaging and treatment.

In this study, we report the synthesis of an asymmetric zinc phthalocyanine derivative, $ZnPc(COOH)_4$, and its conjugation with biologically directed carriers and gold nanoparticles (AuNPs) to enhance biocompatibility and increase the accumulation of the photosensitizer within the target tissue. The obtained hybrid nanostructures provide an additional level of selectivity while reducing the effective concentration of the photosensitizer required for therapeutic action.

The proposed strategy represents a promising approach toward the development of next-generation multifunctional materials for photodynamic therapy and biomedical imaging. Owing to the unique optical properties, excellent biocompatibility, aqueous dispersibility, and facile surface functionalization of gold nanoparticles, ZnPc–AuNP conjugates offer significant potential as smart theranostic platforms. These hybrid systems combine efficient ROS generation with targeted delivery of the photosensitizer, providing improved therapeutic selectivity and enhanced treatment efficacy while minimizing adverse side effects.

ACKNOWLEDGEMENTS. This paper was supported financially by the project PN-IV-P8-8.3-ROMD-2023-0048 (DSUPRAMED), within PNCDI IV.

ADVANCES IN KAEMPFEROL FORMULATIONS: EXTRACTION, STRUCTURAL CHARACTERIZATION AND BIOLOGICAL ACTIVITY

I. Coretchi[1], A. Casian[1], I. Casian[1], A. Besliu[1], A. Chiaburu[1], C. Ceban[1], D. Peptanariu[2], M. Balan-Porcarasu[2], S.L. Nica[2], M.-F. Zaltariov[2]
[1]*Nicolae Testemitanu State University of Medicine and Pharmacy, Chisinau, Republic of Moldova;*
[2]*Petru Poni Institute of Macromolecular Chemistry, Iaşi, Romania.*
*E-mail: ana.casian@usmf.md

A normal cornea is avascular and translucent. Corneal neovascularization can impair vision, leading to blindness and transplant failure. The risk for neovascularization is promoted in myopia corrected with contact lenses which also enhance the corneal hypoxia, but also is caused by inflammation. As a result, treating corneal neovascularization has a major impact on the public health. The easy route against cornea neovascularization is the use of ophthalmic eye-drop formulations. The main limitation of their administration is the retention dose for a long-lasting effect. It was demonstrated that only 5% of the eye-drop solutions are maintained in the ocular tissue after five minutes. Increasing drug bioavailability in ocular tissue is currently the main focus of ophthalmology therapy.

In this study we used an original extraction procedure to obtain kaempferol from a very promising natural source – horseradish leaves. Kaempferol exhibits a dual role: inhibition of angiogenesis and reducing the inflammation in cornea.

The idea of this work was to prepare new formulations based on kaempferol using natural deep eutectic solvents, which not only provide a good solubilization of kaempferol, also a good interaction with corneal surface and maintain a good dosage during the treatment.

Different eutectic mixtures with kaempferol 1% were designed and prepared by mixing various ratios of choline chloride, urea, glycerol, PEG and β-cyclodextrin. The eutectic mixtures were characterized by FTIR, 1D and 2D NMR, rheology, antimicrobial and cytotoxicity and the results are discussed highlighting the role of the eutectic mixture in the solubilization and stabilization of kaempferol to produce a therapeutic effect upon administration.

ACKNOWLEDGEMENT. This work was supported by a grant of the Ministry of Research, Innovation and Digitization, CNCS – UEFISCDI, project PN-IV-PCB-RO-MD-2024-0372, within PNCDI IV.

MICROWAVE ASSISTED REACTION OF FLUORESCENT PYRROLOQUINOLINE BUILDING BLOCKS

G. Zbancioc[1,*], A. M. Birgoanu[1], C. Moldoveanu[1], I. I. Mangalagiu[1], G. Tataringa[2], A.M. Zbancioc[2]
[1] *„Al. I. Cuza" University of Iași, Faculty of Chemistry, 11 Carol 1st Boulevard, 700506, Romania;*
[2] *"Gr. T. Popa" University of Medicine and Pharmacy, Faculty of Pharmacy, Str. Universitatii 16, 700115 Iași, Romania*
*E-mail: gheorghita.zbancioc@uaic.ro

In recent years, azaheterocycle derivatives have been reported to exhibit a wide range of applications in medicinal chemistry, notably as antimicrobial, anticancer, antioxidant, and anti-HIV agents [1]. Interest in pyrroloquinoline derivatives also stems from their highly efficient fluorescence emission [2]. This property makes them attractive materials for optoelectronic applications, such as blue organic light-emitting diodes (OLEDs) [3], while the combination of their biological and optical properties suggests promising applications as fluorescent biomarkers [4].

In this study, substituted pyrrolo[1,2-a]quinoline derivatives were synthesized and characterized using both conventional thermal heating and microwave irradiation. The resulting compounds were subsequently brominated to functionalize the heterocyclic ring. This crucial step generated reactive intermediates, enabling the introduction of new structural fragments with potential fluorescent properties. Thus, the binding of these fluorescent molecules to various macromolecules (amino acids, peptides, proteins, DNA) is watched closely.

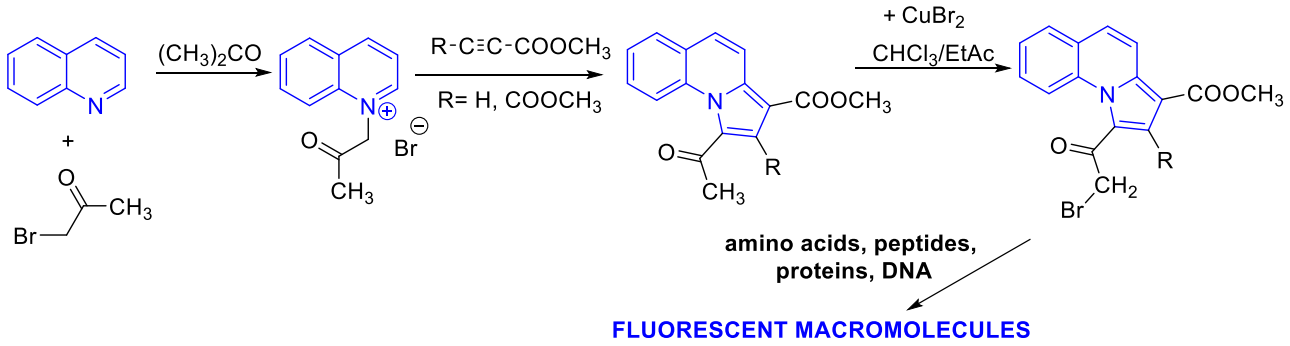


Figure 1. The chemical reaction equation for the preparation of fluorescent pyrroloquinoline building blocks

All reactions were carried out both under conventional TH and MW irradiation, in order to study the reaction selectivity. Structural confirmation was achieved by NMR spectroscopy (^{1}H, ^{13}C, and two-dimensional 2D COSY, HMQC, and HMBC experiments).

ACKNOWLEDGEMENTS. The authors express their gratitude to the RECENT AIR project (grant MySMIS no. 127324) for facilitating access to the laboratory, and to the POSCCE-O 2.2.1 project (SMIS-CSNR 13984-901, no. 257/28.09.2010, CERNESIM) for supporting the NMR experiments.

[1] C. Sandeep, P. Basavaraj, K.N. Venugopala, S.K. Rashmi, V. Rashmi, B. Odhav. *Asian J. Chem.* **28** (2016) 1043–1048. Doi: https://doi.org/10.14233/ajchem.2016.19582.
[2] T. Mitsumori, I.M. Craig, I.B. Martini, B.J. Schwartz, F. Wudl. *Macromolecules* **38** (2005) 4698−4704, Doi: https://doi.org/10.1021/ma048091y.
[3] T. Mitsumori, M. Bendikov, O. Dautel, F. Wudl, T. Shioya, H. Sato, Y. Sato. *J. Am. Chem. Soc.* **126** (2004) 16793−16803, Doi: https://doi.org/10.1021/ja049214x.
[4] L. Wu, X. Qu. *Chem. Soc. Rev.* **44** (2015) 2963−2997, Doi: https://doi.org/10.1039/C4CS00370E.

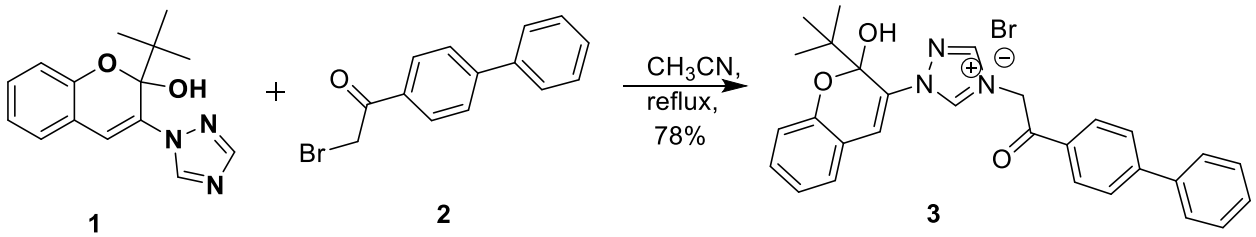
NOVEL QUATERNARY AMMONIUM SALT OF 2-*TERT*-BUTYL-3-(1*H* -1,2,4-TRIAZOL-1-YL)-2*H*-CHROMEN-2-OL WITH POTENT ANTIFUNGAL ACTIVITY

M. P. Ceabanova[1], E. P. Stingaci[1*], E. C. Gorincioi[1] , G. Balan[2], N. E. Dina[3], F. Z. Macaev[1]
[1]*Moldova State University, Institute of Chemistry, Chisinau, Moldova*
[2]*Nicolae Testemitanu State University of Medicine and Pharmacy, Department of Preventive Medicine, Chișinău, Moldova*
[3] *National Institute for Research and Development of Isotopic and Molecular Technologies, Department of Isotopic and Molecular Technologies, Cluj-Napoca, Romania*
*E-mail: eugenia.stingaci@sti.usm.md

Triazole-based molecules exhibit a broad spectrum of pharmacological effects, being particularly renowned by their antifungal properties [**Error! Bookmark not defined.**]. At the same time, derivatives bearing both triazole unit and structural scaffold of 2*H*-chromene were reported as lead antimicrobials [2].

In continuation of our previous contribution to this field [3], we now report on the synthesis of a novel ammonium salt, incorporating both mentioned pharmacophores, aimed at expanding the biological potential of active 2*H*-chromen-2-ol derivatives, with improved water solubility.

Target compound, 1-(2-(tert-butyl)-2-hydroxy-2H-chromen-3-yl)-4-(2-(3,4-dichlorophenyl)-2-oxoethyl)-1*H*-1,2,4-triazol-4-ium bromide (**3)** was prepared according to the Scheme. Its structure was confirmed by IR, NMR, Raman and SERS spectroscopic data and by elemental analysis.



Scheme. Synthesis of 1-(2-(tert-butyl)-2-hydroxy-2H-chromen-3-yl)-4-(2-(2,4-dichlorophenyl)-2-oxoethyl)-1H-1,2,4-triazol-4-ium bromide (**3)**.

Compound (**3**) has demonstrated a good activity against three species of the yeast-like fungi of the genus *Candida*, with MICs = 115.90 μM and proved to be more selective against severe, life-threatening fungal pathogen *Cryptococcus neoformans* CECT 1043 with the MIC value of 57.97 μM, comparable to that of reference drug Fluconazol (MIC = 52.32 μM).

ACKNOWLEDGEMENTS. This study is supported by the research subprogram "Chemical study of secondary metabolites from local natural sources and valorization of their application potential basing on broadening molecular diversity with multiple functionality (MetNatVal)" (code 010601) funded by the Ministry of Education and Research of the Republic of Moldova. N.E.D would like to acknowledge the financial support through the "Nucleu" Program within the National Research Development and Innovation Plan 2022–2027, Romania, carried out with the support of MEC, project no. 27N/03.01.2023, component project code PN 23 24 01 02.

[1] S. Kumar, H., Kavitha. Mini-Reviews in Organic Chemistry 10 (2013) 40-65.
[2] K. Kushwaha, N. Kaushik, S.C. Jain. Bioorg. Med. Chem. Lett. 24 (2014) 1795–1801.
[3] M. Zveaghintseva, E. Stingaci, S. Pogrebnoi *et al.* Molecules 14 (26) (2021) 26144303.

NEW BIS-IMIDAZOLIUM IONIC LIQUIDS WITH DIFFERENT ANIONS

V. S. Pogrebnoi[1,*], N.Sucman[1], M. Ceabanova[1], Neamtu M.[2], S. Shova[3], F. Z. Macaev[1].
[1]*Moldova State University, Institute of Chemistry, Chisinau, Republic of Moldova;*
[2]*„Alexandru Ioan Cuza" University, Iaşi, Romania;*
[3]*„Petru Poni" Institute of Macromolecular Chemistry, Iasi, Romania*
*E-mail: seva.antivirus@gmail.com

Imidazole and its derivatives possess various useful properties [1]. Imidazole takes a special place among synthetic chemists due to its chemical properties, namely, pretty readily to form ionic liquids *via* quaternization reaction [2]. Recently, ionic liquids found application in different area of science and technology [1]. Herein, we bring and discuss the synthesis of novel ionic liquids with imidazole fragment, and its structures have been determined by various physicochemical methods. Our further target is to try **2** and **3** as catalysts for degradation of some pharmaceuticals in aqueous media.

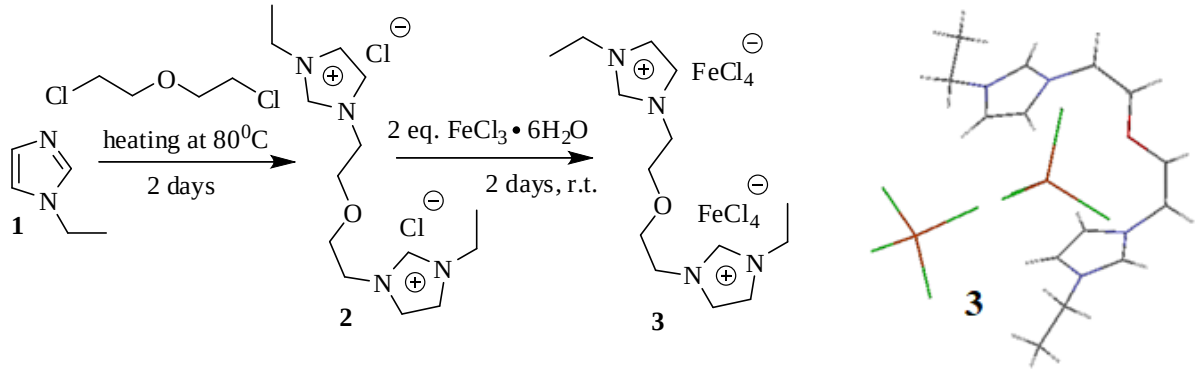


Figure 1. Synthesis of ionic liquids **2** and **3** and the structure of **3**.

The heating of N-ethylimidazole with dichloride on water bath for two days yielded brown oil **2** and its structure was determined by NMR. It was found that the reaction doesn't occur in solvents (acetonitrile, toluene). The next step involved in mixing of **2** with two equivalents of ferrum chloride hexahydrate with next maintaining at room temperature for 24 hours. After getting of the drafted water and drying in a desiccator for two days, yellow-brown amorphous crystals were obtained. For these crystals was recorded an IR spectrum, but its structure was established and confirmed using X-ray data.

Thus, we have demonstrated and realized the synthesis of new ionic liquids **2** and **3**, which may find application as catalysts in the degradation of pharmaceuticals in water or other media.

ACKNOWLEDGEMENT. The authors are grateful for the funding of this research project number 25.80013.5107.23ROMD and the Romanian Ministry of Education and Research, CNCS-UEFISCDI, project number PN-IV-PCB-RO-MD-2024-0011, within PNCDI IV.

[1] C. Huijiao, H. Yimin. *Journal of Molecular Liquids* **319** (2020) 114354.
[2] C.R. Dunbar, F.G. West. *Canadian Journal of Chemistry* **93(4)** (2015) 468-476.

MECHANICAL PROPERTIES MODIFICATION OF 316L STAINLESS STEEL AFTER SHOT PEENING TREATMENT

M. Hitsiuc[1], O. Shikimaka[1,*], N. Serban[2], C. Pyrtsac[1, 3], N. Kazak[1], A. Cuharuc[1]
[1]*Institute of Applied Physics, Moldova State University, Chisinau, Moldova;*
[2]*Material Science and Engineering Faculty, National University of Science and Technology POLITEHNICA Bucharest, Romania;*
[3]*Technical University of Moldova, Chisinau, Moldova;*
*E-mail: olga.shikimaka@ifa.usm.md

Shot peening is a powerful and effective tool for strengthening the surface layers of a material, especially metals and alloys, inducing improved mechanical properties for special purposes. The method implies inducing plastic deformation through mechanical cold-working treatment by bombarding the surface with small metallic or ceramic beads.

Shot peening is widely used in different branches of the industry, like aerospace, automotive, yet not so largely applied for biomaterials. Recently, it was shown that AISI 316L steel subjected to "metal/metal" dry friction modifies his structure near the friction surface, which results in an increase of microhardness (H) and Young's modulus (E), as well as, a change in plasticity index (H/E) and resistance index (H^3/E^2) [1]. 316L stainless steel (SS) has wide application in medicine (surgical instruments, orthopedic implants, lab equipment) because of its biocompatibility, corrosion resistance and low carbon content. There is a potential to improve the mechanical and corrosion parameters of 316 SS that will offer new opportunities for its applications, especially in implantology.

Shot peening treatment has a potential to change easily different working parameters, like size and material of shot media, velocity and duration of the impact, which in turn induce different structure and mechanical parameters of the treated material. In this work we have investigated the duration of the shot peening impact maintaining the other working parameters constant. Three impact times were tested (15, 30 and 60 min) and the change in structure and mechanical parameters (H and E) were evaluated with respect to those of untreated steel. The nanoindentation tests were performed on the cross sections of the treated sample to trace the changes when moving away from the treated surface. A series of indentation were performed on each of the samples testing H and E at different depth from the treated surface to evaluate the influence of shot peening in connection with the treatment time. First row of indentations was made in close proximity of about 40 μm from the treated surface (Fig. 1a), the second one was made at the depth of 1000 μm (Fig. 1b), where presumably the shot peening treatment has no influence. The third row of indentations was made perpendicular to the surface allowing to investigate the depth of the hardened layer (Fig. 1c). The results showed that the hardening of material is extended at the depth of about 80 μm from the treated surface and the hardness increase did not exhibit a linear dependence on the treatment time.

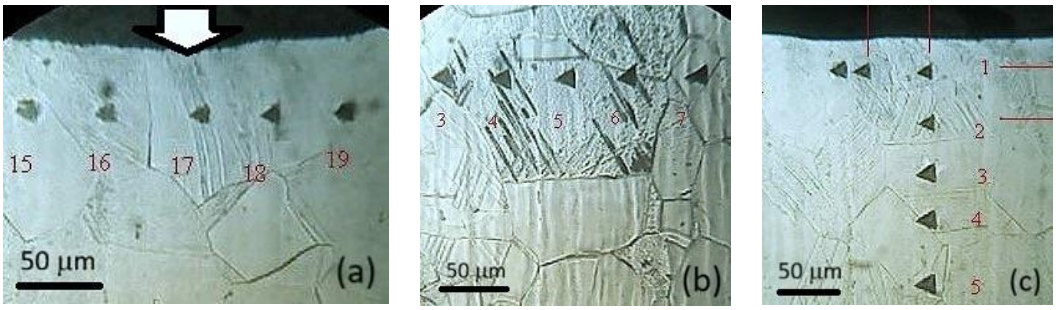


Figure 1. Rows of indentations made by load P = 400mN: (a) near the treated surface, shown by arrow, (b) at the distance of about 1000 μm from the treated surface and (c) perpendicular to the treated surface.

[1] D. Grabco, O. Shikimaka, C. Pyrtsac, D. Topal, D. Vilotic, M. Vilotic, S. Alexandrov. *Metals* **13 (**2023) p. 1278-1290.

THIOSEMICARBAZIDE BASED MATERIALS AS DUAL MR2 RNR AND COLCHICINE-SITE TUBULIN INHIBITORS

O. Palamarciuc[1,2,*], B.I. Ciubotaru[2,3], A.C. Stoica[2], M. Balan-Porcarasu,[2] S. Shova,[2] D. Peptanariu,[4] M. Dascalu,[2] M. Cazacu,[2] V. B. Arion[2,5]

[1]*Physics of Semiconductors and Devices Laboratory, Faculty of Physics and Engineering and Institute of Applied Physics, Moldova State University, MD-2009 Chișinău, Republic of Moldova*

[2]*Department of Inorganic Polymers, "Petru Poni" Institute of Macromolecular Chemistry, Romanian Academy, Aleea Gr. Ghica Voda 41 A, Iasi 700487, Romania*

[3]*Department of Biomedical Sciences, Faculty of Medical Bioengineering, Grigore T. Popa University of Medicine and Pharmacy, 11-13 Kogalniceanu Street, 700454 Iasi, Romania*

[4]*Centre of Advanced Research in Bionanoconjugates and Biopolymers, ICMPP, Romanian Academy, Grigore Ghica Voda Alley 41 A, 700487 Iasi, Romania*

[5]*Institute of Inorganic Chemistry, Faculty of Chemistry, University of Vienna, Währinger Strasse 42, A-1090 Vienna, Austria*

*E-mail: oleg.palamarciuc@usm.md

Cancer is a cunning disease that is difficult to treat. Although modern anticancer chemotherapy has made progress, there are still many problems caused by drug resistance and by the low selectivity of anticancer drugs generating serious side effects. Therefore, the search for new chemotherapeutics remains an essential challenge. Many validated oncotargets are well-documented.[1] Among them the R2 subunit of the ribonucleotide reductase (RNR) enzyme, and tubulin, the repeating subunit of microtubules (MTs), attracted our attention for the development of anticancer drugs, as they play crucial roles in cell proliferation and other vital cellular processes.

In the current study we searched for innovative metal thiosemicarbazonates as inhibitors of both R2 RNR and tubulin polymerization in cell-free settings and the evaluation of their anticancer potential in vitro. To achieve this goal the following work was performed: (i) the preliminary in silico screening of thiosemicarbazones derived from substituted *N*4-phenylthiosemicarbazides and quinoline-8-carboxaldehyde and their metal complexes able to associate with the colchicine binding site and selection of the most prospective candidate(s) followed by (ii) synthesis of selected quinoline-8-carboxaldehyde *N*4-(3,4,5-trimethoxyphenyl)thiosemicarbazone **(HL)** and Cu(II), Pd(II) and Fe(III) complexes of 1:1 and 1:2 metal-to-ligand stoichiometry and dichloroacetato (DCA) and/or chlorido anion(s) as co-ligands; (iii) characterization of the compounds prepared by elemental analyses, spectroscopic methods, Electrospray Ionization Mass Spectrometry (ESI-MS) and single crystal X-ray diffraction (SC-XRD); (iv) determination of their thermodynamic solubility, speciation studies and evaluation of their stability in aqueous media; (v) investigation of their potential to directly reduce the tyrosyl radical ($Y^{\bullet}$) in mouse R2 RNR (mR2) protein and inhibit tubulin polymerization; (vi) studies of their antiproliferative activity in breast cancer cell line MCF-7 by fluorescence microscopy and CellTiter-Glo luminescent cell viability assay, as well as cell cycle; (vii) finally insights into the underlying mechanism of antiproliferative activity supported by experimental evidence and molecular modeling.

ACKNOWLEDGMENTS. This work was funded by a grant from the Romanian National Authority for Research, project no. PNRR-III-C9-2023-I8-99 within the National Recovery and Resilience Plan and by the Ministry of Education and Research of the Republic of Moldova through the research subproject "Abundant-element-based materials and structures for radiation detection and efficient energy conversion", no. 011207 (DETCONV).

[1] M. Hawash, Highlights on Specific Biological Targets; Cyclin-Dependent Kinases, Epidermal Growth Factor Receptors, Ras Protein, and Cancer Stem Cells in Anticancer Drug Development. *Drug Res.*, 2019, **69**, 471–478.

[2] O. Palamarciuc et all, Metal Thiosemicarbazonates as Dual mR2 RNR and Colchicine-Site Tubulin Inhibitors: From Biochemical Inhibition to Mitotic Arrest in MCF-7 Breast Cancer Cells, *paper under revision.*

SYNTHESIS AND FUNCTIONAL EVALUATION OF TIO_2-MODIFIED ACTIVATED CARBON COMPOSITES OBTAINED FROM PEACH STONES

R. Nastas[1,*], M. Stefan[2], I. Ceban[1], A. Varadi[2], I. Nesterovschi[2,3], D. Toloman[2], A. Popa[2], I. Balan[1], S. Macavei[2], T. Lupascu[1]
[1]*Institute of Chemistry of Moldova State University, Chisinau, Republic of Moldova;*
[2]*National Institute for Research and Development of Isotopic and Molecular Technologies, Cluj-Napoca, Romania;*
[3]*Doctoral School of Physics, Babeş-Bolyai University, Cluj-Napoca, Romania*
*E-mail: raisa.nastas@sti.usm.md; nastasraisa@yahoo.com

Biomass-derived activated carbon is a sustainable and cost-effective adsorbent obtained from abundant renewable resources. The conversion of agricultural residues into activated carbon supports waste valorization and sustainable resource management. Owing to its high surface area, well-developed porosity, and tunable surface chemistry, activated carbon is widely used for pollutant removal, catalysis, and energy storage. Moreover, combining activated carbon with other functional materials yields multifunctional composites with enhanced physicochemical properties, making them promising for a wide range of environmental and engineering applications [1–4].

This study is devoted to the synthesis and comprehensive characterization of innovative activated carbon (AC)-based composites functionalized with titanium dioxide (TiO_2). The AC/TiO_2 composites were prepared by combining activated carbon (from peach stones, samples differing in surface chemistry and pore structure,) and TiO_2 in a 1:1 weight ratio, using polyallylamine hydrochloride (PAH) as a polymeric linking agent.

The structural, textural, and morphological properties of the synthesized composites were examined by XRD, BET, Raman, TEM/SEM/EDS) and XPS. Their photocatalytic performance was evaluated through the degradation of rhodamine B (RhB), employed as a model organic pollutant, under visible-light irradiation. The rhodamine B adsorption and photodegradation mechanisms were identified by density functional theory (DFT) calculations. In addition, the electrochemical behavior of initial activated carbons and the AC/TiO_2 composites was investigated using cyclic voltammetry (CV), potentiostatic electrochemical impedance spectroscopy (PEIS), and galvanostatic charge–discharge measurements with potential limitation (GCPL).

Results and Concluding remarks: (i) BET results reveal that activated carbons are micro-mesoporous; (ii) XRD confirms the presence of TiO_2 rutile in the composites; (iii) The Raman spectra of the initial activated carbons reveal the presence of two distinct peaks corresponding to activated carbons (the D band and the G band). In all composite samples, three additional bands appear in the low-wavenumber region, assigned to rutile TiO_2. (iv) TEM/SEM images and EDX results confirm the nanorods shape of TiO_2 that form a composite with the carbon structures. (v) The AC/TiO_2 composite photocatalytic tests against RhB under visible light irradiation reveal an increase in the RhB removal capacity of the synthesized composites by 2–5 times compared to TiO_2 nanotubes alone. (vi) All samples show energy efficiency above 99%, confirming excellent capacitive behaviour with negligible energy losses after 10000 cycles.

ACKNOWLEDGEMENTS. This work was funded by project MatPhotScs (project code PN-IV-PCB-RO-MD-2024-0349) within the program Complex Bilateral projects with the Republic of Moldova, grants of the National Research Authority (CNCS-UEFISCDI, PNCDI IV / 44PCBROMD / 01/09/2025) and of the National Agency for Research and Development (NARD RM, PN-IV-PCB-RO-MD-2024-0349/ 25.80013.7007.39ROMD).

[1] J. Matos, A. García, P.S. Poon. *Journal of Material Science*, **45** (2010**)** 4934–4944.
[2] T.J. Bandosz, A. Policicchio, M. Florent, W. Li, P.S. Poon, J. Matos. *Carbon*, **156** (2019) 10–23.
[3] E.D. Huang Kong, C.W. Lai, J.C. Juan, Y.L. Pang, C.S. Khe, A. Badruddin, F.I. Gapsari, K. Anam. *iScience*, **28** (2025) 112368.
[4] S. Liu, L. Wei, and H. Wang. *Appl. Energy*, **278** (2020) 115436.

NEW 3,4-DIHYDROPYRIMIDIN-2(1*H*)-THIONE DERIVATIVE THAT ACTIVATES THE Nrf2-DRIVEN ANTIOXIDANT RESPONSE

N. Ciobanu[1], B. Buttari[2], E. Profumo[2], N. Sucman[1], N. Bolocan[1], M. Rusu[1], E. Gorincioi[1*], F. Z. Macaev[1]

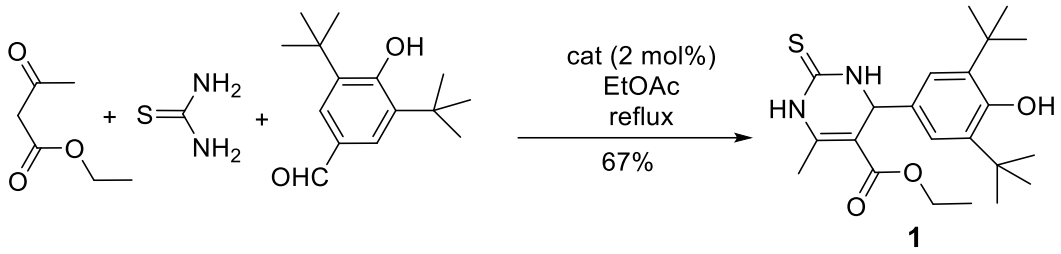
[1]*Moldova State University, Institute of Chemistry, Chisinau, Moldova*

[2]*National Institute of Health, Dept. of Cardiovascular and Endocrine-Metabolic Diseases and Aging, Rome, Italy*

*E-mail: elena.gorincioi@gmail.com, elena.gorincioi@sti.usm.md

The 3,4-dihydropyrimidin-2(1*H*)-one and its thione derivative core represents an essential pharmacophoric motif, central to a series of medically significant heterocycles collectively referred to as DHPMs [1].

Advancing our ongoing program in green chemistry methodology, we report herein about the synthesis of a congener of monastrol, namely ethyl 4-(3,5-di-tert-butyl-4-hydroxyphenyl)-6-methyl-2-thioxo-1,2,3,4-tetrahydropyrimidine-5-carboxylate **1**, by using the recently reported eco-friendly protocol [2]. The preparation of DHPM derivative **1** is based on the use of low methoxyl pectin as a convenient recyclable catalyst *via* the Biginelli multicomponent reaction (Scheme). The structure of **2** was confirmed by using IR-, NMR spectroscopy and elemental analysis, as well.



Scheme. Synthesis of ethyl 4-(3,5-di-tert-butyl-4-hydroxyphenyl)-6-methyl-2-thioxo-1,2,3,4-tetrahydropyrimidine-5-carboxylate **(1)**.

The potential of compound **1** as activator of the nuclear factor erythroid 2-related factor 2 (Nrf2) was evaluated, since transient activation of Nrf2 has been shown to protect cells against oxidative stress, inflammation, and toxic insults through on the induction of antioxidant and cytoprotective genes [3]. The cocrystal structure of Keap1 Kelch domain with the 16mer Nrf2 peptide (PDB ID: 2FLU) [4] was used as template for modeling studies, identifying **1** as the only compound that prefers the binding site of Nrf2 with a binding affinity of -7.2 kcal/mol, from a library of 22 compounds.

Biological evaluation, including cytotoxicity assessment, CETSA-based analysis of cellular Keap1 target engagement, and Western blot analysis of Nrf2 downstream targets, demonstrated that **1** is a non-cytotoxic Keap1-binding molecule that stabilizes endogenous Keap1 and selectively promotes HO-1 expression in THP-1 cells, consistent with activation of the Keap1–Nrf2 axis.

These preliminary data provide a rationale for further studies to characterize its mechanism of action and evaluate its potential as a modulator of cellular antioxidant responses.

ACKNOWLEDGEMENTS. This study is supported by the research subprogram (MetNatVal) (code 010601) funded by the Ministry of Education and Research of the Republic of Moldova.

[1] Dihydropyrimidinones as Potent Anticancer Agents. 2023, Editor(s): Mashooq Ahmad Bhat, Muneeb U. Rehman, Amita Verma, Elsevier, 2023, 279 pag

[2] Ciobanu N., Gorincioi E. et al. *Chemicke Listy*, **119** (2025) 340-344.

[3] Davies T.G., Wixted W. et al. *J Med Chem.* **59** (2016) 3991-4006.

[4] Crisman E, Duarte P. et al *Med Res Rev*. **43** (2023) 237–287.

NEW ANTICANCER QUATERNARY AMMONIUM SALT OF 2-*TERT*-BUTYL-3-(1*H*-1,2,4-TRIAZOL-1-YL)-2*H*-CHROMEN-2-OL WITH IMPROVED BIOAVAILABILITY

E. P. Stingaci[1], M. P. Ceabanova[1], E. C. Gorincioi[1,*], N. E. Dina[2], K. Vuković Đerfi[3], T. Matijević Glavan[3], F. Z. Macaev[1]

[1]*Moldova State University, Institute of Chemistry, Chisinau, Moldova*

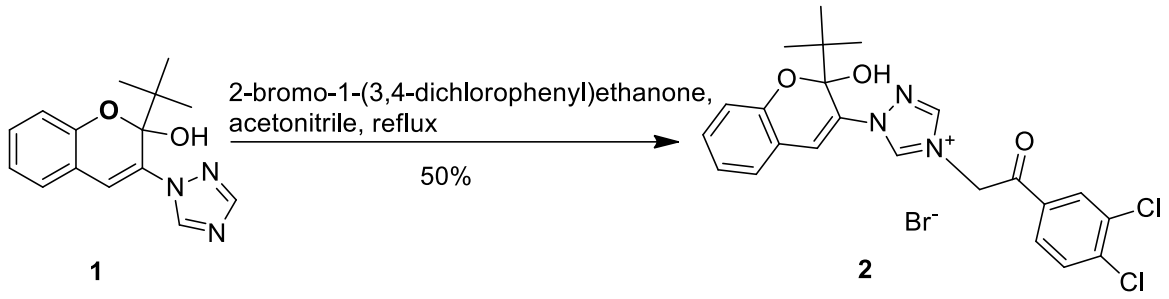
[2]*National Institute for Research and Development of Isotopic and Molecular Technologies, Department of Isotopic and Molecular Technologies, Cluj-Napoca, Romania*

[3]*Ruder Boskovic Institute, Department of Molecular Medicine, Zagreb, Croatia.*

*E-mail: elena.gorincioi@gmail.com

Converting triazoles into triazolium salts is a smart way widely used in medicinal chemistry, as it allows improving the aqueous solubility and biological targeting of antifungal and antibacterial agents [1]. Amongst the privileged scaffolds for various pharmaceuticals, chromenol-triazole hybrids continue to attract interest in the scientific community, particularly due to their antimicrobial activity [2].

As a follow-up to our previous work in this area, here we present the preparation of an ammonium salt of 1*H*-1,2,4-triazole functionalized chromenol of original structure, namely, 1-(2-(*tert*-butyl)-2-hydroxy-2*H*-chromen-3-yl)-4-(2-(3,4-dichlorophenyl)-2-oxoethyl)-1*H*-1,2,4-triazol-4-ium bromide **(2)**. Its synthesis has been accomplished according to the Scheme. The structure of salt **(2)** was identified by using modern physicochemical methods: IR, NMR, Raman and SERS spectroscopy and elemental analysis, as well.



Scheme. Synthesis of 1-(2-(tert-butyl)-2-hydroxy-2H-chromen-3-yl)-4-(2-(3,4-dichlorophenyl)-2-oxoethyl)-1H-1,2,4-triazol-4-ium bromide **(2)**.

The influence of compound **(2)** on colon cancer stem cells (CSCs), HCT-116 cell line, has demonstrated significant efficacy against HCT-116 tumor spheres, reducing cell survival to 42% at a 10 μM concentration and further drastically decreasing it to just 1% at 20 μM. Comparison of the IC_{50} values for 3D tumor spheres and adherent cells advocates for prospective use of salt **(2)** as a specific drug against CSCs, potentially opening avenues for targeted cancer stem cell therapies.

ACKNOWLEDGEMENTS This study is supported by the research subprogram "Chemical study of secondary metabolites from local natural sources and valorization of their application potential basing on broadening molecular diversity with multiple functionality (MetNatVal)" (code 010601) funded by the Ministry of Education and Research of the Republic of Moldova. N.E.D would like to acknowledge the financial support through the "Nucleu" Program within the National Research Development and Innovation Plan 2022–2027, Romania, carried out with the support of MEC, project no. 27N/03.01.2023, component project code PN 23 24 01 02.

[1] J. Song, J. Zou, J. Jin *et al.* Chem. Eur. J. 29, (2023) e202203661.
[2] M. Zveaghintseva, *et al.* Molecules 14 (26) (2021) 26144303.

Ga_2O_3 BASED COMPOSITE FIMS AND AEROMATERIALS FOR MICROFLUIDIC, OPTOELECTRONIC AND PHOTO-ELECTROCHEMICAL APPLICATIONS

V. V. Ursaki[1,2*], V. Morari[3], I. M. Tiginyanu[1,2]
[1]*National Center for Materials Study and Testing, Technical University of Moldova, Chisinău, Republic of Moldova*
[2]*Academy of Sciences of Moldova, Chisinau, Republic of Moldova;*
[3]*Institute of Electronic Engineering and Nanotechnology „D. Ghitu", Technical University of Moldova, Chisinău, Republic of Moldova*
*E-mail: vvursaki@gmail.com

Metal oxide composite materials are widely used in electronics as transistors and microprocessors, gas sensors, energy production and storage, catalysis and chemical processing, environmental remediation, medicine and biology [1]. Among them, gallium oxide (Ga_2O_3) has potential to revolutionize high-power electronics, optoelectronics, and telecommunications, owing to its ultra-wide bandgap, massive breakdown voltage and radiation hardness making it ideal for extreme environments and high-efficiency energy conversion [2,3]. On the other hand, aero-semiconductor are an emerging class of highly porous, ultra-lightweight inorganic materials with wide prospects for practical applications [4]. This report addresses preparation and characterization of both this forms of the Ga_2O_3 related materials.

Ga_2O_3, $(In_{1-x}Ga_x)_2O_3$ with x-value of 0.1 to 0.5, as well as $(Ga_2O_3)_{0.75}(SnO_2)_{0.25}$ and $Ga_{1.75}Al_{0.25}O_3$ films were prepared by spray pyrolysis, which has a number of advantages over other technologies, such as simplicity and cost-effectiveness, versatility, suitability for different substrates, low processing temperatures, ability to efficiently control the film properties. The relationships between the composition established in the precursor solutions and the actual composition of the prepared films were determined by EDX analysis. The surface topology of the deposited thin films was investigated by atomic force microscopy (AFM), and their crystal structure was determined by XRD analysis. A direct relationship was found between surface roughness and film wettability determined by measuring the contact angle of a water droplet on the surface of the $(In_{1-x}Ga_x)_2O_3$ and $(Ga_{1-x}Al_x)_2O_3$ films, with both surface roughness and contact angle increasing with increasing x value. An inverse relationship was found for $(Ga_2O_3)_{1-x}(SnO_2)_x$ films, in which the contact angle increases with the increasing Sn content, while their roughness decreases. An explanation was proposed for this behavior in terms of a combined effect of the surface roughness and the nature of chemical bonds, which is determined by the electronegativity of the metals contained in the films. These data are supposed to be relevant for a range of practical applications, specifically for microfluidic applications. The study of optical properties demonstrated the possibilities of bandgap engineering in $(In_{1-x}Ga_x)_2O_3$ films, with the bandgap changing from 3.5 eV to 4.8 eV with an increase in x value from 0 to 1. The sensibility of the prepared films to visible and UV radiation, as well as the effect of annealing on wettability and optical properties, were investigated.

Ga_2O_3-based aero-semiconductors were prepared with ZnO sacrificial templates consisting of 3D architectures built up from interconnected microrods, tetrapods or multipods, used for the production of aero-GaN in the first technological step, followed by annealing in air under various process conditions. The produced materials were comprehensively investigated from the point of view of prospective applications in light scattering, luminescence, photocatalysis and energy storage.

[1] M. A. Ahmed et al. *Inorganic Chemistry Communications* **179** (2025) 114641.
[2] J. Zhang, et al. *Advances in Colloidal and Interface Science* **328** (2024) 103175.
[3] S. Ganguly, K. N. Manjunatha, S. Paul. *Advanced Electronic Materials* **11** (2025) 2400690.
[4] V.V. Ursaki, et al. *Applied Surface Science Advances* **26** (2025) 100708.

FUNCTIONAL NANOSTRUCTURES AND NANOMATERIALS FOR NEUROMORPHIC COMPUTING

A. S. Sidorenko*
Technical Uniiversity of Moldova, Institute of Electronic Engineering and Nanotechnologies „D.GHITU“, Chisinau, Republic of Moldova
*E-mail: sidorenko.anatoli@gmail.com

Development of artificial intelligence increasingly depends not only on advances in computing architectures and learning algorithms but also on the emergence of novel functional materials capable of integrating computation, memory, and adaptive behavior within the same physical platform. Conventional CMOS technologies are approaching their fundamental limits in terms of power dissipation, scalability, and memory bottlenecks, stimulating worldwide efforts to develop alternative hardware solutions for energy-efficient information processing [1].

This work presents a materials-oriented perspective on neuromorphic computing, emphasizing the transition from conventional semiconductor technologies toward superconducting spintronic systems. Particular attention is devoted to magnetic Josephson junctions (MJJs), which combine superconductivity and ferromagnetism within multifunctional quantum nanostructures. Owing to their intrinsic nonlinear dynamics, programmable magnetic states, ultrafast switching, and extremely low energy dissipation, MJJs represent promising building blocks for future neuromorphic hardware.

Josephson junctions naturally exhibit threshold behavior analogous to biological neurons, making them attractive candidates for implementing artificial neurons operating at cryogenic temperatures. Their compatibility with established superconducting digital technologies additionally enables integration with energy-efficient superconducting logic circuits. Furthermore, ferromagnetic layers incorporated into Josephson junctions provide non-volatile memory functionality, allowing realization of adaptive artificial synapses with programmable synaptic weights [2].

Based on these principles, superconducting artificial neurons employing magnetic Josephson junctions together with superconducting artificial synapses can be combined into artificial neural networks implementing non-von Neumann information processing with ultralow energy consumption. In such systems, computation and memory become physically integrated within the same functional nanostructures, closely resembling biological neural architectures.

The presented analysis demonstrates that multifunctional superconducting spintronic materials represent a promising platform for next-generation neuromorphic computing. More broadly, the evolution of intelligent hardware indicates a transition toward **materials-driven computing**, where computation, memory, adaptation, and learning increasingly emerge directly from the intrinsic physical properties of engineered quantum materials rather than being implemented solely through circuit architecture [3]. This approach opens new opportunities for highly energy-efficient artificial intelligence systems operating beyond the limits of conventional semiconductor technologies.

[1] I.I. Soloviev, N. V Klenov, S. V Bakurskiy, M.Y. Kupriyanov, A.L. Gudkov, A.S. Sidorenko, Beyond Moore’s technologies: operation principles of a superconductor alternative, *Beilstein J. Nanotechnol.* **8** (2017) 2689-2710, Doi: https://doi.org/10.3762/bjnano.8.269.

[2] A.Sidorenko, H. Hahn and V. Krasnov. Frontiers of nanoelectronics: intrinsic Josephson effect and prospects of superconducting spintronics. *Beilstein J. Nanotechnol.* **14** (2023) 79-82, Doi: https://doi.org/10.3762/bjnano.14.9.

[3] A.S. Sidorenko, "Superconducting Artificial Neural Networks and Quantum Circuits," *Beilstein J. Nanotechnol*. **17** (2026), 744-747, Doi: https://doi.org/10.3762/bjnano.17.51

LAYERED SEMICONDUCTORS AND THEIR NANOSTRUCTURES: EXCITONS, POLARITONS, AND OPTICAL PHENOMENA

V.V. Zalamai[1,*], A.V. Tiron[1,] I.G. Stamov[2], E.V. Rusu[3]
[1]*National Center for Materials Study and Testing, UTM, Chisinau, Republic of Moldova;*
[2]*T.G. Shevchenko State University of Pridnestrovie, Tiraspol, Republic of Moldova;*
[3]*Institute of Electronic Engineering and Nanotechnologies, UTM, Chisinau, Republic of Moldova*
*E-mail: victor.zalamai@cnstm.utm.md

Excitons have been observed in many layered (van der Waals) semiconductors, where excitonic effects are often particularly pronounced owing to weak Coulomb screening and reduced dimensionality. For example, MoS_2 (molybdenum disulfide) is a direct-bandgap semiconductor exhibiting prominent A and B excitons, while WSe_2 (tungsten diselenide) is among the most extensively studied two-dimensional excitonic materials. Rydberg excitons have also been reported in WS_2 (tungsten disulfide). Excitonic states have been investigated in $MoSe_2$, where both the exciton binding energy and many-body interaction effects have been experimentally determined. Another notable layered semiconductor is InSe (indium selenide), in which free excitons, biexcitons, and exciton-exciton scattering (the P-band) have been observed, with the exciton binding energy exceeding 20 meV. Excitonic phenomena have also been extensively studied in GaSe (gallium selenide), where both free and bound excitons have been identified. In most cases, excitons have been observed in monolayers of these materials, with the exception of GaSe [1].

The paper examines excitonic states observed in various layered semiconductors, using SnSe, SnS_2, GaSe, and GaS as representative examples. The influence of nanostructuring on these excitonic states is also discussed. For instance, no excitonic features were detected in undoped SnSe because of its high free-carrier concentration. Following silver doping, the absorption edge shifted towards higher energies, and four excitonic series became observable. Exciton-related features were identified in the reflectance spectra, enabling the determination of the main excitonic parameters [2]. Nanostructuring also allowed excitons to be observed in photoluminescence spectra. In GaSe single crystals, well-resolved excitonic transitions were detected in reflectance, transmission, and low-temperature photoluminescence spectra [3]. In contrast, GaSe nanoplatelets produced by ultrasonic milling followed by centrifugal separation exhibited narrow photoluminescence lines in the excitonic region that were shifted towards higher energies. In GaS and SnS_2 single crystals, excitonic states are weakly resolved and are not observed in reflectance spectra.

ACKNOWLEDGEMENTS. The work was supported by the institutional subprogram 02.04.02 no. 4/FI «Development of technologies and investigation of the properties of layered semiconductor compounds, hybrid nanostructures and laser sources».

[1] X. Chen, Z. Lian, Y. Meng et al. Excitonic Complexes in Two-Dimensional Transition Metal Dichalcogenide*s Nature Communications* **14** (2023) 8233 DOI: 10.1038/s41467-023-44119-9.
[2] N.N., Syrbu, V.V. Zalamai, Excitonic and band parameters in SnSe crystals; *Journal of Luminescence* **221** (2020) 117093(8) DOI: 10.1016/j.jlumin.2020.117093
[3] N.N., Syrbu, V.V., Zalamai, I.G. Stamov Interference of exciton polariton waves in GaSe nanocrystals. *Materials Today Communications* **27** (2021) 102355(7) DOI: 10.1016/j.mtcomm.2021.102355

MORPHOLOGY DESIGN IN POROUS GALLIUM ARSENIDE THROUGH CRYSTALLOGRAPHIC CONTROL AND ELECTROCHEMICAL NANOSTRUCTURING

E. V. Monaico[1,*], E. I. Monaico[1], V. V. Ursaki[1,2], I. M. Tiginyanu[1,2]
[1]*National Center for Materials Study and Testing, Technical University of Moldova, Bd. Stefan cel Mare 168, Chisinau 2004, Republic of Moldova;*
[2]*Academy of Sciences of Moldova, Bd. Stefan cel Mare 1, 2001 Chisinau, Moldova.*
*E-mail: eduard.monaico@cnstm.utm.md

Porous gallium arsenide (GaAs) has attracted considerable attention due to its unique structural properties and its potential for applications in nanoelectronics, photonics, sensing, and hybrid semiconductor systems. The morphology of porous GaAs is strongly influenced by the crystallographic orientation of the substrate, which determines the preferential direction of pore propagation during electrochemical anodization [1]. Understanding and exploiting this relationship provides new opportunities for the controlled fabrication of semiconductor nanostructures.

In this work, we investigate the role of crystallographic orientation and electrochemical processing conditions in controlling the morphology of porous GaAs. By combining photolithographic patterning with electrochemical anodization of GaAs wafers with different crystallographic orientations, various porous architectures and localized nanostructures were obtained. The evolution of pore propagation, nanowire formation, and morphology development was analyzed as a function of crystallographic orientation and anodization parameters.

The results demonstrate that crystallographic orientation represents the key factor governing pore growth direction, while electrochemical conditions influence the dimensions and evolution of the porous structure. This combination enables the fabrication of ordered porous layers, localized nanowire arrays, and complex hierarchical morphologies with good reproducibility and spatial control. The study highlights the possibility of designing the morphology of porous GaAs by selecting suitable crystallographic orientations together with appropriate electrochemical processing parameters [2].

The proposed approach provides a versatile top-down route for the fabrication of semiconductor nanostructures and creates opportunities for the subsequent integration of porous GaAs with metals, metal oxides, and other functional materials for advanced electronic, photonic, and sensing applications [3].

ACKNOWLEDGEMENTS. This work was funded by Ministry of Education and Research from the Republic of Moldova (institutional subprogram #02.04.02 “Development of technologies and investigation of the properties of layered semiconductor compounds, hybrid nanostructures and laser sources”.

[1] E. I. MONAICO, E. V. MONAICO, V.V. URSAKI, S. HONNALI, V. POSTOLACHE, K. LEISTNER, K. NIELSCH, I. M. TIGINYANU. Electrochemical Nanostructuring of (111) Oriented GaAs Crystals: From Porous Structures to Nanowires. *Beilstein J. Nanotechnol*. **(11)**, 2020, pp. 966–975, doi:10.3762/bjnano.11.81
[2] E. I. Monaico, E. V. Monaico, V. V. Ursaki, I. M. Tiginyanu. Micro- and Nano-Integration in the Production of GaAs and Ga_2O_3 Nanowire Arrays by Top-Down Design. *Journal of Manufacturing and Materials Processing*, **(9)**, 2025, 376, doi: 10.3390/jmmp9110376
[3] E. I. MONAICO, E. V. MONAICO, V. V. URSAKI, I. M. TIGINYANU. Controlled Electroplating of Noble Metals on III-V Semiconductor Nanotemplates Fabricated by Anodic Etching of Bulk Substrates. *Coatings*, **(12)**, 2022, 1521, doi:10.3390/coatings12101521

THICKNESS-INDUCED TUNING OF ELECTRICAL AND PHOTOELECTRIC PROPERTIES IN ULTRALIGHT AERO-GaN/ZnO TETRAPOD NETWORKS

T. Braniste[1,*], I. Tiginyanu[1,2]
[1]*National Center for Materials Study and Testing, Technical University of Moldova, Chisinau, Republic of Moldova;*
[2]*Academy of Sciences of Moldova, Chisinau, Republic of Moldova;*
*E-mail: tudor.braniste@cnstm.utm.md

Ultralight three-dimensional semiconductor architectures based on hollow aero-gallium nitride (aero-GaN) microtetrapods offer unique opportunities for advanced optoelectronics, sensing, and harsh-environment applications. While previous studies have focused primarily on the morphological synthesis and mechanical compliance of these networks, the mechanisms governing their charge transport and optoelectronic behavior remain insufficiently understood. In this work, we demonstrate that the electrical resistance and UV photoresponse of 3D aero-GaN networks are strongly governed by the wall thickness of the constituent hollow tetrapods. Importantly, the hollow aero-GaN arms behave as GaN/ZnO heterostructures because of an ultrathin residual ZnO layer that remains chemically stabilized on their inner surfaces following the sacrificial-template etching process [1–3].

Through temperature-dependent electrical measurements and transient photoresponse measurements under 355 nm pulsed UV excitation over the temperature range of 30–330 K, we identify two contrasting charge-transport regimes. Aero-GaN networks with microtube wall thicknesses below 50 nm exhibit conventional semiconducting behavior, with the dark resistance decreasing monotonically as the temperature increases from 30 to 330 K. Under UV illumination, the thin-walled samples display conventional positive photoconductivity over the entire temperature range, governed predominantly by thermally activated carrier generation and surface- and interface-assisted carrier detrapping.

In contrast, aero-GaN networks with microtube wall thicknesses above 120 nm undergo an anomalous transport crossover at approximately 150 K. Below this temperature, the networks exhibit conventional semiconducting behavior, whereas above 150 K, their resistance increases monotonically with increasing temperature. Concurrently, the photoresponse changes from positive photoconductivity below 150 K to negative photoconductivity above this temperature.

A coupled carrier-density–mobility model, $\sigma = qn\mu$, is proposed to explain this behavior. In thick-walled aero-GaN structures, a bulk-like GaN conduction pathway coexists with the internal GaN/ZnO heterojunction and external surface states. At temperatures above 150 K, thermally activated trap centers, interfacial polarization, and carrier scattering by charged dislocation lines induce a pronounced reduction in the effective carrier mobility, μ, which outweighs the increase in photogenerated carrier concentration, n. Under UV excitation, photoassisted charge redistribution at the internal GaN/ZnO interface further widens the local space-charge depletion regions, resulting in light-induced suppression of electrical conductivity.

These findings establish the wall thickness of hollow aero-GaN microtetrapods as a critical design parameter for controlling charge-transport pathways in three-dimensional aeromaterials. This approach provides a promising route toward adaptive photodetectors, thermally controlled switches, and other functional micro- and nanodevices.

ACKNOWLEDGEMENTS. This work has received partial funding from the Ministry of Education and Research, program No. 020402 ETISEL.

[1] I. Tiginyanu, T. Braniste, D. Smazna, M. Deng, F. Schütt, A. Schuchardt, M. A. Stevens-Kalceff, S. Raevschi, U. Schürmann, L. Kienle, N. M. Pugno, Y. K. Mishra, R. Adelung. *Nano Energy* **56** (2019) 759–769.
[2] V. Ciobanu et al. *H e l i y o n* **10** (2024) e40989
[3] M. Dragoman, V. Ciobanu, S. Shree, D. Dragoman, T. Braniste, S. Raevschi, A. Dinescu, A. Sarua, Y. K. Mishra, N. Pugno, R. Adelung, I. Tiginyanu. *Phys. Status Solidi RRL* (2018), 1900012

NANOINDENTATION OF MgO: POP-IN EVENTS DEVELOPMENT UNDER DIFFERENT LOADING CONDITIONS

O. Shikimaka[1,*], D. Grabco[1], C. Pyrtsac[1, 2], A. Prisacaru[1, 2], D. Spoiala[1]
[1]*Institute of Applied Physics, Moldova State University, Chisinau, Moldova;*
[2]*Technical University of Moldova, Chisinau, Moldova;*
*E-mail: olga.shikimaka@ifa.usm.md

The depth-sensing nanoindentation method, offering the deformation registration of very high spatial resolution up to hundredths of nanometer, opened the exclusive possibility to capture and investigate a range of subtle effects in the deformation behavior of materials at nano- and micro-level. The pop-in effect is one of such phenomena revealed under nanoindentation of crystalline materials representing a sudden jump, registered on the loading part of nanoindentation curve. This jump is caused by sharp drop of material resistance during the elastic-plastic transition when the homogeneous generation of dislocations takes place. The appearance of pop-in was found to be influenced by different factors like structure of material, density of native dislocations and indenter tip radius. In this work we have investigated the influence of load and loading rate on the development of pop-in event.

For this purpose, the nanoindentation of MgO single crystal was performed by using two loads, P (50 and 100mN), and for each of these loads two loading rate, v (0.5 and 5 mN/s) were applied. For each of the four loading regimes used an amount of 20-25 indentations were made to have enough statistical data. Tree main type of behavior were revealed: large pop-in (Fig. 1a), small pop-in (Fig. 1b) and absence of pop-in (Fig. 1c). The probability of the pop-in appearance and extend of pop-in jump were evaluated depending on the load, loading rate, the strain rate of material, as well as the mean contact pressure during indentation.

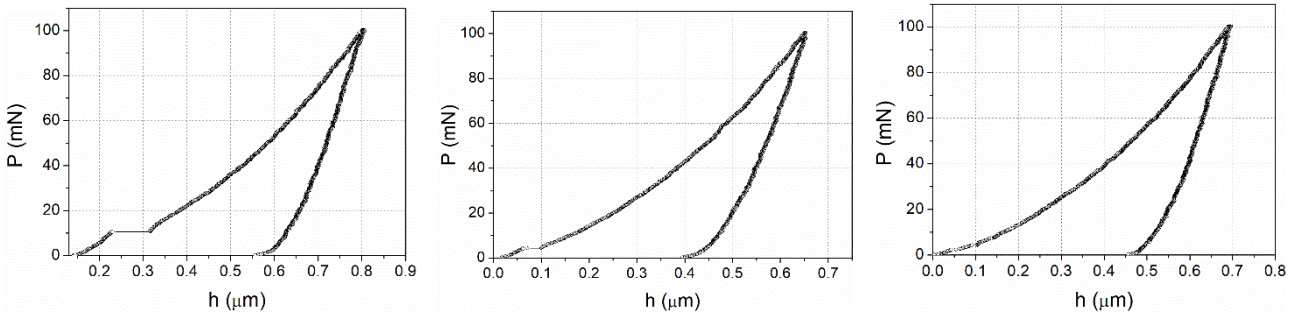


Figure 1. Load-displacement (P-h) dependences at nanoindentation of MgO single crystal under P = 100 mN and v = 0.5 mN/s, exhibiting: (a) large pop-in effect, (b) small pop-in effect and (c) absence of pop-in effect.

As the pop-in is caused by homogeneous dislocation generation, one can expect the influence of the pop-in on the final dislocation structure formed around the indentations. In our previous work on LiF single crystals the analysis of dislocation rosettes around the indentations showed that the appearance of the first pop-in event and succeeding additional pop-ins correlate with load and sequential development of various dislocation processes [1]. Taking into account this result, the dislocation structure formed around the indentations were analyzed in this work too, in connection with the loading conditions for pop-in formation and development. This comprehensive analysis allowed to understand whether the loading rate in combination with load applied can influence the pop-in appearance and development, as well as to find out the reasons of some specific behavior.

[1] D. Z. Grabko, K. M. Pyrtsak, L. Z. Ghimpu, G. F. Volodina. *Surf Eng Appl Electrochem* **52(4)** (2016) pp. 319-333.

NONLINEAR DYNAMICS OF QUANTUM DOT LASERS UNDER CONVENTIONAL AND FILTERED OPTICAL FEEDBACK

Vasile Tronciu[1,*], Spiridon Rusu[1], Tatiana Oloinic[1]
[1]*Department of Physics, Technical University of Moldova, Chisinau, Republic of Moldova;*
*E-mail: vasile.tronciu@fiz.utm.md

In this paper, we investigate the nonlinear dynamics of a quantum dot laser in the presence of double optical feedback: one conventional and the other filtered. We use the second branch of the filtered feedback to control laser emission. The system can evolve in two ways: continuous wave emission or an optical chaos generator. The latter can be employed in chaos-based communication systems. The dynamics of quantum dot lasers under the influence of optical feedback from two different cavities can be analysed using a system of differential rate equations. This incorporates the Lang-Kobayashi model for conventional optical feedback [1] and the model by M. Yousefi and D. Lenstra for filtered feedback [2], [3], adapted for a quantum dot laser using the scheme shown in Fig. 1. The rate equations for the complex field amplitudes E and F, the probability of occupation in the quantum dots ρ, and the charge carrier density N are

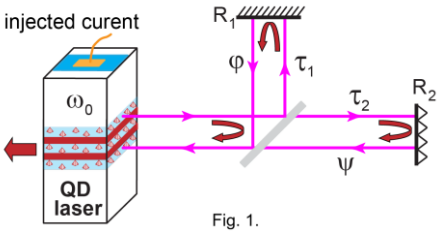


Fig. 1.

$$\frac{dE}{d\tau}=\frac{1}{2}(1+i\alpha)\left[-\gamma_{np}+g(2\rho-1)\right]E(\tau)+\Gamma_1 e^{i\varphi}E(\tau-\tau_1)+\Gamma_2 F(\tau).$$

$$\frac{dF}{d\tau}=\Lambda E(\tau-\tau_2)e^{i\psi}+(i\Delta\omega-\Lambda)F(\tau),\quad \frac{d\rho}{d\tau}=-\gamma_{ns}\rho-(2\rho-1)|E|^2+(CN^2+BN)(1-\rho),$$

$$\frac{dN}{d\tau}=J-N-2[(CN^2+BN)(1-\rho)],$$

where J is the dimensionless pump current, τ_1 and τ_2 are the round-trip times through the external cavities, Γ_1 and Γ_2 the feedback intensity controlled by the reflection R_1 and R_2. The frequency dependent reflectivity in the filter branch is described by a Lorenzian function with width Λ and detuning $\Delta\omega$ with respect to the solitary laser frequency ω_0.

Using the above model, the stationary states (so-called external filtered modes) of a quantum dot laser under the influence of double feedback can be obtained analytically and plotted in a two-parameter plane (see Fig. 2(a)). It was shown that the ellipse, the characteristic shape of conventional optical feedback, is strongly distorted and breaks into several bubbles in the case of double feedback. The results presented in this paper demonstrate that, under certain conditions, the laser system can exhibit various behaviours, including continuous wave, periodic, and robust chaotic behaviour (see Fig. 2(b)). We believe that our work provides a solid basis for future experimental studies of the dynamics of quantum dot lasers under the influence of conventional and filtered feedback.

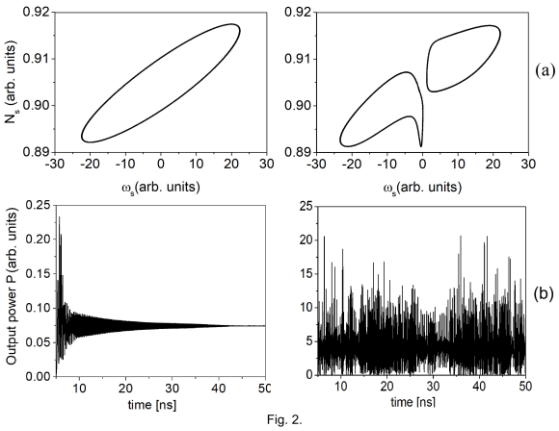


Fig. 2.

ACKNOWLEDGEMENTS. This work was supported by project 02.04.02 "Development of technologies and investigation of the properties of layered semiconductor compounds, hybrid nanostructures and laser sources".

[1] R. Lang, K. Kobayashi External optical feedback effects on semiconductor injection laser properties. *IEEE J Quantum Electron*, vol. 16 (1980) 347- 355. DOI: 10.1109/JQE.1980.1070479

[2] M. Yousefi, D. LENSTRA Dynamical behavior of a semiconductor laser with filtered external optical feedback. *IEE J. Quantum Electron*. vol. 35, nr. 6 (1999) 970-976. DOI: 10.1109/3.76684

[3] I. V. Ermakov, V. Z. Tronciu, Pere Colet, and Claudio R. Mirasso, Controlling the unstable emission of a semiconductor laser subject to conventional optical feedback with a filtered feedback branch, Opt. Express vol 17 (2009) 8749-8755 https://doi.org/10.1364/OE.17.008749

LUMINESCENCE AND RADIATIVE DECAY KINETICS OF BOUND EXCITONS IN HALOGEN-INTERCALATED TRANSITION METAL DICHALCOGENIDES

N. Siminel*, A. Micu, C. Slobodeniuc, A. Siminel, L. Kulyuk
Institute of Applied Physics, Moldova State University, Chisinau, Republic of Moldova
*E-mail: nikita.siminel@ifa.usm.md

Transition metal dichalcogenides (TMDs), including MoS_2, WS_2, $MoSe_2$, and WSe_2, possess unique optoelectronic properties that can be strategically modified by intercalating diatomic halogen molecules (Cl_2, Br_2, I_2) into their van der Waals (vdW) gaps. These halogens embed into quasi-tetrahedral voids to form neutral centers, functioning similarly to isoelectronic impurities that enable efficient radiative recombination of bound excitons in otherwise indirect-gap bulk crystals.

This work presents a comprehensive study of the steady-state and time-resolved photoluminescence (PL) of bulk TMDs, focusing on 2H-$MoSe_2$ single crystals intercalated with I_2 via chemical vapor transport. Measurements conducted between 2 K and 150 K reveal that the PL spectra of $MoSe_2$:I_2 are dominated by a zero-phonon excitonic doublet, identified as states A and B, located at $E_A = 1.0360\ eV$ and $E_B = 1.0416\ eV$, respectively (separated by an energy gap of $\Delta_{AB} = 5.6$ meV).

Time-resolved kinetics demonstrate that at low temperatures (11–12 K), the exciton states are not in thermal equilibrium. This is evidenced by significantly different exponential decay times, where the A-state lifetime is approximately 205–210 μs, which is roughly 1.6 times longer than that of the B-state ($\tau_A \approx 1.6\tau B$). As the temperature exceeds 20 K, the decay kinetics of both lines equalize, marking the onset of thermal equilibrium. The PL intensity initially increases up to 35 K due to the thermal population of the highly radiative B-state ($\tau_B \ll \tau_A$), followed by rapid thermal quenching above 60 K with an activation energy of 0.14 eV, caused by extrinsic self-trapping and exciton dissociation. A two-level rate equation model indicates that bound excitons initially form in state A before thermally populating state B through phonon-induced non-radiative transitions.

Furthermore, steady-state PL serves as a reliable tool for structural identification; for instance, in MoS_2:Cl_2, the B-line of the 3R-polytype shifts 3.5 meV lower in energy compared to the 2H-polytype. Density Functional Theory (DFT) calculations and comparative studies between WS_2:Br_2 and WS_2:I_2 confirm that larger intercalant molecules expand the vdW gap, inducing local band gap widening and inhomogeneous spectral broadening. Ultimately, manipulating the intercalant concentration and species size provides a robust method for tailoring the electronic structure and exciton dynamics in bulk TMDs and their respective van der Waals heterojunctions.

MAGNETIC METAMATERIALS FOR SPIN – VALVE STRUCTURES AND FOR ARTIFICIAL NEURAL NETWORK BASE ELEMENTS

V. I. Boian[1,*], R. Morari[1], V. M. Fomin[2,3], N. P. Rodriguez[2], J. Scheiter[2], A. Sidorenko[1]
[1]*Technical University of Moldova, D. Ghitsu Institute of Electronic Engineering and Nanotechnologies, str. Academiei 3/3, MD-2028 Chisinau, Republic of Moldova;*
[2]*Institute for Emerging Electronic Tehnologies, Leibniz IFW Dresden, Helmholtzstrabe 20, D-01069 Dresden, Germany*
[3]*Moldova State University, str. Alexei Mateevici 60, MD-2009 Chisinau, Republic of Moldova.*
*E-mail: vladimir.boian@iien.utm.md

Mathematical modelling based on molecular dynamics is used for analyse how various parameters influence the formation of the structure and morphology of Nb/Co superconducting heterostructures and the magnetic metamaterials (MM) derived from them. The developed technology, which employs magnetron sputtering of metallic films combined with nonmetallic protective layers, leads to a significant improvement in the superconducting properties of thin Nb films and Nb/Co nanostructures compared to conventional deposition methods. The fabricated films exhibit a higher superconducting critical temperature and retain their properties without degradation for at least two years, making them promising for the development of reliable spintronic devices. In addition, Josephson junctions were fabricated from Nb/MM/Nb heterostructures using focused ion beam (FIB) etching technology. Based on two such junctions, a Gaussian artificial neuron intended for artificial neural networks was designed. The study examines both the static and dynamic activation functions of the proposed neuron. The use of Nb/MM/Nb heterostructures in superconducting artificial neural networks is considered a highly promising solution for the development of non-von-Neumann computing architectures. Furthermore, the research presents the results of computer simulations of superconducting spin valves based on Josephson junctions with weak links fabricated from the artificial MM [1, 2], as well as superconducting synapses created from layered superconductor/ferromagnet hybrid structures.

ACKNOWLEDGEMENTS. The study was supported by the project "Nanostructures and advanced materials for implementation in spintronics, thermoelectricity and optoelectronics", no. 020201, and the National Agency for Research and Development project "ReBrain", no. 25.80013.5007.07RE (Republic of Moldova). VMF gratefully acknowledges support from ZIH TU Dresden.

[1]. A. Vakhrushev, A. Fedotov, V. Boian, R. Morari, A. Sidorenko, Molecular dynamics modeling of the influence forming process parameters on the structure and morphlogy of a superconducting spin valve. *Beilstein Journal of Nanotechnology*, **11** (2020) 1776–1788. Doi: https://doi.org/10.3762/bjnano.11.160
[2]. N. Klenov, Y. Khaydukov, S. Bakurskiy, R. Morari, I. Soloviev, V. Boian, T. Keller, M. Kupriyanov, A. Sidorenko, B. Keimer, Periodic Co/Nb pseudo spin valve for criogenic memory. *Beilstein Journal of Nanotechnology*, **10** (2019) 833–839. Doi: https://doi.org/10.3762/bjnano.10.83

OBSERVATION OF YAMAJI MAGIC ANGLES IN BISMUTH SURFACES

L. A. Konopko[1,*], A. A. Nikolaeva[1], T. E. Huber[2]
[1]*Technical University of Moldova, Chisinau, Republic of Moldova;*
[2]*Howard University, 500 College St. N.W., Washington, DC 20059, USA.*
*E-mail: leonid.konopko@iien.utm.md

Bismuth is a candidate material for the three dimensional higher dimensional topological insulators. We performed electronic transport experiments on small diameter (~50 nm) crystalline bismuth nanowires to clarify the role of the proposed hinge conducting channels in the interlayer coupling. The magnetoresistance presents a sequence of peaks at Yamaji magic angles [1] for which the interlayer group velocity is zero pointing to flat bands due to the layered structure. Also, we observe the peak at high fields (10 T > B > 14 T) for B applied parallel to the layers, a definitive signature of interlayer coherence [2] that enable the interlayer transfer integral (t ≈ 8 meV) to be deduced. We demonstrate transport by a corrugated open Fermi surface of holes that is extended, with the high angular precision of ~ 0.016 (rad) in the interlayer direction.

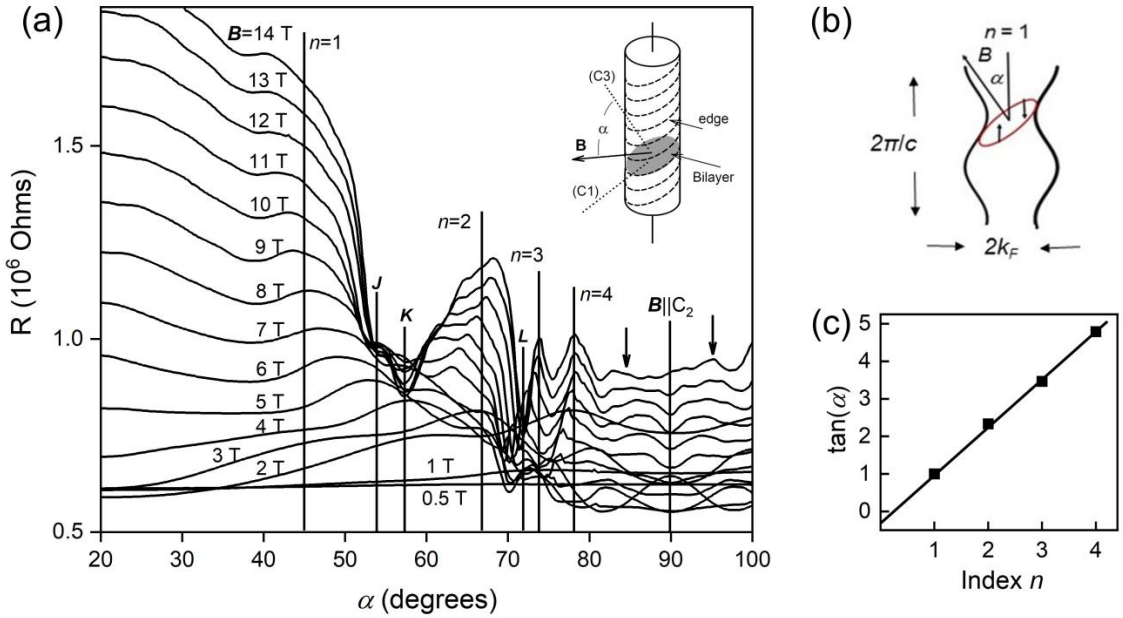


Figure 1. (a) Angular dependence of the magnetoresistance (AMR) versus α, for different magnetic fields B. The experimental geometry is illustrated in the inset. The magnetic field is perpendicular to the wire axis. The angle dependent magnetoresistance (MR) was observed experimentally by rotating B around the wire axis. The resistance shows maxima at the magic angles indexed as n = 1, 2, 3 and 4. The angles indicated as J, K and L are MR minima. (b) Illustration of corrugated tube showing bellies. The behavior of $v_z = (2\pi/h)(dE/dk_z)$ for the first Yamaji angle, as indicated. The orbit is represented with an ellipse and the velocities are black arrows. In the latter case, the average of v_z in the orbit, called drift velocity is zero, which leads to zero conductance and causes the MR peaks. (c) Observation of the linear dependence of tan(α) versus index n.

The identification of flat bands in bismuth due to the Fermi surface corrugation is intriguing because flat bands promote correlated electron behavior such as superconductivity in bilayer graphene and superconductivity has also been observed in low-dimensional bismuth.

ACKNOWLEDGEMENTS. This work was supported by the Ministry of Education and Research of Moldova (project no. 020201). In the U.S., the work was sponsored by the U.S. NSF STC Center, The Boeing Company, and the Keck Foundation.

[1] K. Yamagi. *J. Phys. Soc. Jpn.* **58** (1989) 1520–1523.
[2] J. Singleton, P. A. Goddard, A. Ardavan, et al. *Phys. Rev. Lett.* **88** (2002) 037001.

ELECTRICAL TRANSPORT PROPERTIES OF $Bi_{0.98}Sb_{0.02}$ NANOWIRES IN SEMIMETAL AND SEMICONDUCTOR STATES

A. A. Nikolaeva[1], L. A. Konopko[1,*], T. E. Huber[2], Gh. I. Para[1], I. Gh. Ghergishan[1]
[1]*Technical University of Moldova, Chisinau, Republic of Moldova;*
[2]*Howard University, 500 College St. N.W., Washington, DC 20059, USA.*
*E-mail: leonid.konopko@iien.utm.md

Bismuth–antimony ($Bi_{1-x}Sb_x$) alloys are a unique class of materials, which can be in the semimetal, gapless, and semiconductor state depending on antimony concentration. We report an investigation of the electrical transport properties, thermoelectric properties, the Shubnikov de Haas (SdH) oscillations of single crystal $Bi_{0.98}Sb_{0.02}$, micro and nanowires in semimetal and semiconductor states. Glass-insulated Bi-Sb microwires were prepared by liquid-phase casting in glass capillary by the Ulitovsky method [1]. It has been predicted that in the semimetal region ($x < 0.04$) the critical diameter d_c of nanowires is shifted to higher values compared with those in pure Bi; at these values, the overlap between the L-point electron subbands and the T-point hole subbands vanishes due to the quantum dimensional effect (semimetal–semiconductor transition).

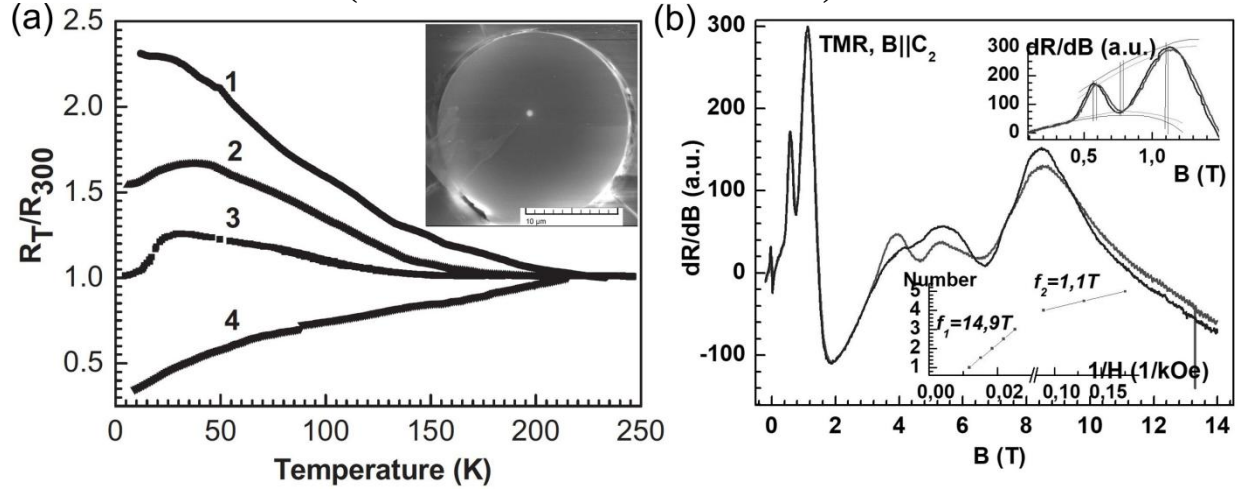


Figure 1. (a) Temperature dependences of residual resistance $R/R_{300}(T)$ for $Bi_{0.98}Sb_{0.02}$ wires of various diameters d: 1 - d=300 nm, 2 - d=400 nm, 3 - d=600 nm, 4 - d=1600 nm. Inset: SEM image of the cross-section of a Bi-Sb glass-coated wire with 650 nm diameter. (b). Shubnikov–de Haas (SdH) oscillations for $Bi_{0.98}Sb_{0.02}$ wire, d=600 nm on the derivative of the transverse magnetoresistance dR/dB, $B||C_2$, at T= 2.1 and 4.2 K. Top inset: SdH oscillations from electron ellipsoids L_b. Bottom inset: dependence of the SdH oscillation index on the inverse magnetic field 1/B.

The quantum size effect (QSE) occurs in the Bi-2at%Sb wires with diameter 4-5 times larger, than in pure Bi wires, where d_c = 80 nm: – the semimetal-semiconductor transition in nanowires, manifested in "semiconductor" temperature dependences of resistance *R(T)*, occurs at diameters $d \leq 400$ nm (see Fig. 1.(a); – the sign of the thermopower changes from negative to positive at lower temperatures and at larger diameters than in pure Bi. The peak of positive polarity in *α(T)* reaches values of 150–170 μV/K at 30–50 K in wires with d = 200–300 nm; – the onset of negative magnetoresistance in a transverse magnetic field ($B||C_2$ and $B||C_3$) occurs at $d \leq 400$ nm. From the SdH oscillations shown in Fig. 1 (b), we obtain the mobility of charge carriers from light L-electrons μ_e=(80-100)*10³ cm²/Vs in wires at 4.2 K, which indicates the high structural perfection of the studied nanowires.

ACKNOWLEDGEMENTS. This work was supported by the Ministry of Education and Research of Moldova (project no. 020201). In the U.S., the work was sponsored by the U.S. NSF STC Center, The Boeing Company, and the Keck Foundation.

[1] N.B.Brandt, D.V.Gitsu, A.A.Nikolaeva, Y.G.Ponomarev *Sov. Phys. JETP* **45**(6) (1977) 1226-1232
[2] A. Nikolaeva, L. Konopko, T. Huber, P. Bodiul, I. Popov. *J. Solid State Chemistry* **193** (2012) 71-75.

ELECTRICAL AND PHOTOELECTRICAL PROPERTIES OF Ga-DOPED Zn2:1Sn THIN FILMS OBTAINED BY SPRAY PYROLYSIS

V. Morari[1,*], D. Bragari, V. Suman[1], E. V. Rusu[1],
[1]*Institute of Electronic Engineering and Nanotechnologies „D. Ghitu", Technical University of Moldova, Academiei str. 3/3, Chisinau 2028, Republic of Moldova;*
*E-mail: vadim.morari@iien.utm.md

Zinc stannate (Zn_2SnO_4), a wide-bandgap spinel-type semiconductor, has attracted considerable attention for ultraviolet photodetection applications due to its high optical transparency, chemical stability, and favorable electrical properties. Recent studies have demonstrated that controlled doping and thermal treatment can effectively modify the defect structure and charge transport mechanisms, leading to improved UV photodetector performance [1,2]. Gallium-doped (containing 1, 2, and 3 vol.%) Zn2:1Sn thin films was successfully deposited on Si (100) substrates by the spray pyrolysis technique and subsequently annealed in air and vacuum to investigate the influence of dopant concentration and post-deposition annealing atmosphere on their photoelectrical properties. The electrical transport behavior was systematically investigated by current–voltage (I–V) measurements performed under dark conditions and under illumination with a 50 W halogen lamp, while the photodetection performance was evaluated in terms of electrical resistance, responsivity, and specific detectivity (at 8 V bias voltage). All samples exhibited nearly ohmic current–voltage characteristics under dark conditions, accompanied by a pronounced increase in photocurrent upon illumination, confirming the efficient photogeneration, separation, and transport of charge carriers within the Zn2:1Sn matrix. The results demonstrate that both Ga incorporation and the annealing atmosphere play a decisive role in determining the electrical transport behavior and UV photoresponse by modifying the concentration of oxygen vacancies, defect states, and free charge carriers. Vacuum-annealed films exhibited a gradual increase in responsivity from 13.1 to 14.3 $A \cdot W^{-1}$ with increasing Ga concentration (1–3 vol.%), accompanied by a significant decrease in electrical resistance from 780 to 260 Ω. This behavior indicates enhanced electron transport arising from the formation of donor-like oxygen vacancies and improved electrical conductivity. In contrast, air-annealed films showed lower responsivity values ranging from 10.5 to 12.1 $A \cdot W^{-1}$, while their electrical resistance increased markedly from 230 to 1120 Ω. This behavior can be attributed to oxygen incorporation during annealing, which compensates oxygen vacancies, suppresses donor states, and consequently reduces the free-carrier concentration. Interestingly, the undoped Zn2:1Sn reference film exhibited the highest responsivity, reaching 18.3 $A \cdot W^{-1}$ after air annealing and 15.6 $A \cdot W^{-1}$ after vacuum annealing. These results suggest that excessive Ga incorporation does not necessarily improve the photodetection performance, as the additional dopant-related defects may introduce recombination centers that limit the lifetime and transport of photogenerated charge carriers. The calculated specific detectivity values of the Ga-doped films ranged from 3.4×10^8 to 8.1×10^8 Jones, whereas the undoped Zn_2:$_1$Sn film exhibited the highest detectivity of 8.6×10^8 Jones, highlighting its excellent intrinsic ultraviolet photodetection capability. These findings demonstrate that controlled Ga doping, combined with an appropriate annealing treatment, provides an effective strategy for tailoring the defect, electrical transport, and optoelectronic properties of Zn2:1Sn thin films, thereby enabling the optimization of their performance for high-sensitivity ultraviolet photodetector applications.

ACKNOWLEDGEMENTS. This work was supported by the National Agency for Research and Development (NARD) of the Republic of Moldova under Young Researchers 2025-2026 Project No. #25.80012.5007.31TC, and Institutional Subprogram Project #02.02.01 no. 4/FI „Nanostructures and advanced materials for applications in spintronics, thermoelectricity and optoelectronics".

[1] Y. Zhang, X. Wang, Y. Wang, *et al.* Fabrication and characterization of ultraviolet detector based on epitaxial Ta-doped Zn_2SnO_4 films. *Optical Materials* **108** (2020) 1110224. Doi: https://doi.org/10.1016/j.optmat.2020.110224.

[2] S. C. Shih, C. Y. Guo, H. Y. Liu, R. M. Ko, W. C. Hsu. A Study of Different Annealing Ambiences on the Performance of $ZnGa_2O_4$ UVC Photodetectors by Ultrasonic Spray Pyrolysis Deposition. *IEEE Sensors Journal* **25(4)** (2025) 6242-6249. Doi: https://doi.org/10.1109/JSEN.2024.3432136.

INTRINSIC PEROXIDASE-LIKE ACTIVITY OF ZNO/MGFE$_2$O$_4$ PEG NANOCOMPOSITES AND THEIR APPLICATION IN THE COLORIMETRIC DETECTION OF H_2O_2

T. D. Gutsul[1,*], I. O. Rastimesina[1], A. J. Sibaev[1], E. P. Condrea[2], I. I. Belotercovschii[1]
[1]*Technical University of Moldova, Institute of Electronic Engineering and Nanotechnologies "D. Ghitu," str. Academiei 3/3, Chisinau, Republic of Moldova;*
[2]*Technical University of Moldova, Institute of Microbiology and Biotechnology, str. Academiei 3/3, Chisinau, Republic of Moldova*
*E-mail: tatiana.gutul@iien.utm.md

It has been shown that nanoferrites are nanomaterials exhibiting intrinsic enzyme-like activity. Magnesium ferrite nanoparticles ($MgFe_2O_4$ NPs) have been effectively used as nanozymes; they have been shown to behave like a peroxidase in the oxidation of 3,3', 3,5'-tetramethylbenzidine (TMB) [1],[2]. These materials have been used in various fields, such as biosynthesis, environmental protection, and bioelectronic sensor devices. In this paper, a method for synthesizing an ZnO/$MgFe_2O_4$PEG nanocomposite and studying it as a peroxidase enzyme mimetic has been described. The resulting nanocomposite has been characterized by X-ray powder diffraction (XRD), scanning electron microscopy (SEM), and FT-IR spectroscopy. The morphology of the ZnO/$MgFe_2O_4$PEG powder has been studied by SEM; it has been shown that the ZnO/$ZnFe_2O_4$ PEG nanocomposite synthesized in the presence of a polymer have a spherical form and a size of 12–25 nm. Since the NPs have a high surface energy, they undergo a rapid interparticle interaction and coarsening and aggregate into spherical structures with a diameter of 60–90 nm. Composition has been determined by EDX with an Zn: Mg: Fe ratio of 1:1:2.1. Experimental results have shown that the ZnO/$MgFe_2O_4$/PEG nanocomposites exhibit peroxidase-like activity in a linear range of 0.05–0.36 μM. In addition, the color change dependent on hydrogen peroxide concentration can offer a convenient approach to detecting H_2O_2 both with the naked eye and spectrophotometrically. Therefore, the ZnO/$MgFe_2O_4$/PEG nanocomposites are a promising candidate for the colorimetric detection of H_2O_2 in rainwater.

[1] L. Gao, M. Liang, X. Yan. *Standardize dassays for determining the catalytic activity and kinetics of peroxidase like nanozymes*. Nat. Protoc., 13, 1506−1520. 2018. DOI: 10.1038/s41596-018-0001-1.
[2] J. Zhuang, J. Zhang, L. Gao, Y. Zhang, N. Gu, J. Feng, D. Yang, X. Yan, *A novel application of iron oxide nanoparticles for detection of hydrogen peroxide in acid rain*. Materials Letters., 62(24), 3972–3974. 2008. DOI: 10.1016/j.matlet.2008.05.025

MICRO AND NANOWIRE AND ITS APPLICATION

S. A. Baranov*
Institute of Applied Physics, Moldova State University ,
str. Academiei 5, Chisinau, MD-2028 Republic of Moldova
*E-mail: sabaranov48@gmail.com

The natural ferromagnetic resonance (NFMR) in cast glass-coated amorphous magnetic micro- and nanowires (GCAMNWs) produced by the Taylor-Ulitovsky method [1, 2] has been studied theoretically and experimentally [3-6]. The NFMR reveals large residual stresses appearing in the microwire core in the course of casting; these stresses, together with the magnetostriction, determine the magnetoelastic anisotropy. In cylindrical coordinates the residual tension is characterized by the axial, σ_z, radial, σ_r, and tangential, σ_φ, components, whose values depend on the ratio of the radius R_m of the metallic kernel to the total microwire radius R_c:

$$x = \left(\frac{R_c}{R_m} \right)^2 - 1, \qquad (1)$$

Using the cylinder-shell model, simple analytical expressions were obtained for these stresses, the maximum stress in the metallic kernel being $\sigma_0 \sim 2$ GPa [3]. Besides the residual stresses, the NFMR frequency is influenced by externally applied stresses on the microwire or the composite, the so-called stress effect: when the microwire is embedded in a solid matrix that itself deforms under external influence, an additional axial term $\sigma_{ez} = P_o/[S_m(kx + 1)]$ appears, where P_o is the force applied to the composite, $S_m = \pi(R_m)^2$ is the cross-sectional area of the kernel and k is the ratio between the Young's moduli of the glass and the metal. The NFMR frequency then reads [4-6]:

$$\omega(GHz) \approx \omega o \left(\frac{0.4x}{0.4x+1} + \frac{\sigma_{ez}}{\sigma_o} \right)^{1/2}, \qquad (2)$$

where $\omega_0(\mathrm{GHz}) \approx 1.5(10^6\lambda)^{1/2}$.

These expressions clearly show the dependence of the stresses on the ratio of the external radius of the microwire to the radius of the metal kernel and on the ratio of the Young's moduli of glass and metal. The dependence of the NFMR frequency on the deformation of the microwires is proposed to be used in the distant diagnostics of dangerous deformations of critical infrastructure objects and for remote diagnostics in medicine. Such objects are periodically scanned with floating-frequency radar to determine the deviation of the initial NFMR frequency due to potentially dangerous deformations of the monitored object. Unlike the alternative approach based on the giant magnetoimpedance effect [7], the NFMR method requires no external magnetization of the sample.

[1] G.F. Taylor, *Phys. Rev., 23*, 655, (1924).
[2] M. Vazquez, A. P. Zhukov, *J. Magn. Magn. Mat., 160*,223, (1996).
[3] S. A. Baranov, V. S. Larin, A. V. Torcunov, *Crystals* , *7*, 136, (2017).
[4] S. A. Baranov, *Tech .Phys .Lett., 24*,549, (1998).
[5] S. A. Baranov, M. Yamaguchi, K. L. Garcia, M. Vazquez, *Surf. Engin. Appl. Electrochem., 44*, 245, (2008).
[6] S. A. Baranov, *Moldavian J. Phys. Sci.,* , *14*, 201, (2015).
[7] D. Makhnovskiy, A. Zhukov, V. Zhukova, J. Gonzalez, *Adv. Sci. Technol.* , *54*, 201, (2008).

SOLVENT-DEPENDENT EFFICIENCY OF ULTRASONIC LIQUID-PHASE EXFOLIATION OF TMD CRYSTALS

S. Barladean[1,2,*], N. Siminel[2]
[1]*Faculty of Physcis and Engineering, Moldova State University, Chisinau, Republic of Moldova*
[2]*Institute of Applied Physics, Moldova State University, Chisinau, Republic of Moldova*
*E-mail: barladeanstepa@gmail.com

This study investigates methods for exfoliating molybdenum disulfide (MoS_2), a layered transition metal dichalcogenide (TMD), and subsequently characterizing the resulting atomically thin two-dimensional structures. The relevance of this work stems from the unique properties of MoS_2: upon transition from a bulk crystal to a monolayer, quantum confinement transforms the material from an indirect-gap semiconductor into a direct-gap semiconductor. This change is accompanied by a sharp increase in the photoluminescence quantum yield.

The primary objective of this study is to investigate the physicochemical methods for exfoliating bulk MoS_2 and to determine the optimal conditions for the stable formation of monolayers. Mechanical and liquid-phase exfoliation (LPE) are considered theoretically and compared, with the experimental emphasis on the latter. The LPE method is based on ultrasonic cavitation, which generates microjets that overcome the weak interlayer van der Waals forces holding the crystal layers together.

To identify the most effective medium, two different solvents were used in the experiment:

- isopropyl alcohol (IPA), which provides thermodynamic stabilization by reducing the interfacial energy;
- an aqueous solution of bovine serum albumin (BSA), whose macromolecules create a steric barrier that prevents restacking of the monolayers.

The results show that, for the large-scale production of MoS_2 nanosheets by the LPE method, the use of BSA protein macromolecules is more than twice as effective as thermodynamic stabilization with alcohol.

OPTIMIZATION OF THE GROWTH TECHNOLOGY OF TIS_2, WS_2, AND MOS_2 SINGLE CRYSTALS FOR SUPERCAPACITOR APPLICATIONS

V. Goremichin*, N. Siminel, C. Slobodeniuc, L. Kulyuk
Institute of Applied Physics, Moldova State University, Chisinau, Republic of Moldova
*E-mail: vgoremichin@gmail.com

The development of novel hybrid materials for the fabrication of supercapacitor electrodes is a promising and rapidly advancing field in energy generation and storage technologies. The main advantages of supercapacitors include high-speed energy delivery, high power density, fast charge–discharge rates, excellent cycling stability, and long service life [1]. These devices are widely used in renewable energy management and electric transportation, as well as in powering smart and wearable electronic devices. Transition metal dichalcogenides (TMDs) are among the most promising candidates for the development of high-performance electrode materials. Their attractiveness arises from their large effective surface area, tunable surface properties, abundance of active coordination sites, and their ability to exhibit both Faradaic and non-Faradaic electrochemical behaviour [2].

High-quality bulk single crystals of TiS_2, WS_2, and MoS_2 were synthesized by the chemical vapor transport (CVT) method. The precursor mixtures were loaded into evacuated quartz ampoules (14 mm inner diameter) sealed under a vacuum of approximately 10^{-4} Torr. Iodine (99.95% purity) was employed as the transport agent. The sealed ampoules containing the polycrystalline precursor materials were placed in a two-zone horizontal tube furnace with independently controlled temperature zones. The temperature profile was monitored and maintained with an accuracy of ±0.1 °C. The temperatures of the source and growth zones were varied to optimize the crystal growth conditions. The growth of TMD single crystals was found to be strongly influenced by several parameters, including the heating rate of the precursor, growth temperature, temperature gradient between the furnace zones, growth duration, and iodine concentration.

The optimum iodine concentration was determined to be 5 $mg \cdot cm^{-3}$. For TiS_2, the optimal temperatures of the source and growth zones were 1030 °C and 1000 °C, respectively. In the case of WS_2, the precursor charge was held at the synthesis temperature for 24 h prior to crystal growth. The optimal source and growth temperatures were 1060 °C and 1040 °C, respectively. For MoS_2, the corresponding temperatures were 1080 °C for the source zone and 1050 °C for the crystal growth zone. The synthesis and crystal growth processes were carried out for 10 days. After completion of the growth process, the ampoules were cooled inside the furnace at a controlled rate of 30–40 °C h^{-1} to minimize thermal stress and preserve crystal quality.

X-ray diffraction (XRD) analysis confirmed that the synthesized TiS_2 crystallized in the desired metallic 1T phase [3]. The diffraction pattern was indexed to the trigonal crystal structure (space group $P\bar{3}m1$) with octahedral coordination, demonstrating the successful formation of the target phase with high crystallinity. The MoS_2 samples exhibited intense excitonic photoluminescence, characteristic of stoichiometric 2H-MoS_2 with a uniform layered morphology, which indicates the high crystalline and optical quality of the semiconducting 2H phase.

Therefore, the obtained high-quality single crystals provide an excellent platform for the preparation of ultrathin flakes and subsequent phase engineering aimed at developing high-performance electrodes for next-generation supercapacitors.

[1] M. Czagany, S. Hompoth, A. K. Keshri, N. Pandit, I. Galambos, Z. Gacsi, P. Baumli. Supercapacitors: An Efficient Way for Energy Storage Application. Materials 2024, 17, 702. https://doi.org/10.3390/ma17030702
[2] M. Ali, A. M. Afzal, M. W. Iqbal, S. Mumtaz, M. Imran, F. Ashraf, A. U. Rehman, F. Muhammad. 2D-TMDs based electrode material for supercapacitor applications. Int. J. Energy Res. 2022, 46, 22336–22364. https://doi.org/10.1002/er.8698
[3] M. Ashton, J. Paul, S. B. Sinnott, R. G. Hennig. Topology-Scaling Identification of Layered Solids and Stable Exfoliated 2D Materials. Phys. Rev. Lett. 2017, 118, 106101. https://doi.org/10.1103/PhysRevLett.118.106101

HIGH-ENTROPY $(FeCoNiCrMn)_3O_4$ FILMS FOR CAMOUFLAGE COATINGS IN MICROWAVE REGION

S. Vatavu[1,*], Ig. Narolschi[1], O. Shapoval[1], M. Rusu[1,2], A. Belenchuk[1], Gh. Ghilețchii[1], A. Varzari[1], V. Crăciun[3], J. Lančok[4], Ș.-A. Irimiciuc[3,4]
[1]*Moldova State University, Chișinău, Moldova;*
[2]*Helmholtz-Zentrum Berlin für Materialien und Energie GmbH, Berlin, Germany*
[3]*National Institute for Laser, Plasma and Radiation Physics, Măgurele, România*
[4]*Institute of Physics of the Czech Academy of Sciences, Prague, Czechia*
*E-mail: sergiu.vatavu@usm.md

Among microwave camouflage materials, a relatively new class of high-entropy compounds deserves attention. Specifically, oxides of transition metals (Cr, Mn, Fe, Co, and Ni) with a spinel crystalline phase could simultaneously exhibit acceptable magnetic, dielectric, and electronic properties. Camouflage technology must meet the requirements for synthesizing high-entropy compounds with the ability to apply coatings. The technology for producing oxide films from organometallic compounds (Metalorganic Aerosol Deposition [1]) fully meets these challenges.

Using Metalorganic Aerosol Deposition, one can easily manipulate the number of organometallic compounds β - diketonates (e.g., Cr-, Mn-, Fe-acetylacetonates) in the aerosol solution. The main challenge is the varying synthesis efficiency for each precursor and the dependence of this efficiency on the synthesis temperature. EDS analysis was used to control the equimolar element distribution in the film. Five films of single oxides and a film of five metal oxides were deposited under identical conditions. A clear relationship between the amount of the elements in the film and the magnitude of the EDS signal was found by combining the analysis of the crystal phase by XRD and of the film thickness by XRR. A third-party NIST DTSA-II Oberon program with the ability to simulate the EDS spectrum from a film on a thick substrate was used. As a result, we synthesized a 70 nm single-phase film with a spinel structure and a near-equimolar distribution of 5 transition metal elements. In addition, the electronic properties of the films were investigated in a combined Kelvin probe and photoelectron yield spectroscopy setup [2], demonstrating a n-type conductivity of the film with Fermi level at 0.43 eV from CBM.

The physical properties of the high-entropy oxide (HEO) thin films were investigated in the microwave frequency range of 8-18 GHz. The measurements of the scattering parameters S_{11} and S_{21} were carried out using a rectangular waveguide of WR-90 type (X-band) and WR-62 (Ku band) TE_{10} mode and a vector network analyzer. The decrease in reflection ($R=|S_{11}|^2$) from 5.22% (-12.82) *dB* at 8.7 *GHz* to 1.96% (-17.08) *dB* at 18.0 *GHz* confirms that the microwaves easily penetrate the material, with no major losses at the interface. Along with the transmission attenuation $T=|S_{21}|^2$ decreasing from 0.52 *db* down to 2.64 *dB*, the surface impedance decreases from 3181.2 Ω/□ to 531.3 Ω/□, determining an increase in dynamic conductance (σ_{ac}) from $3.14\times10^3 S/m$ up to a maximum of $1.88\times10^4 S/m$ at 18.0 *GHz*. The resulting data demonstrated the applicability of the HEO films for electromagnetic camouflage coating use and showed a decrease in radar cross section (RCS) in the range of X and Ku bands. Additional analysis on the physics of the HEO thin films in the microwave region of the electromagnetic spectrum considers the frequency behavior of the electrical permittivity and magnetic permeability [3].

ACKNOWLEDGEMENTS. Ministry of Education and Research of the Republic of Moldova, subprogram 011207; the NATO grant SPS MYP G6153

[1] V. M. Moshnyaga, et al, *Appl. Phys. Lett.* **74** (1999) 2842-2844
[2] M. Rusu et. al. *ACS Appl. Mater. Interfaces* **13** (2021) 7745-7755
[3] J. Luo, et al, *Phys. Rev. B* **90** (2014) 165128 (9pp.)

PHASE-TRANSITION-DRIVEN THERMOCHROMIC RESPONSE MODELLING IN VO_2-LIKE SYSTEMS

A. Varzari[1,*], A. Cliucanov[1], Gh. Ghilețchii[1], S. Vatavu[1]
[1]*Moldova State University, Chișinău, Moldova*
*E-mail: alexandru.varzari@usm.md

Vanadium dioxide (VO_2) belongs to the broad class of transition-metal oxides characterized by partially filled d orbitals and a pronounced interplay between electronic and lattice degrees of freedom [1]. Thermochromism in VO_2 is driven by a Peierls-Mott phase transition, arising from the interplay between electron-electron and electron-phonon interactions [2]. This transition is accompanied by a structural transformation from the low-temperature insulating monoclinic M1 phase to the high-temperature metallic rutile R phase at $\sim 67\ ^oC$ [1,2].

A minimal microscopic model for describing the Peierls-Mott transition in VO_2-like systems is provided by the Hubbard-Holstein Hamiltonian [2,3]:

$$H = -\sum_{\langle i,j\rangle,\sigma} t_{ij}\left(n_{ij\sigma} + n_{ji\sigma}\right) + U\sum_{i,\sigma} n_{ii\sigma} + \hbar\omega_0 \sum_i b_i^+ b_i + g\sum_{i,\sigma} n_{ii\sigma}(b_i^+ + b_i) \qquad (1)$$

Here, the first term represents the electronic kinetic energy associated with hopping between neighboring lattice sites and is related to the bandwidth $W \sim 2z|t|$. The second term describes the on-site Coulomb repulsion between electrons with opposite spins and is characterized by the interaction parameter U. The third term represents the phonon contribution and is characterized by the phonon energy $\hbar\omega_{\mathrm{ph}}$, whereas the final term describes the local electron-phonon interaction with coupling constant g. Thus, the relative strengths of the Mott and Peierls contributions are characterized by U/W and $\lambda = 2g^2/\hbar\omega_{ph}W$, respectively.

The optical properties are described by the complex dielectric function in terms of the optical conductivity. Within linear-response theory, the optical conductivity is decomposed into paramagnetic and diamagnetic contributions [4]:

$$\varepsilon(\omega) = \varepsilon_\infty + \frac{i}{\varepsilon_0\omega}\sigma_{ab}(\omega), \qquad \sigma(\omega) = \frac{i}{\omega + i0^+}\left(D_{ab} + \Pi_{ab}(\omega)\right) \qquad (2)$$

By deriving the current and diamagnetic tensor operators and introducing the group velocity $v_\alpha(k)$ and band curvature $m_{ab}^{-1}(k)$, both contributions can be formulated in terms of the one-particle Green's function $G^{-1}(k, i\omega_n) = i\omega_n + \mu - \varepsilon_k - \Sigma(k, i\omega_n)$. Thus, the interaction effects on the optical response are associated with the self-energy $\Sigma(k, i\omega_n)$.

Within Dynamical Mean-Field Theory (DMFT) [5,6], the self-energy is approximated as local, i.e., momentum independent, while retaining its full frequency dependence, $\Sigma(k, i\omega_n) \to \Sigma_{loc}(i\omega_n)$. So, the interacting lattice problem turns into a self-consistent single-site quantum impurity problem embedded in an effective bath, characterized by the Weiss field $\mathcal{G}_0(i\omega_n)$ and the hybridization function $\Delta(i\omega_n)$. Thus, the self-energy is determined from the impurity Green's function, which can be evaluated using numerical impurity solvers such as quantum Monte Carlo (QMC) or exact diagonalization (ED) [6].

ACKNOWLEDGEMENTS. CNCS-UEFISCDI, project number 18ROMD/20.05.2024, project PN-IV-P8-8.3-ROMD-2023-0186, within PNCDI IV and Ministry of Education and Research of the Republic of Moldova, subprogram 011207

[1] Gh. Ghilețchii, A. Varzari, Ș.-A. Irimiciuc, J. Lančok, S. Vatavu. *Materials* **19(14)** (2026) 2943.
[2] A. Varzari, Gh. Ghilețchii, Ș.-A. Irimiciuc, J. Lančok, S. Vatavu. *Materials* **19(12)** (2026) 2610.
[3] F. Hébert, B. Xiao, R. T. Scalettar, G. G. Batrouni, *Physical Review B* **99(7)** (2019) 075108.
[4] A. J. Millis. Optical conductivity and correlated electron physics. In: Baeriswyl, D., Degiorgi, L. (eds) Strong interactions in low dimensions. *Physics and Chemistry of Materials with Low-Dimensions* **25** (2004) Springer, Dordrecht.
[5] A. Georges, G. Kotliar, W. Krauth, M. J. Rozenberg. *Reviews of Modern Physics* **68(1)** (1996) 13-125.
[6] G. Kotliar, S. Y. Savrasov, K. Haule, V. S. Oudovenko, O. Parcollet, C. A. Marianetti. *Reviews of Modern Physics* **78(3)** (2006) 855-951.

MASKLESS ONE-STEP MICROPATTERNING OF AZOPOLYMER THIN FILMS BY DIRECT ELECTRON BEAM RECORDING

C. Losmanschii*, E. Achimova, V. Abaskin, S. Moldovanu, V. Botnari,
A. Meshalkin, V. Cazac, D. Muntean, D. Spoială
Moldova State University, Institute of Applied Physics, Chisinau, Moldova;
*E-mail: constantinlindemann@gmail.com

In this study, we report a direct electron beam recording (EBR) approach for the one-step fabrication of micropatterns on azopolymer thin films. The photosensitive material employed was poly-*N*-epoxypropylcarbazole–Solvent Yellow 3 (PEPC-SY3), a carbazole-based azopolymer containing 30 wt% of the azochromophore Solvent Yellow 3 (SY3). Most reported approaches for patterning azopolymer thin films are based on light-induced mass transport driven by the photoisomerization of azobenzene chromophores or on multistep lithographic processes involving photoresists, masks, and subsequent pattern transfer. While these techniques have enabled the fabrication of a wide variety of micro- and nanostructures, they may impose limitations on the achievable pattern geometry, feature resolution, and fabrication flexibility. Furthermore, multistep processing increases fabrication complexity and cost, whereas light-induced patterning is inherently constrained by the optical exposure conditions and the material's photoresponse. Consequently, there is a growing interest in alternative direct-write techniques capable of producing permanent microstructures with high spatial precision through simplified and resist-free fabrication methods.

This work is based on the hypothesis that localized electron beam irradiation may induce chemical bond cleavage and structural rearrangement within the azopolymer matrix, potentially accompanied by localized mass transport. These electron-induced modifications were expected to produce permanent topographical changes, enabling direct one-step micropatterning of the polymer surface.

Several representative microstructures fabricated using the proposed direct EBR patterning approach, including dot arrays, diffraction gratings, diffractive optical elements (DOEs), and amplitude structure are presented in Fig. 1. The successful fabrication of these structures demonstrates the versatility of the method and its capability to produce functional photonic components with high pattern fidelity. These results highlight the potential of direct EBR patterning of azopolymer thin films as a promising fabrication route for next-generation photonic devices, while also opening opportunities for applications in micro-optics, optical sensing, and other fields requiring high-resolution surface microstructuring.

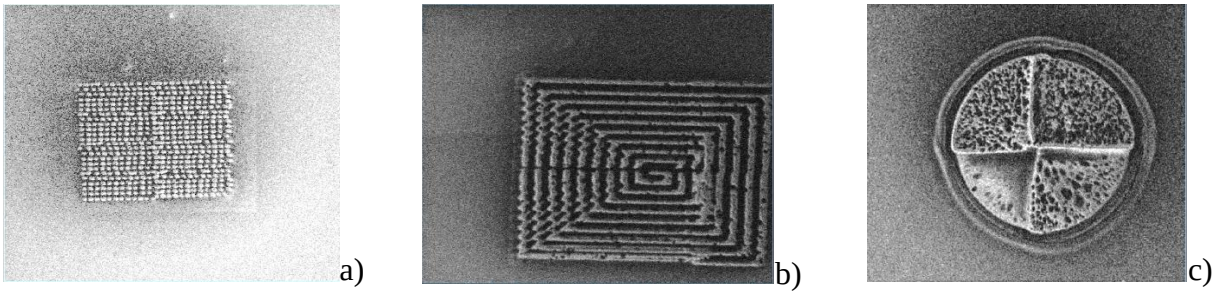


Figure 1. Examples of microstructures fabricated by direct electron beam recording (EBR): (a) dot array, (b) spiral microstructure, and (c) a four-level amplitude object, in which each quadrant of the circular pattern has a different relief height.

ACKNOWLEDGEMENTS. This research was funded by the Ministry of Education and Research of the Republic of Moldova under the research sub-programme **011201**, and by the National Agency for Research and Development of the Republic of Moldova (NARD) under Project No. **25.80013.8007.01ROMD**.

TECHNOLOGY AND ELECTRONIC PROPERTIES OF NiO DOPED BY Cu AND Ga FOR CHROMOGENIC AND PHOTOVOLTAIC APPLICATIONS

Gh. Ghileţchii[1,*], O. Shapoval[1], M. Rusu[1,2], A. Varzari[1], A. Belenchuk[1], Ig. Narolschi[1], V. Nicorici[1], V. Crăciun[3], P. Garoi[3], V. Grumezescu[3], Ș.-A Irimiciuc[3], S. Vatavu[1]

[1]*Moldova State University, Chișinău, Moldova;*

[2]*Helmholtz-Zentrum Berlin für Materialien und Energie GmbH, Berlin, Germany*

[3]*National Institute for Laser, Plasma and Radiation Physics, Măgurele, România,*

*E-mail: gheorghe.ghiletchii@usm.md

Nickel Oxide (NiO) is a unique *p*-type semiconductor, exhibiting a rock-salt structure and a wide bandgap ranging from 3.4-4.0 eV along with high optical transparency (>75% in the visible spectrum). Within the Ni–O system, NiO is the sole oxide exhibiting thermodynamic stability across a broad range of temperatures and oxygen partial pressures. NiO is successfully applied in optoelectronic [1] and photovoltaic [2] devices. For application in electrochromic coatings, monovalent and trivalent doping of NiO stands out as a key method for enhancing its performance [3].

This work aims to prepare NiO films controllably doped with Cu and Ga elements, revealing a highly crystalline structure. The Metalorganic Aerosol Deposition [4] technology's strengths lie in the precise control of impurity concentration and the flexibility to alter the doping element, making it a valuable tool for optimizing electrochromic functionality and optoelectronic properties. The deposition solution was prepared by dissolving nickel acetylacetonate [$Ni(acac)_2$] along with one of the dopant precursors – acetylacetonates of Cu or Ga. The concentration of Cu or Ga was varied from 0.1 to 6.0 at.% in solution. The experiments on NiO growth were carried out using SiO_x/Si(111) and r-cut Al_2O_3 substrates. To improve the accuracy of the impurity content, a dilution technique was used. Doped nickel oxide films were successfully synthesized by tuning the substrate temperature (ranging from 420 to 650°C).

The electronic properties of the films were investigated in a combined Kelvin probe and photoelectron yield spectroscopy setup [5]. For Cu-doped NiO films, we found a sharp dependence of the work function (WF) and ionization energy (IE) on the Cu dopant concentration. Incorporation of only 0.02 at.% of Cu leads to significant and abrupt changes of the WF and IE, which result in essential variations of the valence band maximum position with respect to Fermi level position, $E_F - E_{VBM}$, of more than 400 meV compared to that of the undoped intrinsic NiO layers. By using the Boltzmann statistic, we estimate the concentration of holes to vary between 2.6×10^{13} cm^{-3} and 1.8×10^{14} cm^{-3} for the Cu concentration varying from 0.02 to 2.77 at.%, respectively. High career concentrations of about the later magnitude were achieved also by using Ga doping. However, the decrease of the $E_F - E_{VBM}$ with the increasing the doping was found to show a monotonic behavior and strong fluctuations from mean values. The maximum concentration of holes was found for Ga doping concentrations of 3.30 at.%.

ACKNOWLEDGEMENTS. Ministry of Education and Research of the Republic of Moldova, subprogram 011207 DETCONV; CNCS-UEFISCDI through the Bilateral România-Moldova project DUALCHROM, Grant No. 18ROMD/20.05.2024, PN-IV-P8-8.3-ROMD-2023-0186.

[1] M. Napari, T. N. Huq, R. L. Z. Hoye, J. L. *MacManus-Driscoll, InfoMat.* **3** (2021) 536–576.
[2] M. M. Hasan et al. *Front. Mater.* **12** (2025) 1652733 (17 pp.).
[3] R. Cao, H.-X. Deng, J.-W. Luo, ACS Applied Materials & Interfaces **11** (2019) 24837–24849 .
[4] V. M. Moshnyaga, et al, *Appl. Phys. Lett.* **74** (1999) 2842-2844.
[5] M. Rusu et. al. *ACS Appl. Mater. Interfaces* **13** (2021) 7745-7755.

DIFFRACTION EFFICIENCY AS A MEASURE OF OPTICAL PARAMETER MODULATION IN RECORDING MEDIA

A. Meshalkin*, E. Achimova, V. Abaskin, C. Losmanschii, V. Botnari, D. Muntean
Institute of Applied Physics, Moldova State University, Chişinău, Republic of Moldova
*E-mail: alexei.meshalkin@ifa.usm.md

Diffraction efficiency is commonly used as a key performance parameter of diffractive optical elements. At the same time, it can serve as a convenient indirect measure of the photoinduced modulation of optical and structural parameters in photosensitive recording media. In this work, the relationship between diffraction efficiency and phase modulation formed during holographic recording is analyzed for surface-relief diffraction gratings. Multilayer As_2S_3–Se chalcogenide structures are considered as recording media, in which optical irradiation produces simultaneous refractive-index modulation and photoinduced material redistribution.

For a sinusoidal phase grating, the diffraction efficiency of the *m*-th diffraction order can be described within the Raman–Nath approximation by the squared Bessel function of the phase modulation depth. The latter is determined by the optical path difference introduced by the refractive-index variation and/or surface relief. Consequently, the experimentally measured diffraction efficiency contains integrated information about the modification of the recording medium. With increasing exposure, the phase modulation depth increases and the diffraction efficiency exhibits a characteristic oscillatory behavior, providing a possibility for quantitative analysis of the recording process.

Holographic gratings were recorded in As_2S_3–Se multilayer structures in a two-beam interference configuration with oppositely circularly polarized beams. The evolution of the first-order diffraction efficiency was monitored in situ using a 650 nm probe beam. Atomic force microscopy confirmed the formation of sinusoidal surface-relief structures with different modulation depths. Good agreement between experimentally measured and theoretically modeled diffraction-efficiency kinetics demonstrates that diffraction efficiency can be used to characterize the evolution of phase modulation during recording.

An important aspect of the proposed approach is the possibility of separating the contributions of refractive-index modulation and surface relief. In particular, measurements performed in transmission and reflection geometries provide complementary information because transmission is sensitive to the combined optical and geometrical phase modulation, whereas reflection is particularly sensitive to the surface-relief contribution. Analysis of diffraction patterns produced by Gaussian-beam recording further enables the reconstruction of diffraction-efficiency evolution from a single recorded structure. The appearance of concentric diffraction rings with increasing exposure provides information about the sequential growth of the phase modulation depth.

Thus, diffraction efficiency can be considered not only as a final quality parameter of a diffractive structure, but also as a sensitive optical indicator of the degree of modification of a photosensitive recording medium. Model-assisted analysis of diffraction efficiency provides a non-destructive and experimentally simple approach for estimating phase modulation and evaluating the contributions of refractive-index change and surface relief. The proposed methodology can be useful for optimization and control of holographic recording processes and for the development of high-efficiency DOEs based on photosensitive chalcogenide glasses and azopolymer materials.

ACKNOWLEDGEMENTS. This research was supported by the Ministry of Education and Research of the Republic of Moldova (Subprogram 011201) and the National Agency for Research and Development through projects 25.80012.5007.39TC and 25.80013.8007.01ROMD.

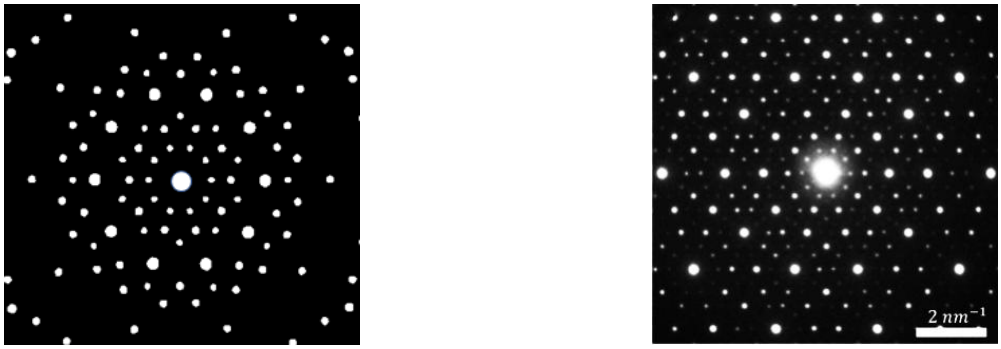
MULTI-BEAM LIGHT DIFFRACTION FROM CROSSED GRATINGS

S. Sergeev, A. Meshalkin, I. Cojocaru*
Institute of Applied Physics, Moldova State University, Chişinău, Republic of Moldova
*E-mail: ion.cojocaru@ifa.usm.md

Relief groups of N superimposed crossed gratings with equal grating periods of 2 μm were formed in As_2S_3 film by e-beam recording followed by chemical etching. The own raster scanning system of SEM BS 300 was used. The orientation of each recorded grating was determined by respective sample rotation angle, which was equal to 180°/N. Thus, the grating structures with rotational symmetry were created. Multi-beam light diffraction from crossed gratings was studied in the transmission mode at normal incidence of He-Ne laser beam (λ=0.633 μm). Observed diffraction patterns indicated the formation of a set of additional diffraction gratings along with recorded ones.

The diffraction pattern from two crossed line grating with grating periods of 2 μm was previously modelled. It was assumed that the set of nodes of line intersection forms the dot lines, that in turn form diffraction gratings with different orientations. Both grating periods and angles of orientation of these additional gratings were calculated, and the corresponding diffracting pattern was simulated as a result. A good agreement of calculated diffraction patterns with observed ones was obtained for different angles between lines of two crossed gratings.

On the basis of obtained results, the crossed gratings with N>2 were considered as a combination of grating pairs. According to this model a complex diffraction pattern with a lot of additional spots can be calculated. For example, in the case of N=5 (rotational symmetry) the angles between two gratings equal to 36° and 72° were used. The calculated diffraction pattern from N=5 crossed gratings is shown on Fig 1a. Here the white spots with larger size are related to first-order diffracted beams from recorded gratings.



a b

Figure 1. (a) Calculated diffraction pattern from N=5 crossed gratings; (b) electron diffraction pattern of icosahedral quasicrystal with five-fold rotational symmetry [1].

Note, that according to the used simple model the linear ordered sequences of nodes of intersection localized on different pairs of crossed gratings were not considered. Some additional gratings, probably, may be formed by such nodes. Nevertheless, in the cases of N=4 and N=5 a good agreement of calculated diffraction patterns with observed ones was obtained. Can also be noted the similarity between calculated diffraction pattern from N=5 crossed gratings and electron diffraction pattern of icosahedral quasicrystal with five-fold symmetry (Fig. 1b, [1]).

ACKNOWLEDGEMENTS. This research was funded by the Ministry of Education and Research of the Republic of Moldova (subprogram 011201).

[1] S. Nakamura, Y. Usui, K. Nakayama, A. Hirata and Y. Koyama. *Philosophical Magazine*, **106** (2026), 552-570.

POLYMER/CHALCOGENIDE SEMICONDUCTOR STRUCTURE FOR X-RAY AND HOLOGRAPHIC IMAGING

A. Chirita*, N. Nasedchina, S. Vatavu
Physics of Semiconductors and Devices Laboratory, Institute of Applied Physics, Moldova State University, Chisinau, Republic of Moldova
Faculty of Physics and Engineering, Moldova State University, Chisinau, Republic of Moldova
*E-mail: arc_chirita@yahoo.com

The development of multifunctional recording media capable of operating over a broad spectral range is of considerable interest for optical information processing, security technologies, and X-ray imaging. In this work, a polymer/semiconductor structure based on a polyepoxypropylcarbazole thermoplastic layer and a chalcogenide glassy semiconductor $(As_2S_3)_{0.6}(As_2Se_3)_{0.33}Sn_{0.07}$ thin film is investigated as a universal medium for recording both X-ray images and holographic diffraction gratings in the visible spectral region.

The recording structure consists of a transparent conductive substrate, a thin photoconductive CGS layer, and a thermoplastic polymer layer [1]. X-ray exposure generates a latent electrostatic charge distribution in the semiconductor layer due to radiation-induced photoconductivity [2]. After corona charging and thermal development, the charge pattern is transformed into a surface-relief image in the thermoplastic layer [3].

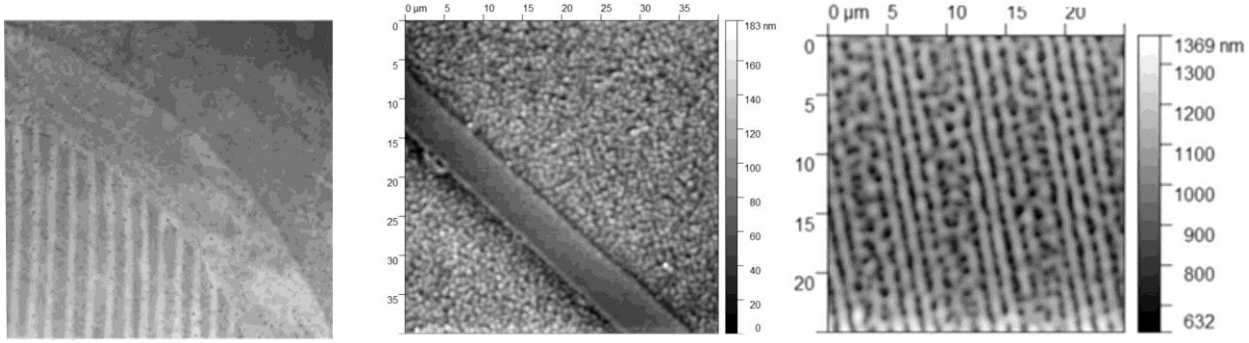


Figure 1. a) X-ray image of copper mesh target, b) AFM image of the tin wire with a diameter of 8 µm, c) AFM image of the thermoplastic layer surface

Experimental investigations demonstrate successful recording of X-ray images with high spatial resolution and efficient formation of relief-phase holographic gratings. Fig.3a shows the image of the copper grid with a period of 62 µm registered under X-ray irradiation. Fig.3b shows an AFM image of the tin wire with a diameter of 8 µm recorded under X-ray irradiation. The same structure is subsequently used for recording holographic gratings during simultaneous irradiation with blue (460 nm), green (532 nm), and red (647 nm) lasers. Atomic force microscopy (Fig.3c) confirms the formation of well-defined surface microrelief after holographic exposure. Such multifunctional structures may be employed for high-resolution X-ray detectors, hybrid optical recording systems, diffractive optical elements, and advanced security holograms incorporating invisible X-ray-recorded information [4-5]. The results demonstrate the potential of polymer/semiconductor structures as versatile recording media for integrated optical and X-ray imaging applications.

ACKNOWLEDGMENTS. The present study was performed within the state National Agency for Research and Development of the Republic of Moldova, under the Physics project no. 011207.

[1] A. Chirita, V. Prilepov. *Chalcogenide Letters* **19(6)** (2022) 439-545
[2] A.Chirita, D.Spoiala, S.Vatavu. *Chalcogenide Letters* **19(10)** (2022) 683-690
[3] A.Chirita, A. Hustuc, N. Nasedchina, S.Vatavu. *Chalcogenide Letters* **20(11)** (2023) 803-809
[4] A.Chirita et.al. *Laser Physics* **23** (2013**)** 036002-036006
[5] A.Chirita. *Journal of Modern Optics* **57** (2010) 854 – 858

TOPOLOGICAL AND PHOTOELECTRICAL PROPERTIES OF In- AND Al-DOPED ZnSnO THIN FILMS PREPARED BY SPRAY PYROLYSIS

V. Morari[1,*], V. Suman[1], E. Monaico[2], E. V. Rusu[1]
[1]*Institute of Electronic Engineering and Nanotechnologies „D. Ghitu", Technical University of Moldova, Academiei str. 3/3, Chisinau 2028, Republic of Moldova;*
[2]*National Center for Materials Study and Testing, Technical University of Moldova, Bv. Stefan cel Mare 168, Chisinau 2004, Republic of Moldova*
*E-mail: vadim.morari@iien.utm.md

Undoped and Al-, In- (1–3 vol.%) doped ZnSnO thin films were successfully deposited on Si substrates by the spray pyrolysis technique to investigate the effect of dopant type and concentration on their topological and photoelectrical properties. The surface morphology and topological characteristics were analyzed by atomic force microscopy (AFM), while the electrical transport behavior and photodetection performance were evaluated through current–voltage (I–V) measurements performed under dark conditions and under illumination from a 50 W halogen lamp. The photoresponse characteristics were assessed in terms of responsivity (R) and specific detectivity (D) as a function of the applied bias voltage. All investigated films exhibited nearly linear I–V characteristics, indicating the formation of low-resistance ohmic contacts and efficient charge transport within the ZnSnO matrix. AFM investigations revealed that dopant incorporation significantly influenced the surface morphology, grain distribution, and roughness of the films, resulting in a more compact and homogeneous microstructure. These morphological modifications contributed to enhanced carrier transport and more efficient collection of photogenerated charge carriers. Under illumination, all samples demonstrated a pronounced increase in photocurrent, confirming their high photosensitivity and potential for UV photodetection applications. The incorporation of Al and In dopants resulted in a remarkable enhancement of the photoelectrical performance compared with the undoped ZnSnO film. The highest responsivity value, reaching approximately 27 $A \cdot W^{-1}$ at an applied bias voltage of 8 V, was achieved for the ZnSnO (In 3%) sample, highlighting the beneficial role of In incorporation in promoting photogenerated carrier transport and collection. In comparison, the ZnSnO (Al 2%) film exhibited the highest specific detectivity, reaching approximately 1.0×10^{12} Jones, due to the favorable balance between enhanced photocurrent generation and reduced dark current. The undoped Zn2:1Sn film exhibited the lowest photoelectrical performance, with a responsivity of 8.9 $A \cdot W^{-1}$ and a specific detectivity of 5.6×10^{10} Jones, indicating the significant influence of controlled Al and In incorporation on improving the UV photodetection capability of ZnSnO thin films. These results demonstrate that while higher In concentrations are effective in maximizing responsivity, moderate Al incorporation provides improved detectivity by suppressing leakage current and reducing noise contributions. The enhanced photoresponse is attributed to the combined effects of improved charge transport, reduced carrier recombination, and controlled modification of surface morphology induced by dopant incorporation. Overall, these results confirm that controlled Al and In doping represents an effective strategy for tailoring the optoelectronic properties of ZnSnO thin films, making them promising candidates for the development of high-performance ultraviolet photodetectors. The observed improvements are consistent with recent reports on Al-Zn_2SnO_4 thin films, where dopant-induced changes in morphology, defect states, and carrier transport mechanisms were shown to strongly influence ultraviolet photodetection performance [1].

ACKNOWLEDGEMENTS. This work was supported by the National Agency for Research and Development (NARD) of the Republic of Moldova under Young Researchers 2025-2026 Project No. #25.80012.5007.31TC, and Institutional Subprogram Project #02.02.01 no. 4/FI „Nanostructures and advanced materials for applications in spintronics, thermoelectricity and optoelectronics".

[1] S. Ghosh, S. Mondal, S. Pal, D. Basak. High performance broad-band ultraviolet-B to visible photodetection based on planar Al-Zn_2SnO_4-Al structure. *Sensors and Actuators A: Physical* **347** (2022) 113898. Doi: https://doi.org/10.1016/j.sna.2022.113898.

DFB LASER-BASED PROTOTYPE METHANE SENSOR

D. P. Dvornikov[1,*], A.V. Siminel[2]
[1]*Ghitu Institute of Electronic Engineering and Nanotechnologies, Technical University of Moldova, Chisinau, Republic of of Moldova;*
[2]*Institute of Applied Physics, Moldova State University, Chisinau, Republic of Moldova.*
*E-mail: dmitri.dvornikov@iien.utm.md

Rapid accumulation of greenhouse gases due to human activities creates an excess heat trapping within the lower atmosphere which leads to negative climate impacts. Methane is the second-largest greenhouse gas after carbon dioxide and is the main component of natural gas, leaks of which lead to economic losses and increase the methane content in the atmosphere. In addition, methane is highly explosive. Developing sensors to detect methane in the air is a pressing challenge.

The development of a prototype optical sensor based on tunable diode laser absorption spectroscopy (TDLAS) using a distributed feedback (DFB) laser is reported for detecting elevated concentrations of greenhouse gas methane caused by leaks in localized areas, such as pipelines and other industrial facilities. The 1653.7 nm absorption line in 1.65 μm overtone band (1630-1690 nm) was selected as the target spectral line for methane detection. Although absorption at selected wavelength is significantly lower than at the 3270 nm mid-infrared fundamental band, this choice allows the use of available semiconductor DFB lasers, high sensitive photodetectors operating at room temperature and quartz fiber optics when long-distance measurements are required. A significant shift of absorption spectra in frequency from the 1654 nm region prevents interference from carbon dioxide, other atmospheric gases, water vapor and light hydrocarbons from the methane family (ethane, propane, butane).

Emission of single-mode 1653.7 nm DFB laser diode with ultra-narrow linewidth of 2 MHz ($\approx 1.8 \bullet 10^{-5}$ nm) and temperature tuning coefficient of 0.1 nm/°C precisely matches the selected methane absorption line. Laser driver with 0.05 mA current resolution and temperature controller to stabilize DFB laser temperature with 0.01°C resolution and 0.004°C stability over 1 hour enable high-precision measurements with a 1653.7 nm wavelength and 2 MHz linewidth DFB diode laser. To simulate air-methane mixture, a gas cell with optical length of 320 mm and internal volume of 100 cm^3 was used, which allowed for precise control of volumetric concentration of injected methane and dosing up to maximum 5% by volume, which is the lower limit of the explosive range of methane concentrations in air. Small amounts of methane were obtained by the Dumas reaction After 5 μm filter, methane filled a small buffer volume, from where it was taken in controlled portions for injection into the gas cell.

Since detection of small amounts of methane is of particular interest, the measurements were carried out in a range of concentrations from the minimum achieved in the experiment to those not exceeding the lower explosion limit, i.e. 0.1-5% by volume. At direct absorption spectroscopy, the photodetector signal depends exponentially on the methane concentration. For small amounts of gas in the optical path and in the range of small changes in its concentration, the value of which is part of the exponent, the concentration-photodetector signal dependence is approximately linear, which is consistent with the measurement results. Injection of the initial methane content into the gas cell was reliably detected, which is the result of resonant absorption of laser radiation due to exact coincidence of the spectral position and spectral width of the laser line and the absorption line of methane.

ACKNOWLEDGEMENTS. This work was supported by the BRIDGE-BS project, funded by the European Union's Horizon 2020 research and innovation programme under grant agreement No. 101000240. The views expressed do not necessarily reflect those of the European Commission.

INVESTIGATION OF CLOSE-SPACED SUBLIMATION DEPOSITION OF SOLAR CELL ABSORBER LAYERS USING $AgSbS_2$ AS SOURCE MATERIAL

D. Untila[1,2,*], D. Rusnac[2], G. Colibaba[2], C. Radu[3], A. E. Bocirnea[3], C. Besleaga[3], A. C. Galca[3], M. Koltsov[1], A. Katerski[1], I. O. Acik[1], N. Spalatu[1,2]
[1]*Tallinn University of Technology, Tallinn, Estonia;*
[2]*Moldova State University, Chisinau, Republic of Moldova;*
[3]*National Institute of Materials Physics, Magurele (Ilfov), Romania*
*E-mail: dumitru.untila@yahoo.com

$AgSbS_2$ is considered a promising absorber material for thin-film photovoltaic devices owing to its favorable optoelectronic characteristics, including a high optical absorption coefficient and a direct band gap suitable for efficient solar energy conversion. As a ternary chalcogenide semiconductor composed of abundant and relatively non-toxic elements, $AgSbS_2$ represents an attractive alternative to conventional absorber materials and is compatible with cost-effective thin-film fabrication techniques [1-3].

In this study, the feasibility of depositing the absorber layers by the close-spaced sublimation (CSS) technique was investigated using $AgSbS_2$ as the evaporation source. $AgSbS_2$ ingots were obtained by the Bridgman-Stockbarger method from high-purity elemental constituents combined in stoichiometric ratios. X-ray diffraction (XRD) and energy-dispersive X-ray spectroscopy (EDX) analyses confirmed the formation of $AgSbS_2$ compound, with good structural quality and the expected chemical composition.

Thin films were deposited under different processing conditions, with source temperatures ranging from 350 to 500°C and substrate temperatures between 250 and 400°C. CdS buffer layers were prepared on FTO-coated glass substrates by chemical bath deposition (CBD) prior to absorber deposition. Prototype solar cells fabricated using these layers achieved a power conversion efficiency of 0.83%, demonstrating the feasibility of employing $AgSbS_2$ as a source material for absorber layer deposition by the CSS method and providing a basis for further optimization of the deposition process and device architecture.

[1] Y. Gu, W. Liang, H. Wang, T. Chen. *Small* **21/34** (2025) 2504888.
[2] E. Dutková, M. Baláž, J. Kováč, M. J. Sayagués, M. Wohlgemuth, Z. Lukáčová Bujňáková, L. Findoráková, J. Kováč Jr, S. Kováčová, M. Marton, P. Jacko. *Journal of Materials Science* **60/33** (2025) 14605–14620.
[3] U. Chalapathi, A.S. Reddy, P.R. Prasad, G. Manjula, S. Sangaraju, R. Cheruku, B.A. Al-Asbahi, S. Alhammadi, C.P. Reddy, K. Mohanarangam, B.P. Reddy. *Materials Science in Semiconductor Processing* **168** (2023) 107821.

HETEROGUNCTION DEVICES FABRICATED USING n-TYPE ZnO SPUTTERING COMBINED WITH p-TYPE Cu_2O RF SPUTTERING

V. Suman[1], L. Ghimpu[1], V. Morari[1], I. Lungu[2], V. Ursu[3], V. Zalamai[3], E. Monaico[3], E. Rusu[1], Ed. Monaico[3]

[1]*D. Ghitu Institute of Electronic Engineering and Nanotechnologies, Technical University of Moldova,*
Academiei Str. 3/3, MD-2028, Chișinău, Republic of Moldova;
[2] *Laboratory of Organic/Inorganic Materials for Optoelectronics, Moldova State University, A. Mateevici str. 60, MD-2009, Chișinău, Republic of Moldova;*
[3]*National Center for Materials Study and Testing, Technical University of Moldova, Chișinău, Republic of Moldova*
*E-mail: victor.suman@iien.utm.md

This paper reports on the properties of heterostructures consisting of transparent n-type ZnO layers deposited by magnetron sputtering on glass substrates coated with a transparent, conductive ITO film, combined with p-type Cu_2O layers deposited by RF magnetron sputtering. The constituent layers exhibit high crystalline quality, and a local epitaxial relationship between Cu_2O and ZnO was achieved with [110] Cu_2O and [001] ZnO. The Cu_2O films exhibited low resistance and high mobility values of 130–470 ohms and 19 $cm^2/(V \cdot s)$, respectively. The Cu_2O/ZnO heterostructures exhibit nonlinear rectification behavior characteristic of a p-n junction, a self-powered photoresponse under sunlight, and an average transmittance of 72% in the visible region of the electromagnetic spectrum. Following a comprehensive investigation of the properties of the individual layers, the junctions fabricated on glass substrates coated with a transparent ITO layer showed a considerable improvement, with an open-circuit voltage of 720 mV for Cu_2O. This demonstrates in practice the favorable band alignment between ZnO and Cu_2O with a small conduction band gap. Furthermore, it is shown that the interface between ZnO and ITO does not hinder charge carrier transport, opening up new possibilities for the design of solar cell architectures and optoelectronic devices.

ACKNOWLEDGEMENTS. This paper was supported financially by the Ministry of Education and Research of the Republic of Moldova, MSU, Research Subprogram: „Nanostructures and Advanced Materials for Applications in Spintronics, Thermoelectricity, and Optoelectronics" Code: #020201

[1] L. Fara, I. Chilibon, I.C. Vasiliu, D. Craciunescu, A. Diaconu and S. Fara. On Numerical Modelling and an Experimental Approach to Heterojunction Tandem Solar Cells Based on Si and Cu2O/ZnO - Results and Perspectives. *Coatings*, **14(3)** (2024) 244. Doi: https://doi.org/10.3390/coatings14030244

[2] P. Narin, E. Kutlu-Narin, S. Ardali, B. Sarikavak-Lisesivdin, E. Tiras and S.B. Lisesivdin.Temperature controlled phase transition and characterization of Cu_2O and CuO tgin films grown at different growth temperatures via mist CVD. *J.Applied Physics A*, **132** (2006) art. nr. 377. Doi: https://doi.org/10.1007/s00339-026-09555-6

[3] Th. Dimopoulos, R. A. Wibowo, S. Edinger, M. Wolf and Th. Fix. Heterojunction Devices Fabricated from Sprayed n-Type Ga_2O_3, Combined with Sputtered *p*-Type NiO and Cu_2O. *Nanomaterials*, **14(3)** (2024) 300. Doi: https://doi.org/10.3390/nano14030300

[4] C. de Melo, M. Jullien, Y. Battie, A. En Naciri, J. Ghanbaja, F. Montaigne, J.-F. Pierson, F. Rigoni, N. Almqvist, A. Vomiero, S. Migot, F. Mücklich, D. Horwat. Semi-Transparent p-Cu_2O/n-ZnO Nanoscale-Film Heterojunctions for Photodetection and Photovoltaic Applications. *ACS App. Nano Mater.*, **2(7)** (2019) 4358-4366. Doi: https//doi.org/10.1021/acsanm.9b00808

ASSESSMENT OF RADIOFREQUENCY LEVELS FOR PUBLIC ELECTROMAGNETIC FIELD EXPOSURE CHARACTERIZATION IN URBAN 2G–5G AND WI-FI NETWORKS: A CASE STUDY

A. Prisacaru[1,2*], C. M. Popescu[3], V. Mirovski[2]
[1]*State University of Moldova, Chisinau, Moldova;*
[2]*Technical University of Moldova, Chisinau, Moldova;*
[3]*National Institute for Research and Development in Electrical Engineering ICPE-CA, Bucharest, Romania.*
*E-mail: andrian.prisacaru@ifa.usm.md

The rapid deployment of next-generation wireless communication systems requires continuous assessment of radio-frequency (RF) electromagnetic environments to support public electromagnetic field (EMF) exposure characterization. This work presents an experimental measurement campaign conducted in Chisinau, Republic of Moldova, aiming to investigate RF signal levels across commercial 2G, 3G, 4G, 5G and Wi-Fi networks in representative urban environments, including crowded public areas, university buildings and high-rise administrative facilities.

Measurements were performed using calibrated mobile network diagnostic equipment by recording Reference Signal Received Power (RSRP), Received Signal Strength Indicator (RSSI), operating frequency, serving cell identification and geographical coordinates. The investigated frequency range extends from 758 MHz to 3800 MHz and includes the major national mobile network operators. The adopted measurement methodology follows recent experimental approaches for multi-band RF characterization and EMF exposure assessment reported in the literature [1,2].

The experimental results reveal significant differences between outdoor and indoor propagation conditions. Outdoor measurements exhibited the highest received signal levels, with RSRP values ranging from −51 dBm to −61 dBm in frequency ranges lower than 1 GHz, whereas indoor LTE measurements reached values as low as −109 dBm because of building penetration losses. Commercial 5G NR deployments operating at 3671 MHz presented RSRP values between −83 dBm in outdoor locations and approximately −97 dBm inside elevated office buildings. Indoor Wi-Fi access points operating at 5 GHz produced RSSI values up to −38 dBm owing to the short communication distance. Figure 1 summarizes the representative RF signal levels measured in indoor and outdoor environments for the investigated wireless technologies.

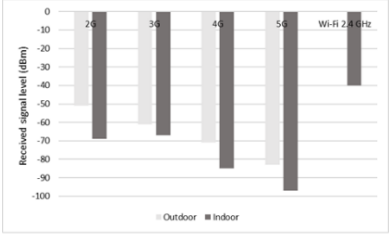


Figure 1. Comparison of representative RSRP/RSSI values measured in indoor and outdoor environments across commercial 2G, 3G, 4G, 5G and Wi-Fi networks.

The obtained results provide a systematic experimental dataset supporting the characterization of public EMF exposure across multi-generation wireless communication networks in the Republic of Moldova. Under the investigated conditions, the measured RF signal levels associated with commercial 5G deployments are comparable to those of existing cellular technologies, supporting the evidence-based assessment of public EMF exposure and the implementation of 5G networks within the national digitalization framework.

ACKNOWLEDGMENTS. This work was supported by the Ministry of Education and Research of Romania, UEFISCDI, within the PNCDI IV Program, Project PN-IV-PCB-RO-MD-2024-0294, Contract 48PCBROMD/2025, and by the National Agency for Research and Development (ANCD) of the Republic of Moldova, Project 25.80013.5007.62ROMD.

[1] G. Aerts et al., *5G RF EMF Spectral Exposure Assessment in Four European Countries*, Bioelectromagnetics, 2025.
[2] L. Chiaraviglio et al., Dominance of Smartphone Exposure in 5G Mobile Networks, *IEEE Transactions on Mobile Computing*, vol. 23, no. 3, pp. 2284–2299, 2024.

JONES MATRIX CHARACTERIZATION OF POLARIZATION GRATINGS RECORDED IN AS_2S_3–SE NANOMULTILAYERS

Vladislav Botnari[1,*], Veronica Cazac[1], Vladimir Abashkin[1], Elena Achimova[1], Constantin Losmanschii[1], Diana Muntean[1] .
[1]*Moldova State University, Institute of Applied Physics, Chisinau, Moldova*
*E-mail: vladislav.botnari@ifa.usm.md

This work presents a polarimetric investigation of polarization diffraction gratings based on Jones matrix reconstruction. The gratings were fabricated on As_2S_3–Se nanomultilayer structures using a single-beam direct polarization recording technique with continuous-wave laser irradiation. Spatial modulation of the polarization state was achieved by combining a half-wave plate with a liquid crystal polymer depolarizer (LCPD). Appropriate adjustment of the depolarizer orientation and position generated a periodic polarization distribution, enabling the fabrication of diffraction gratings with a spatial period of approximately 15 μm. The recording beam was expanded, spatially filtered, and shaped using an iris diaphragm and a 4-f optical system.

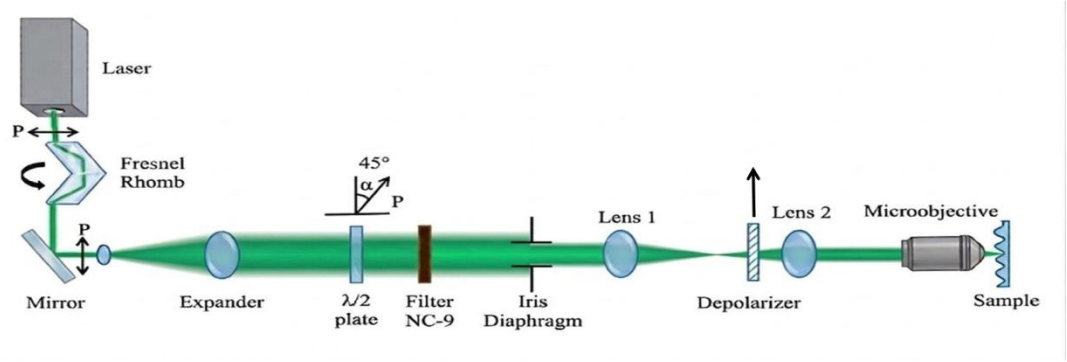


Figure 1. One-beam direct polarization grating Recording CW DPSS laser (λ = 532 nm, P = 100 mW, power density on the sample ≈ 6.4 mW/mm²), Expander, Grating -recorded on NML; λ/2- half wave plate

The recorded gratings were characterized by reconstructing the Jones matrices from polarization-sensitive digital holograms. The obtained polarization maps reveal a periodic phase retardation between orthogonal polarization components, confirming the formation of pronounced birefringence induced during the recording process in the nanomultilayer structure.

ACKNOWLEDGMENTS. The National Agency for Research and Development of Moldova (NARD) project under project number 25.80012.5007.39TC

STUDY OF ELECTROHYDRODYNAMIC INSTABILITIES IN AN ELECTRICALLY CHARGED DIELECTRIC LIQUID UNDER MICROGRAVITY FOR ELECTROMAGNETIC RADIATION DETECTION AND CONVERSION

B. Constantinov*
Moldova State University, Institute of Applied Physics, Research Laboratory Environmental Physics and Modeling Complex Systems (ePhysMCS Lab), Chişinău, Republic of Moldova
*E-mail: constantinov_66@mail.ru; boris.constantinov@usm.md

This work presents a physical-mathematical and numerical model of electrohydrodynamic (EHD) instabilities and dissipative-structure evolution in an electrically charged rheological dielectric layer. The model is based on previous laboratory experiments with a dielectric liquid–metallized support (DILI-SM) system and is extended to microgravity conditions. The objective is to investigate whether a system maintained in a subcritical state close to the EHD instability threshold can be used for electromagnetic-radiation detection and conversion. In the proposed mechanism, incident radiation produces only a local perturbation of the electrical and/or interfacial state, whereas the energy required for amplification is supplied by the external electrostatic field.

The physical system consists of a rheological dielectric layer of initial thickness h deposited on a rigid metallized support at $z=0$. The undeformed free surface is located at $z=h$, while during EHD evolution it is described by $z=h+\zeta(x,y,t)$. The model is based on the incompressible Navier–Stokes equations coupled with the Maxwell stress tensor and appropriate mechanical and electrostatic boundary conditions. The externally imposed normal electric field is assumed approximately homogeneous, $E_{n,ext}=E_0\simeq const.$, whereas the surface potential may vary spatially, $V_s=V_s(x,y,t)$. Its gradients generate a tangential field, $E_{\parallel}=-\nabla_s V_s$, which can redistribute mobile positive surface charge and locally modify the Maxwell stresses, favouring nucleation of an unstable EHD mode.

For a Fourier perturbation with wavenumber $k=2\pi/\lambda$, where λ is the wavelength of the dissipative structure, the mode amplitude obeys:

$$\frac{d\zeta_k}{dt}=\omega(k,t)\zeta_k. \tag{1}$$

In the adopted reduced approximation, the instability growth rate is

$$\omega(k,t)=\frac{h^3}{3\eta(t)}\left[\left(\frac{3\sigma_s^2(t)}{2\varepsilon_0 h}-\rho g_{\text{eff}}\right)k^2-\gamma k^4\right]. \tag{2}$$

Here, $\boldsymbol{\sigma}_s(t)$ is the surface charge density, $\boldsymbol{\eta}(t)$ the apparent viscosity, $\boldsymbol{\rho}$ the layer density, $\boldsymbol{g}_{\text{eff}}$ the effective gravitational acceleration, $\boldsymbol{\gamma}$ the surface tension, and $\boldsymbol{\varepsilon}_0$ the vacuum permittivity. The electric contribution is destabilizing, gravity is restoring, and the $\boldsymbol{k}_4$ term represents capillary stabilization at short wavelengths. The sign of Re$\boldsymbol{\omega}$ determines damping, the instability threshold, or growth of the perturbation.

Under microgravity (MG) conditions, $\boldsymbol{g}_{\text{eff}}\to 0$, the gravitational restoring contribution in eq. (2) tends to zero, and the dispersion relation becomes

$$\omega_{\text{MG}}(k,t)=\frac{\sigma_s^2(t)h^2}{2\varepsilon_0\eta(t)}k^2-\frac{\gamma h^3}{3\eta(t)}k^4. \tag{3}$$

The instability spectrum is then governed predominantly by electrostatic destabilization, capillary stabilization, and the rheological response of the layer. Operation near Re$\boldsymbol{\omega}\simeq 0^-$ may therefore allow a weak radiation-induced local perturbation to shift a mode into the unstable region, Re$\boldsymbol{\omega}>0$, converting the initial event into a detectable electrical and/or relief response.

The results support further numerical and experimental investigation of near-threshold DILI-SM states as nonlinear media for radiation conversion and amplification.

TECHNOLOGICAL AND MORPHOLOGICAL ASPECTS OF GaSe THIN FILMS PREPARED ON SAPPHIRE SUBSTRATES

D. Spoială[1,*], E. Vatavu[1], Ig. Narolschi[1], V. Nicorici[1], M. Rusu[1,2], S. Vatavu[1]
[1]*Physics of Semiconductors and Devices Laboratory, Faculty of Physics and Engineering, Moldova State University, Chișinău, Moldova;*
[2]*Structure and Dynamics of Energy Materials, Helmholtz-Zentrum Berlin für Materialien und Energie GmbH, Berlin, Germany*
*E-mail: dorin.spoiala@usm.md

Gallium selenide (GaSe) is a prominent representative of layered AIII-BVI semiconductors, renowned for its unique structural, optical, and electrical properties. Due to these characteristics, GaSe crystals are widely used in quantum electronics and for manufacturing optical radiation detectors in the visible and near-infrared spectral regions, for the creation of highly efficient photovoltaic cells, gas sensors, and thermoelectric converters. This work reports on the preparation of GaSe films with a vertically stacked, wall-like structure and investigates their physical properties. GaSe films were prepared by CSS on sapphire (0001) substrates. During synthesis, the evaporator temperature was maintained at 700°C, and the substrate temperature was varied between 450 and 600°C. The GaSe layers were investigated by X-ray fluorescence (XRF), X-ray diffraction (XRD), Raman spectroscopy (632.8 nm), and atomic force microscopy in non-contact mode (AFM).

The elemental composition of the films was studied by means of XRF. The atomic ratio percentages of the elements present in the evaporation source material were found to be 50.87 % Ga and 49.13 % Se, with a Ga/Se ratio of 1.035. For GaSe films synthesized at substrate temperatures of 450°C, 500°C, 550°C and 600°C, the Ga/Se ratio is 0.950, 0.893, 0.966, and 0.938, respectively. The high-frequency (90÷350 cm^{-1}) Raman spectra of GaSe single crystals contain lines at 132.70, 208.16, 211.64, 251.47, and 306 cm^{-1}. These frequencies are very close to the known data for the ε-GaSe polytype (D_{3h}^1 space group) and identified as $A_1'(2)$, $E''(4)$, $E'(4)$(TO), $E'(4)$(LO) and $A_1'(4)$ modes respectively. Unlike the spectra of the GaSe single crystal, the spectra of the as-prepared films contain a broad band in the 220-280 cm^{-1} region with a pronounced doublet. The positions of the maxima of these lines at ~243 and ~251 cm^{-1} remain virtually unchanged with increasing substrate temperature. At the same time, the intensities of both peaks increase, reaching a maximum at t_{substr}=600°C. The positions of the remaining lines exhibit a slight low-frequency shift of ~1 cm^{-1} compared to similar lines in the spectrum of the ε-GaSe single crystal. It should be noted that the spectra of the studied single crystals and obtained films do not contain lines characteristic for Ga_2Se_3 or other GaSe polytypes, indicating the predominant content of the ε-GaSe polytype in them.

By using AFM methods, the main amplitude, spatial, and correlation parameters characterizing the surfaces of the synthesized films, as well as their dependence on the substrate temperature, were determined. It was established that the root-mean-squared roughness, average roughness, ten-point average roughness, skewness, and developed area ratio decrease with increasing substrate temperature, passing through a minimum at t_{substr}=550°C. The attempts to describe the surface morphology of the obtained films within the framework of the self-affine scaling model encounter difficulties. Fractal dimensions of the GaSe films surfaces determined by the box counting, triangulation, variance and height-height correlation function (HHCF) methods fluctuates within the range D_f=2.141÷2.348, showing a slight increase with substrate temperature increasing. Fractal dimensions determined from high-frequency regions of the power spectral density function (PSDF) take higher values of 2.422÷2.981. However, the presence of maxima on the HHCF and PSDF indicates that to describe the surface properties of the studied films it is more likely should be used a mounded surface model, rather than a self-affine one.

ACKNOWLEDGEMENTS. Ministry of Education and Research of the Republic of Moldova, subprogram 011207

EXTERNAL FACTORS' INFLUENCE ON THE PARAMETERS OF InP PHOTOVOLTAIC CELLS

E. Bercu[1], L. Gorceac[1,*], A. Scafaru[1], P.I. Chetruș[1], I. Maistruc[1], S. Vatavu[1]
[1]*Physics of Semiconductors and Devices Lab, Faculty of Physics and Engineering, Moldova State University, Chișinău, Moldova;*
*E-mail: leonid.gorceac@usm.md

InP based solar cells are being investigated as promising candidate for solar energy conversion devices implying low production costs [1]. This work is focused on the influence of external factors (temperature, corpuscular radiation (electron and proton fluxes), degradation over time) on the photovoltaic parameters of solar cells (SC) based on nCdS-pInP heterojunctions with an intermediate epitaxial layer p^oInP ($p = 5 \cdot 10^{16}$ cm^{-3}, $\mu_p = 90 \div 100$ cm$^2 \cdot$V$\cdot$s^{-1}, $\rho = 0.3 \div 1.0\ \Omega \cdot$cm).

The influence of temperature in the range of 180÷365 K on the current-voltage dependencies of the n^+CdS-p°-p^+InP SC with a photoactive surface of 2.2 cm^2 under AM0 conditions demonstrated that the open circuit voltage (U_{oc}) linearly decreases with decreasing temperature, the coefficient characterizing this change (K_T^{Uoc}) varying in the range of -0.25÷-0.22 %/degree. The decrease in U_{oc} with temperature is the result of the decrease in ΔE_g of InP and the increase in the reverse saturation current I_o with increasing temperature from $2 \cdot 10^{-12}$ (180 K) to $1.5 \cdot 10^{-5}$ A$\cdot$cm^{-2} (365 K). The short-circuit current (I_{sc}) increases from 42.3 mA$\cdot$cm^{-2} (180 K) to 50.3 mA$\cdot$cm^{-2} (365 K) which is determined by the increase in the diffusion length of the charge carriers with increasing temperature and the shift of the absorption edge towards lower temperatures due to the decrease in ΔE_g. The temperature coefficient of the short-circuit current K_T^{Isc} varies in the interval of 0.008÷0.07 %/grad. The coefficient characterizing the temeprature change in maximum power generated K_T^W for the investigated SCs does not change significantly, increasing from -0.28 to -0.25 %/degree.

The influence of the electron flux having an energy of 1 MeV and a density of $5 \cdot 10^{15}$ cm^{-2} and the integral proton flux with E=20.6 MeV and density 10^{12} cm^{-2} on the main photoelectric parameters of the n^+CdS-p°-p^+InP SC under AM0 illumination conditions was investigated. It was found that U_{oc} decreases from 0.776 V to 0.727 V in the case of electron irradiation and from 0.790 V to 0.776 V in the case of proton irradiation. This decrease in U_{oc} by about 5-6% is caused by the increase in the recombination of charge carriers at the heterojunction interface as a result of the increase in the density of radiative defects. I_{sc} also decreases by about 7-8% as a result of the influence of the proton flux with a density of 10^{12} cm^{-2} and the electron flux with about $5 \cdot 10^{15}$ cm^{-2}. This decrease may be caused by the decrease in the diffusion length of minority charge carriers from 3.24 μm to 1.5 μm in the case of irradiation of the SC with protons and up to 2.3 μm as a result of electron irradiation.

The degradation over time of the photovoltaic parameters of the n^+CdS-p°-p^+InP SC, having an antireflectant SiO_2 layer prepared by the electron beam evaporation at 300 K were studied at 100 W$\cdot$cm^{-2}. Testing of the same SC was carried out in September 2009, October 2018 and April 2026. It was found that in 16 years the efficiency of the n^+CdS-p°-p^+InP SC decreases on average by 0.38% annually, which confirms the relative stability of this parameter over time. This decrease is primarily related to the decrease of the fill factor in 16 years from 73% to 67.6%, which constitutes approximately 0.49% annually.

The parameters of the SC under investigation have been numerically investigated by SCAPS-1D [2]. The results of the numerical analysis give 2-3% higher values for U_{oc} and about 5% higher for I_{sc}.

ACKNOWLEDGEMENTS. Ministry of Education and Research of the Republic of Moldova, subprogram 011207 DETCONV.

[1] M. Zheng et al. *Prog. Photovolt: Res. Appl.* **24** (2016) 871–878.
[2] M. Burgelman et al. *Thin Solid Films* **361** (2000) 527-532.

SYNTHESIS AND CRYSTAL STRUCTURE OF A NOVEL Cu(II) COORDINATION POLYMER BASED ON N-(2-(MORPHOLIN-4-YL)ETHYL)THIOSEMICARBAZONE OF 3-ETHOXYSALICYLALDEHYDE

A. Ciursin[1,*], R. Rusnac[1], S. Shova[2], A. Gulea[1]
[1]*Laboratory of Advanced Materials in Biopharmaceutics and Technics, Institute of Chemistry, Moldova State University, 60 Mateevici Street, MD-2009 Chisinau, Republic of Moldova;*
[2]*"Petru Poni" Institute of Macromolecular Chemistry, Romanian Academy, 700487, Iasi, Romania*
*E-mail: ciursin.andrei@usm.md

Thiosemicarbazones represent an important class of organic compounds exhibiting a broad spectrum of biological activities. In addition, they serve as highly effective ligands for the synthesis of coordination compounds with 3*d* transition metals. Numerous studies have demonstrated that the complexation of thiosemicarbazones with 3*d* metal ions can significantly enhance their biological properties, thereby increasing their potential for pharmaceutical and biomedical applications.

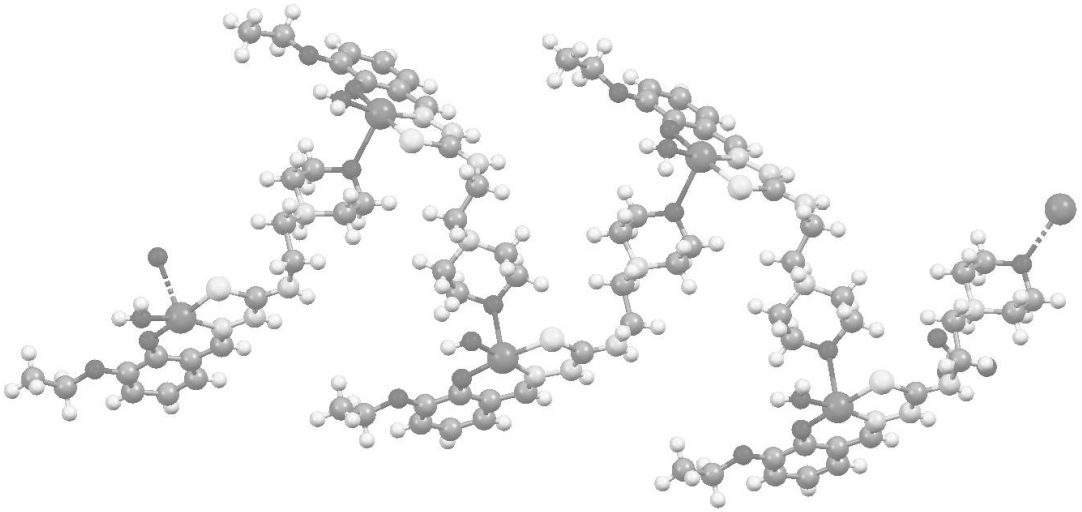


Figure. 2D layer seen along the c axis $[Cu(H_2O)(Et\text{-}Mof\text{-}Ligand)]_n$-

In this work, the synthesis and characterization of a new Cu(II) coordination polymer based on N-(2-(morpholin-4-yl)ethyl)thiosemicarbazone of 3-ethoxysalicylaldehyde (*Et-Mof-Ligand)* are described. The ligand was obtained through the condensation reaction of N-(2-(morpholin-4-yl)ethyl)thiosemicarbazide with 3-ethoxysalicylaldehyde. The reaction was carried out under reflux conditions in ethanol for 3 hours.

For the coordination compound preparation, solutions of copper(II) nitrate and the ligand were prepared in propan-1-ol. The solutions were preheated before being mixed, and the synthesis was performed for 40 minutes at the boiling temperature of the solvent. After cooling and filtration, single crystals were obtained from the filtrate after standing overnight. The obtained crystals were subsequently analysed by single-crystal X-ray diffraction, leading to the determination of the molecular structure of the coordination polymer (illustrated on the figure).

In conclusion, a new Cu(II) coordination polymer based on N-(2-(morpholin-4-yl)ethyl)thiosemicarbazone of 3-ethoxysalicylaldehyde was successfully synthesized and structurally characterized by single-crystal X-ray diffraction. The obtained results confirm the formation of a coordination framework, highlighting the potential of thiosemicarbazone ligands for the development of novel metal-based compounds.

2-SUBSTITUTED 1H-PERIMIDINES AS A BUILDING BLOCKS FOR ELECTROACTIVE FUNCTIONAL MATERIALS

B.Gajewska[1,*], R. Malik[2], R. Motyka[2], A. Blacha-Grzechnik[1,3], M. Łapkowski[1,2,3], M. Czichy[1,3]
[1]*Silesian University of Technology, Faculty of Chemistry, Department of Physical Chemistry and Technology of Polymers, Gliwice, Poland;* [2]*Polish Academy of Sciences, Center of Polymer and Carbon Materials, Zabrze, Poland;* [3]*Silesian University of Technology, Center for Organic and Nanohybrid Electronics, Gliwice, Poland;*
*E-mail: Beata.Gajewska@polsl.pl

The current scope of applicability of electrochemical techniques in the field of materials chemistry is not limited only to fundamental studies on the activity of components in redox reactions. As interdisciplinary tools, they also support the development of specialized, electroactive organic materials. By precisely controlling the potential, it is possible to achieve kinetic, thermodynamic and spatial control of electrosynthesis, which in turn promotes the achievement of the desired structure of the target material and the tuning of their physicochemical properties[1].

2-Substituted 1H-perimidine derivatives are used in the areas of medicinal, dye, catalytic and biotechnological chemistry in the form of ligands of complex compounds or separate entities[2]. Previous studies have shown that under electrochemical oxidation conditions, the perimidine system can also be a building block for the formation of π-conjugated polymers with multiredox characteristics[3]. To address the still insufficiently recognized electrochemical activity of perimidine derivatives, current research is aimed at identifying the steps of the mechanism and way of combining precursor units, optimizing the electrosynthesis process, as well as characterizing the obtained products with evaluation of their applicability as functional materials. As a consequence, significant efforts are being made to develop efficient synthesis routes for new, advanced conductive materials that can be used as sensor-related systems or electrode modifying layers, including anti-corrosion coatings, as well as catalytic systems or capacitors.

The structure of products obtained by electrochemical oxidation of 2-substituted 1H-perimidines may consist of protonated fragments stabilized by hydrogen bonds and prototropic tautomerization, as well as π-conjugated fragments connected by a single bond or two bonds (ladder structure) (*Fig 1*). The final form and structural homogeneity of the material, as well as the efficiency and selectivity of the addition/coupling process, depend on the choice of precursor (type of substituent attached, presence of aromaticity), the parameters used (e.g., the potential range that allows or does not allow coupling through the substituent), and the conditions present in the system, such as the atmosphere (aerobic or anaerobic) or the polarity of the solvent. Perimidine materials are also characterized by a stable, reversible redox system located at low potential values. The obtained products exhibit specific interactions that may enable the coordination or binding of various analytes, including heavy metal ions, as well as interactions between perimidine units and electrode surfaces.

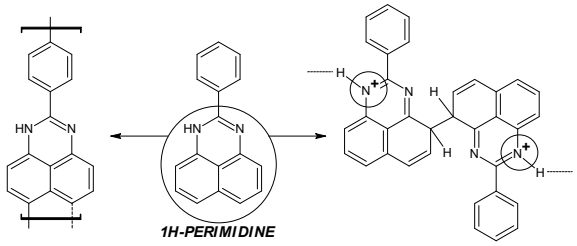


Figure 1. Diagram of representative product structures obtained during the electrochemical oxidation of 2-substituted 1H-perimidine derivatives.

[1] B. Gajewska, M. Czichy. *Monograph of the Silesian University of Technology* **2** (2025) 193-213.
[2] A. F. Pozharskii *et al. Russian Chemical Reviews* **89** (2020) 1204-1260.
[3] P. Janasik et al *Scientific Reports* **14** (2024) 1-17.

INVESTIGATION OF ACRIDAN DERIVATIVES ELECTROCHEMISTRY BEHAVIOUR WITH IN-SITU AND EX-SITU METHODS

Natallia Kareva[1,*], Malgorzata Czichy[1,2]
[1]*Faculty of Chemistry, Silesian University of Technology, Gliwice, Poland;*
[2]*Centre for Organic and Nanohybrid Electronics, Silesian University of Technology, Gliwice, Poland;*
*E-mail: natallia.kareva@polsl.pl

There is certainly growing interest in energy-efficient devices. The rapid development of modern technologies leads to growing need on device performance and functionality. As a result, new materials are required to provide improved conversion characteristics, enhanced stability, reduced energy consumption, and compatibility with miniaturized and multifunctional systems.

Acridan derivatives (A) are three-ring heterocyclic compounds that were mostly studied as dyes, light-emitting materials or drugs [1-3]. We assume that it's possible to use these compounds as precursors for energy storage applications layers thank to its ability of forming structures like A-L or A-L-A (Fig. 1). N-functionalization and substitution in 9-position can give a possibility to adjust structure towards tuning it's morphology and electrochemical activity.

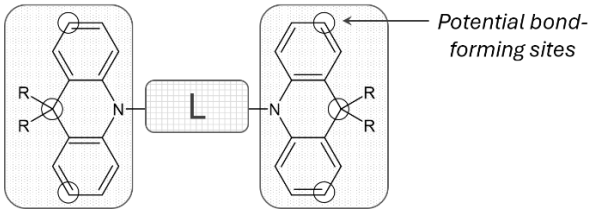


Figure 1. Structure of acridan derivatives

In current work we investigate electrochemical properties of acridan and its derivatives 9,9-dimethyl-acridan. Such methods as cyclic voltammetry, and it's combination with UV-Vis spectroscopy, Electron Spin Resonance were used to distinguish redox forms and intermediates. Besides the investigation of electrochemical properties, cyclic voltammetry also provides insight into the polymerization mechanism and enables control over the thickness of the deposited layer when the precursor is polymerizable, allowing the direct formation of a thin conductive film on the electrode surface. Additionally, NMR analysis supported by TLC chromatography was attempted to identify soluble products formed during electrochemical polymerization, particularly low-molecular-weight species that may precipitate during electrodeposition.

Investigated compounds are electrochemically active and form several intermediates but do not form a polymer film in tetrabutylammonium tetrafluoroborate. Nevertheless it can be caused by electrolyte which is weakly nucleophilic and can deactivate reactive centers and limit cation-radicals interaction. Then aforementioned acridan derivatives study can be still interesting for its behavior understanding and designing appropriate multifunctional monomers. Preliminary investigation of A-L-A-type acridan compounds shows polymer formation demonstrating their potential relevance for polymeric electrode in energy-storage applications. Hence understanding the relationship between chemical structure and electrochemical properties in it polymerization possibilities is crucial to evaluate their suitability as acridine precursors for electroactive materials.

[1] B. Zhang, X. Li, B. Li, C. Gao, and Y. Jiang, "Acridine and its derivatives: A patent review (2009-2013)," Expert opinion on therapeutic patents, vol. 24, pp. 647–64, Jun. 2014.
[2] N. Srividya, P. Ramamurthy, P. Shanmugasundaram, and V. T. Ramakrishnan, "Synthesis, Characterization, and Electrochemistry of Some Acridine-1,8-dione Dyes," J. Org. Chem., vol. 61, no. 15, pp. 5083–5089, Jan. 1996.
[3] S. Wang et al., "Blue thermally activated delayed fluorescence based on tristriazolotriazine core: Synthesis, property and the application for solution-processed OLEDs," Dyes and Pigments, vol. 182, p. 108589, Nov. 2020.

FUNCTIONAL TiO_2 NANOMATERIALS AND IRON-BASED CATALYTIC SYSTEMS FOR ADVANCED OXIDATION OF EMERGING PHARMACEUTICAL POLLUTANTS

Larisa Mocanu[1,*], Maria Gonta[1]
[1]*Institute of Chemistry of Moldova State University, Chisinau, Republic of Moldova*
*E-mail: larisa.mocanu@usm.md

Emerging pharmaceutical contaminants represent a growing environmental challenge due to their persistence and resistance to conventional treatment processes. Among the most frequently detected pharmaceutical residues are β-lactam antibiotics and non-steroidal anti-inflammatory drugs, which may accumulate in aquatic environments and adversely affect ecosystem quality. Advanced oxidation processes (AOPs) based on catalytic and photocatalytic mechanisms have attracted considerable attention as efficient approaches for the degradation of recalcitrant organic compounds through the generation of highly reactive oxygen species.

In this work, iron-based catalytic systems and TiO_2 nanoparticle photocatalysts were investigated as functional materials for the degradation and mineralization of representative pharmaceutical pollutants, namely amoxicillin and diclofenac, in aqueous media. Particular attention was paid to the influence of catalyst loading, oxidant concentration, pH, and UV irradiation on oxidation efficiency and reaction kinetics. The investigated systems included homogeneous Fenton oxidation (Fe^{2+}/H_2O_2) and heterogeneous photocatalytic oxidation ($TiO_2/H_2O_2/UV$), both relying on hydroxyl-radical-mediated oxidation pathways [1].

The experimental results demonstrated [2] the high catalytic activity of the Fenton system toward pharmaceutical degradation. For amoxicillin, degradation efficiencies of approximately 90% and oxidation/mineralization degrees up to 96% were achieved under optimized conditions (pH 2.2-2.5). Kinetic analysis revealed pseudo-first-order behavior, indicating efficient radical generation and rapid substrate transformation. For diclofenac sodium, degradation and mineralization efficiencies exceeding 80% were obtained, confirming the effectiveness of iron-based catalytic systems for the oxidation of persistent aromatic pharmaceutical compounds [3].

Photocatalytic oxidation employing TiO_2 nanoparticles and H_2O_2 under UV-C irradiation also showed significant oxidation performance [2,3]. Maximum efficiencies were achieved at pH 3.5-4.0, where amoxicillin degradation reached approximately 65%, while oxidation/mineralization attained values up to 97%. The enhanced activity of TiO_2 nanomaterials is associated with the formation of electron–hole pairs and reactive oxygen species capable of initiating complex oxidation reactions and promoting deep mineralization of organic pollutants.

The obtained results demonstrate that TiO_2 nanomaterials and iron-based catalytic systems represent promising functional materials for advanced environmental remediation technologies. The combination of catalysis, photocatalysis, and nanostructured materials provides efficient pathways for the elimination of emerging pharmaceutical contaminants and contributes to the development of innovative and sustainable oxidation technologies. The study highlights the interdisciplinary connection between materials engineering, nanotechnology, catalytic processes, and environmental applications, corresponding to the scientific directions of Materials Engineering for Innovative and Sustainable Technologies (MEST).

[1] Kosar Hikmat Hama Aziz, Fryad S. Mustafa, Mozart A. H. Karim and Sarkawt Hama. *Materials Advaced*, **6** (2025), 3433-3454.
[2] M. Gonta, L. Mocanu, V. Porubin-Schimbator. *Handbook of Research on Water Sciences and Society*, **Chapter 14** (2022), 315-340.
[3] M. Gonta, L. Mocanu, I. Popaz. *Book Scientific Seminar Advanced Materials to Reduce the Impact of Toxic Chemicals on the Environment and Health*, 2023, 45.

ASPECTS OF DIFFERENTIATED FRACTIONATION OF SERUM PROTEINS DURING WHEY ELECTROACTIVATION

I.V. Paladii*, E.Gh. Vrabie, V.Gh. Vrabie, T.G. Stepurina,
A.A. Policarpov, C.Gh. Sprincean
Moldova State University, Institute of Applied Physics, Chisinau, Republic of Moldova;
*Email: irina.paladii@ifa.usm.md

Industrial development is increasingly driven by technological innovation, economic efficiency, and environmental sustainability. In the dairy industry, whey has evolved from a waste product to a valuable secondary resource due to its high content of biologically active compounds, particularly whey proteins. Electroactivation offers a sustainable, zero-waste approach for efficient whey processing with minimal environmental impact.

This study investigated the electroactivation of three types of whey differing in protein content: high-protein whey (WHPC), medium-protein whey (WMPC), and low-protein whey (WLPC), supplied by joint-stock company "JLC" (Chișinău, RM). The electroactivation was carried out using several diaphragm electrolysers (EDP-2, EDP-4, EDC-3, and EDC-pilot) designed for both periodic and continuous-flow treatment. The electrolysers enabled efficient, non-residual whey processing under specified technical and operational conditions.

The efficiency of protein recovery into protein-mineral concentrates (PMCs) depended on the whey composition, electrolyser design, and processing conditions. Differences in protein fractionation were associated with the mechanisms of protein complexes formation: ion flotation; salinisation of whey proteins; transition of aquacomplexes into hydroxo-complexes; protein precipitation at the isoelectric point; sulfhydryl-induced aggregation through disulfide bond interactions; and the formation of calcium phosphate-caseinate complexes. These mechanisms collectively determined the selective recovery of individual protein fractions.

The major whey protein fraction, β-lactoglobulin, exhibited the highest recovery during the initial stages of electroactivation, reaching 83–92% for WHPC processed in the EDC-3 electrolyser under periodic conditions (10 mA/cm²) and approximately 77% for WMPC under continuous-flow treatment (20 mA/cm²). Maximum α-lactalbumin recovery was achieved with WLPC processed in the EDC-pilot under periodic conditions (73.2–88.9%) and with WMPC under continuous treatment in EDC-3 (approximately 66%). Enhanced α-lactalbumin extraction concurred with maximum lactose isomerization to lactulose through both the Amadori rearrangement and LA-transformation mechanisms, promoting the formation of calcium–lactulose complexes and facilitating the "release" of α-La from the lactose syntase complex, resulting in its recovery into PMCs [1]. Caseins were recovered most effectively from WHPC processed in the EDP-2 electrolyser under periodic conditions (about 29%), whereas continuous processing of WMPC achieved a recovery of 15.9–22.6%. High-molecular-weight proteins showed the highest recovery of 27.2–33.9% during periodic processing of WHPC and 18.6–30.5% during continuous processing of WMPC [2].

Overall, electroactivation is an environmentally friendly technology for processing whey and other secondary dairy products. The method enables the differential protein fractionation, reduces or eliminates the need for chemical reagents, lowers energy consumption and emissions, and improves the quality and value of the resulting products, demonstrating strong potential for sustainable industrial dairy processing.

[1] Paladii, I., Vrabie, E., Bologa, M., Vrabie, V., et al. *Journal of Engineering Science* **31** (2024) 80-93.
[2] Vrabie, E.G. et al. *ICNBME 2021. IFMBE Proceedings, Springer, Cham*. **87** (2022) 522-529.

METHODS FOR OBTAINING MoS_2 NANOMATERIALS VIA ULTRASOUND-ASSISTED ELECTROCHEMICAL INTERCALATION AND EXFOLIATION

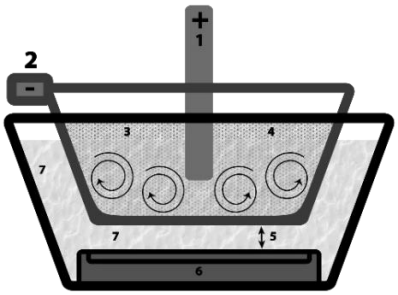
R. I. Lascova-Baciu *, S. S. Belevskiy
Moldova State University, Institute of Applied Physics,5, Academiei str., MD-2028, Chişinău, Republic of Moldova
*E-mail: lascovarenata@gmail.com

Transition metal nanomaterials, such as molybdenum disulfide MoS_2, have attracted considerable scientific interest owing to their remarkable physicochemical properties and unique morphological and structural characteristics, including high electrical conductivity and a layered crystal structure that enables exfoliation into individual monolayers. Materials with these characteristics are particularly valuable for applications in sensors, electronic and optoelectronic devices [1,2], as well as in chemical and electrochemical catalysis.

Chemical methods for the synthesis of MoS_2 nanomaterials exhibit significant limitations, including difficulties in controlling particle size, ensuring material homogeneity, and achieving process scalability during synthesis [3].

Electrochemical intercalation followed by exfoliation is considered one of the most effective approaches for the preparation of MoS_2 nanomaterials. The combination of ultrasonic treatment with these processes provides enhanced potential for the development of an efficient nanomaterial production method with improved exfoliation efficiency. The proposed approach offers several advantages, including reduced energy consumption, improved reproducibility, and enhanced scalability of the nanomaterial synthesis process.

Electrochemical intercalation followed by exfoliation has proven to be one of the most promising approaches for the preparation of MoS_2 nanomaterials. Dimethyl sulfoxide (DMSO) was employed as the electrolyte, while MoS_2 powder 2 μm served as the precursor. Medium-frequency ultrasonic irradiation was simultaneously applied to enhance the efficiency of both the electrochemical intercalation and the subsequent exfoliation processes, resulting in the establishment of a stable synergistic effect. A stainless-steel cup served as the cathode and was immersed in an ultrasonic bath throughout the intercalation and exfoliation processes, whereas a platinum electrode was employed as the anode. The particle sizes ranged from approximately 4 nm to 250 nm, with a significant population of particles measuring 5 nm or less. The method results in the formation of a complex mixture of nanomaterials with a wide range of geometric parameters (sizes and shapes), which poses a challenge for their subsequent application. The presence of such mixture of nanomaterials creates an urgent need for an effective method to separate these mixtures into their constituent components.



The feasibility of using industrial MoS_2 powders as a precursor has been demonstrated, offering numerous technological advantages.

Figure 1. Schematic representation of the electrochemical cell: (1) Pt anode; (2) stainless-steel cathode; (3) DMSO electrolyte containing the reagents; (4) MoS_2 powder (reaction mixture); (5) interelectrode distance; (6) ultrasonic transducer; (7) water bath.

[1] M. Zhao, C. Casiraghi, K. Parvez, *Chem. Soc. Rev.* **53** (2024) 3036 – 3064.
[2] K. Rho, E. B. Sohn, S. J. Lee, P. S. Toth, A. Vali, N. Myung, C. Janáky, K. Rajeshwar, *ACS Appl. Energy Mater.* **4** (2021) 7562−7570.
[3] N. M. Abdelazim, Y. J. Noori, S. Thomas, V. K. Greenacre, Y. Han, D. E. Smith, G. Piana, N. Zhelev, A. L. Hector, R. Beanland, G. Reid, P. N. Bartlett, C. H. de Groot, *Adv. Electron. Mater.* **7** (2021) 2100419 p8.

INVESTIGATION OF THE EFFICIENCY OF THE EXTRACTION TECHNOLOGY FROM KIWI USING ELECTROPLASMOLYSIS AND MICROWAVE TREATMENT

A.Ya. Papchenko*, G.D. Grecu
Institute of Applied Physics, Moldova State University,
MD-2028, 5 Academiei str., Chisinau, Republic of Moldova
*E-mail: andrei.papcenco@mail.ru

The preparation and performance of the experiments were carried out in three stages: 1. In the first stage, the dependence of the kiwi juice yield on the particle size after grinding was studied: 1 – coarse grinding 5–6 mm; 2 – medium grinding 3–4 mm; 3 – fine grinding 1–2 mm. Investigation of the influence of the particle size after grinding on the efficiency of juice extraction from kiwi fruit. The results are given in Table 1 and in the graphs in Fig. 1.

Table 1

No.	Pressing time, min	Pressure, kg/cm²	Juice yield, %		
			Curve 1	Curve 2	Curve 3
			Coarse grinding	Medium grinding	Fine grinding
	0	0	0	0	0
1	0.5	0.15	0	16.3	28.81
2	1.0	0.30	9.46	26.06	39.99
3	1.5	0.45	15.02	29.39	44.59
4	2.0	0.60	18.88	33.02	47.66
5	2.5	0.75	22.51	39.9	49.22

Table 2

No.	Pressing time, min	Pressure, kg/cm²	Juice yield, %		
			Curve 1	Curve 2	Curve 3
			Control	microwave treatment	Electroplasmolysis
	0	0	3.74	11.81	12.87
1	0.5	0.15	26.56	32.58	36.81
2	1.0	0.30	36.82	43.09	48.77
3	1.5	0.45	45.44	48.92	53.91
4	2.0	0.60	50.47	52.95	55.88
5	2.5	0.75	52.43	52.80	56.95
6	2.5	0.75	53.21	55.67	57.91

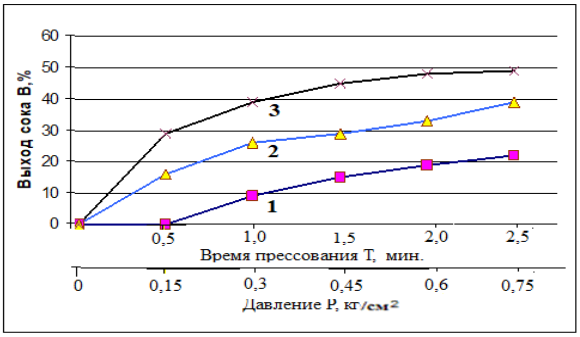


Figure 1

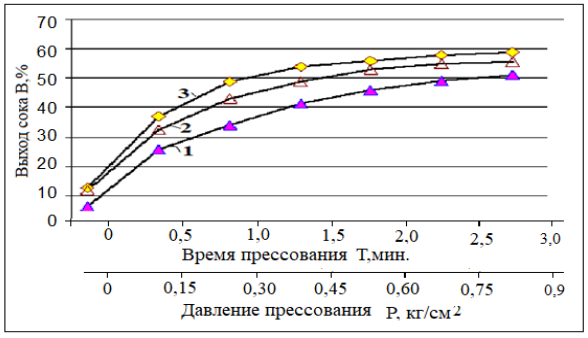


Figure 2

Fig. 1 shows the dependence of the juice yield from kiwi fruit on the particle size after grinding: 1 – coarse grinding 5–6 mm; 2 – medium grinding 3–4 mm; 3 – fine grinding 1–2 mm. Table 1 and the graphs in Fig. 1 show that the studies established an increase in the juice yield from pulp with small particle sizes obtained by grinding before the pressing process. This is explained by the damage of a larger number of cells during fine crushing of the raw material compared with coarse grinding.

2. In the second stage, the influence of electroplasmolysis and microwave treatment on the efficiency of juice extraction from kiwi fruit was studied. The results are given in Table 2 and in the graphs in Fig. 2.

Fig. 2 shows the dependence of the juice yield from kiwi fruit on the treatment: 1 – grinding; 2 – microwaves and 3 – electroplasmolysis. Table 2 and the graphs in Fig. 2 show that the studies established an increase in the juice yield from kiwi pulp with small particle sizes after treatment: by 4.7% with electroplasmolysis and by 2.46% with microwave treatment.

INDUSTRIAL-SCALE TESTING OF THE MODIFIED BIOGAS TREATMENT TECHNOLOGY OF LIQUID WINERY WASTES

Gh.Duca*, O.Covaliova, L.Romanciuc, C.Tasca
Moldova State University, Institute of Chemistry, Republic of Moldova
*E-mail: ggduca@gmail.com

Alcohol production industry entails the formation, along with the principal products, the significant amounts of the liquid and solid wastes, which in case of the mismanagement can provoke serious environmental pollution [1]. At the same time, these wastes can be sources of a series of value-added products including biogas (containing specifically biomethane and/or biohydrogen) as a renewable energy source, treated water, fermented sludge, bioactive substances, etc. that can be reused in the industrial processes and auxiliary technologies [2].

Among the most promising technologies of liquid winery wastes treatment remains to be biogas processes, specifically modified method based on the introducing into the fermented medium of the micro-additives with bioactive and antioxidant properties (such as rutozide, betulinol, aescin, sclareol, etc.) capable to accelerate the fermentation rate and enhance the biomethane contents in the biogas contents, close to the natural methane gas composition. [3,4].

Such a technology including the application of dihydroxyfumaric acid (DHFA) as an additive to the anaerobically fermented biomass, have been initially studied under the bench-scale conditions as well as using the theoretical approach, and further tested under the industrial-scale conditions at the ”Garma-Group” S.A., Farladeni, Republic of Moldova [5]. Within the frames of the industrial testing, a bioreactor containing a mixture of winery waste biomass with the bovine manure (in a ratio 3:1) with total volume of 3313 m^3, with DHFA introduced in the amount of 113,28 g per reactor, was operating under the mesofil regime at 37,6 °C. Generated biogas volume reached the maximum of 46,2%, demonstrating intensive fermentation and efficient biomass conversion rate.

Another bioreactor operating under the standard conditions, with no bioactive substance introduced, had the biomass volume of 2907 m^3, at the temperature of 39,6 °C, and showed the biogas production of 40,7%, i.e. by 6% less. In addition, the concentration of carbon dioxide has decreased from 37,5% in the test reactor to 32,1% in the reactor with bioadditive, which testifies the more stable anaerobic digestion regime in the presence of DHFA. H_2S contents in the presence of bioactive substance was reduced by about 700 ppm, which suggests that DHFA can put indirect limitations to the vital activity of sulfate-reducing bacteria or the availability of sulfur precursors in the studied process.

Industrial test has demonstrated the increased energy efficiency of the anaerobic digestion in the presence of bioactive additive, which implies a potential reducing of the external consumption of resources and increasing the energetic autonomy of the equipment.

ACKNOWLEDGEMENT. This work has been performed under the Research Project Nr.010603 implemented at the Moldova State University, Institute of Chemistry.

[1] M.Cook, N.Critchlow, R.O'Donnell, S.MacLean *Health Promot Int*. **39(1)** (2024) daae004. Doi: https://doi.org/10.1093/heapro/daae004. PMID: 38305639; PMCID: PMC10836053.
[2] M.Mesta-Corral, N.Ramirez-Guzman, et al. *Int J.Mol.Sci*. 26(22) (2025) 10820. Doi: https://doi.org/10.3390/ijms262210820.
[3] V.Covaliov, *Academos*, **4(39)** (2015) 38-44.
[4] Gh.Duca, V.Covaliov, O.Covaliova, In: *Emerging Developments and Environmental Impacts of Ecological Chemistry.* Chapter 13. IGI Global Publ. House, USA (2020) pp.291-306.
[5] C.Tașca, *Journal of Social Sciences*, **8(2)** (2025) 17-27. Doi: https://doi.org/10.52326/jss.utm.2025.8(2).02.

TRIBOLOGICAL BEHAVIOR OF ELECTRICAL CONTACTS PRODUCED BY THE ELECTROSPARK ALLOYING METHOD

V. Mihailov[1*], S. Ivașcu[1], M. V. Lungu[2], D. Croitoru[1], Sp. Iațco[1], A. Ianachevici[1], I. Ion[2], D. Pătroi[2], V. E. Marinescu[2], D. Tălpeanu[2]
[1]Moldova State University, Chisinau, Republic of Moldova;
[2]National Institute for Research and Development in Electrical Engineering ICPE - CA Bucharest, Romania
*E-mail: valentin.mihailov@gmail.com

The Electrospark Alloying (ESA) method, also known as Electrospark Deposition (ESD), is an advanced technological solution for the manufacture of electrical contacts. This method is based on the polar transfer of material from the processing electrode (anode) to the substrate (cathode) surface through pulsed electrical discharges. Compared with conventional methods such as electroplating and brazing, ESA provides distinct advantages in the production of electrical contacts.

The principal advantages of the ESA method include the high adhesion of the deposited coating to the substrate, preventing delamination under the action of frictional forces or switching electric arcs. ESA also enables the localized deposition of noble metals (e.g., silver, gold, and platinum), composites, or special alloys only on the active contact area, significantly reducing material costs.

In this study, copper was used as both the substrate material and the static element of the tribological pair. Copper substrate specimens with dimensions of 50 mm × 10 mm × 5 mm and static elements measuring 23 mm × 17 mm × 5 mm were fabricated. Silver (Ag), tungsten (W), and graphite (C) bars (35 mm × 4 mm × 4 mm) were used as processing electrodes. Coatings of the same materials were deposited by ESA on both the substrate specimen surface and the corresponding static element.

Tribological testing of the ESA-produced electrical contacts was performed using a specialized tribometer equipped with a mechanism that generated linear reciprocating motion of the static element relative to the test specimen, thereby simulating the switching process. The tribometer was also equipped with a computerized data acquisition system for measuring the friction force, coefficient of friction, and temperature in the contact zone.

Each tribological test was conducted under a normal load of 10 N, for 50000 cycles (double strokes), corresponding to 4 h 36 min. Wear resistance was evaluated from the mass loss of the coated substrates, which was 0.1 mg for the Ag coating, 0.2 mg for the graphite coating, 0.5 mg for the Ag + C coating, and 1.0 mg for the Ag + W coating. These results confirm that the ESA method effectively improves the wear resistance of electrical contacts.

ACKNOWLEDGMENTS. This work was supported by a grant of the Ministry of Education and Research, CCCDI – UEFISCDI, Romania, project number PN-IV-PCB-RO-MD-2024-0544, grant number 51PCBROMD/2025, within PNCDI IV, Program 5.8. European and international cooperation, Subprogram 5.8.3 – Bilateral/Multilateral, and by the Ministry of Education and Research, NARD, Republic of Moldova, grant number 25.80013.5007.55ROMD.

INTENSIFICATION OF PHASE-STRUCTURAL TRANSFORMATIONS IN THE SURFACE LAYERS OF METALS UNDER THE COMBINED ACTION OF ELECTRIC-SPARK ALLOYING, PLASTIC DEFORMATION AND PLASMA-CHEMICAL TREATMENT

V. Mihailov[1,*], S. Ivascu[1], N. Kazak[1], A. Ianachevici[1]
[1]*Institute of Applied Physics, Moldova State University, Chisinau, Republic of Moldova*
*E-mail: valentin.mihailov@gmail.com

Electric spark alloying (ESA) is notable for the simplicity of its technological process, the high adhesion of the formed layers to the substrate, the possibility of using any electrically conductive material as a working electrode, and the possibility of treating strictly localized areas without dismantling the equipment. However, the layers formed by ESA, of the order of tenths of a millimeter (0.1-0.5 mm), do not meet the durability requirements of machine parts treated in this way. Attempts to increase the thickness of the deposited coatings by raising the treatment regime (the energy of the electrical discharges) did not yield positive results, because increasing the regime gives rise to a number of other undesirable effects, such as the build-up of residual tensile stresses in the surface layers of the treated part, which contributes to a decrease in fatigue resistance. At the same time, the roughness of the treated surface increases (parameter Ra).

Samples of structural carbon steels of the OLC3 and OLC45 types and of commercially pure titanium VT1-0, of various geometric shapes – square prisms measuring 15×15×6 mm and cylinders 30 mm long and 8 mm in diameter – were used as research objects. Technical nickel NP-2, chromium and several types of graphite were selected as working electrodes: the first two metals because they form coatings with greater continuity, and graphite because, besides readily forming high-hardness carbides with iron and titanium, it also possesses solid-lubricant properties. Plastic deformation (PD) was carried out using balls and rollers made of ShKh-15 bearing steel over a wide range of loads of 0.2-1.5 kN. Rapid plasma-chemical treatment (PCT), lasting 2-5 min, was performed in a solution of salts containing carbon and nitrogen at voltages of about 100-170 V and average currents of 15-25A. The combined treatment was carried out in the following sequence: ESA → PD → PCT.

It was established that the advantage of the combined treatment performed in this sequence was a gradual reduction of the roughness parameter Ra from approximately 9 μm after ESA down to 0.53 μm after PCT. As a result of the proposed combined treatment, in addition to the improvement of the surface quality of the surface layer, the microhardness increased considerably. Metallographic analysis of the cross-section of the zone of the sample subjected to the combined treatment revealed a modification of the initial structure through grain refinement, as well as solid-state diffusion of carbon into the steel and titanium matrices. After the combined treatment, the modified (hardened) zone is characterized by high hardness and has a width 3-4 times greater than that obtained by ESA alone, which demonstrates the efficiency of the proposed method.

ACKNOWLEDGEMENTS. The authors are grateful for the subprogram 011204, financed by the Ministry of Education and Research of R. Moldova "Technology for modifying the surfaces of construction and medical steels in the complex action with electrical impulse discharges, plastic deformation and plasmochemical treatment in electrolytes".

MODIFICATION OF METAL SURFACES THROUGH THE DEVELOPMENT OF ELECTRIC SPARK ALLOYING TECHNOLOGIES USING POWDERS

S. Ivașcu[1,*], V. Mihailov[1], D. Croitoru[1], Sp. Iațco[1], A. Ianachevici[1]
[1]*Moldova State University, Chisinau, Republic of Moldova*
*E-mail: sergiu.ivascu@gmail.com

In the domain of contemporary surface engineering, the enhancement and optimisation of the operational performance of machine components is a pivotal concern. In many cases, these issues can be addressed in a more straightforward and cost-effective manner by applying protective coatings to the working surfaces of machine parts and equipment. Such treatment, by modifying the physical and mechanical properties of the working surfaces, increases hardness, wear resistance, corrosion resistance, and so on.

A typical technological process, in which the energy source is low-voltage discharge plasma, is based on the phenomenon of polar material transfer from the anode (processing electrode) to the cathode (workpiece) when discharges occur between them. A comprehensive review of extant studies on the ESA process, conducted over the course of its history, demonstrates the simplicity of the process, characterised by the ability to treat surfaces without special preparation, high adhesion of the applied material to the substrate, equipment reliability and portability, etc. Concurrently, methodologies employed for the formation of coatings from powders introduced into the working gap – either in the absence of contact or with periodic contact between the electrodes – have become extensively utilised. These methodologies are distinguished by their high productivity and the substantial breadth of materials employed.

However, these processes are not without their drawbacks, including the inability to use electrodes or powders with high resistivity, difficulties in depositing materials onto certain types of substrates, relatively low productivity, and limited thickness of the deposited layers, among others. These factors significantly hinder the widespread use of this method in industry.

One method of addressing these issues and expanding the capabilities of the ESA method has been the transition to pulsed plasma technologies. The aim of this transition is to create multicomponent coatings using various mixtures of powders made from different materials, including carbides, borides, nitrides, and high-hardness refractory oxides (Al_2O_3, ZrO_2, TiO_2), as well as metal or composite powders intended for special applications.

This conceptual evolution, from the melting of a solid electrode to the interaction with dispersed powder particles, has paved the way for the latest scientific efforts in the field of producing metal-ceramic coatings through the interaction of pulsed plasma with metallic and non-metallic powders. In this pioneering process, the conventional concept of a localized electric spark is expanded to the level of a high-energy pulsed plasma channel, which functions as a dynamic thermochemical reactor for the in situ synthesis of metal-ceramic layers.

ACKNOWLEDGEMENTS. This work was supported by a grant of the Ministry of Education and Research, National Agency for Research and Development, Republic of Moldova, grant No.25.80013.5007.08RE.

MICROSTRUCTURE AND TRIBOMECHANICAL PROPERTIES OF ELECTROSPARK-DEPOSITED SILVER-BASED COATINGS ON COPPER SUBSTRATES

M. V. Lungu[1,*], V. Mihailov[2], S. Ivașcu[2], D. Pătroi[1], V. E. Marinescu[1], D. Tălpeanu[1], I. Ion[1], E. M. Lungulescu[1], A. R. Caramitu[1], E. Manta[1]
[1]*National Institute for Research and Development in Electrical Engineering ICPE - CA Bucharest, Romania;*
[2]*Moldova State University, Institute of Applied Physics, Chisinau, Republic of Moldova*
*E-mail: magdalena.lungu@icpe-ca.ro

In this study, pure silver (Ag) and silver-tungsten (Ag-W) composite coatings with a thickness of about 20 μm were deposited on disc-shaped copper (Cu) substrates (Ø20 mm × 5 mm) by electrospark deposition (ESD) using Ag and W rod electrodes. The coatings were characterized in terms of their microstructure, phase composition, surface roughness, and tribomechanical properties using scanning electron microscopy (SEM) coupled with energy-dispersive spectroscopy (EDS), X-ray diffraction (XRD), contact profilometry, nanoindentation, and tribological testing.

All coatings exhibited strong metallurgical bonding to the Cu substrate, a refined microstructure, and the characteristic splash-like surface morphology of ESD coatings. The Ag coatings showed lower surface roughness ($Ra \leq 2.2$ μm) than the Ag-W coatings ($Ra \leq 3.6$ μm), reflecting the dissimilar properties of Ag and W. Owing to its low melting temperature, high ductility, and high thermal conductivity, Ag melts and spreads easily during each discharge pulse, forming relatively smooth splats. In contrast, the very high melting temperature, high hardness and limited diffusivity of W in Ag restrict its melting and transfer during deposition, leading to the incorporation of W-rich particles and partially melted fragments that increase surface irregularity and coating roughness.

XRD and EDS analyses identified Ag as the predominant phase in both coatings, together with Cu originating from the substrate as a result of simultaneous melting of the electrode and substrate during ESD. Localized interfacial mixing caused partial dilution of the deposited layer with Cu. The Ag-W coatings contained approximately 4.4 wt.% W, indicating limited incorporation of W during deposition. This low W content is attributed to the refractory nature of W, whose very high melting temperature restricts its erosion and transfer efficiency during ESD.

The Ag-W coatings exhibited substantially higher indentation hardness (2.64 GPa) than both the Ag coatings (1.75 GPa) and the Cu substrate (1.38 GPa). The ~50% increase in hardness of the Ag-W coatings relative to the Ag coatings demonstrates that even a small addition of W effectively reinforces the Ag matrix. Unlike hardness, the Cu substrate exhibited the highest indentation modulus (118 GPa), followed by the Ag-W coatings (107 GPa), while the Ag coatings showed the lowest value (84 GPa), reflecting the lower stiffness of Ag. This trend is consistent with the elastic properties of the constituent materials and the composite nature of the ESD coating.

All coatings exhibited superior tribological performance compared with the Cu substrate under ball-on-disk tests performed in the rotating configuration at normal loads of 5–10 N over a sliding distance of 500 m. The Ag-W coatings showed higher wear resistance than the Ag coatings due to their enhanced mechanical properties. Overall, the electrospark-deposited Ag-based coatings demonstrated superior tribomechanical performance relative to the Cu substrate, highlighting the potential of Ag-W coatings for electrical contact applications, where high wear resistance and mechanical durability under repeated switching and sliding are required while maintaining good electrical conductivity.

ACKNOWLEDGEMENT. This work was supported by a grant of the Ministry of Education and Research, CCCDI – UEFISCDI, Romania, project number PN-IV-PCB-RO-MD-2024-0544, grant number 51PCBROMD/2025, within PNCDI IV, Program 5.8. European and international cooperation, Subprogram 5.8.3 – Bilateral/Multilateral, and by the Ministry of Education and Research, NARD, Republic of Moldova, grant number 25.80013.5007.55ROMD.

PHYSICO-CHEMICAL PROPERTIES OF INDUSTRIAL GLASSWARE FROM THE POSITION OF SYSTEM ANALYSIS

V. A. Sharagov*, G. I. Curicheru
Alecu Russo Balti State University, 38, Pushkin str., Balti, Republic of Moldova
*E-mail: vsharagov@gmail.com

The most important operational properties of industrial glassware for various applications are mechanical strength, microhardness, thermal stability and chemical resistance. The purpose of the undertaken experiments was to reveal the factors that influence the physico-chemical properties of industrial glassware with the help of system analysis.

The notion of system analysis has a multipronged character [1-2]. From the position of the system analysis the physico-chemical property is a system of correlated factors. A unified approach to the presentation of the physico-chemical properties of industrial glassware has been developed for the first time. In order to install the elements that influence the properties of glassware the authors considers that three main blocs of elements have to be assigned: "1. Parameters and properties of glassware", "2. Raw materials and conversion technology them into glassware" and "3. The glassware interaction with environment".

The first direction includes the parameters and properties of industrial glassware that characterize any material object: composition, structure, homogeneity, surface properties, etc. The second direction contains the elements that influence the glassware manufacturing (raw materials and their conversion in glassware etc.). The third direction characterizes glassware interaction with the environment, otherwise said with other objects. Every block consists of several groups and sub-groups of elements.

In the next stage we ascertain the influence of each factor on the physico-chemical property of glass (mechanical strength, microhardness, thermal stability, water resistance etc.). Then, the most difficult and responsible stage comes: arranging the factors according to the degree of their importance. For this the quantity link between each factor and the physico-chemical property of glassware is established. In cases when there is no quantitative criterion, we take into account the qualitative influence of this factor on the physico-chemical property of glassware. It must be mentioned that there is not much information concerning the influence of many factors on the physico-chemical properties of industrial glassware.

The final stage is the design and execution of the measures to meet all the requirements at the given stage of the technological process of glassware manufacturing.

Thus, from the position of the system analysis we can get an integral representation of the factors that influence the physico-chemical properties of industrial glassware, of the correlation between them, and we can arrange the factors according to the degree of their importance. Such an approach allows optimization of manufacturing of industrial glassware with high physico-chemical properties.

[1] Shelly, Gary B., Rosenblatt, Harry J. *Systems Analysis and Design:* ninth Edition. Publisher: Course Technology, (2024) 737 p.
[2] Satzinger, John W., Jackson, Robert B., Burd, Stephen D. *Systems Analysis and Design in a Changing World*. 6th Edition. Publisher: Course Technology (2011) 576 p.

IMPROVING PHYSICO-CHEMICAL PROPERTIES OF ANNEALED HOLLOW INDUSTRIAL GLASSWARE

V. A. Sharagov*, G. I. Curicheru, I. N. Olaru
Alecu Russo Balti State University, 38, Pushkin str., Balti, Republic of Moldova
*E-mail: vsharagov@gmail.com

Thermochemical treatment by acid gases, which takes place during the process of glassware manufacturing, is a simple method to improve the physico-chemical properties of industrial glassware. The purpose of the undertaken experiments was to investigate the possibility of intensification of the dealkalization process of annealed hollow industrial glassware as well as of those stored with acid gases using impulse magnetic field.

Experiments were held in laboratory and industrial conditions. Industrial glassware of different purposes served as objects of investigation: containers (bottles, jars and flasks) of transparent colorless glass, bottles and flasks of green glass, ampoules made from medical glass, illuminating glassware made from transparent colorless, rosaline and milk glasses, laboratory and assorted glassware etc. SO_2, SO_3, NO_2, HF, HCl, CCl_2F_2, $CHClF_2$ and mixtures of these gaseous reagents ($CCl_2F_2 + SO_2$, $CHClF_2 + NO_2$, SO_2 + HCl and others) were used for thermochemical treatment of annealed hollow glassware.

The procedure of thermochemical treatment in the laboratory conditions was carried out in the following way. Samples of glassware were inserted into the kiln at room temperature. Then the samples were heated to the designed temperature and treated with gas reagent and impulse magnetic field. The main regimes of glassware treatment are the following: temperature – between 300 and 600 ^{0}C, duration – 5 min, value of vector's magnitude of the magnetic induction – between 0.05 and 0.25 T, gas reagent with a flow rate of 0.05-5.0 μmol/m^2 of glass surface.

The main regimes of annealed hollow glassware treatment by gaseous reagents and impulse magnetic field on processing lines are the following: temperature – between 500 and 600 ^{o}C, the value of vector's magnitude of the magnetic induction – up to 0.2 T, duration – between 1 and 8 s, gas reagent with a flow rate of 0.05-5.0 μmol/m^2 of glass surface. The gaseous reagents were fed into the glassware mainly in gaseous state and in the form of solutions and solid substances.

The following hollow glassware properties were determined: water resistance, acid resistance, impact strength, thermal stability and microhardness. Mechanical strength of jars, flasks and bottles was characterized by value of internal hydrostatic pressure resistance. Additionally the jars were tested on the resistance of the compression in the directions both along and perpendicular to the body walls. The experiments studied the influence of temperature, chemical composition of glass and gaseous reagent, quantity of gas reagent feeded into the camera and glassware, duration of treatment and value of vector's magnitude of the magnetic induction on dealkalization rate of alkaline cations. We have determined that the rate of dealkalization of industrial glasses with gaseous reagents under the impact of impulse magnetic field has increased by 2–4 times.

As a result of the simultaneous treatment of annealed hollow industrial glassware with impulse magnetic field and dealkalization with gaseous reagents, water resistance of the glass surface increasing tenfold, as well as increases the mechanical strength by 30-50 %, the thermal stability and microhardness - by 10-15 %. It has been established that with increase of temperature, quantity of gas reagent feeded into the camera and glassware, value of vector's magnitude of the magnetic induction and duration of treatment, physico-chemical properties of annealed hollow industrial glassware grows up.

ULTRASONICALLY ASSISTED EXTRACTION (UAE) OF BIOLOGICALLY ACTIVE SUBSTANCES FROM SPIRULINA

T. D. Kubritskaya, G. K. Balan, T. D. Shemyakova*
Institute of Applied Physics, State University of Moldova, Chisinau, Republic of Moldova
*E-mail: tatiana.shemyakova@ifa.md

Microalgae are promising raw materials for producing various biologically active substances (BAS). In the last decade, there has been considerable commercial interest in the cyanobacterium spirulina (*Spirulina platensis*). It can be a source of valuable food additives, as it contains a large amount of protein, as well as pigments such as carotenoids, chlorophylls, and phycocyanins. In particular, phycocyanin is a valuable food colorant, has a protein structure and an intense blue color. Various methods have been developed for the isolation and purification of phycocyanin. The main disadvantage of these processes is that the carotenoids and chlorophylls contained in spirulina biomass are wasted. To preserve these beneficial substances, for example, another approach is proposed – a continuous chain of pigment extraction stages [1].

Published data show that ultrasonically assisted extraction (UAE) is the most widely used method for obtaining phycobiliproteins (PBP) [2]. It is also an environmentally friendly process [3]. The use of ultrasound reduces processing time and solvent consumption, and allows for an increase in product yield, but increases the temperature of PBP samples, which are heat-sensitive compounds. Therefore, temperature control is necessary to maintain PBP activity [4, 5].

The aim of this study was to use ultrasonic cavitation to improve the standard method and reduce the time of *S. platensis* cell destruction, bypassing the freezing and thawing cycles of the raw biomass. Standard *S. platensis* biomass with a concentration of 10 mg/ml, obtained in the Phycobiotechnology Laboratory of the Institute of Microbiology and Biotechnology, Chisinau, Moldova, was used.

The efficiency of cell destruction was assessed using a Digi-Microscop400x digital USB microscope and spectrophotometric analysis using a UV spectrometer (T60). For various BAS types (chlorophylls, carotenoids, and PBP), an analysis of the spectral dependences of optical density was performed for a more intensive processing mode (1) at 22 kHz and a less intensive mode (2) at 44 kHz. The values of the BAS yield correlate with the degree of cell membrane destruction. The BAS yield for mode (1) is higher, but the final product is more contaminated, apparently with small fragments of destroyed cell membranes. Therefore, the use of a less intensive mode (2) is preferable.

A range of BAS (chlorophylls, carotenoids, and phycobiliproteins) was isolated from the biomass of the microalgae spirulina (*S. platensis*). A preferred mode of ultrasonic treatment of spirulina biomass was determined - frequency 44 kHz, amplitude 8-15 μm, duration 5-8 s. Ultrasonic treatment of the biomass was found to increase the yield of BAS, reducing the duration and temperature of the extraction process for the final products while maintaining their quality.

[1] S. Marzorati, A. Schievano, A. Idàb, and L. Verotta, *Green Chemistry*, **22** (2020) 187–196.

[2] H. T.Tan, F. M. Yusoff, Y. S. Khaw, S. A.Ahmad, et al., *Plants*, **10** (2021) art. ID 2358.

[3] J. S. Gomes-Diaz, J. A. Teixeira, and C. M. Rocha, *Food and Bioprocess Technology*, **15** (2022) 1948–1976.

[4] V. K. Kannaujiya, S. Sundaram, and R. P. Sinha, *Phycobiliproteins: Recent Developments and Future Applications.* Singapore: Springer, 2017.

[5] D. P. Jaeschke, I. R. Teixeira, L. D. F. Marczak, and G. D. Mercali, *Food Research Int.*, **143** (2021) art. ID 1110314.

IMPACT OF ANION ASYMMETRY MIXED SODIUM SALTS ELECTROLYTES ON ELECTRICAL CONDUCTIVITY

K.D. Pershina[1,*], M.I. Gorobets[1], T.V. Trifonova[2]
[1]*V.I. Vernadsky Institute of General and Inorganic Chemistry, National Academy of Sciences of Ukraine, 32/34 Palladina Ave., 03142 Kyiv, Ukraine;*
[2]*F. D. Ovcharenko Institute of Biocolloidal Chemistry, National Academy of Sciences of Ukraine, 42, Akademika Vernadskoho boulevard, Kyiv, 03142, Ukraine*
*E-mail: PershinaKD@nas.gov.ua

Finding a molten salt electrolyte with low melting temperature, sufficient low solubility of sodium metal (i.e. low self-discharge rate) and ionic conductivity of Na^+ is the key issue for Na-LMBs [1]. This disadvantage can be eliminated by using low-melting salt mixtures as electrolytes (thiocyanates, acetates, and formats). The main task in this case is to create the key principle of electrolyte anion impact on ionic conductivity and temperature stability of whole electrolyte. To solve this task the Sodium salt electrolyte systems with organic anions (NaSCN–HCOONa, CH_3COONa–HCOONa, and CH_3COONa–NaSCN) were investigated in terms of phase stability and electrical conductivity. Measurements were performed over the temperature range 0–500 °C using the Kohlrausch compensation scheme, AC conductometry in a capillary, melt density determination, XRD, and thermal analysis. Phase transition temperatures were identified from sharp discontinuities in the polythermal dependences of specific electrical conductivity (κ), enabling construction of liquidus lines. Eutectic points were located from double extrema on conductivity isotherms (Table 1).

Table 1. The electrical conductivity, ratio of anion dipole moment and anion ionic radius ratio of melted Sodium salt electrolytes.

System	Anion I,D ratio	Anion R *ion* ratio	Singular points**, (°C)**	Optimal compositions (mol. fraction)
CH_3COONa-NaSCN	2,05	0,58	E(240)	0.5CH_3COONa -0.5NaSCN
CH_3COONa -HCOONa	2,60	0,65	E(244)	0.1CH_3COONa -0.9HCOONa
NaSCN -HCOONa	1,27	1,12	P(184) E(174)	0.45NaSCN- 0.55HCOONa

Table Key: E - eutectic; P - peritectic

In the NaSCN–HCOONa system, a glassy state was identified, characterized by a peritectic transition at 184°C (conductivity minimum) and a eutectic at 174°C (conductivity maximum). Premelting transitions at temperatures as low as 320°C were observed in systems with cation-to-anion size ratios near 3:1. The glass-like behavior in CH_3COONa–HCOONa and CH_3COONa–NaSCN systems is attributed to changes in anion dipole moment associated with ionic asymmetry. These findings provide insight into the structure–property relationships of organic sodium salt melts relevant to ionic liquid and energy storage research.

[1] Rambukwella, I., Zheng, J. C., & Yan, C. *Advanced Functional Materials*, **34(31)** (2024) 2309706.

KINETICS OF TETRACYCLINE HYDROCHLORIDE DEGRADATION IN UV/$S_2O_8^{2-}$ AQUEOUS SYSTEM

T. Isac-Gutsul*, D.L. Nika
Moldova State University, 60 Mateevici str., Chisinau, MD 2009, Republic of Moldova
*E-mail: tanea.isac@gmail.com, tatiana.isac.gutul@usm.md

The kinetics of tetracycline hydrochloride (TCH) oxidation of in a homogeneous medium under UV-Vis irradiation and the UV/$S_2O_8^{2-}$ system was investigated. In the research there was used the 250 mg capsules of TCH produced by *Antibiotice SA*, Iasi, Romania. For both systems, the kinetic behavior of the TCH degradation process was established. The degradation degree (efficiency- DD) was evaluated by varying the oxidant concentration, the TCH concentration, temperature, and pH value. It was observed that, after 1 h of irradiation with a DRT-1000 high-pressure mercury lamp, the DD of TCH in the UV system ranged from 41.8% to 81.1% over the TCH concentration range of 29-5 mg/L (Figure 1). Furthermore, the degradation efficiency increased with decreasing initial TCH concentration. The degradation kinetics followed a pseudo-first-order model with apparent rate constant ranging from 0.0051 to 0.0272 min-1 (Figure 1).

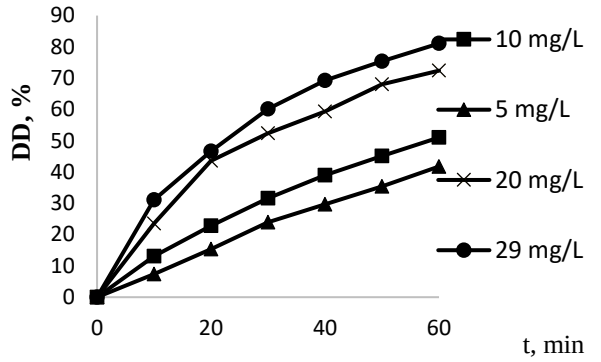


Figure 1. Degradation degree of TCH by UV radiation att = 25 °C and λ = 355 nm

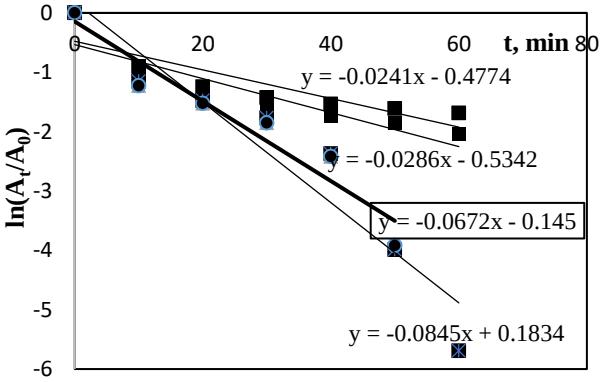


Figure 2. Pseudo-first order kinetic plot in TCH/UV/$S_2O_8^{2-}$ system: [$S_2O_8^{2-}$]=29,8-148,8 mg/L, t=25 °C and λ=355nm

In the presence of $S_2O_8^{2-}$ ions, the degradation efficiency increased significantly, ranging from 81.46 % to 99.66 % under the following optimal conditions ([TCH] = 28,4 mg/L, T = 25°C, λ = 355 nm, [$S_2O_8^{2-}$] = 119,5 mg/L, t = 50-60 minutes). The corresponding apparent rate constants ranged from 0.0241 to 0.0845 min^{-1} (Figure 2). The predominant reactive species generated in the investigated system at pH values between 2 and 7 is the sulfate radical ($SO_4^{\bullet-}$), which is formed by the photolytic activation of persulfate: $S_2O_8^{2-} + h\nu \rightarrow 2\ SO_4^{\bullet-}$. The effect of pH on the degradation process was also investigated. As the pH increased from 2.6 to 8.5, the degradation efficiency decreased from 97.09 % to 88.75 %, indicated that TCH degradation is more efficient under acidic conditions. Under the optimal conditions, the degradation efficiency in the UV/ $S_2O_8^{2-}$ system approached 100%. TCH contains several electron-rich functional groups, including C=C double bonds, aromatic rings, and phenolic groups, which are susceptible to attack by the free radicals generated in the reaction system. According to the literature [1, 2], electron-donating functional groups enhance the reactivity of the sulfate radical ($SO_4^{\bullet-}$). Consequently, the $-NH_2$ and –OH groups can be attacked by this radical, leading to hydroxylation, demethylation, and decarboxylation of tetracycline hydrochloride. Based on the obtained results, it can be concluded that the UV/$S_2O_8^{2-}$ homogeneous system can be proposed for the degradation of tetracycline hydrochloride (TCH) in aqueous solution.

ACKNOWLEDGEMENTS. T.I.-G., and D.L.N. acknowledge the financial support from the Ministry of Education and Research of the Republic of Moldova (research program no. 011208).

[1] L. Pang, Y. Liu, Z. Meng, et al. *Environ. Sci.: Nano.* **12(12)** (2025) 5116–5145.
[2] I. Ayaka, M. Nichayanan, K. Hideya. *Journal of Water and Environment Technology,* **22(4)** (2024) 194–203.

VISIBLE-LIGHT ACTIVE PHOTOCATALYST. EFFECT OF ELECTROCHEMICAL SYNTHESIS CONDITIONS ON THE PROPERTIES

T. Ya. Datsko[1,*], V. I. Zelentsov[1], D. P. Dvornikov[2]
[1]*Institute of Applied Physics, Moldova State University, Chișinău, Republic of Moldova;*
[2]*D. Ghitu Institute of Electronic Engineering and Nanotechnologies, Techical University of Moldova, Chisinau, Republic of Moldova*
*E-mail: datsko.tatiana@yandex.ru

In recent decades, the use of nanoscale TiO_2-based materials has gained widespread acceptance in photocatalysis, solar cells, and solar-powered hydrogen production. However, the large band gap of anatase (3.2 eV) limits the practical use of visible light, particularly sunlight with wavelengths greater than 387 nm. To enhance the photocatalytic activity of TiO2, numerous studies have been conducted to reduce the band gap by doping the anatase. Cations such as Fe, Cr, Al, Ag, and Mn have been used as dopants, as well as nonmetals such as N, C, and S.

However, the introduction of dopants is often associated with thermal instability, expensive setup, and a significant carrier recombination rate. Among the listed methods for improving the photocatalytic properties of anatase, self-doping TiO_2 by introducing Ti^{3+} defects and oxygen vacancies into the titanium oxide crystal lattice has attracted particular attention. This method produces so-called black TiO_2, which exhibits high absorption of visible light and significant photochemical properties for applications such as the photodegradation of organic pollutants and photocatalytic water splitting.

However, based on the electrode potential, the reduction of Ti^{4+} to Ti^{3+} is difficult under normal conditions, and the resulting Ti^{3+} is very easily reoxidized to Ti^{4+}. Titanium dioxide self-alloying methods are based on "reduction" by heating TiO_2 in a vacuum or a strongly reducing atmosphere, such as H_2 or CO, or by bombarding TiO_2 with high-energy particles (electrons, argon ions). These methods often involve elevated temperatures and pressures, ultrahigh vacuum, and have several limitations in practical application, such as multi-step reactions, harsh conditions, long reaction times, and expensive equipment. Moreover, since reduction reactions typically occur on the surface of TiO_2 particles, the resulting Ti^{3+} can easily be oxidized by O_2 in air or dissolved oxygen in water, reducing the stability of self-doped Ti^{3+} TiO_2.

Thus, developing a simple and cost-effective strategy for synthesizing stable self-doped Ti^{3+} TiO_2 nanoparticles remains a significant challenge.

We have devised and implemented a simple electrochemical method for producing black Ti dioxide nanoparticles under reducing conditions in the cathode chamber of a two-chamber electrolyzer at normal temperature and pressure using titanium tetrachloride as an anatase precursor. Stainless steel and platinum were used as cathode materials. An electric current with a density of 25-100 mA/cm^2 was passed through the catholyte for different periods of time to achieve the required pH.

For comparison titanium dioxide samples were also synthesized in other (non-reductive) experimental settings.

The effect of parameters of electrolysis and subsequent processing, namely- washing procedure, drying mode- in air and at 100^{o}C on the properties of the obtained material were studied.

As a criterion for the photocatalytic activity of the prepared samples under visible light (VIS) the degree of photodecomposition of a standard dye, methylene blue solution, was used. The samples were also tested under UV light irradiation.

To simulate the visible light 150W halogen lamp OSRAM was applied (max at 621 nm). As for UV light irradiation, 120W high-pressure Hg lamp was used (max at 355 nm).

The obtained results show that the synthesized samples have photocatalytic activity: 35% more in VIS and 56% more under UV irradiation than that the control samples. This allows us to assume that the samples have TiO_2/TiO_{2-x} core-shell heterostructure, where the core TiO_2 is crystalline anatase and the shell is disordered TiO_{2-x}.

CALCULATION OF THERMODYNAMIC FUNCTIONS OF METHYLENE BLUE SORPTION ON DIATOMITE

Veaceslav Zelentsov[1,*], Tatiana Datsko[1], Oleg Bolotin[2]
[1]*Institute of Applied Physics, Moldova State University, Chișinău, Republic of Moldova;*
[2]*The institute of Geology and SeismologyUSM, Chișinău, Republic of Moldova*
Email: vzelen@yandex.ru

The effect of temperature on the thermodynamic parameters (changes in molar Gibbs free energy, molar enthalpy, and molar entropy) of methylene blue (MB) sorption from an aqueous solution onto a natural mineral from a deposit near the village of Maramonovka, Donduseni district, Moldova, is considered in this paper. According to X-ray diffraction, chemical, and elemental analyses, this material contains 73.46% SiO_2, corresponds to clay-carbonate diatomite, and was used as a sorbent for the removal of MB dye. The experimental conditions, physicochemical and adsorption-structural characteristics, as well as the equilibrium and kinetic models of sorption are discussed in detail in [1]. Here, at the first stage of the study, experimental kinetic curves of MB sorption were obtained at three different temperatures –20, 30 and 40°C (figures not shown) and they served as the initial data for calculating the thermodynamic parameters of the process (Table 1).

Table 1. Experimental data for calculation of thermodynamic parameters sorption MB

t, °C	C_e. mg/l	C_s, mg/l	K = C_s/C_e	ln K
20°C	1.3	89.2	68.6	4.23
30°C	6.0	84.5	14.1	2.64
40°C	18.0	72.5	4.3	1.39

Note: Co = 90.5 mg/l, m = 0.050 g, v = 0.050 l, mixing speed, rpm/min - 800.

Thermodynamic parameters such as change in free energy (ΔG^0), enthalpy (ΔH^0) and entropy (ΔS^0) were determined using the following equation:

$$K = Cs/Ce;\ \Delta G^o = -R*T*\ln K;\ \Delta G^o = \Delta H^o - T*\Delta S^o;\ \ln K = \Delta S^o/R - \Delta H^o/RT,$$

Where K- is the distribution coefficient, Cs -is the solid phase concentration MB at equilibrium (mg/l), Ce- is liquid concentration of MB at equilibrium (mg/l), R -is the gas constant and equal 8,314 (J/mol*K), T- is absolute temperature in Kelvin. Values ΔH^o and ΔS^0 were obtained from the slope and intercept on plots lnK vs 1/T. The final values of the calculated thermodynamic functions of sorption of MB on diatomite are presented in Table 2.

Table 2. Calculated thermodynamic parameters of the sorption process of MB on diatomite

T, K	ΔG^o, kJ/mol	ΔH^o, kJ/mol	ΔS^0, J/mol
293	- 10.342	-107.325	- 331,1
303	-7.032		
313	-3.722		

The negative values of ΔG^0 confirm the feasibility of the process and the spontaneous nature of adsorption with a high preference of Methylene Blue by diatomite. It is clear (tablte1) that the adsorption of MB on diatomite is exothermic process, because parameter K decrease with rise in temperature. The negative values of ΔH^0 suggest that the process is exothermic, so a decrease of temperature encourages methylene blue adsorption. Negative value of ΔS^0 suggests that enthalpy is responsable for making the ΔG^0 negative *и* and that the degree of freedom of movement of MB molecules on the surface of diatomite is significantly limited.

[1] V.I.Zelentsov, T.Ya.Datsko and O.A.Bolotin, *Surface Engineering and Applied Electrochemistry*, **61(6)** (2025) 890 -897.

SYNTHESIS AND PHYSICO-CHEMICAL CHARACTERIZATION OF TiO_2 – MODIFIED ACTIVATED CARBONS FOR PHOTOCATALYTIC AND ADSORPTION APPLICATIONS

I. Ceban[1,*], R. Nastas[1], N. Timbaliuc[1], I. Nesterovschi[2],
M. Stefan[2], A. Varadi[2], D. Toloman[2], A. Popa[2]
[1]*Institute of Chemistry of Moldova State University, Chisinau, Republic of Moldova;*
[2]*National Institute for Research and Development of Isotopic and Molecular Technologies, Cluj-Napoca, Romania*
*E-mail: irina.ginsari@outlook.com; irina.ceban@sti.usm.md

The increasing demand for sustainable materials with multifunctional properties has stimulated the development of activated carbons derived from renewable agricultural residues. In the present study, nanostructured activated carbons obtained from peach stone, walnut shells and apple wood were synthesized and subsequently modified with titanium dioxide (TiO_2) nanoparticles to produce the same hybrid carbon-based materials with potential applications in environmental remediation. Four activated carbon samples were investigated: AMPC, CAP, AC-MR and AC-1 prepared using different activation methods and biomass precursors. Their physico-chemical and structural characteristics were comparatively evaluated in order to assess the influence of precursor type and preparation method on the final properties of the composites.

The porous structure of the materials was characterized by nitrogen adsorption-desorption analysis (BET), revealing significant differences in specific surface area and pore volume. The activated carbon prepared from walnut shells (AC-1) exhibited the highest specific surface area and the most developed porous network, indicating superior adsorption potential. SEM and TEM analyses confirmed the successful deposition and homogenous dispersion of TiO_2 nanoparticles on the carbon surface, while Raman spectroscopy evidenced the coexistence of graphitic domains and structural defects, which may promote electron transfer and improve photocatalytic performance.

Electrochemical measurements demonstrated that TiO_2 modification significantly enhanced the charge-retention capability of the activated carbon, resulting in higher electrochemical stability compared with the unmodified material. The combination of a highly porous carbon matrix with well dispersed TiO_2 nanoparticles is expected to generate a synergetic effect between adsorption and photocatalysis, improving the efficiency of pollutants removal from aqueous media.

The results demonstrate that agricultural wastes can be successfully transformed into high value carbon-based composites with promising applications in sustainable water treatment and environmental remediation.

Acknowledgments: This work was supported by a grant of the National Research Authority, CNCS-UEFISCDI, Complex Bilateral projects with the Republic of Moldova, within PNCDI IV / 44PCBROMD / 01/09/2025) (project code PN-IV-PCB-RO-MD-2024-0349 and by a grant of the National Agency for Research and Development (NARD RM), Complex Bilateral projects with the Republic of Moldova, PCB-RO-MD-2024, project code: PN-IV-PCB-RO-MD-2024-0349/25.80013.7007.39ROMD

[1] B. Tryba. *International Journal of Photoenergy* (2008) 15 pages. Doi: https://doi.org/10.1155/2008/721824

DEVELOPMENT OF CITRIC ACID-MODIFIED ACTIVATED CARBONS FROM WALNUT SHELL BIOMASS: STRUCTURAL, CHEMICAL AND SURFACE CHARACTERIZATION

I. Ceban[1,*], C. Vicol[1], E. Moraru[1], M. Buga[1], M. Rusu[1], V. Ceban[1], S. Moldovanu[2], M. Mihet[3]
[1]*Institute of Chemistry of Moldova State University, Chisinau, Republic of Moldova;*
[2]*Institute of Applied Physics of Moldova State University, Chisinau, Republic of Moldova;*
[3]*National Institute for Research and Development of Isotopic and Molecular Technologies, Cluj-Napoca, Romania*
*E-mail: irina.ginsari@outlook.com; irina.ceban@sti.usm.md

The conversion of agricultural residues into value-added carbon materials represents a sustainable approach for waste management and the development of efficient adsorbents for environmental applications [1]. Walnut shells, an abundant lignocellulosic waste generated by the walnut processing industry, are promising precursors for activated carbon production due to their high carbon content, low ash fraction and renewable nature. In the Republic of Moldova, large quantities of walnut shell residues are generated annually, providing an attractive local resource for the preparation of sustainable carbon-based materials.

The activated carbons were prepared from walnut shells using citric acid as an environmentally friendly activating agent. The influence of thermal treatment conditions on the physico-chemical properties of the obtained carbon materials was investigated. The samples were characterized by elemental analysis, Fourier-transform infrared spectroscopy, scanning electron microscopy coupled with energy-dispersive X-ray spectroscopy, nitrogen adsorption-desorption measurements, thermogravimetric analysis and antioxidant properties.

The obtained results demonstrated that citric acid activation promotes the development of oxygen-containing surface functionalities, including hydroxyl, carbonyl and carboxylic groups, which contribute to the chemical reactivity of the carbon surface (Figure 1).

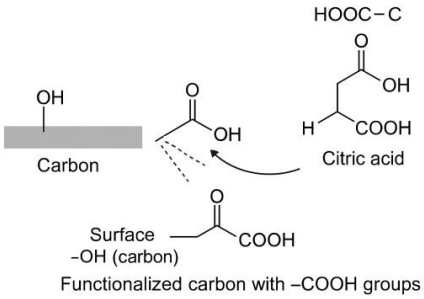


Figure 1. Functional groups on the surface of activated carbon by activation with citric acid

FTIR analysis confirmed the preservation of oxygenated groups (-OH, C=O, -COOH) after carbonization, while elemental analysis indicated an increase carbon content (~ 84%) and progressive removal of volatile components during thermal treatment. BET measurements revealed the formation of a porous structure, with textural parameters strongly dependent on activation temperature. SEM observations showed heterogeneous carbon surface characterized by cavities and irregular pores generated during the carbonization process, while EDX analysis confirmed carbon and oxygen as the predominant surface elements. The samples showed negative inhibition values (3.0% and -76.8%) indicating signal enhancement caused by possible pro-oxidant effects oe assay interference.

This study demonstrates that walnut shell waste from the Republic of Moldova can be successfully transformed into functional activated carbons through a greener citric acid activation route, contributing to the principles of circular economy and sustainable water treatment technologies.

ACKNOWLEDGMENT. This work was carried out within the project *"Valorization of local waste by obtaining activated carbon for water treatment"*, supported under the Program for Young Researchers, 25.80012.7007.17TC.
[1] M. Yaman, M. H. Demirel. *Pollution*, **6** (2020), 935-944.

REMOVAL OF Fe(II) IONS ON CARBONACEOUS CATALYSTS AT DIFFERENT pH CONDITIONS

I. Ceban[1,*], R. Nastas[1], T. Lupascu[1]
[1] *Institute of Chemistry, Moldova State University, Chisinau, Republic of Moldova*
*E-mail: irina.ginsari@outlook.com; irina.ceban@sti.usm.md

The development of efficient catalysts for removal and transformation of iron species from aqueous system is of significant interest in water treatment technologies. In present study, the catalytic oxidation behavior of Fe(II) ions was investigated using two carbonaceous materials, namely ACCN-H_2O activated carbon and Fe-4 iron containing catalyst. The ACCN-H_2O material was obtained from lignocellulosic precursor through physical-chemical activation with water steam, while Fe-4 catalyst was synthesized by a hydrothermal method.

The ability of these materials to promote Fe(II) ions removal by adsorption and/or oxidation to Fe(III) species was evaluated under static conditions over a broad pH range (2-10). The obtained results revealed a strong dependence of iron transformation processes on the solution acidity, which governs both the surface charge of carbon materials and the speciation of dissolved iron ions. At acidic pH values, protonation of surface functional groups limited Fe(II) oxidation (for ACCN-H_2O ~ 3.85 - 26.9%, for Fe-4 ~ 4.5%), while with increasing pH, deprotonation of oxygen containing groups facilitated complexation processes. These progressive increase in Fe(II) oxidation efficacy at neutral and alkaline pH values was associated with enhanced oxidation reactions (ACCN-H_2O ~ 85.42 - 95.19% and for the Fe-4 sample ~ 41.53 - 53.27%) promoted by surface functional groups and iron containing active sites.

Comparison of two materials demonstrated distinct catalytic behaviors. The sample ACCN-H_2O showed high oxidation capacity due its developed porous structure and abundance of surface oxygen functionalities, whereas Fe-4 exhibited enhanced catalytic activity related to the presence of iron species incorporated during hydrothermal synthesis, which can act as active centers for electron transfer and Fe(II)/Fe(III) redox transformation.

The obtained findings highlight the potential of carbon-based materials, both metal free and iron modified, as promising catalysts for the oxidation of Fe(II) ions, providing valuable insights into the design of sustainable materials for water purification applications.

Acknowledgements: This research was funded by the subprogram "Advanced research in computational and ecological chemistry, identification of technological procedures for treatment, formation of water quality and quantity" (code 010603) of the Institute of Chemistry of Moldova State University.

IN-SITU REAL TIME MEASUREMENT OF LASER INDUCED DAMAGE THRESHOLD OF METALLIC THIN FILMS USED FOR NS AND FS LASER MIRRORS

C Milos[1,*], D. Craciun[1], R. Udrea[2], P. Garoi[2], S.A. Irimiciuc[1], G. Dorcioman[1], G. Bleotu[3], F. Al-abedj[3], P. Pandele[3], R. Radoi[3], E. Matache[3], S. Das[3], D. Sandu[3], D. Cracana[3], T. Jitsuno[3], A. Tanaseanu[3], D. Ursescu[3], V. Craciun[1,3]

[1]*National Institute for Laser, Plasma and Radiation Physics, Magurele, Romania*

[2]*Apellaser, Mogosoia, Romania*

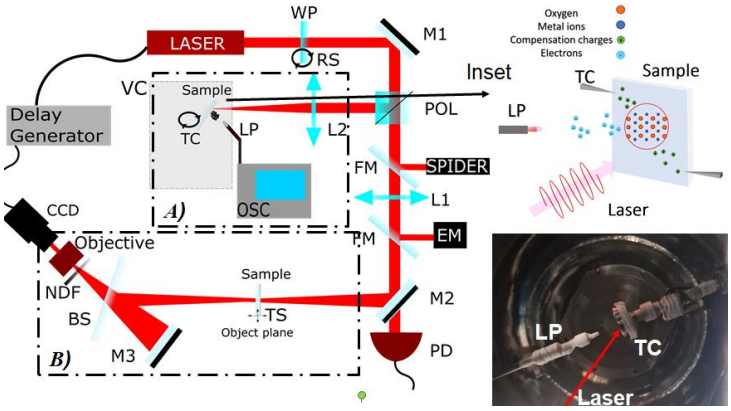
[3]*Extreme Light Infrastructure for Nuclear Physics, IFIN-HH, Magurele*

*E-mail: cristi.milos@gmail.com

This study investigates the behavior of metallic mirrors subjected to laser induced damage threshold (LIDT [1]). Specifically, silver and aluminum mirrors were systematically examined. Al and Ag thin films were deposited using rf magnetron sputtering. The LIDT values for these mirrors were obtained using optical microscopy investigations as well as Langmuir probe and compensating target current measurements.

Ag and Al thin films were deposited using rf-MS technique on fused quartz substrates at room temperature. After deposition, the structure of the films was investigated using X-ray reflectivity and X-Ray diffraction and the composition by X-ray photoelectron spectroscopy.

Experimental setup:



An alternative method for estimating LIDT is introduced in this context, relying on a combination of Langmuir Probe and Target Current measurements. This innovative approach provides an alternative path to assess the LIDT of optical materials.

1-on-1 and S-on-1 LIDT tests were performed in vacuum and air for several samples (Al, Ag) with different carbon thicknesses.

The quantitative detection of the contamination was validated through dispersion measurements. With the increase of the incidence angle the sensitivity of the dispersion method can be increase.

The plasma (dielectric discharge in Ar and O_2) cleaning shows an 88% (LIDT) and 95%+ (dispersion) properties recovery.

[1] ISO 21254-1-4, Lasers and laser related equipment – Test methods for laser induced damage threshold – Part 1-4.
[2] P.G. Bleotu et.al, Exploring fs-laser irradiation damage subthreshold behavior of dielectric mirrors via electrical measurements, High Power Laser Science and Engineering 12 (2024) e15.
[3] G- P. Bleotu et al., LIDT station development with femtosecond pulses at ELI-NP, in: Laser-Induced Damage in Optical Materials 2022, SPIE, 2022.

INCORPORATION OF SnS_2 IN NANOFIBERS FOR PHOTOCATALYTIC APPLICATIONS

C. Creciunel*, A. Tiron, V. Ciobanu, A. Mamoico, T. Galatonova, E. Rusu, I. Tiginyanu
National Center for Materials Study and Testing, Technical University of Moldova, Chisinau, Moldova
*E-mail: catalin.creciunel@cnstm.utm.md

Tin disulfide (SnS_2), a two-dimensional layered semiconductor, is a promising material for photocatalytic applications due to its suitable band gap, high chemical stability, and unique layered crystal structure [1]. In this work, SnS_2 crystals synthesized by chemical vapor transport (CVT) were subjected to ultrasonic treatment to produce micro- and nanostructures for subsequent incorporation into composite ZnO/SnS_2 nanofibers by electrospinning technique.

Ultrasonic processing resulted in particles with characteristic sizes ranging from **50 to 1000 nm**. This size distribution increases the specific surface area and the number of catalytically active sites, which are essential for improving photocatalytic performance. The obtained SnS_2 structures are considered as functional fillers for polymer composite fibers, where they are expected to enhance photocatalytic activity while maintaining the mechanical integrity of the fiber matrix [2].

The morphology of the samples was investigated by scanning electron microscopy (SEM). SEM analysis revealed that ultrasonic treatment effectively fragmented the as-grown CVT crystals while preserving the characteristic platelet-like morphology of SnS_2. The samples consisted of individual nanosheets and thin platelets smaller than 1000 nm. The observed particle size distribution indicates successful exfoliation of the material without significant destruction of its crystalline structure, which is essential for the fabrication of composite fibers with uniformly distributed photocatalytic fillers.

The structural properties of the obtained materials were further characterized by Raman spectroscopy. The Raman spectra of all samples exhibited a pronounced $\mathbf{A_1g}$ vibrational mode of hexagonal SnS_2 located at approximately **315.2 cm^{-1}**, confirming that the crystal structure was preserved after ultrasonic treatment [3]. No additional Raman bands associated with tin oxides or other tin sulfide phases were detected, indicating the high phase purity of the synthesized material.

For the preparation of ZnO/SnS_2 nanofibers, a solution consisting of PVA, zinc acetate and SnS_2 nanosheets was prepared with concentrations of 4 wt%, 10 wt%, and 0.5 wt%, respectively. The nanofibers were produced at 20 kV at a distance of 10 cm from the needle syringe to the collector. The EDX analysis showed the presence of the desired elements and their stoichiometry into the nanofiber structures. The obtained composite nanofibers will be further investigated for environmental applications, including the photodegradation of organic pollutants and water purification under visible-light irradiation.

ACKNOWLEDGEMENTS. This work was supported by the "Young Researchers" project #25.80012.5007.38TC.

[1] M. Chhowalla, H. S. Shin, G. Eda, L.-J. Li, K. P. Loh, H. Zhang, *The chemistry of two-dimensional layered transition metal dichalcogenide nanosheets.* ***Nature Chemistry***, **5**, 2013, pp. 263–275. **DOI:** 10.1038/nchem.1589
[2] D. Voiry, A. Mohite, M. Chhowalla, *Phase engineering of transition metal dichalcogenides.* ***Chemical Society Reviews***, **44**, 2015, pp. 2702–2712. **DOI:** 10.1039/C5CS00151J
[3] L. A. Burton, D. Colombara, R. D. Abellon, F. C. Grozema, L. M. Peter, T. J. Savenije, G. Dennler, A. Walsh; Synthesis, Characterization, and Electronic Structure of Single-Crystal SnS, Sn_2S_3, and SnS_2. *Chemistry of Materials*. **25,** 2013, pp. 4908–4916. **DOI:** 10.1021/cm403046m

COMPARISION OF UV, UV/H_2O_2 AND UV/$S_2O_8^{2-}$ PROCESSES FOR THE DEGRADATION OF ROSUVASTATIN IN AQUEOUS SOLUTION

E. I. Tutovan*, T. V. Isac-Gutul
D*epartment of Chemistry, Moldova State University, Chisinau, Republic of Moldova*
*E-mail: elenatutovan@gmail.com

Elevated levels of Low-Density Lipoprotein (LDL) in the blood are one of the main risk factors for cardiovascular disease. Statins are increasingly being used to lower LDL levels in the blood [1].

Statins are present in wastewater. For example, the maximum concentration of rosuvastatin in wastewater reaches 979 ng·L^{-1} [2]. This drug is largely not metabolised, and 77% of it is excreted from the body unchanged. Statins are potential pollutants of ecosystems, which may have adverse effects on aquatic organisms and lead to their accumulation in the human body [3].

Advanced oxidation processes (AOPs) are highly promising methods for removing organic pollutants from wastewater. Their mechanism of action is based on the generation of $^{\bullet}OH$ [4] and $SO_4^{\bullet-}$ [5] radicals, which are strong oxidizing agents capable to oxidize organic contaminants to the high mineralization degree.

In this abstract there are presented the results of a comparative study of Rosuvastatin (RS) degradation in aqueous solution by UV, UV/H_2O_2 and UV/$S_2O_8^{2-}$ processes.

It was established that the degradation efficiency (DE, %) of RS by applied processes increases as follows: UV < UV/H_2O_2 < UV/$S_2O_8^{2-}$ (Fig. 1).

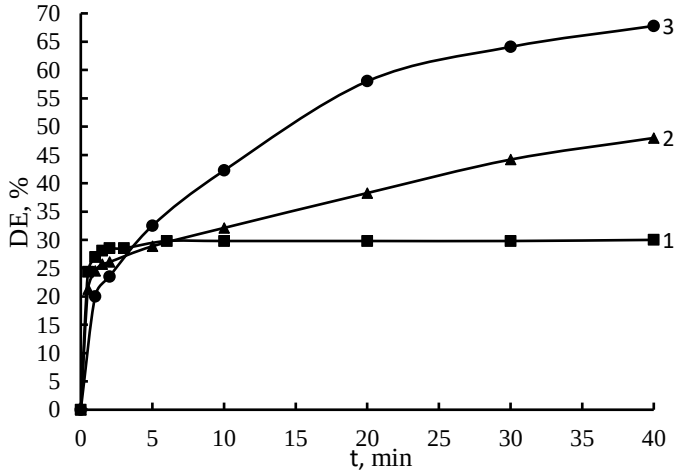


Figure 1. RS degradation efficiency vs reaction time for the processes: (1) UV (pH=6.0); (2) UV/H_2O_2, (pH=6.0, c(H_2O_2)=1.0×10^{-3} M); (3) UV/$S_2O_8^{2-}$ (pH=3.0, c($S_2O_8^{2-}$)=1.0×10^{-4} M (c(RS)=20 mg×L^{-1})

It was found that RS degradation efficiency increases with a decrease in the drug concentration in all three systems, and with an increase in the concentration of H_2O_2 in the UV/H_2O_2 system. In the case of the UV/$S_2O_8^{2-}$ system, DE decreases with a significant increase of the $S_2O_8^{2-}$concentration. In the UV and UV/H_2O_2 systems, the highest DE of drug is achieved at pH = 6.0, and in the UV/$S_2O_8^{2-}$ system - at pH = 7.0. It was established that under UV irradiation, the reaction doesn't follow either pseudo-first-order or pseudo-second-order kinetics. In the UV/H_2O_2 and UV/$S_2O_8^{2-}$ systems the reaction follows the pseudo-first-order kinetics.

[1] F. Mach, C. Baigent, A. Catapano, A., et al. *European Heart Journal*, 41 (2020), pp. 35-46.
[2] N. Beqqal, M. Sh. Yahya, M. E. Karbane, et al. *Journal of Materials and Environmental Science*, 12 (2017), pp. 4399-4407.
[3] D. M. Souza, J. F. Reichert, V. R. Do Nascimento, et al. *Open Science Research*, 5 (2022), pp. 528 – 540.
[4] P. K. Pandis, Ch. Calogirou, E. Kanellou, et al. *Chemical Engineering*, 6 (2022), 22 p.
[5] F. Juni, M. J. Bashir, Z. H. Jaffari, et. al. *Separations*, 10 (2023), 18 p.

ELECTRODEPOSITION OF IRON ALLOYS FROM CITRATE AND GLUCONATE ELECTROLYTES

S. Kh. Ivashku*, Zh. I. Bobanova, S. P. Yuschenko, S.M. Iatco
Moldova State University, Institute of Applied Physics, Chișinău, Republic of Moldova
*E-mail: sergiu.ivascu@gmail.com

Electrodeposition of iron alloys from complex electrolytes (citrate or gluconate) containing Zn, Ni, Co salts, as well as salts of refractory metals (W, Mo), made it possible to obtain alloys with a new chemical and phase composition possessing a nanocrystalline structure.

The formation of a nanocrystalline structure makes it possible to obtain materials with superior physical and mechanical properties (microhardness, wear resistance, and corrosion resistance) compared with coatings having a coarse-grained structure.

Wear resistance was studied using a reciprocating sliding wear testing machine. Microhardness was measured with a PMT-3 microhardness tester. The oxidation kinetics of the alloys were determined using a MOM derivatograph over the temperature range of 20–1000 °C at a heating rate of 5 °C/min. Phase transformations were investigated by X-ray diffraction analysis. Diffraction patterns were recorded using a URS-50M diffractometer with Co Kα radiation. The chemical and phase compositions, as well as the features of the crystal structure affecting the properties of the electrochemical coatings, were investigated.

The microhardness of Fe–Ni alloys increases almost proportionally with current density as the concentration of potassium sodium tartrate is increased up to 5 g/L. X-ray diffraction patterns of Fe–Zn coatings indicate the formation of a highly dispersed solid solution with a lattice parameter of a = 2.900 Å. The wear resistance of Fe–Zn alloys increases with increasing cathodic current density and exceeds that of electrodeposited iron and cast iron. Fe–Co alloys are used for restoring the strength of worn components because, while maintaining sufficiently high hardness, they are less susceptible to cracking. As the current density increases, the wear resistance of iron alloys decreases, and their hardness is also reduced. Iron–zinc alloys with a hardness below 2 GPa undergo scuffing at contact pressures of 2.5–5.0 MPa. This should be taken into account when restoring components operating under wear conditions. Fe–Co alloys are used for restoring the strength of worn components because, while maintaining sufficiently high hardness, they are less susceptible to cracking. As the current density increases, the wear resistance of iron alloys decreases, and their hardness is also reduced. Iron–zinc alloys with a hardness below 2 GPa undergo scuffing at contact pressures of 2.5–5.0 MPa. This should be taken into account when restoring components operating under wear conditions.

The study of Co–W alloy deposits obtained from a gluconate electrolyte showed that, with increasing tungsten content in the coating, the alloy forms a solid solution containing the intermetallic compound Co_3W.

Electrodeposition of Co–W alloys from concentrated electrolytes showed that comparison of various electrolytes with increased component concentrations relative to the base electrolyte supports maintaining the ligand concentration at the level used in the base electrolyte. In such electrolytes, the current efficiency increases to 90–95%. The use of these electrolytes makes it possible to maintain an almost constant microhardness over the current density range of 3–5 A/dm².

The formation of a nanocrystalline structure makes it possible to obtain materials with high physical and mechanical properties. The hardness of nanocrystalline Co–W coatings is higher than that of their coarse-grained counterparts.

The production of materials with a nanocrystalline structure exhibiting a favorable combination of strength and ductility is a promising direction.

A

Aazou S. 75
Abashkin V. 160, 162, 170
Achimova E. 160, 162, 170
Acik I. O. 167
Airinei A. 97
Akhmedova R. 91
Al-abedj F. 196
Andronic S. C. 63
Anefnaf I. 75
Arama E. 80
Arîcu A. 124, 126
Arion V. B. 138
Arushanov E. 75, 77, 85
Avdeev M. 65
Avdeev V. 113
Avram A. 27

B

Baca S. G. 58, 87, 92, 98, 99, 100, 101, 117, 118, 120
Balan G. K. 89, 135, 188
Balan I. 125, 128, 139
Balan-Porcarasu M. 133, 138
Baranov S. A. 155
Barba A. 95
Barladean S. 156
Barsuk A. A. 34
Batanov A. S. 89
Batîr V. 75, 77, 85
Bayer M. 45
Beanland R. 70
Bejan D. 109
Beleaev E. 58, 92, 99, 100, 101
Belenchuk A. 158, 161
Belevskiy S. S. 179
Belotercovschii I. I. 154
Bercu E. 173
Besleaga C. 167
Besliu A. 90, 131, 133
Birgoanu A. M. 134
Blacha-Grzechnik A. 175
Bleotu G. 196
Bobanova Zh. I. 199
Bocirnea A. E. 167
Boian V. I. 150
Bolocan N. 95, 140
Bolotin O. 192
Boris Iu. B. 43
Bosneaga Iu. 96
Botnari V. 160, 162, 170
Bourosh P. N. 104, 105, 106, 108, 110, 113, 116, 127, 129, 130
Bragari D. 153
Braniste T. 146
Brinzari V. 49
Brüx D. 100, 101, 117
Buga M. 194
Bulhac I. 69, 71, 72, 104, 105, 106, 107, 116
Bulimestru I. 123
Buse G. 26
Buttari B. 140
Buzdugan A. 69

C

Capbătut O. 117, 118
Caragacian S. I. 43
Caramitu A. R. 185
Cârlig S. 64
Casian I. 90, 131, 133
Casian A. 90, 131, 133
Cazac V. 160, 170
Cazacu M. 138
Ceabanova M. P. 119, 135, 136, 141
Ceban C. 133
Ceban I. 139, 193, 194, 195
Ceban V. 52, 194
Cebotari I. 52
Cebotaru P. 102
Cecoi E. 56
Celiberti L. 30
Cernica I. M. 61, 62
Cesiulis H. 32
Chertopalov S. 24
Chetruș P. I. 173
Chiaburu A. 90, 131, 133
Chirita A. 164
Chumakov Yu. 58, 104, 105, 106, 114
Cichoň S. 24
Ciobanu N. 46, 140
Ciobanu V. 197
Ciocârlan A. 124, 126
Ciornea V. 56, 64
Ciubotaru B.-I. 90, 131, 138
Ciursin A. 88, 174
Cliucanov A. 159
Cocemasov A. 49
Cocu M. 104, 106
Cojocaru I. 69, 71, 163
Cojocaru S. 35
Colibaba G. V. 79, 81, 82, 84, 167
Condrea E. P. 73, 154

Constantinov B. 171
Coretchi I. 90, 131, 133
Cotovaia A. S. 127
Covaliova O. 181
Cracana D. 196
Craciun D. 196
Craciun N. 103
Crăciun V. 24, 158, 161, 196
Creciunel C. 197
Crisan M. E. 110
Croitor L. 110
Croitori D. 68, 78
Croitoru D. 182, 184
Cuba L. 72
Cudreașov A. 52, 60
Cuharuc A. 137
Culeac I. 69, 71, 72, 107
Curicheru G. I. 186, 187
Curmei N. 75, 77, 85
Cuzan O. 102, 112
Czichy M. 175, 176

D

Danilescu O. 104, 105, 106, 107
Das S. 196
Dascalu M. 138
Datsko T. Ya. 191, 192
Deisenhofer J. 23
Derivolcova R. 118
Dermenji L. 75, 77, 85
Dina N. E. 93, 135, 141
Dinescu A. 27
Diru M. 59
Dobrovolschi V. 53
Dohotaru L. 35
Donten M. 32
Dorcioman G. 196
Dragancea D. 122
Dragland R. S. 70
Dragoman D. 27
Dragoman M. 27
Druta V. 121
Dub M. 25
Duca Gh. 95, 181
Dvornikov D. P. 74, 166, 191

E

Enachescu M. 69, 71
Ernits K. 65

F

Feldman D. 93
Filippova I. 68, 78
Fomin V. M. 28, 150
Fonari M. S. 103, 113
Franchini C. 30

G

Gajewska B. 175
Galatonova T. 197
Galca A. C. 167
Garbuz O. S. 127, 129, 130
Garí-Galíndez J. 33
Garoi P. 161, 196
Geru I. I. 41, 94
Ghenea V. 69, 71, 72, 107
Ghergishan I. Gh. 152
Gherman C. 64
Ghileț chii Gh. 88, 158, 159, 161
Ghimpu L. 168
Goglidze T. 76
Goncearenco E. 76
Gonta M. 177
Gorbaciov M. 128
Gorceac L. 173
Goremichin V. 157
Gorinchoy N. 128
Gorinchoy V. 111, 112
Gorincioi E. C. 89, 93, 95, 135, 140, 141
Gorobet A. 110
Gorobets M. I. 189
Goryunov Yu. 83
Grabco D. 147
Graur I. I. 129, 130
Graur V. O. 127, 129, 130
Grecu G. D. 180
Grendal O. G. 68, 70, 78
Grossberg-Kuusk M 67
Grumezescu V. 24, 161
Gubceac N. 46, 54
Guc M. 33, 66, 75
Gulea A. P. 86, 88, 127, 129, 130, 174
Gurieva G. 65, 66, 67, 85
Gutsul T. D. 154

H

Hahn T. 30
Hitsiuc M. 137
Houtput M. 30
Hruška P. 24
Huber T. E. 151, 152

I

Ianachevici A. 182, 183, 184
Iațco Sp. 182, 184, 199
Inculet I. 79
Ion I. 182, 185
Irimiciuc Ș.-A. 24, 158, 161, 196
Isac-Gutul T. V. 190, 198
Isar A. 44, 50, 56

Israr-Qadir M. 33
Ivanov O. 42
Ivaşcu S. 182, 183, 184, 185, 199
Izquierdo-Roca V. 33, 66

J

Jitsuno T. 196
Jovmir T. 115

K

Kanarovskii E. Yu. 55, 57
Kareva N. 176
Katerski A. 167
Kauk-Kuusik M. 67
Kazak N. 137, 183
Kézsmárki I. 68
Kirkham M. 65
Klimin S. N. 30
Klokishner S. I. 37, 39, 40
Knap W. 25
Kögerler P. 87, 98, 100, 101, 117
Koltsov M. A. 79, 84, 167
Konopko L. A. 151, 152
Kopteva N. E. 45
Korona T. 38
Korotyeyev V. 25
Kravchuk I. S. 127
Kravtsov V. Ch. 87, 98, 99, 103, 106, 118, 120, 127
Kubritskaya T. D. 188
Kulikova O. 105, 106, 110
Kulyuk L. 149, 157

L

Lančok J. 24, 158
Łapkowski M. 175
Lascova-Baciu R. I. 179
Lisunov K. G. 77
Losmanschii C. 160, 162, 170
Lozan V. 102, 109, 111, 114, 115, 121
Lungu I. 59, 97, 168
Lungu M. V. 124, 126
Lungu L. 182, 185
Lungulescu E. M. 185
Lupascu T. 139, 195

M

Macaev F. Z. 89, 91, 93, 94, 119, 135, 136, 140, 141
Macavei S. 139
Macovei M. A. 44, 47, 56, 60, 64
Maistruc I. 173
Malik R. 175
Mammadov B. A. 91
Mamoico A. 197
Mangalagiu I. I. 134
Manjon Sanz A. 65
Manta E. 185
Marešová E. 24
Marinescu V. E. 182, 185
Matache E. 196
Matijević Glavan T. 141
Mehrabyan V. 42
Meier D. 70
Meissner D. 65
Melnic E. I. 69, 107, 129, 130
Melnic S. 109, 112
Meshalkin A. 160, 162, 163
Micu A. 149
Mihaescu T. 44, 51
Mihailov V. 182, 183, 184, 185
Mihet M. 194
Milev P. 48
Milos C. 196
Mînăscurtă M. 115
Mindrescu B. 123
Mirovski V. 169
Mishchenko A. S. 30
Moca C. P. 31
Mocanu L. 177
Moldovanu S. 68, 78, 79, 82, 160, 194
Moldoveanu C. 134
Monaico E. I. 145, 168
Monaico E. V. 145, 165, 168
Morari R. 150
Morari V. 142, 153, 165, 168
Moraru E. 194
Moroz O. 128
Motyka R. 175
Muntean D. 160, 162, 170

N

Narolschi Ig. 158, 161, 172
Nasedchina N. 164
Nastas R. 125, 139, 193, 195
Nateprov A. 83
Neamtu M. 119, 136
Nedeoglo D. 76
Nedeoglo N. 76
Neguta E. 114
Nesterovschi I. 139, 193
Nica S. L. 133
Nicorici V. 161, 172
Niemi E. 33
Nika D. L. 43, 49, 190
Nikolaeva A. A. 151, 152

O

Olaru I. N. 187
Oloinic T. 148
Orlita M. 25
Ostrovsky S. 37, 39

P

Paladi F. 34
Paladii I. V. 178
Palamarciuc O. 138
Paleari F. 48
Pandele P. 196
Pantazi A.-G. 69, 71
Papchenko A. Ya. 180
Para Gh. I. 152
Parvulescu C. 27
Pătroi D. 182, 185
Pavlovschi E. 90
Peptanariu D. 131, 133, 138
Pérez-Rodríguez A. 33, 66
Pershina K. D. 189
Pintea V. 86
Pîntea A. 80
Podgornîi D. 85, 87
Pogrebnoi V. S. 119, 126, 136
Poienar M. 26
Policarpov A. A. 178
Popa A. 139, 193
Popa N. 123
Popescu C. M. 169
Potlog T. 59, 97
Prell H. 67
Prisacaru A. 147, 169
Prodan L. 68, 78
Profumo E. 140
Pyrtsac C. 137, 147

R

Radoi R. 196
Radu C. 167
Ragni S. 30
Rastimesina I. O. 154
Ratajczyk T. K. 32
Reu O. 39, 40
Robu Ș. 59
Rodriguez N. P. 150
Roman G. 111, 114
Romanciuc L. 181
Rotari A. 47, 52
Rotaru V. 66
Rubio R.-F. 33
Rusnac R. 81, 82, 167
Rusnac D. 86, 88, 174
Rusu S. 144, 153, 165, 168, 197
Rusu E. V. 67, 140, 158, 161, 172, 194
Rusu M. 53, 148
Rzayev R. 91, 94

S

Sai P. 25
Sandu D. 196
Sanduleac I. I. 63
Sangalli D. 48
Scafaru A. 173
Scheiter J. 150
Schörnig C. 26
Schorr S. 22, 65, 66, 67
Sekkat Z. 75
Senn M. 70
Serban N. 137
Sergeev S. 163
Shapoval O. 158, 161
Sharagov V. A. 186, 187
Shemyakova T. D. 80, 188
Sheptyakov D. 65
Shikimaka O. 137, 147
Shova S. 68, 78, 86, 89, 102, 109, 111, 112, 114, 115, 121, 122, 123, 124, 136, 138, 174
Sibaev A. J. 154
Sidorenko A. S. 143, 150
Siminel N. 69, 74, 114, 149, 166
Siminel A. V. 65, 149, 156, 157
Simion A. 93
Simionescu O. 27
Sirkeli V. P. 36, 43, 76
Sjøkvist R. 70
Skourski Y. 87
Slavescu R. R. 54
Slobodeniuc C. 149, 157
Soracá-Pérez G. Y. 33
Spalatu N. 79, 81, 82, 84, 167
Spoială D. 147, 160, 172
Sprincean C. Gh. 178
Stamov I. G. 144
Stati D. 98
Stef M. 26
Stefan M. 139, 193
Stegariov V. 59
Stepurina T. G. 178
Stîngaci E. 119, 135, 141
Stoica A. C. 50, 138
Sucman N. S. 89, 91, 94, 119, 136, 140
Sulaiman A. 131
Suman V. 132, 153, 165, 168

T

Talmaci N. 122
Tălpeanu D. 182, 185
Tanaseanu A. 196
Tasca C. 181
Tataringa G. 134
Tempere J. 30
Tiginyanu I. M. 142, 145, 146, 197
Tigoianu I.-R. 90
Tigoianu R. 97
Timbaliuc N. 193
Tiron A. V. 144, 197
Toloman D. 139, 193
Torosyan V. 42
Trifonova T. V. 189
Trofaila A. 120
Tronciu V. 46, 53, 54, 148
Tsapkov V. I. 86
Tsapkov V. 129, 130
Tsirlin A. 68
Tsurkan V. 20, 68, 78
Tsyntsaru N. 32
Tutovan E. I. 198

U

Udrea R. 196
Untila D. 167
Ureche D. 116
Ursaki V. V. 142, 145
Ursescu D. 196
Ursu V. 168
Usenco D. 77, 85

V

van Leusen J. 87, 100, 101, 117
Vanyan D. 42
Varadi A. 139, 193
Varzari A. 158, 159, 161
Vasil'ev A. 42
Vatavu S. 24, 88, 158, 159, 161, 164, 172, 173
Vatavu E. 172
Veber P. 26
Verlan V. 69, 71
Vicol C. 95, 126, 194
Vidal-Fuentes P. 33, 66
Vitiu A. A. 108
Vizman D. 26
Voda I. 121
Volfova L. 24
Vrabie E. Gh. 178
Vrabie V. Gh. 178
Vuković Đerfi K. 141

W

Więckowska A. 38

Y

Yakovlev D. R. 45
Yaltychenko O. V. 55, 57
Yaprintsev M. 42
Yuschenko S. P. 199

Z

Zalamai V. V. 85, 144, 168
Zaltariov M.-F. 90, 131, 133
Zaporojan S. 54
Zappacosta I. 30
Zbancioc A. M. 134
Zbancioc G. 134
Zdunek K. 38
Zeiger C. R. 70
Zelentsov V. I. 191, 192
Zherlitsyn S. 29
Zhezhu M. 42
Zhukov E. A. 45

11TH INTERNATIONAL CONFERENCE ON MATERIALS SCIENCE AND CONDENSED MATTER PHYSICS

SEPTEMBER 1-4, 2026

Bun de tipar 24.08. Formatul *70x100 1/12*
Coli de tipar 18,4
Comanda 71/26. Tiraju 210 ex.

Centrul Editorial-Poligrafic al USM
str. Al. Mateevici, 60, Chișinău, MD-2009
email: cep1usm@mail.ru; usmcep@mail.ru